Selective Area Epitaxy of GaN-Based Nanowire Heterostructures for Applications in Photonic and Electronic Devices

Renjie Wang

Department of Electrical and Computer Engineering
Faculty of Engineering
McGill University
Montreal

July 2018

A thesis submitted to McGill University in partial fulfilment of the requirements of the degree of Doctor of Philosophy

To my wife Shasha Lyu and my family

Table of Contents

Abstract

The development of optoelectronic devices and electronic devices made using conventional GaN-based planar heterostructures is ultimately restricted by the challenges in growing high-quality In-rich InGaN planar heterostructures, using mismatched substrates and/or device fabrications. Moreover, extensive demanding applications require the use of micro-scale and nano-scale GaN-based materials and devices for the integration of optoelectronic devices into a limited space, the integration of dense optoelectronic devices into larger scale systems, or the shrinkage of overall systems. Dislocation-free GaN-based nanowires have emerged as a promising candidate for applications in photonic and electronic devices. This dissertation focuses on the development of GaN-based nanowire heterostructures by using molecular beam epitaxy (MBE) as well as their device applications.

Through the monolithic integration of spontaneously grown blue, green, red (RGB) and yellow/orange InGaN nanowire LEDs on Si substrates, controllable and tunable full-color light generations are demonstrated using a three-step selective-area growth process with SiO_x mask created on Si substrates. The lateral-arranged monochromatic subpixels enable controlled light mixing at the chip level and exhibit color-tunable light emissions with correlated color temperature values in the range from 1900 K to 6800 K, while maintaining excellent color rendering capability.

Selective area epitaxy (SAE) enables one to precisely control the size, position and morphology of nanowires, and hence enables one to precisely control and tune nanowire emission wavelength. Through SAE of RGB InGaN-based nanowire arrays on GaN/sapphire substrate with Ti mask defined by using high-resolution lithography, the overall RGB pixel size was 7×7 μm^2 with monochromatic subpixel sizes of 2.8×2.8 μm^2. By incorporating InGaN quantum dots in single GaN nanowires, diameter-dependent emissions tuning from blue to red were achieved from the single GaN-based nanowires on the same substrate and its mechanism

was investigated. Based on this achievement, we have developed, for the first time, the world's smallest pixel size full-color InGaN/GaN single nanowire LED pixel optimized for ultra-fine projection displays using only one step epitaxial growth process.

Spontaneously grown AlInGaN quaternary core-shell nanowire heterostructures are demonstrated on Si substrate, wherein an In-rich core and an Al-rich shell were spontaneously formed during the epitaxial growth process. Such core-shell structures can largely suppress nonradiative surface recombination, leading to a significant enhancement of carrier lifetime from ~ 0.2 ns to ~ 2 ns and output power. By varying the growth conditions, the emission wavelengths can be tuned from ~ 430 nm to ~ 630 nm.

Electrical transport properties of vertical-aligned GaN single nanowires on Si substrate have been systematically studied by *in-situ* nanoprobing in a SEM chamber. A current density up to 4.65 MA/cm^2 has been achieved from a single GaN nanowire selective-area grown on Si substrate, promising the realization of vertical GaN-based nanowire electronic devices on Si substrates.

SAE of uniform AlInGaN quaternary nanowire array has also been demonstrated on Si substrates. Selective-area grown *p-i-n* AlInGaN nanowire devices can exhibit light-emitting properties and photovoltaic effect over the same chips. Under the AM 1.5G illuminations, AlInGaN nanowire devices exhibit higher photovoltaics efficiency than those ever reported for *p-i-n* InGaN-based nanowire solar cell, benefiting from suppressed nonradiative surface recombination.

Abrégé

Le développement de dispositifs photoniques et électroniques réalisés en utilisant des hétérostructures planaires conventionnelles à base de GaN sont limités par des difficultés quant à la croissance d'hétérostructures planaires en InGaN riches en In de haute qualité, l'utilisation de substrats mésappariés, et la fabrication d'appareils à base d'hétérostructures planaires en GaN. Les nanofils à base de GaN sans dislocation ont émergé comme un candidat prometteur pour de futures applications pour les dispositifs photoniques et électroniques. Cette thèse se concentre sur le développement d'hétérostructures de nanofils à base de GaN en utilisant l'épitaxie par jets moléculaires (MBE), ainsi que leurs diverses applications pour écrans, illuminations, photovoltaïques et transistors.

Grâce à l'intégration monolithique de diodes électroluminescentes (LED) à base de nanofils bleu, vert, rouge (RVB) et jaune/orange sur des substrats de Si, des générations de lumières colorées contrôlables et ajustables ont été démontrées en utilisant un processus de croissance sélective en trois étapes utilisant un masque en SiO_x. Les sous-pixels monochromatiques disposés latéralement permettent un mélange contrôlé de la lumière au niveau de la puce électronique et émettent de la lumière de couleurs ajustables avec des valeurs de température de couleur corrélées comprises entre 1900 K et 6800 K, tout en conservant une excellente capacité de rendement des couleurs.

L'épitaxie sélective (SAE) permet de contrôler avec précision la taille, la position et la morphologie des nanofils, et ainsi d'obtenir une longueur d'onde d'émission contrôlée et ajustable avec précision. Grâce à la SAE, des matrices de nanofils à base de GaN RVB sur des substrats de GaN/saphir avec un masque en Ti, une taille de pixel polychrome de $7 \times 7\ \mu m^2$ a été obtenue avec des tailles de sous-pixels monochromatiques de $2,8 \times 2,8\ \mu m^2$. En incorporant des points quantiques (QDs) en InGaN dans des nanofils individuels à base de GaN, des émissions de couleurs allant du bleu au rouge ont été obtenues en ajustant le diamètre des

nanofils uniques sur le même substrat, et ce mécanisme a été étudié. En se basant sur cette réalisation, nous avons développé, pour la première fois, avec la plus petite taille de pixel au monde, des DELs avec des pixels de nanofils individuels en InGaN/GaN à haute performance en utilisant un seul processus de croissance épitaxiale.

Des hétérostructures de nanofils quaternaires en AlInGaN à croissance épitaxiale spontanée ont été étudiées sur un substrat de Si, dans lesquelles un noyau riche en In et une coquille riche en Al ont été formés spontanément au cours du processus de croissance épitaxiale. De telles structures noyau-enveloppe peuvent largement supprimer la recombinaison de surface non radiante, menant à une augmentation significative de la durée de vie des porteurs de charge, de ~ 0,2 ns à ~ 2 ns, et de la puissance de sortie. En faisant varier les conditions de croissance, les longueurs d'onde d'émission peuvent être ajustées de ~ 430 nm à ~ 630 nm.

Les propriétés de transport électrique de nanofils uniques en GaN alignés verticalement sur un substrat de Si ont été étudiées de manière systématique en utilisant une nanoprobation in situ à l'intérieur d'une chambre d'un microscope électronique à balayage (SEM). Une densité de courant allant jusqu'à 4,65 MA/cm^2 a été atteinte par une seule zone sélective de nanofils en GaN sur un substrat de Si, promettant la réalisation de transistors à nanofils verticaux à base de GaN sur des substrats de Si.

La SAE de réseaux de nanofils quaternaires AlInGaN uniformes a également été démontrée sur des substrats de Si. Sous une illuminations AM 1,5G, les nanofils en AlInGaN de type *p-i-n* démontrent une efficacité photovoltaïque supérieure aux cellules solaires à base de nanofils en InGaN de type *p-i-n* en raison de la suppression de la recombinaison de surface non radiante.

Acknowledgement

This doctoral dissertation would not be finished without the supervision, support and encouragement from many people. I wish to express the sincere appreciation to those who have involved in my works in this dissertation.

I would like to thank my supervisor Professor Zetian Mi who has created one of the best research MBE groups with talented and self-motivated researchers and advanced research facilities. All my achievements presented in this thesis will not be possible without his supervision, tremendous support, encouragement and thoughtful suggestions. He is available almost all the time to discuss research and resolve problems. It is a great happiness to work together with him in the lab. I would like to thank Professor Andrew G. Kirk and Professor Ishiang Shih for for their evaluations and valuable suggestions for my PhD thesis. I would like to present my deep gratitude to Professor Zetian Mi, Professor Andrew G. Kirk and Professor Ishiang Shih who offered me a great opportunity to study and work in McGill University. I would also like to thank my PhD supervisory committee members Professor Nathaniel Quitoriano and Professor Vamsy Chodavarapu for their evaluations and detailed suggestions for my research topics. I would also like to thank Professor Xinyu Liu, Professor William S. Wong and Professor Gianluigi A. Botton for their supports in the collaborative works. I would like to thank Professor Zahangir Kabir for his detailed evaluations and suggestions for my PhD thesis.

I also would like to send my special thanks to my colleagues for their assistance and discussions for my experiments, including Dr. Hieu Pham Trung Nguyen for his suggestions on my research work as well as his training in the device fabrication, MBE operation and MBE maintainence, Dr. Songrui Zhao for his suggestions on my research work as well as advice on PL set up, MBE operation and MBE maintainence, Dr. Xuedong Liu for his skilled STEM characterizations and fruitful discussions on STEM analyses, Dr. Ashfiqua T. Connie for her

advice on PL and EL characterizations, Dr. Shaobo Cheng and Dr. Steffi Y. Woo for her detailed TEM characterizations, my coworkers Dr. Yong-Ho Ra, Dr. Mehrdad Djavid, Juntian Qu, Xianhe Liu, Mohsen Asad, Faqrul Alam Chowdhury, Srinivas Vankat, Yuanpeng Wu and Roksana Tonny Rashid with their help in research works, and other members including Dr. Mohammad H. T. Dastjerdi, Dr. Binh Le, Dr. Kwai Hei Li, Dr. Junjie Kang, Dr. Yichen Wang, Dr. Qi Wang, David Arto Laleyan, Hong Nhung Tran, Dr. Sharif Md. Sadaf, Dr. Shizhao Fan, Dr. Sheng Chu, Dr. Baowen Zhou and Pegah Ghamari for their discussions and encouragement.

I would like to thank Tiffany Wang and David Arto Laleyan for performing the French translation of the dissertation abstract.

Special thanks and appreciation I would like to send to McGill nanotools microfab members including Dr. Zhao Lu, John Li, Peng Yang, Dr. Lino Eugene, Dr. Sasa Ristic, Alireza Hajhosseini Mesgar, Dr. Matthieu Manini and Donald Berry, for their technical support, training and discussions related to my research topic and for helping me speed up the fabrication processes.

I would like to thank my parents, Shaosong Wang and Yiqin Zhou, and my sister, Jinjin Wang for their supports, encouragements and understandings. I would like to thank my parents-in-law, Jiashan Lyu and Meiyang Yao for their encouragements and trusts. I would like to thank my wife, Shasha Lyu for her great supports, encouragements and understandings.

This work would not be possible without financial support for instruments and facilities. I wish to send my deep appreciation to the Natural Sciences and Engineering Research Council of Canada (NSERC) and McGill University for their supports on my research.

List of Figures

List of Tables

List of Acronyms

AMOLED	Active-Matrix Organic Light-Emitting Diode
CCT	Correlated Color Temperature
CRI	Color Rendering Index
CVD	Chemical Vapor Deposition
DFT	Density Functional Theory
DI	Deionized
DMHy	1.1-dimethylhydrazine
η	Conversion Efficiency
EBL	Electron Beam Lithography
EL	Electroluminescence
EQE	External Quantum Efficiency
FF	Fill Factor
FPDs	Flat Panel Displays
GAA	Gate-All-Around
ICP RIE	Inductively Coupled Plasma Reactive Ion Etching
IPA	Isopropyl Alcohol
IQE	Internal Quantum Efficiency
J_{sc}	Short-Circuit Current Density
LCD	Liquid Crystal Display
LEDs	Light Emitting Diodes
MBE	Molecular Beam Epitaxy
MOCVD	Metal-Organic Chemical Vapor Deposition
MOSFET	Metal-Oxide-Semiconductor Field-effect Transistor

MOVPE	Metal-Organic Vapor Phase Epitaxy
MIBK	Methyl Isobutyl Ketone
NHE	Normal Hydrogen Electrode
V_{oc}	Open-Circuit Voltage
OLEDs	Organic Light-Emitting Diodes
PEALD	Plasma Enhanced Atomic Layer Deposition
PECs	Photoelectrochemical Cells
POFs	Plastic Optical Fibers
PL	Photoluminescence
PMMA	Poly(methyl methacrylate)
PMTs	Photomultiplier Tubes
QCSE	Quantum-Confined Stark effect
QDs	Quantum Dots
QWs	Quantum Wells
RIE	Reactive Ion Etching
RGB	Red, Green and Blue
RGBY	Red, Green, Blue and Yellow
RGBO	Red, Green, Blue and Orange
SAE	Selective Area Epitaxy
SAG	Selective Area Growth
SCE	Short-Channel Effects
TRPL	Time-Resolved Photoluminescence
TMGa	Trimethylgallium
TEGa	Triethylgallium

VLCs	Visible Light Communications
VLS	Vapor-Liquid-Solid
V2X	Vehicle-to-Everything
V2V	Vehicle-to-Vehicle
WDM	Wavelength Division Multiplexing

Contribution of Authors

This dissertation work includes the contribution from the candidate and many other individuals. The supervisor of the candidate, Professor Zetian Mi, conceived and supervised the projects. The candidate and Professor Zetian Mi worked closely on discussions and manuscript writings. Professor Andrew G. Kirk and Professor Ishiang Shih, provided suggestions on thesis writings. The contribution of individuals to the works presented from chapter 3 to chapter 7 is described as follows:

Chapter 3 includes the experimental results of a published article written by the candidate and Prof. Zetian Mi. The results presented in the journal article are the collaboration of coauthors. Prof. Zetian Mi conceived and supervised the project. The candidate and Dr. Hieu P. Nguyen fabricated the devices and carried out the PL and EL characterizations. The candidate and Dr. Hieu P. Nguyen conducted the MBE growth of nanowires. The candidate carried out the morphology and structural characterization using SEM and optical microscopy.

Chapter 4 includes the experimental results of one published article about selective area epitaxy and device fabrication of nanowire arrays and the experimental results of one published article about selective area epitaxy and device fabrication of single nanowires. Prof. Zetian Mi conceived and supervised both projects. For the works related to nanowire arrays, the following are the contributions of individuals. The candidate developed, calibrated and conducted the growth process for selective area epitaxy of GaN-based nanowires. The candidate and Dr. Yong-Ho Ra fabricated the patterned substrates for the epitaxy of nanowire arrays. The candidate carried out the PL and SEM characterizations of nanowire arrays. The candidate and Dr. Yong-Ho Ra conducted the device fabrications of nanowire arrays. The candidate and Dr. Yong-Ho Ra carried out the EL characterizations of LEDs made using nanowire arrays. For the works presented in chapter 4 about single nanowires, the following are the contributions of coauthors. Prof. Zetian Mi and Jaesoong Lee conceived the project. The candidate conducted

the MBE growth of single nanowires and the associated MBE growth calibrations, and Dr. Yong-Ho Ra contributed to substrates loading. Dr. Yong-Ho Ra and the candidate fabricated the patterned substrates for the epitaxy of single nanowires. The candidate performed PL characterizations. Dr. Yong-Ho Ra and the candidate conducted the device fabrication. Dr. Steffi Y. Woo and Dr. Gianluigi A. Botton conducted the TEM analysis. Dr. Yong-Ho Ra and Dr. Sharif Md. Sadaf contributed to the electrical characterizations of single nanowire LEDs. A brief and conclusive results about the light extraction efficiency of single nanowires is included in the discussion, and the numerical simulation was conducted by Dr. Mehrdad Djavid.

Chapter 5 includes one published article. Prof. Zetian Mi conceived and supervised the project. The candidate conducted the MBE growth of nanowires. The candidate fabricated the devices and carried out the PL and EL characterizations. The candidate conducted the morphology characterization using SEM. Dr. Xuedong Liu conducted the STEM measurement. The candidate wishes to thank Dr. H. P. T. Nguyen and Dr. Songrui Zhao for their help with the MBE growth. The candidate wishes to thank Mr. X. Liu and Professor M. Andrews for their assistance with the carrier lifetime measurements.

For the results presented in chapter 6, following is the contribution of individuals. Prof. Zetian Mi conceived and supervised the works to develop selective area epitaxy of GaN nanowires on Si substrates and its device applications. The candidate developed, calibrated and conducted the fabrication of patterned Si substrates for the epitaxy of nanowire. The candidate developed, calibrated and conducted the growth process for selective area epitaxy of GaN nanowires on Si substrates. The candidate carried out the SEM characterizations of GaN nanowires. The candidate fabricated the Si solar cells, conducted the growth of AlN on Si solar cell and tested the solar cells. For the study on PEC hydrogen production, the candidate fabricated the patterned Si substrates and conducted the nanowire growth and SEM characterizations. Mr. Srinivas Vanka and the candidate fabricated the PEC cells and conducted

the PEC characterizations. The candidate would like to thank Mr. Srinivas Vanka and Dr. Yong-Ho Ra for their supports in the MBE growth. The results of a manuscript under preparation are included sections 6.5, 6.6, 6.7 and 6.8 about electrical characteristics of single GaN nanowires on Si. Prof. Zetian Mi and Prof. Xinyu Liu conceived and supervised the project. The candidate conducted the fabrication of patterned Si substrates for the epitaxy of GaN single nanowire. The candidate conducted the growth and device fabrications of GaN single nanowires on Si substrates. The candidate carried out the SEM characterizations of GaN single nanowires. Mr. Juntian Qu set up the nanoprobing in SEM chamber. Mr. Juntian Qu and the candidate conducted the electrical characterizations of GaN nanowires by nanoprobing. Dr. Xuedong Liu conducted the TEM characterization of GaN single nanowires.

Chapter 7 includes the results of one manuscript under preparation. Prof. Zetian Mi conceived and supervised the project. The candidate conducted the MBE growth of nanowires and pattern preparation for selective area epitaxy. The candidate fabricated the devices and carried out the PL and EL characterizations. The candidate conducted the photovoltaic characterizations. The candidate conducted the SEM characterization. Dr. Xuedong Liu conducted the STEM measurement. The candidate wishes to thank Mr. Srinivas Vanka for his assistance and suggestions on photovoltaic characterizations.

The following works to which the candidate contributed are not going to be included in this dissertation.

1. Mohsen Asad, Renjie Wang, Yong-Ho Ra, Zetian Mi and William S. Wong, “Coupling of optical function and geometric structure through mechanical manipulation of InGaN nanowire light-emitting diodes”, 2018 (submitted).
2. Faqrul Alam Chowdhury, Renjie Wang, Ishiang Shih, Hong Guo, Zetian Mi, “Synergistic effect of In and Sb in dilute-antimonide InGaSbN nanowire heterostructures for deep-

visible light emitting devices", 12th International Conference on Nitride Semiconductors, Strasbourg, France, July 24th, 2017.

Chapter 1: Introduction

1.1 Overview

In the past decades, optoelectronic devices made of organic and inorganic materials in the visible spectral range have attracted considerable attentions. Tremendous progress has been made in device applications of organic and inorganic materials for illuminations [1, 2], displays [3-13], visible optical communications [14-17], optogenetics [18, 19], energy harvesting [20-23], photoelectrochemical cells (PECs) [24], real-time identifications [25], healthcare and medical equipment [2, 25, 26], signal detection [27-31] and other application purposes [32-34].

After decades of research efforts, numerous organic and inorganic optoelectronic materials, have been invented or discovered and further explored with unique features to satisfy various needs for practical applications. These inventions and discoveries have affected our daily life and promoted applications in the advanced fields. For example, the inventors of efficient blue light-emitting diodes (LEDs) using GaN-based materials [35, 36] and the discoverers of graphene [37] have been awarded the Nobel Prize in Physics respectively in 2014 [38] and 2010 [37, 39] for their breakthroughs and the great benefit to mankind [40].

Organic optoelectronics in the visible spectral range have attracted a significant level of interest from researchers and manufacturers of optoelectronics, due to their numerous advantages including lightweight, flexible substrates, high transparency and ultrathin appearance [41-45]. The light emissions of organic optoelectronic devices can cover the entire visible spectral range [41, 43, 44, 46-50]. However, organic optoelectronic devices in the blue spectral range generally exhibit low efficiency and fade fast [44, 51, 52]. Another shortcoming of organic optoelectronic devices for the practical usage is the poor persistence and poor stability in the daily usage, because the organic optoelectronic materials are extremely sensitive to oxygen and water [41, 43, 44, 53]. Organic optoelectronic devices also have a disadvantage

for its short lifetime [42, 44]. In the above aspects such as lifetime, stability, reliability, efficiency and cost, organic optoelectronic devices cannot compete with inorganic semiconductor counterparts such as III-nitride compound semiconductors.

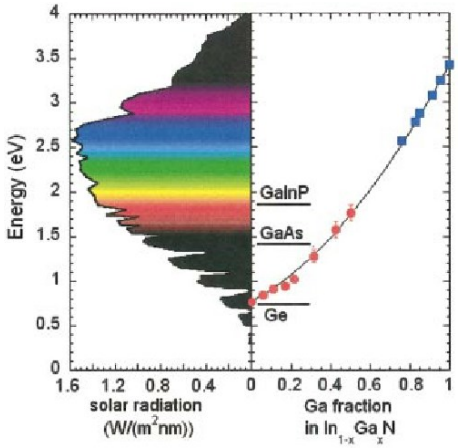

Figure 1-1: Bandgap energies of the InGaN alloy system cover the entire air-mass-1.5 solar spectrum. The gap energies of conventional multijunction solar cell materials (Ge, GaAs, and GaInP) are also shown in the right-hand panel for comparison. Reprinted from journal publication authored by J. Wu et al. in *Journal of Applied Physics* [54], with the permission of AIP Publishing.

To date, however, there are no efficient inorganic semiconductor emitters in the green, yellow and orange spectral range. Efficient red-emitting devices have been achieved by using InGaAlP-based and GaAs-based materials [55-58]. However, the synthesis or growth of high quality InGaP/InGaAlP quantum wells (QWs) heterostructures with strong carrier confinement has remained difficult in the yellow and orange spectral range [59, 60]. It has been discovered that the bandgap of III-nitride compound semiconductors can be continuously varied from ~0.65 eV (InN) to 6.2 eV (AlN) [61-64]. The III-nitrides exhibit many favorable optoelectronic properties, including low effective carrier mass, high carrier mobility, high peak and saturation velocities, and high absorption coefficients, extreme chemical stability, and good thermal stability [61, 62, 65-68].

The direct energy bandgap or absorption spectrum of InGaN alloy can cover the whole spectral range from ~ 0.7 to ~ 3.4 eV, representing the only semiconductor that can match

almost perfectly to the solar spectrum [61-64]. As can be seen from Figure 1-1, energy bandgap of InGaN alloy increase with increasing Ga fraction x_{Ga}, covering almost the entire solar spectrum [54, 69]. Therefore, full-color emissions can be achieved by InGaN emitters and high efficiency is expected from InGaN-based photovoltaic devices. InGaN alloy, which is nontoxic and environmentally friendly, has been widely used for developing high efficiency optoelectronic devices and systems due to its unique material properties and resulting high performance devices. Its device applications includes visible and infrared LEDs [70-76], visible and infrared laser [74, 77-82], solar cells [83-86], photodetectors [27-31], sensors [87-90] and transistors [32-34].

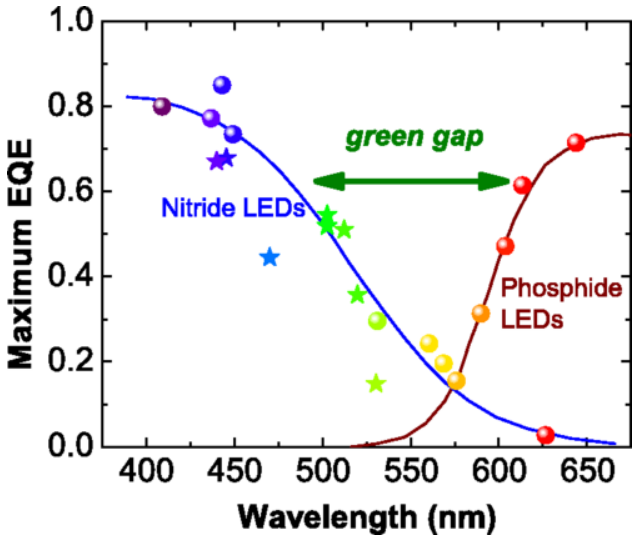

Figure 1-2: Maximum external quantum efficiency (EQE) of commercial nitride and phosphide LEDs, illustrating the "green gap" problem [55, 56, 91]. Reprinted from journal publication authored by M. A. der Maur et al. in *Physical Review Letters* [55], with the permission of American Physical Society.

Although high power InGaN-based optoelectronics have been demonstrated and developed successfully [92-94], the emission wavelengths of high-efficiency InGaN planar heterostructures devices have been limited in the near-ultraviolet, blue, and blue-green spectral ranges [55, 56, 91], as shown in Figure 1-2. Shown in Figure 1-2, "green gap" represents the lack of inorganic materials and devices which can exhibit high efficiency in the green, yellow

and orange spectral ranges [55, 56, 91]. In Sections 1.1.2, 1.1.3, 1.1.4 and 1.1.5, the status and major challenges of LEDs, lasers and solar cells using GaN-based planar heterostructures, will be reviewed respectively.

Benefiting from the effective lateral stress relaxation and terminations of propagating dislocations at the large surface [95], GaN-based nanowire heterostructures grown on lattice mismatched substrate can be nearly free of defects such as dislocations, stacking faults, and twins [96-101], in contrast to the high densities of defects, large polarization fields and the resulting quantum-confined Stark effect (QCSE) in its planar epilayers counterparts [102, 103]. The unique feature of large surface-to-volume ratio also enhances the light extraction/absorption efficiency of nanowire structures [95]. To date, with the use of InGaN nanowire structures, high efficiency emissions across the entire visible spectral range have been demonstrated [104, 105].

The needs of market drive the researchers to be dedicated on making optoelectronic devices and systems faster, cheaper, more efficient, and smarter. After resolving critical technical challenges in various aspects such as optoelectronic material manufacturing, material characterizations, device fabrications, device characterizations and methods of system control and communications [106-112], it is a clear trend that optoelectronic scientists and engineers have been intensely working on the development of optoelectronic materials and individual device units into dedicated optoelectronic devices and systems with comprehensive capabilities and advanced functions, as well as enhancements or integrations of existing functions of individual optoelectronic materials by smartly and monolithically integrating various optoelectronic materials. In addition, the current and future optoelectronic applications generally require smaller (size) devices and systems. The well-known Moore's prediction [113, 114] has been proven in various fields of semiconductor industry, not only for transistors in a

dense integrated circuit [115] but also for optoelectronic components and systems, for example, the red, green and blue (RGB) pixel arrays in digital cameras and displays [116, 117].

To satisfy the practical needs including the shrinkage of overall systems using optoelectronic devices [118], integration of dense optoelectronic devices into large-scale systems such as large micro-LED displays, or integration of optoelectronic devices into a limited space such as cellular scale and the scale of spinal epidural space [18, 19], it requires the employments of micro-scale and nano-scale optoelectronic materials and devices. Compared to bulk materials and large-size devices, these micro-scale and nano-scale optoelectronic materials and devices should exhibit equivalent or better characteristics and performances.

Taking advantages of the nanowire heterostructures, the dimensions of III-nitride materials and optoelectronics devices are flexible to be scaled down to micro-scale or nano-scale [102, 119-126]. In addition, GaN-based nanowires exhibit higher light extraction and better light absorption due to its tunable geometry and large surface-to-volume ratio [127, 128]. Moreover, efficient doping and resulting efficient carrier conduction have been realized by using III-nitride nanowires [129-131]. Compared to its planar counterparts, III-nitride nanowires also exhibit lower thermal resistance and thus more efficient heat dissipation [132, 133]. In this regard, InGaN nanowire heterostructures and its devices promise better performance [102, 124-126], especially for In-rich InGaN which exhibit emissions with long wavelength in visible spectral range [134].

Together with its benefit of size shrinkage, InGaN nanowire heterostructures and its devices also exhibit better performances and higher reliability, enabling the integration of InGaN nanowires into various optoelectronic devices and systems to make faster, cheaper, more efficient, and smarter optoelectronic applications with comprehensive capabilities and

advanced functions. In section 1.2, the status of InGaN nanowire heterostructures and devices, will be reviewed and discussed in detail.

Table 1-1: Material Properties of bulk Si, Ge, GaAs, GaN and InN [62, 135-146].

Material	Crystal structure	Lattice constant (nm)	Bandgap (eV) at 300 K	Thermal Exp. Coeff. ($\mu m \cdot m^{-1} \cdot K^{-1}$)	Electron Mobility[II] ($cm^2 \cdot V^{-1} \cdot s^{-1}$) at 300 K	Hole Mobility[II] ($cm^2 \cdot V^{-1} \cdot s^{-1}$) at 300 K
Si	Diamond cubic	0.5431	1.12	2.6×10^{-6}	1450	500
Ge	Diamond cubic	0.5658	0.664	5.5×10^{-6}	3900	1800
GaAs	Zinc blende	0.5653	1.424	5.5×10^{-6}	9200	400
GaN	Wurtzite[I]	a=0.3189 c=0.5185	3.4	Normal to c-axis 3.43×10^{-6}; Parallel to c-axis 3.34×10^{-6}.	1500	30
InN	Wurtzite[I]	a=0.3545 c=0.5703	~ 0.65	Normal to c-axis 4×10^{-6}; Parallel to c-axis 3×10^{-6}.	Theoretical electron mobility: ~ 4400-10,000 [139-142, 144-146] Experimental electron mobility: > ~ 2000 [143] Electron mobility of InN nanowires: 8000-12000 [145]	

Note I: III-nitride materials generally exhibit wurtzite crystal structure, but GaN can also be grown in a zinc blende crystal structure [147-149]. This dissertation focuses on III-nitride materials in a wurtzite crystal structure.

Note II: Typical values of carrier mobility are presented in this table. The values vary in different publications, depending on material quality and measurement techniques.

The use of Si substrates offers many distinct advantages, including greatly reduced manufacturing costs and improved device reliability. As calculated using the lattice constants shown in Table 1-1, the Si substrate exhibits a large lattice mismatch of –16.9% with GaN along the epitaxial orientation GaN(0001)//Si(111) [150] and a relatively large difference in thermal expansion coefficient compared to GaN, resulting in considerable defects in GaN-based epilayers grown on Si substrates with/without the use of additional buffer layers. In contrast to the challenges in the epitaxy of GaN-based epilayer heterostructures on Si substrates, high quality GaN-based nanowire heterostructures using InGaN active regions can be grown directly on Si substrates, which eliminates the use of other expensive substrates [101, 120, 151].

1.2 Demanding Applications, Status and Challenges of III-Nitride Optoelectronics in the Visible Spectral Range

In what follows, based on the demanding applications in the fields of LEDs, lasers, visible light transmitters for optical communications and solar cells, the status and challenges of the use of III-nitride materials to realize optoelectronics in the visible spectral range will be reviewed and discussed respectively, with special attentions paid to the applications for solid state lighting.

1.2.1 Light Emitting Diodes for Visible Illuminations and Displays

The conventional incandescence bulbs (typically 13-18 lm/W [1]) and fluorescence lamps (typically 55-70 lm/W [1]) are limited in their efficiency, short lifetime, and environmental impact. The wide usage of solid-state lighting sources, such as LEDs (typically more than 100 lm/W in commercial products [1]), is expected to reduce the electricity used for lighting by half, and reduce greenhouse gases and other pollution largely. Currently, high power LEDs can compete with conventional light sources on both a system cost basis and small-area applications. For example, for the illuminations in the entertainment lighting industry, solid-state lighting sources are replacing conventional incandescent tungsten-halogen lamps [152]. For signals and displays, solid-state lighting sources based on white LEDs has been widely applied.

The correlated color temperature (CCT) of color-tunable LED lighting systems can, in principle, be tuned over a wide range, which is essential for various applications, including display [4, 5], mood lighting [2], and real-time identification of biological cells [25]. For example, wide tunable range in CCT is required in smart illumination systems to vary its illumination conditions by adapting emission color and intensity of full-color LEDs. It has been discovered in biological study that constant inappropriate lighting exposure (light intensity, wavelength and duration) will affect the body chemistry and circadian performance, and cause

negative health effects and even disease [2, 25, 26]. A tunable, natural, appropriate and well-designed LED illumination or display systems are essential for humans to have a healthy, efficient and productive daily life [2, 25, 26].

High performance displays require the usage of high efficiency color-tunable LED pixels which exhibit essential features including low power consumption, extremely small size, wide color tunability. To improve the resolution, optimal viewing distance and color rendering of flat panel displays (FPDs), subpixel rendering technique, using three-primary-color (RGB) or four-primary-color (RGYB) LED subpixels to form color-tunable pixels in sub-mm scale (or μm scale), are being developed. On the display panels, monochromatic RGB sub-mm-LED subpixels or μm-LED subpixels with fixed wavelength are so small that human eye cannot resolve their individual colors and thus the overall pixels can present mixed light to the audience. The CCT and color rendering index (CRI) of mixed light can be tuned by varying the ratio of RGB components through the adjustments on the power input to each LED subpixel.

Figure 1-3 summarizes the pixel size and the corresponding luminous efficiency of full-color pixels used in smartphone FPDs produced by two leading smartphone manufacturers, based on the smartphone specifications open to the public and quantitative test results from display technicians and researchers [6-13, 153-158]. In the red plot of Figure 1-3 (a), except the generation of "X" using active-matrix organic light-emitting diode (AMOLED), the reducing pixel size of FPDs used in different generations of smartphone A reflects the state-of-the-art full-color liquid-crystal display (LCD) pixel used for portable FPDs [12, 153-158]. Shown in the blue plot, the reducing pixel size of FPDs used in different generations of smartphone B represents the state-of-the-art full-color pixel in portable FPDs using AMOLED [6-11, 13]. Very recent years, the portable FPDs market is being led by AMOLED-based subpixel rendering technique instead of LCD technique in terms of display pixel size, which can be concluded from Figure 1-3 (a).

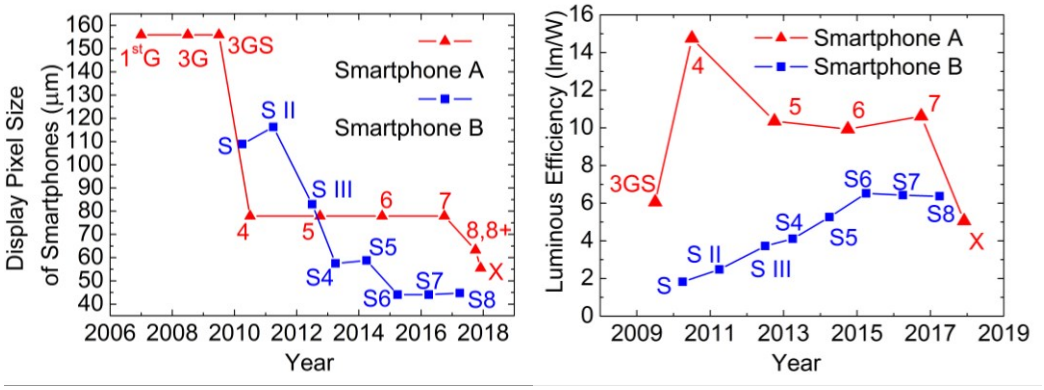

(a) (b)

Figure 1-3: Summary on the (a) pixel size and (b) luminous efficiency of full-color pixels used in flat panel displays (FPDs) of smartphones produced by two leading smartphone manufacturers A and B in the past years, respectively. The red plots are (a) FPD pixel size [12, 153-158] of smartphone A of 1stG, 3G, 3GS, 4, 5, 6,7, 8, 8+ and X generations versus the release time of the corresponding smartphone and (b) luminous efficiency [153-158] of smartphone A of 3GS, 4, 5, 6, 7 and X generations versus the release time of the corresponding smartphone. In contrast, the blue plots are (a) FPD pixel size and (b) luminous efficiency of smartphone B of S, S II, S III, S4, S5, S6, S7 and S8 generations versus the release time of the corresponding smartphone [6-13]. The display pixel sizes are summarized based on the smartphone specifications open to the public and the luminous efficiencies are calculated based on quantitative test results from display technicians and researchers [6-13, 153-158]. The calculation of luminous efficiencies is based on the characterization results of smartphone FPDs adjusted to maximum brightness with full white screens, which exhibit 100% average picture level. In the calculation of luminance of FPDs, the surface of FPDs are calculated as a flat diffuse surface and light is emitted uniformly over the surface [159].

Besides the size and color rendering of a pixel, the efficiency is also a key factor for display applications which require energy-saving and/or high brightness. As shown in Figure 1-3 (b), for portable FPDs, in the past years, the luminous efficiency of LCD-based subpixel rendering technique was higher than that of AMOLED technique [6-13, 153-158]. It is worthwhile mentioning that the luminous efficiencies of "X" AMOLED display and smartphone B AMOLED display are evaluated at different brightness. The calculation of luminous efficiency of "X" is based on the display power consumption for its full white screen

at maxiumum brightness of 634 cd/m^2 [158]. The calculation of luminous efficiency of smartphone B is based on the display power consumption for its full white screen at maxiumum brightness of 420 cd/m^2 [6]. Shown in the red plot in Figure 1-3 (b), the luminous efficiency of AMOLED-based pixel improved dramatically in the years from 2010 to 2015, benefiting from the rapid technical advancements and large financial investments. However, for the AMOLED-based subpixel rendering technique named by "WQHD Super AMOLED" in recent years (2015-2017) [6-8], the advancements in reducing the pixel size and improving luminous efficiency were stagnant or slower than earlier generations (2010-2014).

In addition to the general advantages of organic optoelectronics, with the advantages of fast response time and operations without using a backlight, organic light-emitting diodes (OLEDs) has been largely used in lighting and displays in various commercial applications such as mobile phones, digital cameras, television screens and portable digital media players [41-45]. However, in current white OLEDs or color-tunable OLEDs, one bottleneck is the short lifespan of blue OLEDs leading to loss in color balance and color shifts due to fast fading blue component [51]. OLEDs displays also suffer from being prone to permanent discoloration of a few areas generally known as "screen burn-in" due to cumulative non-uniform usage of the screen pixels [44, 51, 160]. In addition, OLED also share the general shortcomings of organic optoelectronics such as poor persistence, poor stability [41, 43, 44, 161], and short lifetime [42, 44]. Besides the above challenges in the OLED practical applications, the relatively low external quantum efficiency (EQE) of blue OLEDs is also a main bottleneck for the further development of OLED techniques. Various types of organic materials and different device structures have been explored and used to fabricate OLED. To the author's best knowledge, the highest EQE for reported white OLEDs (color-rendering index: 69, CIE coordinate: (0.41, 0.49), and device area: 6.7 mm^2) is 46% (the overall luminous efficacy of 124 lm/W) by combining high-refractive-index substrates with a carefully chosen emitter layer [162].

However, the generally reported green and red OLEDs exhibit the EQE below 20% [46, 47, 49, 50, 163-168]. Moreover, the efficiency and lifespan of blue OLEDs are even poorer than green and red OLEDs [43, 53, 169], which is vital to the further commercialization of OLED technology. In the aspects such as lifetime [170], stability, reliability [171-173], color quality, efficiency and cost (price per lumen) [170], OLEDs lag behind inorganic-based LEDs.

GaN-based LEDs have emerged as a prime candidate for future lighting applications, due to their high efficiency, long lifetime, and reduced environmental impact. However, the current white and full-color LED chips generally consist of GaN-based blue LEDs and appropriate phosphors [174, 175], severely limiting the flexibility to tune the spectral power distribution and to achieve color-tunable emission [176]. This method has the disadvantages of low CRI and Stokes fluorescence loss.

The device performance of conventional quantum well (QW) LEDs is ultimately restricted by the extremely low efficiency in the deep green and yellow wavelength range [134] due to lack of suitable lattice matched substrates. Different from conventional planar QWs devices, nearly defect-free GaN-based nanowire LED heterostructures can be grown directly on lattice mismatched substrates and can exhibit superior device performance and reliability. To date, with the use of InGaN nanowire structures, high-efficiency emissions across the entire visible spectral range have been demonstrated [104, 105, 177]. The use of InGaN nanowires provides an effective approach to reduce the dimensions of LEDs devices, enabling the shrinkage of whole illumination systems and integration of high efficiency light sources in applications in limited space. The use of InGaN nanowires can promise color-tunable micro-LED displays exhibiting higher resolution, higher efficiency, better display quality, longer lifetime, better stability and reliability than the state of the art AMOLED-based display techniques.

1.2.2 Lasers in the Visible Spectral Range for Illuminations and Displays

Driven by the need for reduced power consumption, enhanced efficiency and more advanced functions, future smart lighting technologies and ultrahigh resolution displays require the development of small size and efficient multi-color light sources monolithically integrated on a single chip. Compared to LEDs, recent studies have shown that lasers offer several unique advantages for these applications. It has been demonstrated that the use of four monochromatic lasers can produce white light with high color-rendering quality comparable to a continuous spectrum [3]. Lasers can also offer better performance than LEDs in terms of output optical power and light quality. The efficiency and output power of lasers will surpass that of LEDs, due to the reduced efficiency droop through stimulated emission [94, 178]. The low-divergence light from lasers are much easier to control than lambertian light from LEDs, enabling directional emission and focus-free operation with high color rendering quality [3, 179]. White and full-color (RGB primaries) lasers will also lead to television and computer displays exhibiting much wider color gamut, significantly higher contrast ratio, and much more natural and vivid colors than any existing technologies, thereby providing unparalleled visual experience . Moreover, the operation speed of lasers can be one order of magnitude faster than LEDs, enable high speed and dynamic operations and promising static and in-motion life-like images . Such monolithically integrated multi-color lasers also have a broad range of applications in biological and chemical sensing as well as chip-level wavelength division multiplexing (WDM) [183] and ultrahigh speed Li-Fi. Hence, it is very desirable to develop monolithically integrated multi-color lasers.

In the red and orange spectral range, GaInP/AlGaInP QW lasers have been developed [59, 184-186]. The operating wavelength of these lasers, however, have been restricted to 608 nm [59], or longer wavelengths [59, 184], limited by the poor charge carrier confinement in the those phosphide-based QWs.

Since the invention of blue laser diodes by Nakamura, tremendous progress has been made for GaN-based edge-emitting laser diodes [187, 188]. The world's first InGaN MQW laser at a true green wavelength was reported in 2010 with the wavelength at 524 nm and 531.7 nm under continuous-wave (CW) and pulse electrical biasing [92], and its output power reached 50 mW. More recently, an InGaN QW laser with longer wavelength at 535.7 nm was reported under CW electrical biasing and its output was 75 mW [189]. Under CW operation, the threshold current density of InGaN QW laser is in the range of ~ 3.1-18 kA/cm^2 for lasing wavelengths ranging from 500 nm to 535.7 nm [92, 189-194]. By optimizing QW structure and growth conditions of semi-polar green LDs, low-threshold CW lasers were obtained with threshold current densities as low as 5.4 kA/cm^2 at 533.6 nm, 5.2 kA/cm^2 at 527.2 nm, 4.3 kA/cm^2 at 525.6 nm, and 3.4 kA/cm^2 at 511 nm [195]. However, to date, the operating wavelengths of InGaN QWs lasers have been limited to the near-ultraviolet, blue, and blue-green spectral ranges [55, 56, 91], due to the poor materials quality of In-rich InGaN planar heterostructures. Some of the extraordinary challenges for achieving low threshold electrically injected InGaN QWs green, and possibly yellow, orange and red-emitting lasers include the presence of large densities of defects and dislocations in the device active region due to the large lattice mismatch (~11%) [196-198] and thermal mismatch [199] between InN and GaN. The strong strain-induced polarization fields and the resulting QCSE further decrease the device efficiency and the maximum achievable gain.

Consequently, there have been no commercial semiconductor laser diodes operating in the wavelength range from 536 nm to 607 nm. To date, commercial green lasers generally rely on the use of nonlinear optical conversion. Such devices, however, are bulky, heavy and expensive, and are not suitable for on-chip integration [200, 201].

Besides the difficulties to realize the lasers operating in the "green gap", there is also no established technology for spatially varying In compositions in planar QWs to achieve multi-

color emission on the same substrate. The achievement of full-color InGaN lasers, which are essentially required for practical applications, has remained elusive.

1.2.3 Visible Light Transmitters for Optical Communications

High-output full-color light transmitters such as efficient semiconductor LEDs or efficient semiconductor laser are essentially required for visible light communications (VLCs), which is an aternative optical wireless communication technology to resolve the shortage of the radio frequency spectrum [202-206]. VLCs could be widely used in the vehicle-to-everything (V2X) transportation communications such as vehicle-to-vehicle (V2V) communications [207], paving the way for emerging autonomous car (also known as a driverless car) which currently attract extensive and intense development effort in worldwide industries [208] and academic institutions. The visible lights from vehicle headlights, vehicle tail lights, vehicle brake lights, traffic light, and smart road signs could be used in communications for high resolution vehicle positioning and guidances such as driving directions and emergency braking to a neighboring vehicles [25, 207]. Besides the applications in transportations, indoor VLCs have been also a research spotlight together with the optical multiple input multiple output (MIMO) techniques [209]. Solid state light transmitters, especially lasers which can be one order of magnitude faster than LEDs, is very promising for ultrahigh speed Li-Fi [15-17].

Compared to single-color transmitters, multi-color or full-color transmitters can have more modulation dimensions for higher transmission data rate [14] and transmission capacity [206]. Taking advantages of chip-level WDM [183], data rates of 4.5Gb/s and 8 Gb/s have been achieved in free space by using a RGB-LED based WDM VLC system [210] and by using a RGBY-LED based WDM VLC system [211], respectively. In this regards, it is highly desriable to develop high-efficiency RGB or RGBY monolithic LED chips and laser chips in which the development of high-efficiency full-color devices is essential.

Beside their applications in optical wireless communications, the realization of high efficiency semiconductor light sources in the green, yellow and orange wavelength range, together with the recent development of plastic optical fibers (POFs), will enable many exciting applications in short-reach fiber-based connections including home networks, industrial networks, digital home appliances, automotive, and remote sensing, and medical controls [173, 212, 213]. The emerging plastic optical fibers generally have the lowest absorption window in the green, yellow and orange spectral range. POFs are less brittle, more flexible, and of significantly lower cost, compared to glass optical fibers [214, 215]. Moreover, POFs offer the flexibility of conventional copper cables in installation, due to their large numerical apertures [216]. Recent studies have shown that very high quality signals can be achieved in POF in-house networks [217]. Some of the requirements for POFs in the present home network application include a moderately high bandwidth ~ 1 Gb/s and a link length ~100 m [218]. The traditional PMMA-based POFs, however, exhibit very large loss at the standard telecommunication wavelengths (10^4-10^5 dB/km at the wavelength of 1500 nm). Their lowest attenuation windows are in the green, yellow and orange spectral range. For example, spectral attenuations of 80 dB/km at 530 nm, 65 dB/km at 570 nm, and 150 dB/km at 650 nm have been achieved in graded index PMMA-based POFs [219]. The recently developed perfluorinated-polymer-based POFs (PFP-based POF) offer a relatively low loss of 30 to 50 dB/km in the wavelength range of 850 to 1310 nm [220, 221]. However, to date, there are few optical transmitters that can meet the bandwidth, performance and cost requirements at the lowest POF attenuation windows near 530 nm and 570 nm [219], due to the lack of a mature semiconductor LEDs and laser technology in the green, yellow and orange wavelength range.

In summary, high efficiency semiconductor light sources operating in the green, yellow and orange wavelength range are critical for the development of optical wireless and POF-based communications. However, the emission wavelengths of InGaN QW LEDs and lasers

have been limited to the near-ultraviolet, blue, and blue-green spectral ranges. In contrast, full-color InGaN nanowire LEDs and lasers have been achieved by using InGaN nanowire heterostructures which are nearly free of dislocation and exhibit a very small level of strain field.

1.2.4 InGaN-based Photovoltaics

Concerns about the deteriorating global environment and depleting natural resources have prompted a new wave of technology development for green energy solutions. Clean and virtually unlimited solar energy, in this regard, has drawn considerable attention. The dominant photovoltaics technology in current market is nearly $17.90 per MWh (1.79 cent/kWh) [222], which is lower than that of the conventional coal-fired power (5 cent/kWh) using fossil fuel energy [223]. The market price of crystalline Si photovoltaic cell has decreased from $76.67 per watt in the year of 1977 to $0.23 per watt in the year of 2017 [224, 225], practically proves Swanson's law [226]. The ultimate costs of solar electricity can be further reduced by increasing energy conversion efficiency up to the thermodynamic limit of solar cell efficiency [227-229].

In the past decades, extensive and intensive efforts have been put into the development of high-efficiency photovoltaics including inorganic solar cells using $CuInGaSe_2$ (CIGS), CdTe, and silicon polycrystalline thin films. To date, the energy conversion efficiency of solar cells can reach over 30% for two-junction cells [21, 230] and well over 40% for three-junction cells [20-23] under concentrated sunlight illumination. However, a large portion of the solar spectrum in the energy ranges of 1.0-1.2 eV and 2.5-3.4 eV has not been utilized in the state-of-the-art GaAs/InGaP/Ge triple-junction solar cell [231]. Moreover, such devices are generally grown on GaAs, InP, Ge and/or GaSb [232-235], which are prohibitively expensive and, as a result, their terrestrial applications have been very limited.

Recently, it has been discovered that the absorption spectrum of InGaN alloy can be continuously varied from 0.7 to 3.4 eV, representing the only semiconductor that can match

almost perfectly to the solar spectrum. The use of InGaN alloy for the design of tandem solar cells offer many distinct advantages, including greatly reduced manufacturing costs and improved device reliability, due to the minimal thermal and lattice mismatches. InGaN alloys exhibit many favorable photovoltaic properties including high carrier mobility, high peak and saturation velocities, high absorption coefficients, high thermal conductivity, and high temperature resistance. Compared to other III-V alloy materials such as III-phosphide and III-arsenide, InGaN alloys exhibit a much more reliable and stable optical and electronic properties under concentrated and high-energy photon irradiation (2 MeV or more) [54], providing a great potential for a high-efficiency radiation-hard solar cell for the use in some extreme environment such as space applications. Therefore, drastically improved efficiency is expected from InGaN-based solar cells which match almost perfectly to the solar spectrum.

High efficiencies have also been promised for single junction and tandem InGaN-based solar cells in many theoretical studies. For single-junction solar cells, the overall conversion efficiency of a $In_{0.35}Ga_{0.65}N$ solar cell and a $In_{0.65}Ga_{0.35}N$ cell solar cell can reach about 8% [236] and ~ 20% [237], based on the theoretical studies from Dahal et al. [236] and Zhang et al. [237] respectively. For a two-junction InGaN/GaN solar cells with top and bottom bandgap of 1.74 eV and 1.15 eV, an efficiency of 35.1% was concluded by Zhang et al. [238]. Christiana et al. studied the theoretical solar-cell efficiency for multi-junction InGaN solar cells under the radiation concentration of 500× and a spectrum of 6000 K black body radiation. The derived efficiencies for three, four, five and six stack tandem cells are 56%, 62%, 65% and 67.3%, respectively [239, 240].

Most of the experimental reports on InGaN-based solar cells used planar heterostructures, for example, *p*-GaN/InGaN/*n*-GaN heterostructures or *p*-GaN/InGaN MQWs/*n*-GaN heterostructures, in which an absorption segment using an InGaN layer or InGaN/GaN MQWs is sandwiched by *p*-GaN and *n*-GaN layers. To date, the experimentally measured conversion

efficiency of such single-junction InGaN solar cells remain much lower than their theoretically predicted values corresponding to the specific InGaN energy bandgap. On GaN (0001)/sapphire substrate, Kuwahara et al. fabricated and characterized a single junction *p-i-n* InGaN-based solar cell using an intrinsic InGaN absorption layer [241]. Using a solar simulator (1.5 suns), its open circuit voltage (V_{oc}), short-circuit current density (J_{sc}), fill factor (FF), and conversion efficiency (η) were measured to be 2.23 V, 1.59 mA/cm^2, 61%, and 1.41%, respectively [241]. For an $In_{0.35}Ga_{0.65}N$/GaN MQW solar cells epitaxially grown on GaN substrate, reported by Dahal et al. [236], its V_{oc}, J_{sc}, FF, η and maximum output power were measured to be 1.80 V, 2.56 mA/cm^2, 64%, 2.95% and 2.95 mW/cm^2, respectively. Liou et al. has reported some impressive results of InGaN/GaN MQWs solar cells grown on SiCN/Si(1 1 1) substrate [242, 243]. Such InGaN-based solar cells exhibited V_{oc} in the range of 2.72-2.92 V, J_{sc} in the range of 2.72-2.97 mA/cm^2, FF in the range of 61.5-74.89%, and relatively high efficiencies of 4.97-5.95% [242, 243].

The large gap between the experimental measured efficiencies and the theoretical predicted efficiencies of planar InGaN-based solar cell is mainly related to poor crystalline quality of the heteroepitaxially grown InGaN layers. A high In content from around 25 to 100% is critical to obtain high efficiency InGaN-based solar cells [236]. However, the current material quality of InGaN deteriorate when the In content is high, resulted from phase separation/segregation, the dramatically increased lattice mismatch between InGaN and GaN, and high defect and dislocation densities. The resulting poor efficiency of InGaN materials at long-wavelength visible spectral range have been shown in Figure 1-2, due to the poor material quality of In-rich InGaN layers. When the thickness and the In content of InGaN layer increase, InGaN alloys suffer from phase separations, defects and dislocation, which will lead to lower V_{oc}, lower J_{sc} and lower FFs than theoretical predicted values. The defect states increase nonradiatvie recombination rate, degrading output characteristics of InGaN-based solar cells.

To avoid a large amount of phase separation, defects and dislocations and obtain the good crystalline quality of the InGaN epitaxial layers, in the currently reported InGaN-based solar cells, both of the In content and the thickness of InGaN absorption layers are very limited [242]. This explains the relatively low J_{sc} and η in the currently reported InGaN-based solar cells. In addition, it has been reported that the polarization field of InGaN alloy has adverse effects on the J_{sc} and η of InGaN-based solar cells due to a polarization-induced trap state and the resulting lower minority carrier lifetime [244-247]. In this regard, the increased piezoelectric polarization resulted from the inherent strain of InGaN layers will suppress the J_{sc} and η of InGaN-based solar cells, in addition to the difficulties in increasing the In content and the thickness of InGaN absorption layers [244-247]. Moreover, in the reports of InGaN-based solar cell, to reduce the mismatch between the substrate and epitaxially grown layers the InGaN layered heterostructure are generally grown on GaN substrate, which is expensive and creates the difficulty in integrating InGaN-based solar cell with the well-developed Si-based photovoltaics technology.

As a summary of previous paragraphs, there is a need to develop innovative technologies that can significantly improve the energy conversion efficiency of solar cells while maintaining the economic and environmental advantages of Si-based technology. It is desired to monolithically integrate high efficiency InGaN solar cells directly on low cost, large area Si substrate [248, 249]. High quality InGaN-based nanowires can be grown directly on Si substrates, which eliminates the use of expensive III-V substrates. Moreover, taking advantages of large strain relaxation, InGaN-based nanowires can be epitaxially grown with variable In content and thick absorption segment. Such unique features of InGaN-based nanowires promise a viable approach to achieve the theoretical predicted efficiency of InGaN-based solar cell which are currently difficult for layered InGaN heterostructures.

1.3 Progress and Status of InGaN Nanowire Optoelectronics

1.3.1 InGaN Nanowire Light Emitting Diodes (LEDs)

A wide color-tunable range of InGaN nanowire LEDs can be achieved at various output power levels. Previously, the achievement of high internal quantum efficiency (IQE) InGaN/GaN dot-in-a-wire green, yellow (IQE: ~45%), red (IQE: 32%) and white (IQE: ~60%) LEDs has been reported at room temperature [119, 120, 250, 251]. An output power of more than 5 mW was also reported for an unpackaged InGaN-based nanowire LED [252]. Moreover, the presence of efficiency droop is small in the studies on InGaN/GaN green, yellow, red and white nanowire LEDs on Si(111) substrates [119, 120, 250-254]. Kishino et al. reported on the demonstrations of green, yellow and orange InGaN nanowire LEDs integrated on the same wafer using a single MBE growth [255, 256]. Such multi-color InGaN nanowire arrays were grown on GaN/Sapphire with a thin Ti mask (~ 10 nm) [255, 256].

Tunnel junction enables the stacking of multiple *p*-*n* junctions in LEDs providing the unique opportunity to realize GaN-based nanowire LEDs exhibits multi-color emission and enhanced efficiency [257-259]. Various design schemes of tunnel junctions, including GaN/Al(Ga)N/GaN [260-262], GaN/InGaN/GaN [263-265] and GaN/GdN/GaN [258, 266] have been used in GaN-based LED structures. However, the difficulty in the incorporation of *p*-type dopants has severely limited the tunneling probability [267, 268]. Recently, it has been demonstrated that dopant incorporation can be enhanced in nanowire structures, due to the reduced formation energy of III-substitutional dopants due to effective strain relaxation in the near-surface regions [130, 269]. Using p^{++}-GaN/InGaN/n^{++}GaN tunnel junctions to connect multiple InGaN active regions, white nanowire LEDs have been realized [269]. In the same report, without using an current converting driver, alternating-current operated nanowire LEDs have been realized through monolithic integration of *p*-GaN up and *p*-GaN down nanowire LED structures on the same substrate [269]. However, the epitaxial growth of multiple InGaN

active regions and multi tunnel junctions into the same nanowire encounter the possibility of nanowire coalescence. In addition, the limited color-tunability and the relatively low CRI of white light is the disadvantage for this approach to be used for practical applications of full-color and white LEDs [269].

Nanowire InGaN/GaN LED heterostructures can be grown on various types substrates, providing substantial reductions in production costs and material consumption as well as great flexibility for the integration into systems with comprehensive functions. In addition to Si substrates [270], nanowire InGaN/GaN heterostructures can be fabricated on other low cost substrates, including amorphous glass, aluminum foil and copper substrates [271, 272].

1.3.2 InGaN Nanowire Lasers

The tunable energy bandgap, extremely small surface recombination velocity, and large exciton binding energy (~ 26 meV for GaN) render InGaN nanowires a promising candidate for ultra-low threshold, small scale and compact lasers [273-277].

Using a GaN nanowire with length of ~ 40 μm, the first optically pumped GaN nanowire laser exhibited multiple-mode and a threshold power density of ~ 700 nJ/cm^2 (pulsed excitation) [273]. More recently, single-mode nanowire lasers have been demonstrated by using single GaN nanowire [275, 278, 279]. By significantly reducing nanowire dimensions but maintaining high material gain, with the number of cavity modes reduced, Li et al. reported optically-pumped single GaN nanowire lasers which exhibit a single-mode linewidth of ~ 0.12 nm and threshold power density in the range of 200 to 400 kW/cm^2 depending on nanowire length [275]. By coupling single GaN nanowire to an underlying Au substrate, with multiple transverse-mode suppressed, Xu et al. reported single-mode lasing [279]. By creating cleaved-coupled cavities in single GaN nanowires transferred to Si substrate, Gao et al. theoretically and experimentally demonstrated lasing spectral manipulation of GaN single nanowires [278]. Multi-color lasing emissions have been realized by using InGaN plasmonic optical pump lasers

[280-282]. In the demonstration of InGaN plasmonic lasers, the InGaN/GaN nanowire gain medium was placed on Al_2O_3 coated with Ag film, and the lasing wavelengths can be varied from 474 nm to 627 nm by optical pumping of nanowires with different InGaN compositions [281, 282]. The threshold power densities were in the range of 10-100 W/cm^2. However, the linewidths were ~ 4 nm, which need further improvements [281, 282].

Very recently, with the use of high density spontaneously grown InGaN nanowires on Si substrate, relatively low threshold InGaN edge-emitting lasers were demonstrated in the green [283] and red spectral range [284]. Taking advantages of InGaN/GaN disk-in-a-wire heterostrcutures, a lasing peak with the wavelength of 533 nm and a linewidth of ~ 0.8 nm was achieved by using nanowire edge emitting lasers with the threshold current density of 1.72 kA/cm^2 [283]. By further increasing the In content in the active region, the lasing wavelength was extended to 610 nm with a threshold current density of ~ 2.9 kA/cm^2 [284]. In these structures, a small strain field complements the reduced dislocation densities, and the three-dimensional quantum confinement of charge carrier and the resulting near-discrete density of states leads to large gain and differential gain. With such dot-in-nanowire arrays, diode lasers with emission extending from 533 nm to 1.3 μm have been demonstrated [283-285]. However, it is difficult and complicated to integrate multi-color nanowire edge-emitting lasers into a single chip to achieve tunable-color emissions.

Surface-emitting laser provides a viable and monolithic approach to integrate full-color lasers to achieve tunable-color emissions from a single chip. Nanowire photonic crystal lasers use an external high-Q photonic crystal microcavity providing a strong feedback regardless of the nanowire lengths, offering the possibility of achieving nanoscale lasing. A bottom-up nanopillar photonic crystal lasers has been demonstrated, taking advantages of a GaAs/InGaAs/GaAs axial double heterostructure for accurate, arbitrary placement of gain within the cavity and lateral InGaP shells to reduce surface recombination [286]. The lasers

operate single-mode at room temperature with low threshold peak power density of ~ 625 W/cm^2 [286]. An optically pumped monolithic single GaN nanowire laser (λ=371.3 nm with a linewidth of 0.55 nm) on Si with a 2-D photonic crystal (PC) resonant cavity operating at room temperature has been recently demonstrated [287]. The threshold is observed at a pump power density of ~ 120 kW/cm^2 and the spontaneous emission factor β is estimated to be 0.08 [287].

A few groups have developed optically pumped multiple-color InGaN nanowire photonic crystal lasers [288, 289]. Using the top-down approach to fabricate nanowire photonic crystal lasers, Wright et al. reported single-mode lasing in the blue-violet spectral range with a 60 nm (380-440 nm) tuning range [288]. With a threshold of 130 kW/cm^2, sharp lasing peaks (width < 0.2 nm) appeared at 415 nm. Using the technique of selective area epitaxy on GaN template by MBE, Ishizawa et al. demonstrated optically pumped InGaN nanowire photonic crystal lasing with peak positions varying from 477 nm to 560 nm at room temperature [289]. The spectral linewidths were around 2.7 nm, and the threshold power densities were measured to be around 1 MW/cm^2 [289]. Over the same chip, the lasing peak positions mainly depends on the lattice periodicity of InGaN nanowires array. However, the current demonstrated photonic crystal lasers have large threshold, relatively low efficiency, and low output power. Moreover, there is no corresponding reports of electrically injected surface emitting lasers.

1.3.3 InGaN-based Nanowire Solar Cells

Benefiting from the unique geometry of nanowires and their high aspect ratio, nearly dislocation-free nanowire structures have many advantages for the photovoltaic applications, including efficient radial collection of all carriers, direct and short paths for carriers to reach the electrode and large surface area to absorb the incident light. In the past few years, nanowire solar cells leapfrogged other mature photovoltaics technologies, such as dye-sensitized solar

cells and multicrystaline Si solar cells. The progress of nanowire solar cells is fast in recent years.

Various approaches can be used to fabricate nanowire solar cells, for example, ZnO nanowire arrays synthesized by using aqueous solutions, TiO_2 nanowire arrays synthesized by anodization of Ti foils, and Si nanowire arrays synthesized by chemical vapor deposition (CVD) or vapor-liquid-solid (VLS) approach [290-297]. Intense efforts have been paid on the development of nanowire solar cells by using inorganic material systems and various synthesis techniques. The nanowire structure, synthesis method, V_{oc}, J_{sc} and η of various nanowire material system are summarized in Table 1-2, based on the extensive reports of nanowire solar cells.

Table 1-2: Reports of nanowire solar cells of various material systems.

Structure (Synthesis method)	V_{oc} and J_{sc}	η	First Author Year of report
Ensemble nanowire array Axial *p-i-n* InP (SAE-MOVPE)	One-sun 0.779 V and 24.6 mA/cm^2	13.8%	J. Wallentin [298] 2013
Ensemble nanowire array Core-shell *p-i-n* InP (SAE-MOVPE)	One-sun 0.43 V and 13.7 mA/cm^2	3.37%	E. C. Garnett [299] 2011
Single nanowire Axial *p-i-n* Si (Vapor-liquid-solid growth)	One-sun 0.29 V and 3.5 mA/cm^2	0.5%	B. Tian [296] 2009
Single nanowire Core-shell *p-i-n* Si (Vapor-liquid-solid growth)	One-sun 0.45 V and 9.8 mA/cm^2	3.2%	T. J. Kempa [300] 2012
Ensemble nanowire array Axial *p-i-n* GaAs (MOCVD)	One-sun 0.906 V and 21.3 mA/cm^2	15.3%	Ingvar Aberg [301] 2016
Ensemble nanowire array Core-shell ZnO/CdS (MOCVD)	One-sun 0.8 V and 14.6 mA/cm^2	2.81%	M.-L. Zhang [302] 2014
Ensemble nanowire array *p*-GaN nanowires/*n*-Si substrate (CVD)	One-sun 0.95 V and 7.6 mA/cm^2	2.73%	Y. B. Tang [24] 2008

As shown in Table 1-2, the active photovoltaic elements of nanowire solar cells can be either single nanowire [297] or ensemble nanowire array, depending on the purposes of

experiment. The characterizations of single nanowire solar cell, in which only a single nanowire is connected to electrodes, can rule out the adverse factors introduced in the fabrication process of ensemble nanowire array such as nonuniform metal contact and insufficient carrier collection, revealing the inherent photovoltaics properties of materials. For example, for axial and core-shell *p-i-n* Si single nanowire solar cells grown using VLS approaches, core-shell nanowire structure exhibited nearly five times higher efficiency values than axial nanowire structure, and the V_{oc}, J_{sc} and FF values of core-shell nanowire structure were also much higher than axial nanowire structure [296]. This reveal the importance of suppressing surface recombination for *p-i-n* Si nanowire solar cells. However, the synthesis method and/or fabrication process of single nanowire devices generally require sophisticated skills and high-resolution equipment.

InGaN-based nanowires exhibit large electron mobility and high absorption coefficient over the wide range of InGaN bandgaps (5.7×10^5 and 5.2×10^5 cm^{-1} at the bandgap of 2.95 eV and 2.45 eV, respectively [239]), which can lead to both fast electron transport and high light absorption. Extensive progresses have been made on the development of InGaN-based nanowire solar cells. However, there are still plenty of room for further improvements in InGaN-based nanowire solar cells, as presented in the Table 1-3. for example, due to limited In composition (0 to 0.27) used in coaxial *n*-GaN/*i*-InGaN/*p*-GaN nanowires reported by Y. Dong et al., this nanowire heterostructures were similar to planar InGaN heterostructures and it exhibited high V_{oc} but relatively low J_{sc} [303]. One of the challenge for current InGaN-based nanowire solar cell is the difficulty in suppressing the surface recombination but maintaining fast carrier transports and sufficient carrier collections. As presented in the Table 1-3, for example, using axial *p-i-n* InGaN nanowire, nanowire solar cells reported by M. F. Cansizoglu et al. exhibited relatively high J_{sc} of 4.6 mA/cm^2 but low V_{oc} of 0.22 V, due to surface recombination at the nanowire surfaces [304]. In contrast, as presented in the Table 1-3, using

core-shell *n*-GaN/InGaN MQW/*p*-InGaN nanowires grown on GaN substrates, the nanowire solar cell reported by J.J. Wierer Jr. et al. exhibited a higher V_{oc} of 0.5 V but a lower J_{sc} of ~ 1 mA/cm^2 [305]. Among the reported single-junction InGaN nanowire-based solar cell, ensemble axial *p-i-n* InGaN nanowire array exhibit the highest efficiency of 0.5%, benefiting from its relatively high J_{sc} of 4.6 mA/cm^2 [304].

Table 1-3: Reports of InGaN-based nanowire solar cells.

Structure (Synthesis method)	V_{oc} and J_{sc}	η	Author Year of report
Ensemble nanowires Core-shell MQW GaN/InGaN (MOCVD, *n*-GaN was created by top-down etching)	One-sun 0.5 V and 1 mA/cm^2	0.3%	J. J. Wierer Jr. [305] 2012
Single nanowire Coaxial (Core-shell) *n*-GaN/*i*-InGaN/*p*-GaN (MOCVD, Ni-catalyst)	One-sun, In compositions (0 to 0.27) 2-1 V, 0.059-0.39 mA/cm^2	~0.19%	Y. Dong [303] 2009
Ensemble nanowires Axial *p-i-n* InGaN nanowire (MBE)	One-sun 0.22 V and 4.6 mA/cm^2	0.5%	M. F. Cansizoglu [304] 2015
Ensemble nanowires Axial *p-i-n* InN (MBE)	One-sun 0.14 V and 14.4 mA/cm^2	0.68%	H. P. T. Nguyen [306] 2011

With the advantages of large strain relaxation of GaN-based nanowire heterostructures on Si substrate, intense attentions have been paid to GaN-based nanowire/Si hybrid devices as a double-absorption-band structures for photovoltaics applications. Under the AM 1.5G one-sun illumination, relatively high J_{sc} of ~ 7.6 mA/cm^2, V_{oc} of ~ 0.95 V, FF of 0.38 and η of ~ 2.73% have been measured from a hybrid solar cell in which *p*-GaN nanowire arrays which were grown on *n*-Si substrate [24]. In such a top-illuminated double-absorption-band structure, the top GaN nanowire arrays absorb the light with photon energies larger than the bandgap of GaN, and the bottom Si substrate absorb the light with photon energies smaller than the bandgap of GaN but larger than the bandgap of Si [24]. Through a p^{++}/n^{++} tunnel junction, the feasibility for the monolithic integration of InGaN-based nanowire arrays and Si solar cells have been demonstrated by using MBE growth [307]. With the ideal double-bandgap configuration of

1.75 eV/1.13 eV, such integrated InGaN nanowire/Si tandem photoanodes exhibit a photocurrent density of 16.3 mA/cm^2 under AM1.5G one-sun illumination. At 0.5 V versus normal hydrogen electrode (NHE), the applied-bias-photon-to-current efficiency of 8.3% has been achieved [24].

The efficiency of nanowire solar cell could be further enhanced dramatically by overcoming a few challenges. Nanowire solar cells exhibit high surface-to-volume ratio which leads to a large amount of surface states such as defects which trap the carriers generated by photovoltaics. Surface recombination could result in low efficiency. Moreover, even though the dopant incorporations in nanowire is more efficient than that in planar structures, the proper *p*-type doping of III-nitride nanowires is still difficult and requires careful optimization, further limiting the improvement of the nanowire solar cell performance.

1.4 Progress and Status of GaN-based Field-Effect Transistors (FETs) and the Advantages of Vertical GaN-based Nanowire Field-Effect Transistors

1.4.1 Introduction on GaN-based FETs and the Status of Normally-Off GaN-based Planar HFETs

GaN-based heterojunction field-effect transistors (HFETs), also known as high electron mobility transistors (HEMTs), taking advantages of a high density two-dimensional electron gas (2DEG) formed at the high-mobility heterojunction between GaN and AlGaN, offer an effective alternative to Si metal-oxide-semiconductor field-effect transistor (MOSFET). Due to the advantages of GaN-based materials including large critical electrical field, wide bandgap, high peak electron velocity and high saturation electron velocity, GaN-based electronic devices exhibit low ON-state resistance ($R_{ds\text{-}on}$), high breakdown field and fast switching speed, promising high-power, high-temperature, and high-frequency operations [308-310]. Compared to Si-based devices, GaN-based devices exhibit lower losses at high voltage (typically in the

hundreds of volts) and very stable characteristic parameters such as $R_{ds\text{-}on}$ over varying temperature [308].

Figure 1-4 shows the basic structure of a GaN-based HFET which is a depletion-mode (normally-on) device [311]. The growth of GaN epilayers on Si, SiC and sapphire substrates requires the use of thick GaN, AlGaN and/or AlN buffer layers [311]. Currently, lateral configuration is widely used for GaN-based FETs, due to the challenge in the development of vertical GaN power devices [311, 312]. In contrast to Si MOSFETs which generally use *p-n* junctions [311], GaN-based HFETs do not rely on *p-n* junction, exhibiting symmetric structure of the HFET drain and source. This unique feature of GaN-based HFETs makes possible the self-commutated reverse conduction, and the GaN-based HFETs has no avalanche breakdown [308-310].

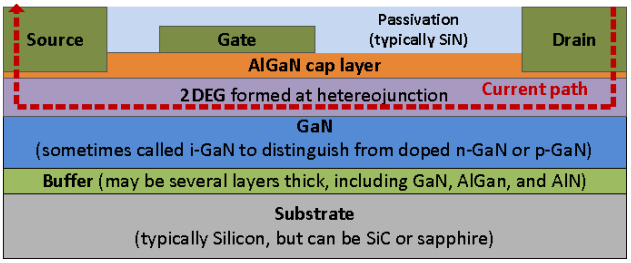

Figure 1-4: The basic structure of GaN-based HFET. Reprinted from journal publication authored by E. A. Jones et al. in *2014 IEEE Workshop on Wide Bandgap Power Devices and Applications (WiPDA)* © [2014] IEEE [311], with the permission of IEEE.

The conventional HFETs are fundamentally normally-on (depletion-mode) device [311]. In such normally-on devices, the devices conduct across the drain to source even without any voltage applied to its gate; a negative voltage is applied to gate to turn the device off by depleting the 2DEG. However, normally-off devices (enhancement-mode devices) are more desirable in power converters, due to simpler driving circuit and more reliable power switching than normally-on devices.

Normally-off HFETs can be fabricated by using three different approaches including insulated gate enhancement mode, non-insulated gate enhancement mode and cascode [311].

Currently, the normally-off GaN-epilayer-on-Si FETs from leading companies generally exhibit maximum current (I_{max}) in the range from 10 A to 30 A, $R_{ds\text{-}on}$ in the range from 25 to 350 mΩ, and $V_{th,\ gs}$ in the range from 0.8 V to 3 V [313-318]. According to published specifications of HRL laboratories [313], normally-off GaN FETs with insulated gate F-plasma treated, exhibits I_{max} of 5.5 A, $R_{ds\text{-}on}$ of 500 mΩ, and $V_{th,\ gs}$ of 0.6 V, which is the lowest $V_{th,\ gs}$ value to the best knowledge of the author. According to published specifications of NEC [314], normally-off GaN FETs with insulated gate which is a recessed gate, exhibits I_{max} of 240 mA/mm and $V_{th,\ gs}$ of 1.5 V.

However, GaN-based FETs generally suffer from a phenomenon called current collapse and the associated device degradation. Along with the switching cycles of ON and OFF, trapped electrons obstruct the current flow when high voltage is applied [319]. Such electron trapping occurs at high electrical field, increasing $R_{ds\text{-}on}$ and hence degrade the performance of FETs [319]. In high-voltage operations, the effects of current collapse irreversibly result in the device failures caused by the heating effect [319]. The trap states originate from crystal defects, dislocations, and/or the presence of impurities [320-323]. However, the detailed mechanisms of current collapse are still under research. The current collapse might be attributed to thermally activated defect diffusion, and a few types of defects such as electric-field-enhanced defects have been identified to be responsible for this phenomenon [322-325]. In addition to current collapse, there are other challenges such as short-channel effects. The short-channel effect hinders the efforts on further reduction of the device size to integrate as many as transistors in a dense integrated circuit [326-328].

To address the current challenges in GaN-based FETs, the main bottleneck is eventually the fundamental challenges in growing high quality GaN-based epitaxial layers on cost effective, large area substrates such as Si substrates. The characteristics of current GaN-based FET devices are directly related to the materials qualities such as defect density, dislocation

density, macroscopic stress and deformations in epilayers, and interface roughness [319, 329-331], which are ultimately limited by large lattice mismatches and large mismatches in thermal expansion coefficient in heteroepitaxy of GaN-based layers.

1.4.2 Normally-Off GaN-based HFETs Using GaN-based Nanowires

Various GaN-based nanowire field-effect transistors [332-334] and InGaAs/InP-based nanostructure devices [335, 336] have been demonstrated, by using 3-dimension (3D) III-V-based active nanostructures which are surrounded by efficient 3D gate structures. Based on the geometries of employed nanostructure active regions, various 3D gate configurations including double-gate [337], triple-gate [334, 335], multi-gate [338], and gate-all-around [339, 340] structures have been demonstrated and developed. III-V-based FETs using 3D active regions and 3D gate exhibit improved performance such as much better electrostatic control and higher temperature operations [338], compared to conventional planar devices. Besides improved materials quality of nanostructures due to effective strain relaxation, it has been observed that transistors using nanostructures can exhibit much reduced short-channel effects [341].

Current GaN-based nanowire FETs generally use top-down approaches to make 3D structures [338-340, 342]. Figure 1-5 illustrates the fabrication process of a gate-all-around hybrid MOS-HFET [311, 339]. To maximize controllability of HFET devices, the entire GaN-based nanowires were surrounded by 3D-distributed gate materials, as shown in Figure 1-5 [332]. Such a normally-off GaN-based transistor consisting of triangle-shaped GaN nanowires arranged horizontally, exhibits a threshold voltage of 3.5 V, an on/off current ratio of 10^8, a transconductance of 3 mS/mm, and a drain current of 8 mA/mm. Its maximum drain current is 0.11 mA and the maximum transconductance is 0.04 mS.

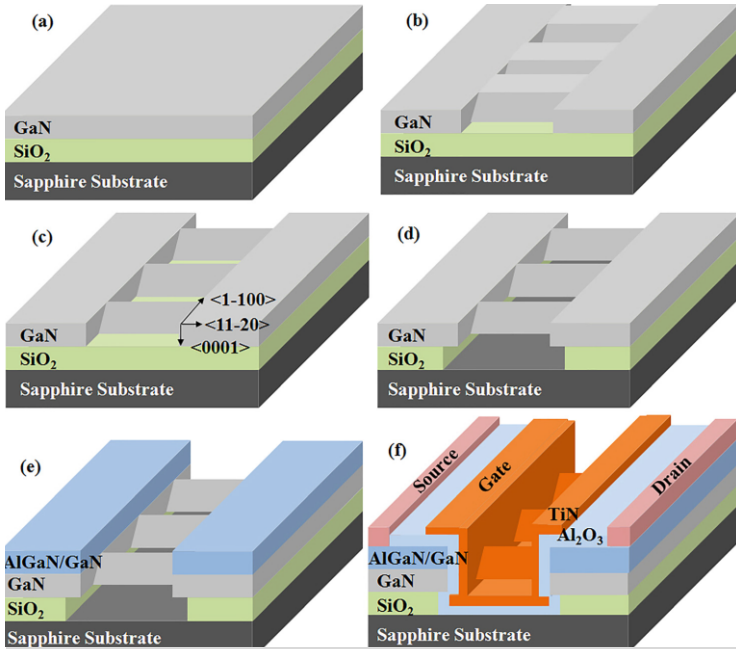

Figure 1-5: Fabrication sequence of a GaN nanowire gate-all-around (GAA) transistor: (a) The structure of GaNOI wafer. (b) The formation of GaN nanowire arrays. (c) Reduced GaN nanowire arrays achieved by etching along <1-100> direction, which resulted in the triangle-shaped nanowire. (d) Release of GaN nanowire arrays by removing the sacrificial SiO_2 buried oxide. (e) Regrowth of AlGaN/GaN heterostructure on the patterned GaNOI wafer. (f) Schematic illustration of the proposed nano-device. Reprinted from the journal publication authored by K.-S. Im et al. in *Applied Physics Letters* [339], with the permission of AIP Publishing.

The fabrication of horizontally-arranged GaN-based nanowire FETs inevitably requires separation of the active region from the underlying bulk substrate [338], which use sacrificial layers such as a selective SiGe epitaxial layer [342] or a buried oxide layer in the fabrication process [339, 340]. The relatively poor material qualities of GaN-based epilayers grown on sacrificial layers limit the transistors performance [338]. Due to the need of multiple etching processes, such a device fabrication is challenging, considering the difficulties to identify multiple proper and effective etching solutions and/or etching procedures.

Compared to lateral-type devices which are generally limited by the short-channel effects, vertical-type devices make it more viable and practical to integrate more transistors in a dense integrated circuit. The source-drain path or electron gas can be configured vertically in a

vertical-type device, instead of occupying a relatively large substrate area to horizontally arrange the source-drain path in lateral-type devices.

As shown in Figure 1-5 [339], the fabrication processes of lateral-type 3D nanostructured GaN-based power-switching devices with 3D-distributed gates, were complicated and difficult [334, 335, 337-340]. Moreover, their fabrication involving multiple etching process which degrades the device performances [334, 338, 339]. The current lateral-type GaN-based power-switching devices generally rely on using *c*-plane Al(Ga)N/GaN heterostructure, exhibiting extremely high sheet electron concentration (>10^{13}/cm^2) induced by strong piezoelectric and spontaneous polarization effects at the heterointerface [343, 344]. However, the extremely high sheet electron concentration increases the difficulties and complexities for making normally-off devices (enhancement-mode devices) in the lateral-type configurations [344-346]. Instead, vertical-type configurations make it possible to use nonpolar planes as the active regions of HFETs [344].

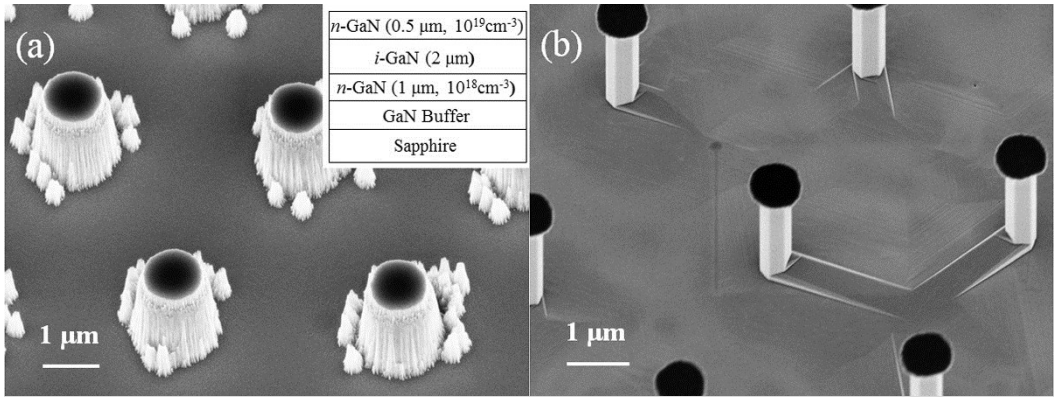

Figure 1-6: SEM images of the tilted (a) GaN trapezoidal wire array after ICP RIE with SF_6 and H_2 gases for 30 min; (b) GaN nanowires after wet chemical treatment of trapezoidal wires in developer at 85 °C for 4 h. Inset: epitaxy structure of GaN layers before etching. Reprinted from the journal publication authored by F. Yu et al. in *Applied Physics Letters* [344], with the permission of AIP Publishing.

Recently, F. Yu et al demonstrated a vertical GaN wrap-around gated field-effect transistors using the nonpolar sidewalls of GaN nanowires on GaN/sapphire substrates [344].

Through inductively coupled plasma reactive ion etching (ICP RIE) of *n-i-n* GaN homo-epilayers grown by MOVPE on *c*-plane sapphire substrates, GaN trapezoidal wires in regular honeycomb array are realized by using e-beam evaporated Cr as a mask layer [344]. The SEM image in Figure 1-6 (a) presents the GaN wire array together with the Cr masks at the top of GaN wires [344]. A "post ICP" wet etching treatment was employed to smoothen the sidewalls of GaN wires, by using a buffered KOH solution (a commercial developer AZ400K). Figure 1-6 (b) presents wires array exhibiting smooth *a*-plane {11-20} sidewalls and reduced wire diameters after "post ICP" wet etching treatment [344].

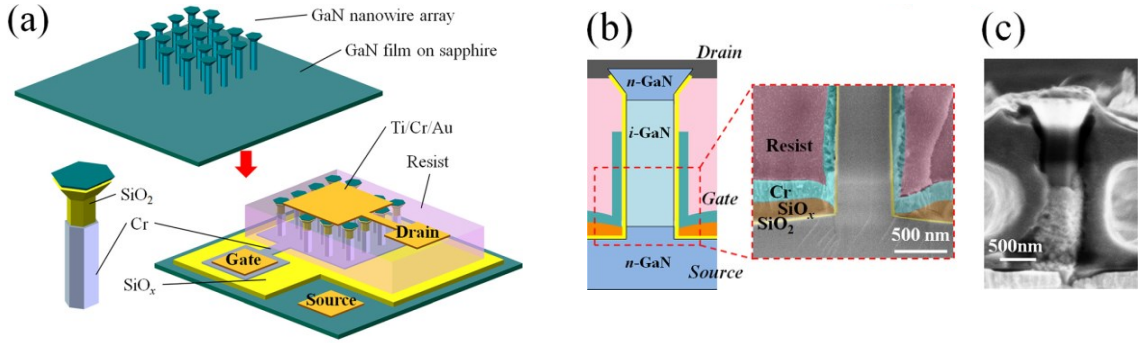

Figure 1-7: (a) Schematics of a vertical GaN transistor with three electrodes formed by mushroom shape nanowire array (bottom right) with the naked array (top) as well as a processed nanowire (bottom left); (b) cross-sectional schematic of one GaN nanowire inside the transistor with layer structure after multi-deposition (left) and a dyed cross-sectional SEM image of its lower part (right); (c) SEM image of a single nanowire in device after processing with a gate length (L_g) of 1.3-1.6 μm. Reprinted from the journal publication authored by F. Yu et al. in *Applied Physics Letters* [344], with the permission of AIP Publishing.

Figure 1-7 (a) is the schematics of vertical GaN nanowire transistors [344]. Shown in Figures 1-7 (a) and (b), 20-nm-thick SiO_2 was firstly deposited by plasma enhanced atomic layer deposition (PEALD) to form a dielectric layer on the *a*-plane sidewalls. A 300-nm-thick Cr layer was deposited by e-beam evaporation to form the wrap-around gate (or gate-all-around) contact, and an organic polymer was used to fill the gaps between the nanowires [344]. Drain-metal contact was deposited at the top of nanowire arrays, and source-metal contact is deposited at the side of nanowire array, due to the use of nonconductive sapphire substrate

[344]. The device fabrication process of such a vertical GaN nanowire transistor with a wrap-around gate is more straightforward than the generally reported lateral-type power-switching devices.

Besides the general advantages of vertical-type transistors, such a vertical enhancement-mode GaN nanowire has a relatively straightforward fabrication process and the advantages of using nonpolar GaN sidewalls. This normally-off GaN transistors consisting of 7 nanowires, exhibited a threshold voltage of 1.2 V, an on/off current ratio of 10^8, a transconductance of 125 mS/mm, and a drain current of 314 mA/mm. However, this GaN nanowire device rely on the dry etching process and the use of GaN/sapphire substrates to make the nanowire arrays [312, 344].

In the current vertical GaN nanowire transistors, the use of nonconductive sapphire substrate limits the heat dissipation and essentially requires a metal contact placed at the side of nanowire arrays. Conductive properties of Si substrates offer unique advantages as a substrate [308-310], compensating the relatively low thermal conductivity of GaN and enabling the use of backside metal contact. The employment of Si substrates reduces the cost, enabling the scale-up of vertical GaN-based nanowire transistors. For the applications in the fields of power transistors, it is very desirable to develop the selective-area epitaxy (SAE) of GaN-based nanowires on Si substrate to grow high quality GaN-based nanowires which can be flexibly and precisely controlled in nanowire geometry and nanowire size. Through the SAE of GaN-based nanowires on Si substrate, GaN-based nanowires with tunable electrical characteristics can be vertically integrated on Si substrates. The flexibility to tailor the nanowire size and position make a relatively simple device fabrication possible, making possible the scale-up of vertical GaN-based nanowire transistors.

1.5 The Organization of this Dissertation

In Chapter 1, the status and challenges of demanding optoelectronics including LEDs, lasers and solar cells in the visible spectral range are reviewed and discussed in sections 1.1 and 1.2, and the status and challenges of GaN-based FETs are reviewed and discussed in section 1.4.1. To realize those demanding applications and overcome the associated challenges, GaN-based epilayers and nanowires have been used to develop efficient and effective GaN-based optoelectronics and GaN-based FETs. The progresses are reviewed and discussed in sections 1.2, 1.3, and 1.4.

It can be concluded based on the overview and discussions in Chapter 1 that the development of optoelectronic devices and FETs made by using conventional GaN-based QWs or planar heterostructures is ultimately restricted by the challenges in growing high-quality In-rich InGaN planar heterostructures, integrating mismatched substrates and/or device fabrications of GaN-based planar heterostructures. These fundamental and practical challenges can be overcome or avoided by using GaN-based nanowires. In addition, the use of nanowire enables the flexibility to tailor the geometry and size of materials and devices, meeting the needs of novel and advanced applications of optoelectronics and transistors.

In Chapter 2, bottom-up approaches and top-down approaches to fabricate or synthesize GaN-based nanowires are introduced in section 2.1, with special attention paid to the bottom-up approaches including vapor-liquid-solid (VLS) growth, catalyst-free spontaneous growth and selective area epitaxy (SAE). The molecular beam epitaxy (MBE) system are introduced in section 2.2, advantages and disadvantages of MBE-grown nanowire are discussed section 2.3. In section 2.4, challenges and opportunities of GaN-based nanowire heterostructures and devices in the aspects of inherent characteristics, growth, device fabrications and practical applications are reviewed and discussed. In section 2.5, the characterization methods used in this dissertation are introduced briefly.

Based on the challenges and opportunities described in section 2.4 about the state-of-the-art GaN-based nanowire heterostructures and devices, a few experimental studies have been conducted. The methods and results of these experimental studies are described and discussed in Chapter 3, Chapter 4, Chapter 5, Chapter 6 and Chapter 7. In Chapter 8, the research works in this dissertation are summarized and future works are proposed.

Chapter 2: Molecular Beam Epitaxial Growth and Characterizations of High Quality GaN-based Nanowire Heterostructures

2.1 Bottom-up Approaches of Nanowires

2.1.1 Introduction

The methods to synthesize or fabricate GaN-based nanowires including bottom-up approaches and top-down approaches [124, 347]. In the top-down approaches, as-grown GaN-based planar heterostructures are selectively etched into GaN-based nanowire heterostructures, taking advantages of the nanoscale patterns created on planar heterostructures [348-351]. Various types of mask materials, such as metal and SiO_x nanoislands [348, 352], have been used to define the geometry and size of resulting nanowire heterostructures. Nanoscale patterns can be defined by using various methods, such as electron beam lithography (EBL) [353] and nanoimprint lithography [349]. The top-down approaches for In-rich GaN-based nanowire heterostructures are ultimately limited by the challenges in the epitaxial growths of In-rich GaN-based planar heterostructures exhibiting long-wavelength emissions. Moreover, the etching process generally introduce damage and defects on nanowire sidewalls [350, 351], limiting the performances of resulting GaN-based nanowire devices.

The bottom-up approaches, in which nanowire heterostructures are grown monolayer by monolayer through the build-up of adatoms on the bottom substrates, mainly include the vapor-liquid-solid (VLS) growth [354], catalyst-free spontaneous growth [355, 356] and selective area epitaxy (SAE) [357].

2.1.2 Vapor-Liquid-Solid (VLS) and Spontaneous Growth of Nanowires

GaN-based nanowire heterostructures provide a viable route to minimize defect concentrations and hence achieve a high radiative recombination efficiency, which has been shown to be essential to maximize GaN-based device performance.

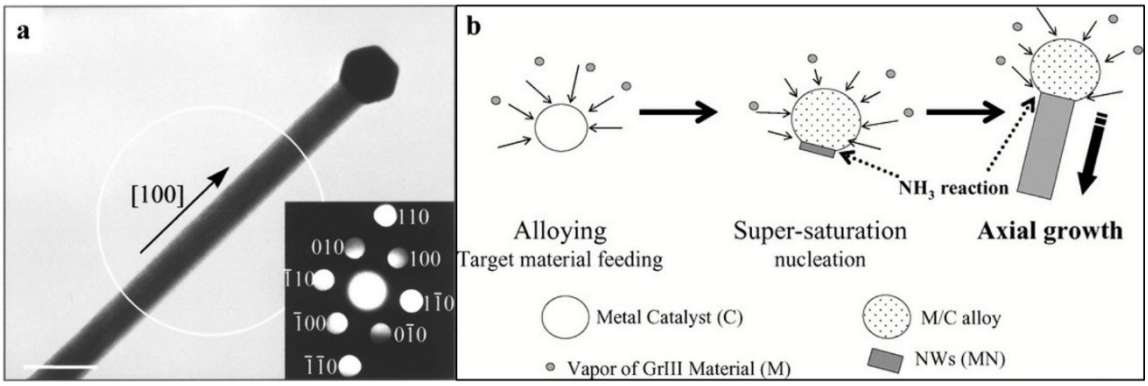

Figure 2-1: (a) Diffraction contrast TEM image of a GaN nanowire that terminates in a faceted nanoparticle of higher (darker) contrast. (Inset) CBED pattern recorded over the region indicated by the white circle. The white scale bar corresponds to 50 nm. Reprinted with permission from the journal publication authored by X. Duan et al. in *Journal of the American Chemical Society* [358]. Copyright (2000) American Chemical Society. (b) A schematic representation of the vapor-liquid-solid (VLS) growth. Reprinted from the journal publication authored by S. Chattopadhyay et al. in *Critical Reviews in Solid State and Materials Sciences* [359], with the permission of Taylor & Francis.

In the VLS growths of GaN nanowires, particles or nanoislands of metal catalysts, such as Ni, Au, Co and Fe [358, 360-363], absorb Ga from gas phases to form supersaturated liquid alloy phases. With the Ga supply from liquid alloy, GaN nanowires nucleate and grow at the interface between liquid alloy and solid surface [364]. Figure 2-1(a) shows the TEM analysis on a GaN nanowire grown by using laser-assisted catalytic growth which is based on VLS growth mechanism [358]. The faceted nanoparticle at the top of GaN nanowire is the alloy containing the Fe catalyst [358]. Figure 2-1(b) is a schematic of the VLS process [359]. Metal catalysts act as preferred nucleation and unidirectional growth sites of nanowires. The size and position of nanowires mainly depends on the size and position of metal catalysts. The size and position of nanowires are also affected by various growth parameters such as vapor pressure and growth temperature [354, 365]. Various VLS growth techniques have been developed to grow GaN nanowires [358]. For example, low pressure metal-organic vapor phase epitaxy (MOVPE) use trimethylgallium (TMGa) [360] or triethylgallium (TEGa) [360] as the Ga

sources, and 1.1-dimethylhydrazine (DMHy) or NH_3 can serve as the N source corresponding to the used Ga source. By using chemical vapor deposition (CVD), Ga_2O_3 and NH_3 have been used to synthetize GaN nanowires [362].

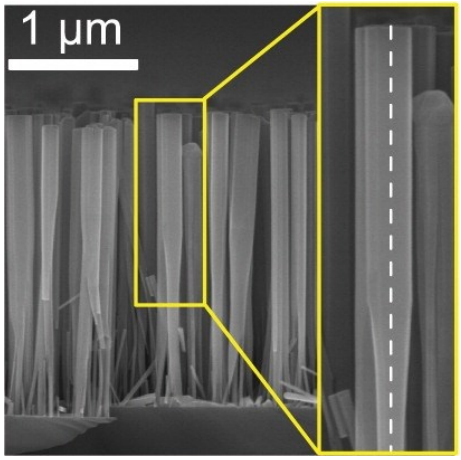

Figure 2-2: Cross-sectional SEM image of spontaneously grown GaN nanowires by using MBE. Reprinted from from the journal publication authored by S. Fernández-Garrido et al. in *Nano Letters* [366]. Copyright (2013) American Chemical Society.

However, the optical and electrical properties of GaN nanowire heterostructures and their devices suffer from the undesirable contaminations from metal catalysts during the VLS growth [363, 367, 368]. The adverse effects of metal contaminations have been well studied in the VLS growths of Si nanowires [369-371]. In GaN nanowire, such metal impurities lead to defects such as stacking faults and create deep-level trap states [367].

In the approach of spontaneous growth which have been widely used in molecular beam epitaxy (MBE), III-nitride nanowires can be formed spontaneously under nitrogen-rich conditions without using any foreign metal catalysts [355, 356, 372], thus there is no metal impurities incorporated in the nanowires. Figure 2-2 shows the SEM image of the cross section of spontaneously grown GaN nanowires by using MBE [366]. It has been concluded from recent experiments that spontaneously grown InN nanowires nucleate and grow from In droplets [373, 374], which is known as a self-catalytic growth process [375]. A few studies

suggest the spontaneous formation of GaN nanowires is also assisted by Ga metal catalysts, and the growth mechanism is also a self-catalytic process [376-378].

However, it has not reached a conclusion on the underlying mechanism for spontaneous formations of GaN nanowires, different epitaxy mechanisms have been proposed instead of self-catalytic process [376, 377, 379-381]. A few studies ruled out the possibility of a self-catalytic process in their experiments due to a few considerations and concluded that the spontaneous formations of GaN nanowires is due to a different mechanism [380-382]. In these experiments, the growth of GaN nanowires used relatively high growth temperature, wherein Ga droplets were unstable and therefore cannot act as catalytic sites [380-382]. In catalytic growth processes, the presence of metal catalysts is commonly observed, as shown in Figure 2-1 (a). However, in spontaneous growths of GaN nanowires, researchers did not observe the presence of Ga droplets on the tip or sidewall of the nanowires [96, 355, 356]. An experimental study show that there is no difference in nanowire size and density whether the pre-deposited Ga droplets (90-340 nm) were used or not [355]. Instead of a self-catalytic mechanism, these studies attribute the self-organized process of GaN nanowires mainly to the variations in sticking coefficients, diffusion coefficients, and surface energies on different crystallographic planes [380, 381].

Figure 2-3 (a) illustrate the self-organized nucleation process and Figure 2-3 (b) illustrate the subsequent nanowire growth from stable nucleation sites [355]. Nucleation of GaN nanowires is initialized through the self-induced nucleation of dislocation-free coherently strained islands driven by a strong lattice mismatch nucleation mechanism (Volmer-Weber growth mode) [381]. At the same time, the higher sticking coefficient on the (0 0 0 1) *c*-plane [382] and nitrogen-rich condition (high V/III ratios) prevent layer growth and nucleation sites coalescence [355, 376, 382]. For the *c*-oriented growth or propagation of GaN nanowires, according to a recent density functional theory (DFT) calculation [383], the large aspect ratio

of GaN nanowires cannot be fully explained by diffusion-induced growth mechanism. This DFT calculation indicates that the diffusion barrier along *c*-axis is anisotropically large and hence the diffusion length is shorter at the lateral *m*-plane surface [383]. To fully explore the spontaneous growth mechanism of GaN nanowires, the models may need to take account in other factors such as the contribution of the direct impingent Ga adatoms to the *c*-oriented propagation and shadowing effect of neighboring nanowires [355].

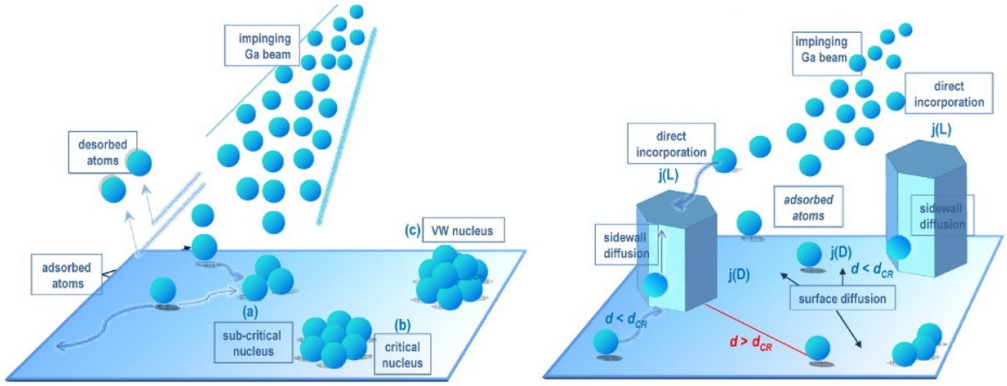

(a) (b)

Figure 2-3: (a) A schematic of the self-organized nucleation process of GaN nanowires. (b) A schematic of nanowire growth from stable nucleation sites. Reprinted from *Journal of Crystal Growth*, Volume 310, J. Ristić, Jelena et al., On the mechanisms of spontaneous growth of III-nitride nanocolumns by plasma-assisted molecular beam epitaxy, Page 4035, Issue 18, Copyright (2008), with permission from Elsevier [355].

2.1.3 Selective Area Epitaxy (SAE)

The self-organized process of spontaneously grown nanowires introduces the variations in nanowire size and length, making it difficult to grow uniform nanowire array or artificially tailor the morphology and sizes of nanowires. Using artificially prepared mask which is flexible in design, selective area epitaxy (SAE) technique enables one to precisely control the size, position and morphology of nanowires and other nanostructures such as nano-stripes and nano-rings. The nano-scale patterns of SAE mask are defined using high-resolution lithography.

Large lattice mismatch can originate from either lattice-mismatched substrates or large composition variations between neighboring layers. Because of efficient strain relaxations in heteroepitaxy with large lattice mismatch, SAE has been reported to effectively accommodate strain and significantly improve III-V material quality on lattice-mismatched substrate such as Si substrate [384, 385]. As shown in Table 1-1, Si substrate exhibits a lattice mismatch of 4.1% with GaAs and a relatively large thermal expansion coefficient compared to GaAs epilayers, resulting in considerable defects in GaAs-based epilayers grown on Si substrates. Hence, the growth of high quality GaAs-based epilayers generally requires expensive substrates such as Ge substrate which exhibits a much smaller lattice mismatch. However, taking advantages of SAE, high-quality and defect-free III-arsenide nanostructures have been achieved on Si substrates by using MBE [386] and MOCVD [384]. On GaAs substrates patterned with SiO_2, the growth of various high quality III-arsenide heterostructures have been achieved using SAE, such as dislocation-free InGaAs film [387], InGaAs QWs [388], large area arrays of GaAs disks and islands [389, 390], GaAs nanowires [391], highly uniform rows of InAs quantum dots (QDs) [392], InAs islands [393, 394], and InAs QDs LED [395]. Besides III-arsenide, the SAE of III-nitrides was also extensively explored by using MOCVD [396, 397] and MBE [357, 398, 399]. The GaN nanostructures selective-area grown on SiC substrates with Si_3N_4 mask exhibit significantly improved quality and longer carrier lifetime compared to planar film [400]. Selective-area grown GaN-based nanowire heterostructures can exhibit effective strain relaxation, and also effectively reduce the dislocations originating from the substrate [401]. SiO_2, SiN_x, and Ti were also used as growth mask materials to grow GaN nanowires by using SAE on GaN templates [399, 402-404].

Recently, GaN-based nanowire arrays, with precisely controlled size and position, have been achieved using SAE technique in RF-MBE [357, 399, 405]. In this process, nanoscale growth patterns were defined on a thin mask layer using high-resolution lithography such as

EBL or nanoimprint. The schematic of selective area epitaxy of GaN-based nanowires on GaN/sapphire substrate is shown in Figure 2-4. Using the ratio of Group-III/N_2 flow rate in appropriate growth window and substrate temperatures much higher than the self-assembled case, group-III metal atoms on patterned substrate either desorb or diffuse to nanoholes and nucleated sites. This leads to the nucleation of GaN occur only on a GaN surface which is exposed in the opening rather than a mask surface. During the epitaxial growth, nanowires nucleate and grow selectively only within the nanoholes, enabling the localization of the epitaxial growth on predetermined sites. High epitaxy selectivity is achieved by optimizing and controlling parameters in each step, including the surface roughness of mask, mask geometry (diameter and spacing), treatment of mask prior to MBE growth, and growth parameters (III/V ratio and substrate temperature) during the MBE growth. The growth dynamics of SAE on GaN/sapphire substrates consists of selective area growth kinetics in the nucleation stage including initial nucleation, coalescence onset and full coalescence, and free-surface-energy minimization in the growth stage including morphological evolution and vertical growth [405, 406].

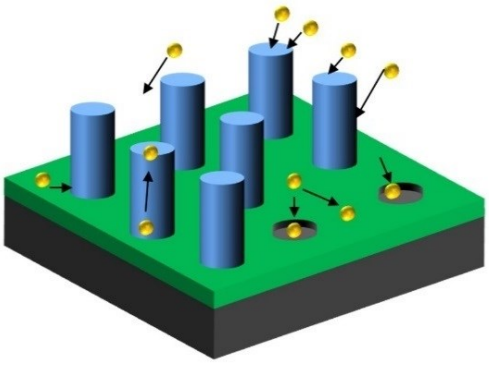

Figure 2-4: Schematic of selective area epitaxy of GaN-based nanowires on GaN/sapphire substrate. The thickness of each layer is not drawn to scale.

2.1.4 Pattern Preparations for Selective Area Epitaxy in this Dissertation

Prior to fabrications of patterned substrates, a thorough solvent cleaning and deposition of a Ti thin mask layers was firstly conducted on commercial GaN/sapphire wafers or Si wafers

with MBE-grown GaN/AlN buffer layers. The wafers were cleaned by using acetone, isopropyl alcohol (IPA) and deionized (DI) water. By using e-beam evaporation, a 10 nm-thick Ti layer was then deposited on top of the GaN as the mask layer, as illustrated in Figure 2-5 (a).

To fabricate Ti mask, a positive resist layer poly(methyl methacrylate) (PMMA) was firstly spin-coated onto the Ti layer and then treated by softbaking. After that, the nanohole array was defined into PMMA layer using e-beam lithography. Various pattern designs, such as different shape and size, can be defined by EBL which can create patterns with the nano-scale feature size. After the designed patterns were exposed in the EBL system (MIRA3 XMH equipped with a Schottky field emission electron gun), the wafers were developed in methyl isobutyl ketone (MIBK).

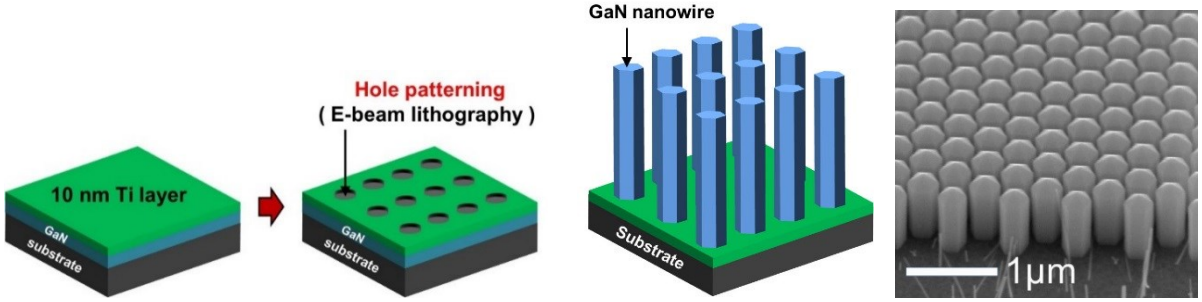

(a) (b) (c)

Figure 2-5: (a) Illustration of nanohole-patterned substrate, (b) Illustration of the selective formation of GaN nanowire array, and (c) a bird's-eye-view SEM image of GaN nanowires grown on patterned substrate.

To transfer the nanohole-array patterns from PMMA to Ti layer, the exposed Ti material was etched down to GaN layer using CHF_3 in a reactive ion etching (RIE) chamber. After that, the remaining PMMA resist was thoroughly removed from the surface by using a two-step process including O_2 RIE and solvent cleaning using NMP based removers (Remover 1165). The patterned substrates underwent a final clean using concentrated hydrogen chloride (HCl, 37%) before being loaded into the MBE chamber for nanowire growth.

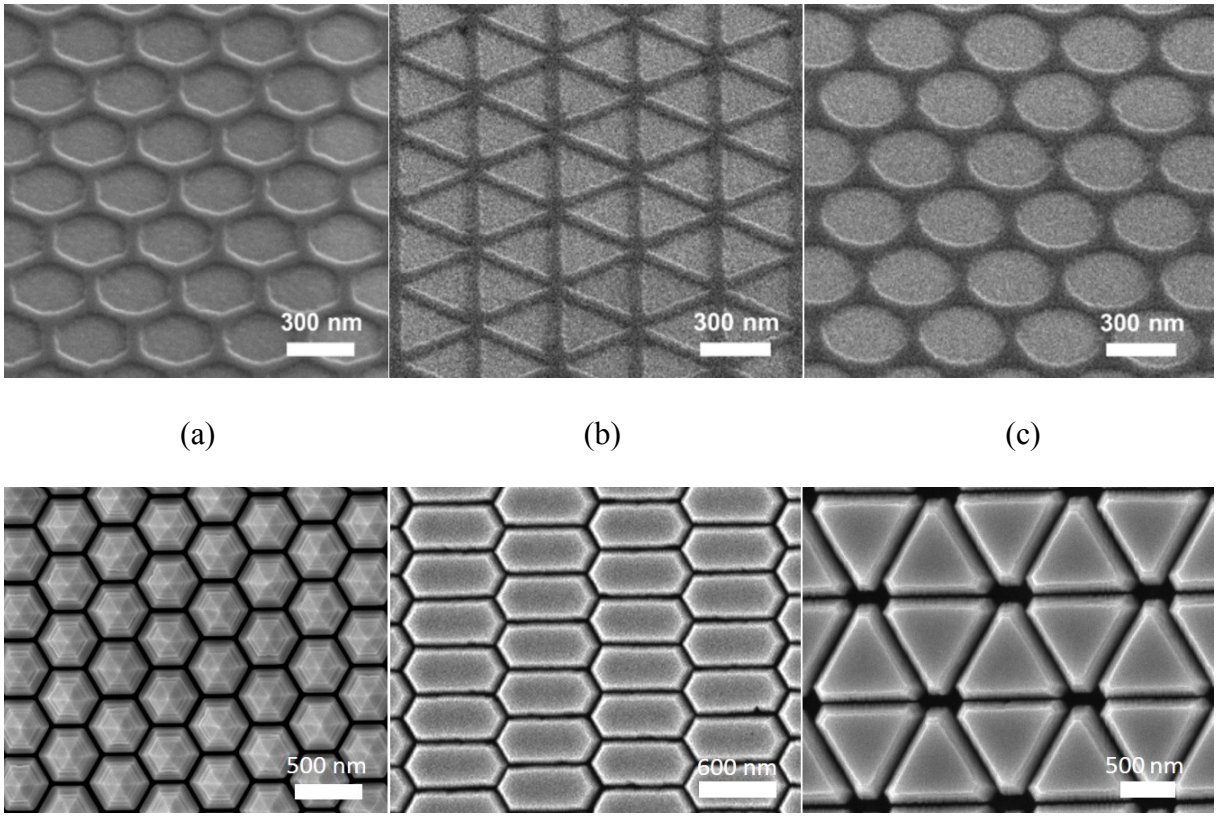

Figure 2-6: Bird's-eye-view SEM images of Ti masks consisting of (a) regular hexagonal nanoholes, (b) triangle nanoholes, and (c) circular nanoholes, and top-view SEM images of GaN-based nanowire array consisting of (d) regular hexagon nanowires, (e) non-regular hexagon nanowires, and (f) triangle nanowires.

Figure 2-5 (a) is an illustration of a patterned substrate with the Ti mask. Figure 2-5 (b) is a schematic of the GaN nanowire array selective-area grown on the patterned substrate. The bird's-eye-view SEM image of the uniform GaN nanowire array grown by using MBE are further shown in Figure 2-5 (c). Various GaN nanostructures, such as nano-stripes, nano-rings and nanowires, can be achieved on patterned substrate with the optimized growth conditions by using MBE. The variations in morphology and size of GaN nanowires can be engineered by varying the designs of mask openings.

Figures 2-6 (a), (b) and (c) show bird's-eye-view SEM images of Ti masks consisting of regular hexagonal nanoholes, triangle nanoholes, and circular nanoholes. To take the SEM

images shown in Figures 2-6 (a), (b) and (c), a 45º tilted sample holder was used. Figures 2-6 (d), (e) and (f) show top-view SEM images of GaN-based nanowire array consisting of regular hexagon nanowires, non-regular hexagon nanowires, and triangle nanowires. The Ti mask layer is treated with nitridation prior to the growth of nanowires.

2.2 Introduction on MBE System and MBE Growth Process

The growth or synthesis of GaN-based nanowires have been successfully developed by using various techniques including chemical vapor deposition [362], chemical beam epitaxy [407], molecular beam epitaxy (MBE) [357, 399, 405], and hydride vapor phase epitaxy [408, 409]. Among the various growth techniques, metal-organic chemical vapor deposition (MOCVD), also known as metal-organic vapor phase epitaxy (MOVPE), has been widely used in industries and academic institutions for manufacturing semiconductor devices, and become a major process to grow III-nitride materials [360, 410] and III-arsenide materials [384, 394].

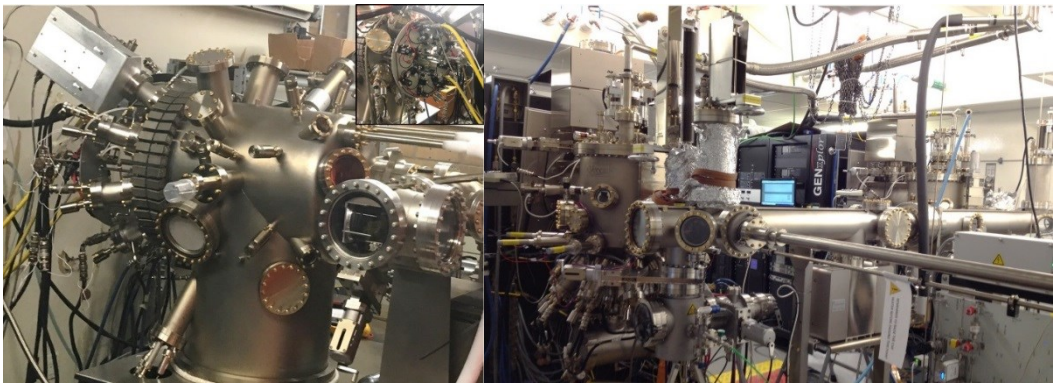

(a) (b)

Figure 2-7: (a) Vacuum Electronic Equipment Co. Gen-II™ molecular beam epitaxial growth system equipped with a radio-frequency plasma-assisted nitrogen source, the inset is the flange ports installed with Ga, In, Al, Ge and Mg effusion cells. (b) Vacuum Electronic Equipment Co. GENxplor™ R&D MBE system containing two growth chambers equipped with radio-frequency plasma-assisted nitrogen sources.

To precisely control the composition and dimensions in the atomic level, *radio frequency plasma-assisted* MBE were used for the growths of GaN-based nanowires in this dissertation. The *radio-frequency plasma-assisted* Vacuum Electronic Equipment Co. (Veeco) GEN-II™

molecular beam epitaxial growth system and Veeco GENxplor™ R&D MBE system are shown in Figures 2-7 (a) and (b), respectively. MBE systems consists of three vacuum chambers including a growth chamber, a buffer chamber, and an intro chamber which are separated by valves. After cleaning substrates thoroughly, the substrates are firstly degassed at 200 °C in the intro chamber. The substrates are subsequently transferred to buffer chamber and a second degassing process at 450-650 °C is applied to the substrates. The growth process is conducted in the growth chamber which has an extremely clean and high-purity environment. In the growth chambers of these two MBE systems, effusion cells containing In, Ga and Al elemental materials are used to provide group-III elements in the epitaxy of III-nitride materials. In *radio-frequency plasma-assisted* MBE system, inert N_2 gas is ionized by a N_2 plasma cell to form active nitrogen plasma supplying the group-V element in the epitaxy of III-nitride materials. In addition, effusion cells containing Si, Ge and Mg elemental materials are used to provide dopants in the epitaxy of III-nitride nanostructures for device applications.

MBE has reached a high level of maturity and now offers several important advantages for III-nitride materials compared to the MOCVD, such as better interface control, in-situ monitoring capability provided by reflection high-energy electron diffraction (RHEED), and lower growth temperature for epitaxy. Driven by the extensive needs to grow high quality epitaxial nanostructures or layers for various applications, MBE system manufacturers have been devoted to the development of novel MBE system design and MBE manufacturing techniques since the invention of MBE system by J. R. Arthur and Alfred Y. Cho in the late 1960s [411, 412]. For example, fully-integrated GENxplor™ R&D MBE system launched in 2013 by Veeco [413], exhibits open-architecture design and efficient single frame integrating all vacuum components with on-board electronics, enabling ease-of-use and convenient access to maintenance [413, 414]. The GENxplor™ R&D MBE system also has the flexibility to

incorporate new functions such as dual-chamber operations and new equipment such as electron beam evaporators [413, 414].

2.3 Advantages and Disadvantages of Nanowires Grown by MBE

Compared to other materials growth/synthesis techniques such as MOCVD, the atom-by-atom epitaxy precision of MBE can enable the highest control of the structural, electronic, and optical properties of various III-nitride nanostructures [357, 399, 405, 415-417] besides other advantages of MBE mentioned in the section 2.3. The unique surface diffusion and atom incorporation kinetics in MBE make possible the self-organized nanowire growth process [355] and SAE of nanowire [405, 406], eliminating the formation of extensive surface defects and usage of foreign metal catalyst. The ultra-high vacuum of MBE ($< 1\times10^{-10}$ Torr) can largely eliminate the unintentional impurity incorporation in III-nitride nanostructures.

In the conventional MOCVD process, the In incorporation is often restricted by the very high growth temperature [91, 418]. The quality of In-rich InGaN QWs epilayers has been limited by severe In phase separation. Taking advantages of *radio frequency plasma-assisted* MBE, catalyst-free In-rich InGaN nanowires [250, 283-285] and InN nanowires [129] have been achieved, indicating unambiguous advantages of MBE in growing In-rich InGaN materials. For example, high efficiency yellow and red LEDs have been developed by using MBE-grown InGaN nanowires [250, 419]. Electrically-pumped visible and near-infrared lasers with emission peak varying from 533 nm (green) to 1.3 μm have also been demonstrated by using MBE-grown InGaN nanowires. Using MBE, monolayer InN QWs in GaN matrix [420] and InN nanowires [129, 144, 421] have been demonstrated.

One another critical advantage of MBE is *p*-type doping is more efficient in MBE than that in MOCVD [129]. The *p*-type conduction is essential and critical for the realization of high efficiency III-nitride devices. The uncontrolled surface charge properties of In(Ga)N materials and the difficulty in realizing *p*-type conductivity have been recognized as one major obstacle

for the practical applications of III-nitride semiconductors in the green, yellow, orange, red and near-infrared spectral range. By using MBE, the precise control over the surface charge properties of InN [421] was achieved, and *p*-type InN was demonstrated recently [129]. It is further discovered that electron accumulation and surface Fermi-level pinning are absent on the surfaces of MBE-grown InN nanowires [144, 421]. The background carrier (electron) concentration in MBE-grown InN nanowire arrays can be reduced to ~ 10^{13} cm^{-3} [144, 145, 421]. *P*-type conduction in InN is confirmed by studying the characteristics of InN:Mg nanowire FETs [129]. By using MBE on Si substrates, efficient incorporations of Mg and Si enables the development of AlN, InGaN and InN nanowire optoelectronic devices [130, 251, 306, 422]. For example, the achievement of *p*-type conduction has led to the first demonstration of InN *p-i-n* LEDs operating at ~ 1.8 μm [422]. Nguyen et al. reported the first InN:Mg/*i*-InN/InN:Si nanowire solar cells grown on Si (111) substrate by using MBE [306]. V_{oc} of 0.14 V, η of ~0.68% and a relatively high J_{sc} of 14.4 mA/cm^2 were measured under one-sun AM 1.5G illumination [306].

With recent advances of production MBE systems, the processing cost and throughput of MBE systems has been brought to a level comparable to MOCVD. Compared to MOCVD [423-425] and HVPE [426], the growths of core-shell single III-nitride nanowires and core-shell III-nitride nanowire arrays are more difficult by using MBE in which axial and non-core-shell GaN-based, InN and AlN nanowires are generally grown [129, 130, 251, 306, 422].

2.4 Opportunities and Challenges for GaN-based Nanowires: From Inherent Characteristics to Practical Applications

2.4.1 The Use of RGB Nanowire LEDs for Color-Tunable Chips

Subpixel rendering technique, which monolithically integrates individual red, green, and blue or additional yellow subpixels into one color-tunable pixel, is being widely used in display industries for various applications such as flat-panel displays (FPDs) and promise the future

applications such as mobile projections [427] and wearable displays [428, 429] including hand-held display media and compact head-mounted display. To achieve power-efficient displays exhibiting high resolution and good image quality, it is highly desirable to make self-emissive display pixels with low power consumption, extremely high pixel density, wide color tunability and accurate color display [430, 431].

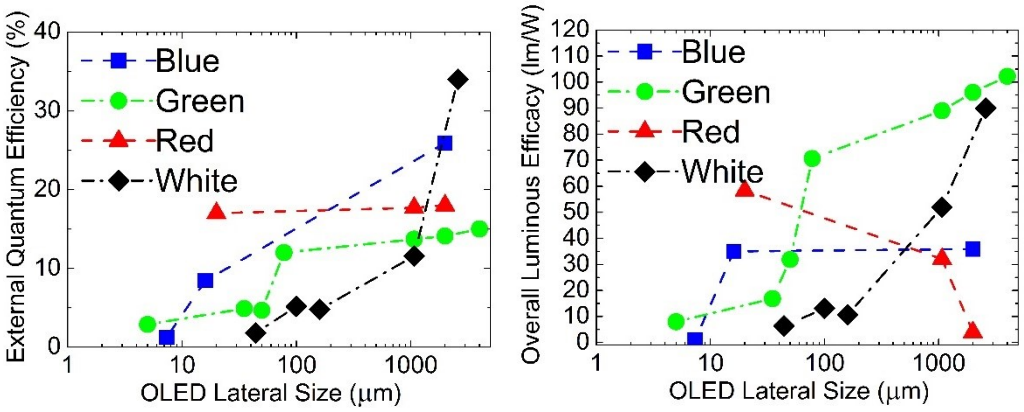

(a) (b)

Figure 2-8: Summary of (a) external quantum efficiency and (b) overall luminous efficacy (or luminous efficacy of a source) versus the OLED device size based on the latest reports of blue, green, red and white OLEDs from various laboratories [46-50, 53, 162-168, 432-436]. Corresponding to the symbol notations in the Figures 2-8 (a) and (b), the symbols of blue, green, red and white OLEDs are plotted with blue, green, red and black colors, respectively. For some literatures which do not provided EQE values directly, their EQE values are calculated from the given overall luminous efficacy using luminous efficacy of radiation function (CIE 1978 Judd−Vos-modified photopic eye sensitivity function) [437, 438]. The detailed information of OLEDs is listed in **Appendix I**.

Portable displays such as smartphones require higher pixel density than large displays such as computer displays and television displays. In other words, color-tunable pixels of current portable displays represent the-state-of-art subpixel rendering technique used for commercial displays. As shown in Figure 1-3 and discussed in the section 1.2.1, OLED technology is currently leading the portable display industries, but its recent advancements in reducing the pixel size and improving luminous efficiency were stagnant or slower than earlier

years. In contrast to its success in portable displays, OLED technology has not obtain the same success in large panels like television and automotive displays [439].

OLED technology suffers from various challenges and bottlenecks in the aspects of manufacturing and practical usage, limiting its further development and commercialization [41-44, 51-53]. Based on the latest reports of the mm-scale and μm-scale OLEDs from various laboratories [46-50, 53, 162-168, 432-436], Figure 2-8 summarizes their EQEs and overall luminous efficacies (or luminous efficacy of a source) of OLEDs versus their lateral device sizes, which are key parameters for display technique. The detailed information of OLEDs is listed in **Appendix I** at the end of this dissertation. Shown in Figure 2-8 (a), EQE of OLED decreases with the lateral device size, which limits the further reduction in the OLED pixel size for its application in high resolution displays and other μm-scale or nm-scale applications [46-50, 53, 162-168, 432-436]. Using organic materials, it is difficult to achieve efficient devices below tens μm and nm-scale devices [214, 440]. The limited performance of μm-scale OLEDs is due to complexity and high cost in high-resolution mask patterning for OLED technology [441], and cross-contamination between organic layers during high pixel density patterning [167, 442-444]. Those difficulties explain the slow advancement of AMOLED-based display technique in recent years shown in Figure 1-3, which represents one of the main bottlenecks for whole display industry. Moreover, large divergence of light emission is the inherent characteristics of OLEDs (a mm-scale illumination area from a μm-scale OLED), also hindering the further development of OLED technology for ultra-high-resolution displays [53]. In contrast, InGaN-based microLED displays do not have most of the issues which OLED technology encounters [439, 445]. With much higher brightness and luminous efficacy as well as lower cost and much larger screen dimensions, the scalable InGaN-based microLED displays improves dramatically in its resolution in recent years [427, 431, 439, 445-449].

Besides high-resolution displays and visible light communications with high modulation bandwidths [202], μm-scale or nm-scale InGaN-based LED chips can also be used as light sources for biological and medical applications. For example, μm-scale full-color InGaN-based LED chips are very suitable for optogenetics which integrate devices such as semiconductor optoelectronic devices into biological systems for gene therapy or alter animals' behaviors [18, 19]. CCT-tunable white illumination sources are essential to identify, count, and sort biological cells [25]. To *in-situ* and real-time render the tiny tissues during some surgery, it is higly desriable to develop a cellular-scale color-tunable InGaN-based LED chips which can be inserted into a limited space or precise location in human body for clinical process [19]. In addition, optimized illumination conditions can facilitate plant growth [25]. Moreover, it has been discovered that body chemistry and circadian performance will be affected by illumination conditions (light intensity, wavelength and duration) [2, 25, 26]. Full-color InGaN-based LED chips promise a color-tunable, natural, healthy, efficient and smart LED illumination systems which are essential for a productive and comfortable daily life [2, 25, 26]. The combination of color-tunable InGaN-based LED chips with biological techniques can facilitate the development of clinical technologies and fundamental biological research [2, 18, 19, 25, 26].

Conventional GaN-based white LED illumination generally uses phosphor-based materials to generate long-wavelength spectral components by down-convert light from GaN or violet/blue- InGaN-based emitters. Similar to that, in the conventional LED displays using subpixel rendering, phosphors-based color converting media are used to make subpixels which generate green red, and/or yellow monochrome light by using down conversion mechanism, or color filters are used to separate white light from conventional GaN-based white emitters ((In)GaN and phorsphor-based materials) into RGB monochrome lights [174, 175, 446, 450-454]. However, these conventional approaches are severely limited in the flexibility to tune the

spectral power distribution of mixed light to achieve accurate color display for good image quality or achieving accurate CCT for appropriate and natural illumiantions [176, 454]. The usage of phosphors for down conversion approach also leads to the disadvantages of short lifetime and Stokes fluorescence loss [446, 450, 455], and the approach using color filters also suffers from short lifetime and the loss of filtered white light [446, 450].

Besides conventional approaches to make color-tunable chips and phosphor-based white LEDs, an alternative approach is to monolithically integrate self-emissive red, green and blue (RGB) InGaN LEDs sources directly on a single chip, instead of using the down-conversion process to produce long-wavelength spectral components [431, 456]. Compared to other conventional approaches for LED displays, the use of self-emissive RGB GaN-based LED sources leads to a few advantages for displays such as high compactness, excellent image quality and low power consumption [430, 431, 456, 457].

The currently reported InGaN RGB devices generally rely on the use of vertically stacked MQWs LEDs. For example, Li et al. reported dual-In content InGaN/GaN MQWs LEDs [458]. The carrier redistribution in the low- and high-In content QWs, depending on the injection current, leads to color-tunable characteristics with a maximum CRI of 85.6 for a CCT of 4895 K. Wang et al. demonstrated that the CCT can be tuned from 7332 K (cool white) to 2362 K (warm white) for a stacked LED tower in which an InGaN blue LED (470 nm), an InGaN green LED (510 nm) and an AlInGaP red LED (640 nm), were bonded together [459]. The performance and efficiency of such vertically stacked LEDs, however, has been severely limited by the light absorption of adjacent narrow bandgap QWs and poor heat conduction. The luminous efficacy of such vertically stacked RGB device was lower than the planar RGB LED assembled using identical chips [459]. Moreover, the device performance, including the luminance and tunability of CCT, is ultimately restricted by the extremely low efficiency of conventional QW LEDs in the deep green and yellow wavelength range [134].

An alternative and more appealing approach to make RGB color-tunable chips is to laterally arrange RGB LEDs consisting of nanowire structures. These monochromatic μm-LED or nm-LED arrays, with their sizes in the μm-scale or nm-scale, can readily generate multi-color emissions for lighting and full-color displays. To date, with the use of dislocation-free InGaN nanowire structures, high efficiency emissions across the entire visible spectral range have been demonstrated [126, 460-466]. It has been reported that phosphor-free nanowire white LEDs can exhibit extremely high CRI (> 94) for both neutral and warm white light emissions [467], but this approach is limited in the tunability of CCT. To achieve real-time color tunability, the light output of red, green and blue components should be varied separately and controllably. However, such monolithic integrations of RGB GaN/InGaN nanowire LEDs devices into single pixel in the μm-scale and nm-scale involve the challenges in epitaxial growth and device fabrication, the solutions to which will be discussed and provided in this dissertation.

2.4.2 The Challenges in Spontaneously Grown Nanowires and the Advantages of Selective Area Epitaxy

Conventional VLS epitaxy of GaN-based nanowires generally rely on the use of foreign metal catalysts which degrade the optical and electrical properties of nanowire heterostructures. Catalyst-free self-organized GaN-based nanowires avoid the usage of foreign metal catalysts in the growth process. However, the self-organized nanowires exhibit considerable variations in nanowire diameter and position, which is illustrated in the schematics of the self-organized evolution of GaN nanowire array shown in Figure 2-9 [366]. Figure 2-9 is sketched based on a combination of the nucleation model proposed by V. Consonni et al. [381] and the kinetic growth model proposed by S. Fernández-Garrido et al. [366].

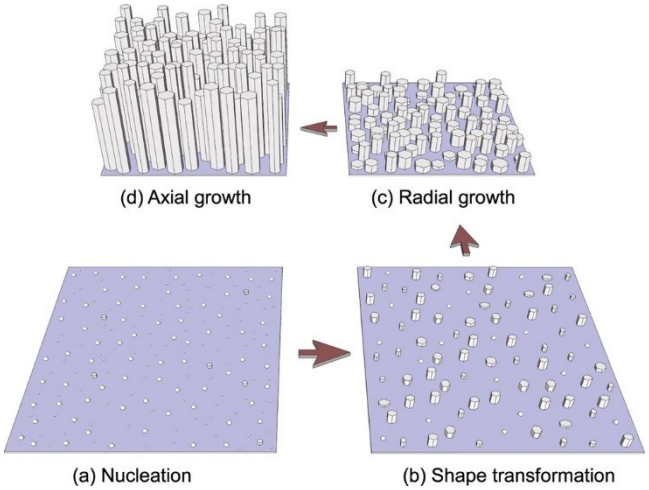

Figure 2-9: Schematic illustrations of the self-organized evolution of GaN nanowire array from the spontaneous nucleation to a dense nanowire array exhibiting non-uniform nanowire diameter, nanowire length and nanowire position. Reprinted from the journal publication authored by S. Fernández-Garrido et al. in *Nano Letters* [366]. Copyright (2013) American Chemical Society.

The considerable variations in spontaneously grown nanowire morphology and geometry originate from the fluctuations in diameters and positions of nucleation sites, as illustrated in the nucleation stage shown in Figure 2-9 (a). The fluctuations are further developed in the shape transformation stage and radial growth stage. Diameter fluctuations and nanowire spacing variation affects the axial growth rate, resulting in non-uniform nanowire length. The considerable variations in nanowire length, diameter and position can be clearly observed in cross-sectional SEM image of self-organized GaN nanowires shown in Figure 2-2.

The variations in nanowire length, diameter and position degrade the performance of nanowire devices. In the nanowire device fabrications, a polyimide resist layer (in this dissertation) or other transparent materials like spin-on-glass (SOG) [468] is generally spin-coated onto the nanowire arrays for planarization, followed by dry etching (O_2 plasma in this dissertation) calibrated to expose the *p*-GaN or *n*-GaN segments at the top of nanowires. The metal layer was subsequently deposited at the exposed nanowire segments to create the conductive path for carrier injections and carrier collections. However, due to the variations in

nanowire length, diameter and position, some *p*/*n*-GaN segments are unexposed in polyimide, and some other nanowires are overexposed, except a few properly exposed *p*/*n*-GaN segments, as shown in Figure 2-10. The nanowires with unexposed *p*/*n*-GaN segments largely increase the overall series resistance and create dark spots in III-nitride nanowire emitters. The overexposed nanowires with active regions exposed make the nanowire device leaky or even result in the failure of nanowire devices. Only the nanowires with properly exposed *p*/*n*-GaN segments can form the ohmic contacts and hence contribute to desirable carrier conductions, light emissions or photovoltaics.

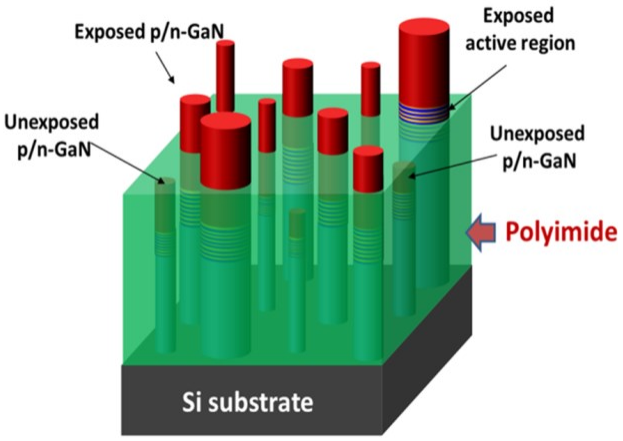

Figure 2-10: Schematic illustrations of polyimide etching in the device fabrication process of spontaneously grown GaN-based nanowire array which exhibits non-uniform nanowire diameter, nanowire length and nanowire position.

To the best of author's knowledge, the diameters of spontaneously grown GaN-based nanowire are generally below ~ 200 nm [366], which might be due to the small size of nanowire nucleation sites (generally ~ 5 nm or smaller) [366], small spacings between neighboring nucleation sites, and small radial growth rate due to N-rich growth conditions [366] in the self-organized process [355, 366, 376, 380-382]. In the axial growth stage, the radial growth rate is more than one order of magnitude lower than the axial growth rate [469-471]. In some cases of self-organized nanowires, the radial growth ceases when the length of nanowires reach a certain value [366]. Besides the difficulty in growing large-diameter InGaN nanowires, it is not

viable to tailor InGaN nanowire diameters and nanowire spacings over the same substrate through the self-organized approach [355, 366, 376, 380-382].

Another challenge of the self-organized approach is the difficulty in growing long nanowires (more than 1 μm) to incorporate multijunction (Al)InGaN active segments which involves the growths of In-rich active regions at relatively low growth temperatures [269]. This difficulty is mainly due to the limited spacings between neighboring nanowires which might result in the coalescence between neighboring nanowires. The coalescence between neighboring nanowires is very detrimental for the optical and electrical performance of nanowire devices.

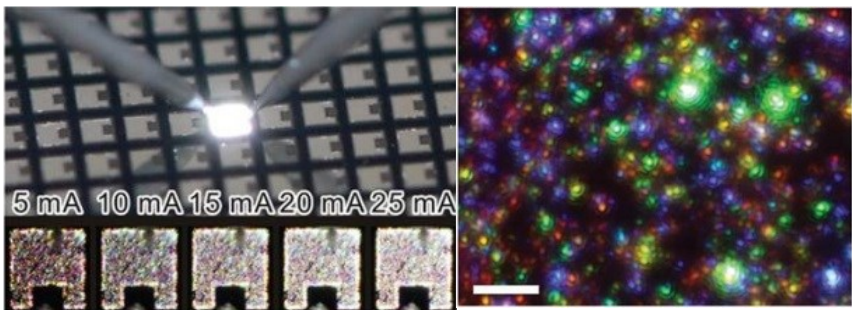

(a) (b)

Figure 2-11: (a) Photograph of spontaneously grown nanowire LED emitting white light at 20 mA injection current. Micro-EL images shown below are acquired under a 10× objective lens at various injection currents. (b) Micro-EL image (20 mA) under a 100× objective lens revealing full-visible-spectrum. Scale bar: 10 μm. Reprinted from the journal publication authored by H.-W. Lin et al. in *Applied Physics Letters* [463], with the permission of AIP Publishing.

Spontaneously grown green InGaN nanowire array generally exhibit spectral linewidths (FWHM) in the range of ~58-87 nm or broader [254, 463, 472, 473]. Broad emissions of self-organized InGaN nanowire array are attributed to large spatial inhomogeneous distribution of In content in each nanowire, inherent phase separation and compositional variations from nanowire to nanowire due to fluctuations in nanowire diameter and position in the self-organized process [463]. It has been realized recently that the In incorporation to nanowires is

closely related to the nanowire diameter and nanowire spacing, which determines emission wavelength of InGaN nanowires [105, 256]. One representative example of broad emissions from spontaneously grown InGaN-based nanowire devices is the white EL emissions shown in Figure 2-11 (a) [463]. Shown in Figure 2-11 (b), the magnified image of the white self-organized InGaN nanowire LEDs shows localized, full-color emissions varying from purple to red within an area of a few μm, indicating the large variations in InGaN composition due to the fluctuations in nanowire diameter and nanowire position [463].

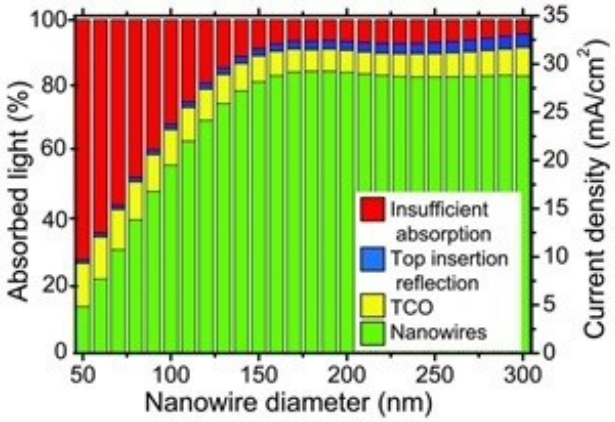

Figure 2-12: Simulated absorbed light as a fraction of the solar spectrum above the InP band gap and calculated J_{sc} of InP solar cell versus nanowire diameter. Different optical losses due to a transparent conducting oxide (TCO) and top insertion reflection are also shown. The originality and copyright of this figure and this figure caption is from the journal publication authored by J. Wallentin et al. in *Science* [474]. Reprinted with permission from American Association for the Advancement of Science (AAAS).

The efficiencies of nanowire-based solar cells and optically-pumped emitters is often limited by light absorption, especially when the nanowires have subwavelength dimensions [474]. By optimizing the diameter and periodicity of nanowire array, light absorption can be dramatically enhanced as well as light reflection can be reduced due to resonant light trapping [474]. As shown in Figure 2-12, keeping constant array periodicity of 470 nm, J. Wallentin et al. reported that the variations in nanowire diameter significantly affect the light absorption and result in the variations in short-circuit current density (J_{sc}) and efficiency of InP solar cells

[474]. This photonic effect is caused by the nanoscale optical index changes [475, 476]. Taking advantages of the superior anti-reflection properties of nanowire array with uniform size and periodicity, the usage of film anti-reflection coating can be avoided in nanowire solar cells. The reduced light loss has been reported for InAs [477], GaP [478, 479], Ge [480], InP [475, 476], Si [481, 482], and GaAs [483, 484] nanowire solar cell. For a double-junction GaAs-on-Si nanowire solar cell, Hu et al. reported that I_{sc} depends on the dimension and periodicity of nanowire and the highest I_{sc} was measured from an array with diameter of ~ 180 nm and periodic spacing of ~ 350 nm [485]. For a GaN nanowire array on Si substrate, A. M. Mozharov et al. found that a diameter of 240 nm and periodicity of 540 nm exhibit the lowest reflectance and the integral reflectance value is only 3% [486].

By using the SAE, the size and periodicity of nanowires can be precisely controlled, enabling photonic crystal effect. Photonic crystal effect of uniform nanowire array has also been used to generate stimulated emission. Recently, stimulated emission from the periodic nanowire arrays arranged in a rectangular lattice has been observed [487], where lasing modes are the photonic band edge modes. The light intensity is enhanced at the photonic crystal band edge modes. By using slow light modes, wherein the in-plane wave vector is zero, photonic crystal structure can be designed to emit light vertically and out-of-plane [488-490]. For example, Wright et al. obtained the light emission from the top surface at Γ point which showed the small in-plane wave vector and large out-of-plane wave vector [491]. Stimulated emissions have been realized in the green and blue wavelength by optically pumping InGaN/GaN nanowire array which is uniform in nanowire size and array geometry [289, 487].

In a summary, by using self-organized approach, the grown GaN nanowires are randomly distributed on the substrate, with significant variations in size, spacing, length and surface morphology. For practical nanowire device applications such as LEDs, lasers and solar cells, it is essential to precisely control the formation and properties of InGaN nanowire arrays.

Arrays of nanostructures grown using SAE provide a much better homogeneity in terms of morphology, electrical and optical properties.

Combined with MBE, SAE technique can exhibit perfect controllability on GaN-based nanowire size and morphology which have been shown in Figure 2-5 (c) and Figure 2-6. The bird's-eye-view SEM image of uniform selective-area grown *p-i-n* GaN-based nanowire array with InGaN active regions is shown in in Figures 2-13. GaN-based nanowire devices promise much better current-voltage characteristics than that of self-organized nanowire devices, benefiting from the uniform planarization and proper exposure of *p/n*-GaN at the top of nanowires.

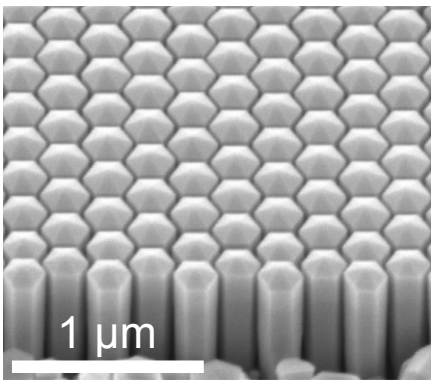

Figure 2-13: Bird's-eye-view SEM image of *p-i-n* InGaN/GaN dot-in-a-wire nanowire heterostructures array which exhibit high degree of uniformity.

It has been reported that nanowire morphology is closely related to SAE growth conditions and its impact on PL was studied [492]. GaN-based SAE nanowire LEDs exhibiting emissions from blue to near-infrared have been demonstrated [493-496]. With precisely controlled nanowire size and position, SAE green InGaN/GaN QWs nanowire arrays exhibit much narrow spectral linewidth, compared to that of spontaneously grown green InGaN/GaN QWs nanowire arrays. For example, SAE green InGaN/GaN QWs nanowire arrays with a ~ 50 nm-thick active segment grown on GaN/sapphire exhibit a linewidths of 27 nm (135 meV) [497] with the peak wavelength of 506 nm and linewidths of 31.5-37.5 nm [495] with the peak wavelength in the range of 529.1-543.3 nm.

By precisely varying nanowire diameters and array periodicity, Kishino et al. reported green, yellow and orange InGaN nanowire array LEDs integrated on the same wafer through a single SAE by using MBE [105, 256]. It was observed that the emission of InGaN/GaN nanowires exhibit a redshift with increasing diameter, which is attributed to the beam shadowing effect of the neighboring nanowires and the resulting less Ga incorporation in the InGaN segment for nanowires with larger diameters. SAE enables the flexibility of tuning the InGaN composition of nanowire array by controlling the nanowire diameters besides the III/V ratio and substrate temperature.

To develop efficient InGaN-based nanowire devices with good current-voltage characteristics, high optical absorption and/or extraction, and desirable emission wavelength, the flexibility of controlling nanowire dimension and position is essential. SAE of GaN-based nanowires can address the aforementioned challenges the approach of spontaneous growth encounters.

2.4.3 Selective Area Epitaxy on Si Substrate Without the Loss of High Electrical and Thermal Conductivity

To make low cost and efficient optoelectronic devices and electronics, it is highly desired to monolithically grow and fabricate high efficiency III-V materials and III-V devices directly on low cost and large area Si substrate, instead of prohibitively expensive substrates, such as GaAs, InP, Ge, CdZnTe and/or GaSb [248, 249, 283, 498-502]. The well-established Si microelectronics industry has perfected the techniques and facilities to produce high quality Si substrates, and Si-based microelectronic and optoelectronic devices has been playing dominant roles in the most fields of current market and industry. While other substrates such as GaN/sapphire has a few considerable disadvantages, Si substrates exhibit comprehensive advantages, including low cost, high electrical conductivity, high crystal quality, and good thermal properties [503].

In the synthesis and fabrication of a vertical-type device, thousands of vertical components such as vertically aligned nanowire, can be processed at the same time, enabling efficient and low-cost production and test process as well as high yield [504-506]. Vertical-type devices such as VCSELs, is very suitable for large area and high-power operation, benefiting from the advantage that they can be arranged in a dense configuration over a single chip for maximum device density [504-506]. The dense configurations of vertical-type devices generally require high heat dissipation. In this regard, it is very desirable to use largely available and low-cost Si substrates for the epitaxy and fabrication of vertical-type devices [507]. Particularly important for the development of efficient photovoltaics and artificial photosynthesis, the epitaxy of InGaN on Si substrate enables the direct integration of the well-commercialized Si solar cell with III-nitride devices exhibiting tunable absorption spectrum, promising double-junction and multijunction InGaN/Si-integrated solar cells [508].

Devices integrated on non-conductive substrates, such as the vertical GaN nanowire wrap-around-gated field-effect transistors discussed in section 1.4.2 [344], requires the use of a horizontally-arranged conductive contact at the side of devices, even though the vertically aligned nanowire array provide the vertical source-drain path. In contrast to devices on non-conductive substrates, vertical-type devices on conductive substrates has the vertical conductive path between top electrode and bottom electrode for efficient carrier collection or carrier injection [509]. The bottom ohmic contact for vertical-type devices can be fabricated at the backside of Si substrates, instead of a complex and indispensable fabrication process to form a parallel contact on non-conductive substrates. For example, devices on nonconductive substrates, the fabrication of a parallel contact may include selectively etching materials down to a bottom *n*-GaN or *n*-AlGaN layers and selectively deposition of metal contact layers over a relative small area at the corner or at the lateral sides of active regions [510-513].

However, due to the large bandgap of AlN and GaN, the Si substrate grown with thick AlN/GaN buffer templates or thick AlN buffer layers cannot be integrated as a part of the vertcailly conductive path, limiting the usages of Si substrate in the vertically-conductive devices of III-nitride materials [344]. Employing *n*-Si substrate as the *n*-contact, A.-L. Bavencove et al. integrated a AlN buffer layer into carrier flowing path of vertically-aligned InGaN/GaN core/shell wire LED and concluded that the AlN buffer layer introduced an considerable parasitic Schottky barrier [514]. The thickness of AlN buffer layer for the epitaxy of GaN or InGaN epilayers on Si substrate is generally 200-300 nm or more [515, 516].

As discussed in section 2.4.2, SAE nanowires have many advantages due to precisely controlled nanowire size and position. The SAE of precisely-controlled nanowires on Si substrate has also been explored [398, 403, 404, 517-521], driven by the advantages of Si substrate over other type substrates. Due to the extremely high size uniformity, large area SAE nanowire devices on Si substrates promise superior performance, which can be developed for the demanding applications of LEDs, lasers, photovoltaics devices and FETs discussed in Chapter 1.

However, there have been no reports on SAE nanowire devices using Si substrates as the contact, due to the issues in either controlling the nanowire size [521], or usage of thick semiconducting buffer layers such as GaN and AlN buffer layers on Si substrates [404, 517-519, 522]. Using MBE, highly uniform arrays of GaN nanowires can be selective-area grown on Ti-mask Si(111) substrates using a 1.6 μm-thick GaN buffer layer which was grown on an AlN/GaN superlattice buffer template (a 13-pairs 0.7 nm AlN/1.6 nm GaN short-period superlattice and a 20-pairs 5 nm AlN/ 20 nm GaN superlattice) on Si substrates [401]. Using a thick GaN buffer layer (~ 120-720 nm thick) grown on a thin SiN_x layer, Ti-mask SAE of In(Ga)N/GaN nanowires was achieved on GaN-buffered Si(111) substrates by using MBE [465]. Taking advantages of SiN_x [404] or SiO_2 [403] masks, the precisely-controlled SAE

nanowires has also been achieved on Si substrates covered by AlN thick buffer layers. For the polarity-controlled III-nitride nanowire epitaxy using SiN_x mask, K. A. Bertness et al. used a relatively thinner MBE-grown AlN buffer layer which was ~ 40 nm thick [404].

Without the use of any buffer layers, using Ti-mask or SiO_x-mask SAE directly on Si, it is difficult to control the nanowire size owing to the spontaneous nucleation of thin GaN nanowires within mask openings, regardless of the opening size [98, 523]. By using Ti-mask nanopatterns with different stripe widths, it was observed that MBE-grown nanowires nanowires spontaneously nucleated and grown on exposed Si surface [523]. In each opening, there are several nanowires with smaller diameter than the opening width [523]. Figure 2-14 shows low and high-magnification SEM images of GaN nanowire array grown by using SiO_2-mask selective area epitaxy on Si substrates [98].

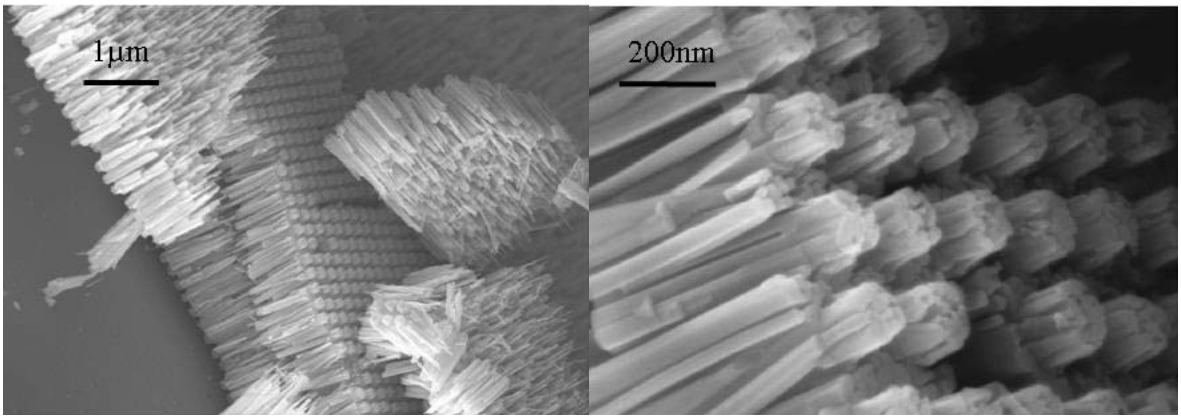

(a) (b)

Figure 2-14: (a) and (b) SEM images of a GaN nanowire array grown by using SiO_2-mask selective area epitaxy on Si substrates with different magnifications. Reprinted from the journal publication authored by E. Calleja et al. in *Physica Status Solidi (B) Basic Solid State Physics* [98], with the permission of John Wiley and Sons.

In a summary, it is highly desirable to develop precisely-controlled GaN-based nanowires on Si substrate by using SAE, however, the current SAE techniques on Si substrate rely on the use of thick semiconducting buffer layers with large bandgap. In this regard, the electrical and

thermal advantages of Si substrate cannot be used for SAE nanowire devices. Without using thick buffer layers, the grown nanowires on Si substrates cannot maintain the quality of SAE.

2.4.4 Nonradiative Recombination on the Nanowire Surfaces

Recent studies have shown that the surface charge properties play a dominant role on the performance of nanowire devices such as nanowire LEDs and nanowire solar cells, due to the large surface-to-volume ratio. For the InGaN/GaN QW nanowire in diameter of ~ 100 nm, the surface recombination velocity was estimated to be ~5×10^4 cm/s [95, 524, 525]. The surface nonradiative recombination are mainly due to various surface states including unoccupied dangling bonds, impurity incorporated along the lateral surfaces, and surface defects induced by the strained active regions [526-528]. The commonly reported axial nanowire LEDs generally exhibit very low output power, due to large surface recombination and the resulting poor carrier injection efficiency [132]. Besides InGaN nanowire LEDs, it has been reported that micro-scale InGaN epilayer LEDs also suffer from non-radiative recombination at sidewalls induced by dry etching process to make micro-scale InGaN epilayers [529], limits the usage of GaN/InGaN QWs heterorstructures for small-size optoelectrical devices including high resolution-displays and color-tunable illuminations in a limited space [530, 531].

Among the various of reports on single-junction InGaN nanowire solar cell, ensembled axial *p-i-n* InGaN nanowire array exhibit the highest efficiency of 0.5%, benefiting from its relatively high J_{sc} of 4.6 mA/cm^2 [304]. However, a relatively low V_{oc}, a poor FF and hence relatively low efficiency were measured [304], due to large surface recombination. Benefiting from the achievement of *p*-type conduction in InN grown by using MBE, the first InN:Mg/*i*-InN/InN:Si nanowire solar cells grown on Si(111) substrate was achieved by Nguyen et al [306]. Under one-sun AM 1.5G illumination, a relatively high J_{sc} of 14.4 mA/cm^2 was measured. However, the output characteristics of such InN nanowire solar cells were limited by surface recombination [306], which is the one bottleneck of nanowire solar cells.

Radial variations of In/Ga distribution have been observed in InGaN/GaN dot/disk/well-in-a-wire heterostructures [119-123]. However, such radial variations were found to be insufficient to suppress nonradiative surface recombination under electrical injection. To tune the effect of surfaces on the optical properties of GaAs nanowire, AlGaAs shell was used for passivating the GaAs nanowire, resulting in a suppressed surface recombination velocity [532]. The use of a large bandgap AlGaN shell covering the surfaces of axial InGaN nanowire LED heterostructures has also been explored, which has shown tremendous promise in reducing surface recombination and in improving the carrier injection efficiency and output power [121, 254, 532]. This can be achieved by epitaxially growing AlGaN shell structures incorporated surrounding InGaN dots. During the growth of the AlGaN:Mg layer, an AlGaN shell spontaneously formed surrounding the nanowire sidewalls, due to the smaller diffusion length of Al adatoms [254, 525]. Detailed studies have further confirmed that the AlGaN shell thickness can be controlled by varying the growth conditions. Al, Ga, and In signals vary along the nanowire lateral dimension, suggesting the formation of an AlGaN shell with a thickness ~10 nm [525]. The Al-rich shell is continuous from each of the AlGaN barriers and propagates well into the *n*-GaN segment [525]. The output power is more than two orders of magnitude larger than that without AlGaN shell structure, due to the suppressed nonradiative surface recombination [132, 525, 533]. In these approaches, however, relatively thick AlGaN layers were incorporated in the device active region in order to form an AlGaN shell for surface passivation. This leads to increased complexity in the device design, growth and fabrication process. Moreover, a fundamental understanding of the impact of the AlGaN shell structure on the carrier dynamics and device performance has remained elusive.

2.5 Characterization Methods of GaN-based Nanowire Heterostructures and Nanowire Devices in this Dissertation

In this dissertation, various characterization methods are used for GaN-based nanowire heterostructures and nanowire devices.

The common characterizations involved in this dissertation include structural characterizations, photoluminescence (PL) characterizations, and electroluminescence (EL) characterizations, which is described as follows.

Structural Characterizations: The bird's-eye-view SEM images were taken with a 45-degree angle using a FEI Inspect F-50 FE-SEM to reveal the lateral morphology and top morphology of nanowire heterostructures. The structural characterizations of nanowire heterostructures were also performed with high-resolution transmission electron microscopy (TEM) and scanning transmission electron microscopy (STEM) by using a S/TEM system (Tecnai F20, FEI) equipped with a 4k×4k CCD camera (Oneview, Gatan). Nanowire heterostructures were dispersed onto copper grid for the S/TEM sample preparation. The high-angle annular dark-field (HAADF) atomic-number contrast images of nanowire heterostrucutres shows bright/dark contrast to reveal the elemental distributions. Based on the HAADF image of nanowire heterostructures, the energy dispersive x-ray spectrometry (EDXS) analysis were conducted to further reveal the elemental profiles in detail.

PL characterizations: PL measurements were performed by using a 405 nm laser or a 325 nm laser as the excitation sources. A high-resolution spectrometer was used to collect and resolve the emitted light from nanowire arrays, and photomultiplier tubes (PMTs) or a liquid N_2 cooled charge coupled device (CCD) was used for the light detection in the visible range. For power-dependent PL measurements by using a 405 nm laser, a visible neutral density filter was used to adjust the power of incident laser beam in the range of 0.03-65.43 mW, which

excited the nanowires. For low-temperature PL measurements, nanowire samples were measured at the temperature of 78.0 K by using a liquid N_2 closed-loop cryostat.

EL Characterizations: The EL characterizations of nanowire LEDs were performed by using a source meter (Keithley, SMU 2400). The *p*-metal pad at the top surface of a sample and *n*-metal contact of samples were probed for current injection to devices. The current-voltage characteristics of nanowire LEDs were measured by using the Keithley Sweep and Acquire Measurements. The EL from samples was collected by optical fiber dedicated for detecting visible wavelength emission at room temperature. The EL was further resolved by a JAZ spectrometer (Ocean Optics) for UV-Vis measurements or a high sensitivity PMT in the visible range.

A few characterization methods are used specially for specific studies. For example, time-resolved photoluminescence (TRPL) is used for characterizing the carrier dynamics of III-nitride nanowires; and AM 1.5G solar simulator is used for characterizing current-voltage characteristics of solar cells. These characterization methods are described as follows.

Time-resolved Photoluminescence (TRPL): TRPL measurements were performed to study the carrier dynamics of nanowire heterostructures. A Horiba DynaMyc system equipped with a time-correlated single photon counting (TCSPC) system was used in this measurement. The FluoroHub (HORIBA Scientific, Jobin-Yvon) is a time-related single photon module with the resolution of 7 picosecond/channel as standard and the measurement time range can be varied from 100 picoseconds to 10 microseconds. A fiber-coupled pulsed 375 nm diode laser (PicoBrite, HORIBA Scientific, PB-375L) with a 100 MHz repetition rate was employed as the excitation source, which was focused on the sample through the Olympus BX51 microscope (objective 50× or 10×). A pass filter (> 500 nm or > 400 nm) was used before the signal was detected by the photon counter (TBX picosecond detection module with the transit

spread time of 200 picoseconds). The carrier lifetime (τ) was then derived by a standard stretched exponential model [534].

Characterizations of Solar Cells: The *p*-metal pad at the top surface of a sample and *n*-metal at the backside of Si substrate were probed, and electrical outputs are collected through probe stations. The current-voltage characteristics of solar cells were measured in the dark environment and under the illumination of 100 mW/cm^2 from an AM 1.5G solar simulator (Newport, Oriel, LCS-100). The current-voltage characterizations under concentrated light were further carried out under the illumination from a Xenon arc lamp (Excelitas Technologies, Cermax, R400-1) with an AM 1.5G filter. The filter tailors the spectral output of the Xenon arc lamp to match the spectrum of AM 1.5G.

2.6 Preview of Experiments and Summary of the Contribution of this Dissertation

This dissertation focuses on the development of GaN-based nanowire heterostructures on Si substrates and GaN/sapphire substrates as well as their various device applications, to address the aforementioned four challenges in section 2.4. The experimental progress achieved in this dissertation largely resolve the challenges and contribute to the development of GaN-based LEDs, photovoltaic devices, FETs and lasers for the demanding applications in the fields of displays, illuminations, energy harvesting, visible optical communications and transistors. A large part of the research has been focused on the development of μm-scale and nm-scale color-tunable chips by monolithically integrating full-color GaN-based nanowire LEDs over the same chip. In addition, this dissertation reports on the achievement of AlInGaN quaternary nanowire LEDs and solar cells on Si substrates exhibiting suppressed nonradiative surface recombination. Without compromise with the loss of electrical and thermal advantages of Si substrates, this dissertation reports on the achievements of GaN-based nanowires exhibiting precisely-controlled size and positions through selective area epitaxy on Si substrates. High electrical conductivity is further demonstrated on the SAE GaN nanowires vertically integrated

on the Si substrates, promising the efficient vertical GaN-based nanowire electronic devices on Si platform. The following is the preview of experiments in each chapter.

In Chapter 3, controllable and tunable full-color light generations are demonstrated through the monolithic integration of blue, green/yellow, and orange/red InGaN nanowire LEDs. Such multi-color nanowire LED arrays are fabricated directly on Si substrate using a three-step selective-area MBE growth process. The laterally arranged multi-color subpixels enable controlled light mixing at the chip-level and yield color-tunable light emission with CCT values in the range from 1900 K to 6800 K, while maintaining excellent color rendering capability. This work provides a viable approach for achieving micro- and nano-scale tunable full-color LED arrays without the compromise between the device efficiency and light quality associated with conventional phosphor-based LEDs. The overall RGB pixel size of ~0.016 mm^2 was achieved with a monochromatic subpixel size of 50×50 μm^2 by using this approach.

In Chapter 4, taking advantages of SAE of InGaN-based nanowires on GaN/sapphire substrates, the overall RGB pixel size is further reduced to 7×7 μm^2 with monochromatic subpixel sizes of 2.8×2.8 μm^2. The emission characteristics of such nanowire LED array can be controllably varied by changing the diameters of nanowires in a single epitaxy step, leading to high efficiency, tunable and full-color RGB pixels. By incorporating InGaN QDs in single GaN nanowires, diameter-dependent emissions tuning from blue to red was achieved from the single GaN-based nanowires on the same substrate and its mechanism has been investigated. Based on this achievement, we have developed, for the first time, with the world's smallest pixel size, high performance full-color InGaN/GaN single nanowire LED pixel optimized for ultra-fine projection displays using only one step epitaxial growth process. Compared to conventional GaN-based planar LEDs and organic LEDs, these single nanowire LEDs exhibit much better performance, including high light extraction efficiency, precisely tunable-color

emission, higher integration density, excellent electrical properties and much less power consumption.

In Chapter 5, the impact of the AlGaN shell structure on the carrier dynamics is discussed, and the experiments provide unambiguous evidence on the importance of incorporating a robust, large bandgap shell structure in dramatically enhancing the performance of nanowire LEDs for the lighting and display applications. AlInGaN quaternary core-shell nanowire heterostructures are demonstrated on Si substrate, wherein an In-rich core and an Al-rich shell were spontaneously formed during the epitaxial growth process. By varying the growth conditions, the emission wavelengths can be tuned from ~ 430 nm to ~ 630 nm. Such core-shell structures can largely suppress nonradiative surface recombination, leading to a significant enhancement of carrier lifetime from ~ 0.2 ns to ~ 2 ns and output power.

In Chapter 6, uniform GaN-based nanowire arrays are demonstrated on Si substrate by using Ti-mask SAE without the loss of the electrical and thermal advantages of Si substrate. Taking advantages of ultra-thin AlN and GaN:Ge buffer layers buffer template, the grown nanowires exhibited precisely controlled nanowire size and position on Si substrate, maintaining the quality of SAE as well as the high electrical conductivity and high thermal dissipations of Si substrates. The properties of *n*-GaN nanowire array selective-area grown on Si substrates were further investigated in photoelectrochemical reactions for hydrogen production. The PEC results further justified the high conductivity of the ultra-thin AlN/GaN:Ge buffer template. The high electrical conductivity of ultra-thin AlN layer has also been justified through photovoltaic characterizations of the Si solar cells deposited with a ultra-thin AlN layer. Electrical transport properties and breakage behavior of vertically aligned GaN single nanowires on Si substrate are systematically studied by using *in-situ* nanoprobing inside a SEM chamber. The contact resistance can be dramatically reduced by increasing the Si doping concentration in n^+-GaN layer of *n*-*i*-*n*-n^+:GaN single nanowires. The dependence of

the GaN nanowire current-voltage characteristics on Si doping concentration of n^+-GaN layer and nanowire diameter are investigated. A current density up to 4.65 MA/cm^2 and maximum electric field up to 17.02 MV/m have been achieved on a single GaN nanowire vertically-aligned on Si substrate, promising the scale-up of vertical GaN-based nanowire electronic devices on Si substrates.

In Chapter 7, uniform and selective-area grown AlInGaN quaternary nanowire heterostructures, exhibiting suppressed nonradiative surface recombination, were demonstrated on Si substrates. SAE *p-i-n* AlInGaN nanowire devices can exhibit the light-emitting properties and photovoltaic effect over the same chips. PL and EL in green spectral range were measured when the AlInGaN nanowire devices were forward biased. Under the AM 1.5 illuminations, SAE AlInGaN nanowire devices exhibited higher photovoltaics efficiency than those ever reported for *p-i-n* InGaN-based nanowire solar cell. Stable and good output characteristics of AlInGaN nanowire devices are measured under the illuminations of concentrated light, showing that selective-area grown AlInGaN nanowire devices on Si substrate are very promising for high-power operations requiring excellent heat dissipations.

In Chapter 8, the summary of this dissertation is presented and future works are proposed.

Chapter 3: Micro-scale RGB pixels: Color-Tunable, Phosphor-Free InGaN Nanowire Light-Emitting Diodes Monolithically Integrated on Silicon

3.1 The Status and Challenges of GaN-based RGB Micro-Scale LEDs

As an alternative approach to conventional phosphor based LED which is not "smart" and not efficient in light mixing to tune the correlated color temperature (CCT) of LED lighting systems, a full-color LED array consists of red, green and blue (RGB) InGaN-based LEDs monolithically integrated within an extremely small size (a microscale area) can be directly used for current demanding applications including flat-panel displays (FPDs), mobile projections [427], wearable displays [428, 429], visible light communications [202], biological and medical applications [2, 18, 19, 25, 26]. RGB or RGBY monochromatic subpixels on the same chip can be separately biased and exhibit emissions which can be mixed and tuned controllably over a wide CCT range. These monochromatic micro-LED arrays, with their sizes in the micron or even sub-micron scale, can generate multi-color emissions to achieve desirable color rendering index (CRI) as well as broad and flexible color tunability, as an efficient approach of subpixel rendering technique.

Recently, researchers have studied the size-reduction effects on the performances and characteristics of μm-scale GaN/InGaN QWs LEDs [133, 529, 530, 535, 536], driven by the strong desires to develop efficient μm-scale color-tunable LEDs. Those InGaN-based LEDs were made by using GaN/InGaN planar heterostructures. As shown in Figure 2-8, the smaller OLED exhibits the lower efficiency. In contrast to that, Z. Gong et al. [133] and P. Tian et al. [529] observed that the EQE of μm-scale violet- and blue-emitting InGaN QWs LEDs exhibited higher efficiency at smaller device size. This observation is consistent with various experimental and theoretical studies [133, 530, 537-539]. Such size-dependent efficiencies are attributed to lower junction temperature [133, 530], better heat distribution [530, 537], more uniform current density distribution [133, 530, 538, 539] and improved light extraction [49,

530] in smaller InGaN LEDs. Size-dependent current density-voltage (J-V) characteristics shows that the current densities of the smaller LEDs at the same voltage bias are remarkably higher than larger LEDs, which may be due to the improved uniformity of the current spreading in the smaller LEDs [133]. With the same injection of current density, the junction temperature in smaller pixels is substantially lower than that in larger pixels, due to larger nonequilibrium carrier thermalization and more serious current crowding effect in larger pixels [133, 538]. In larger pixels, the nonuniformity of the in-plane hole and electron concentrations is much larger, due to a more serious current crowding effect [133, 538], further leading to stronger local heating, larger electron overflow and enhanced local non-radiative recombination such as Auger recombination. In addition to the advantage of higher EQE obtained from smaller μm-scale LEDs, it has also been observed that smaller μm-scale InGaN LEDs exhibit higher maximum endured current density (at an injection level of kA/cm^2) [540]. The higher maximum operation current densities are attributed to lower junction temperature and more uniform current spreading [540]. Micro-scale InGaN-based LEDs show less temperature-dependent decay at same current and thus exhibit more stable performance at high temperature than larger devices [529, 541, 542].

Very recently, EQE in the range of 40.2-48.6% has been reported in μm-scale blue InGaN/GaN MQW LEDs by D. Hwang [536]. The dimensions of those μm-scale blue LEDs were 10×10, 20×20, 40×40, 60×60, 80×80 and 100×100 μm^2, and the peak EQE varied with the LED lateral size [536]. The current density at the peak EQE, J_{droop}, was in the range of ~7.5-26 A/cm^2 and increased with decreasing LED lateral size [536]. Compared to larger μm-scale LEDs, smaller μm-scale LEDs suffered more from etching damage, but it exhibited better current spreading [536]. In D. Hwang's study, high EQE was sustained when decreasing the LED lateral size [536] as the results of both more etching damage and better current spreading in smaller μm-scale LEDs. The detailed information of μm-scale LEDs reported by D. Hwang

[536] was shown in **Appendix II**. As a summary of size-dependent characteristics of InGaN-based epilayer LEDs, smaller μm-scale InGaN LEDs exhibit better current spreading, higher maximum endured current density, more stable performance at high temperature, and wider droop-free regions in terms of current density. It is very promising to use GaN-based LEDs for manufacturing μm-scale color-tunable LED devices, in contrast to OLED technology which currently exhibit lower efficiencies at smaller device size.

However, as shown in **Figure 3-1** plotted based on various publications, the EQEs and luminous efficiencies of InGaN-based epilayer LEDs with size below ~ 40 μm are still lower than those of well-developed InGaN-based epilayer LEDs with size larger than ~ 40 μm [46-50, 53, 162-168, 432-436, 543-545]. This may be due to the fabrication and synthesis processes of InGaN-based epilayer LEDs with size below ~ 40 μm are still in the initial development stage. In addition, more etching-induced defects in smaller devices are also responsible for the lower efficiencies measured from InGaN-based epilayer LEDs with size below ~ 40 μm. In contrast, the use of bottom-up GaN-based nanowires to make color-tunable LEDs avoid the etching process which is essential for creating μm-scale structures from III-nitride planar heterostructures exhibiting large defect density due to large lattice mismatch.

There are very few reports of red μm-scale InGaN-based epilayer LEDs, and the performance of yellow and orange μm-scale InGaN-based epilayer LEDs are relatively poor. It can be noted that true-orange and true-red emitter with long emission wavelengths (> 590 nm) cannot be realized by using InGaN/GaN QWs [546], due to the bottlenecks of growing In-rich InGaN epilayers. The fabrication of yellow, orange and red μm-scale InGaN-based epilayer LEDs also involve the use of etching processes which introduce significant sidewall damage and thus further reduce the device efficiency.

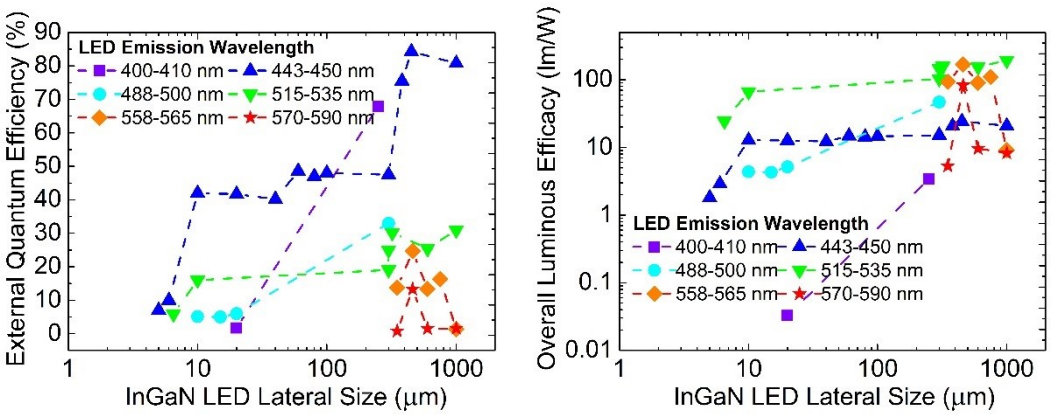

(a) (b)

Figure 3-1: Summary of (a) EQE and (b) overall luminous efficacy (or luminous efficacy of a source) of InGaN-based epilayer LED versus the lateral device size according to published literatures [46-50, 53, 55, 162-168, 432-436, 536, 543-545]. For some literatures which did not provided EQE values directly [459], their EQE values are calculated from the given overall luminous efficacy using luminous efficacy of radiation function (CIE 1978 Judd−Vos-modified photopic eye sensitivity function) [437, 438]. For some literatures which did not provided overall luminous efficacy (lm/W) directly [530], their overall luminous efficacies are calculated from the given EQE values using luminous efficacy of radiation function (CIE 1978 Judd−Vos-modified photopic eye sensitivity function) [437, 438]. A few publications reported lower EQEs and lower overall luminous efficacies than those of publications presented and cited in Figure 3-1. The detailed information of InGaN-based epilayer LEDs is listed in **Appendix II**.

Figures 3-3 (a) and (b) summarize the EQE and the overall luminous efficacy of red-emitting InGaAlP-based epilayer LED versus the lateral device size according to published literatures [547-552]. The detailed information of red-emitting InGaAlP-based epilayer LEDs is listed in **Appendix III**. As presented in the **Appendix III** and as shown in Figure 3-2 (a), the EQEs of 300×300 μm^2 InGaAlP-based LEDs were measured to be 50.0% at the wavelength of 650 nm, 42.5% at the wavelength of 635 nm, and 23.0% at the wavelength of 598 nm [550]. In other words, red-emitting InGaAlP-based LEDs exhibit lower efficiency at the shorter wavelength, which is closer to the spectral range of "green gap". This observation is consistent

with the "green gap" shown in Figure 1-2. In another study, InGaAlP/GaP truncated-inverted-pyramid LEDs exhibit EQE in the range from ~ 17% to 55% depending on the emission wavelength, following the same trend that lower efficiency was measured at the shorter wavelength in the orange/red spectral range [553].

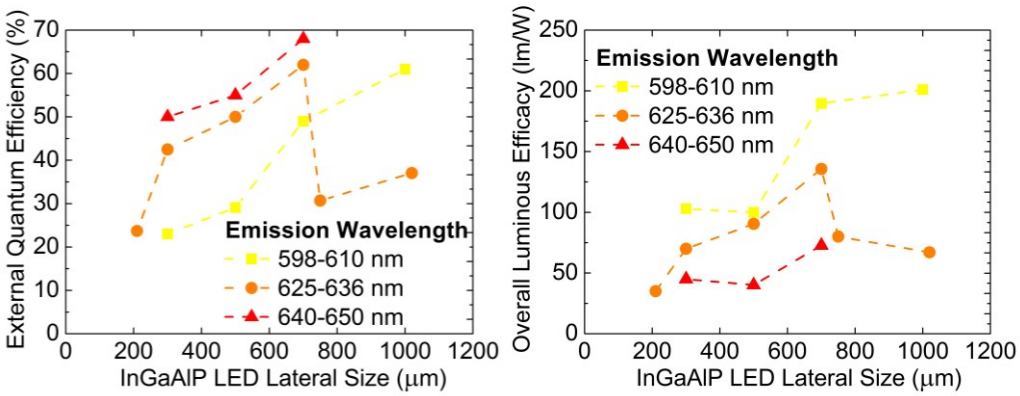

(a) (b)

Figure 3-2: Summary of (a) EQE and (b) the overall luminous efficacy of red-emitting InGaAlP-based epilayer LED versus the lateral device size based on published literatures [547-552]. For some literatures which did not provided EQE values directly, their EQE values are calculated from the given overall luminous efficacy using calculated luminous efficacy function of white light sources. For some literatures which did not provided overall luminous efficacy (lm/W) directly, their overall luminous efficacies are calculated from the given EQE values using luminous efficacy of radiation function (CIE 1978 Judd−Vos-modified photopic eye sensitivity function) [437, 438]. The detailed information of red-emitting InGaAlP-based epilayer LEDs is listed in **Appendix III**.

There are very few reports of red-emitting InGaAlP-based epilayer LEDs with size below 200 μm. In two recent reports, red-emitting InGaAlP-based epilayer LEDs with size of 80 μm [547] and 100 μm [548] exhibited the EQEs of ~ 0.175% and 2.3%, respectively. In contrast, efficient red-emitting GaN-based nanowires LED has been realized [250], and the shrink of nanowire-based LED device size is more flexible and viable.

As shown in Table 3-1, various approaches have been developed to make multi-color III-V-based hybrid LEDs to produce color-tunable light through light mixing [427, 452, 459, 554,

555]. In these multi-color III-V-based hybrid LEDs, μm-scale devices [427, 554] also exhibit lower luminous efficiencies and lower EQEs than those of mm-scale devices [452, 459, 555]. The performance of current μm-scale color-tunable LEDs, such as the efficiency [427, 452, 459, 554, 555] and color-tunability [459], are ultimately limited by the performance of μm-scale monochromatic RGB LED light sources. It is very desirable to use nearly dislocation-free GaN-based nanowires to make color-tunable LEDs.

Table 3-1: Reports of multi-color III-V-based hybrid LEDs exhibiting different lateral size.

Multi-color LEDs & Materials	Overall Luminous Efficacy (lm/W) & External Quantum Efficiency (%)	Lateral Size or Pixel Pitch (μm)	First Author Year
RGB microdisplay A pixel is a stacked RGB LED tower made by III-P and III-N materials	0.193 lm/W & ~1.3% (20000 cd/m^2)	5-10	H. S. El-Ghoroury [427] 2015 R. G. W. Brown [554] 2010
Telescope-pixel-based display technique using RGB backlight.	Overall backlight transmission efficiency of 36%. To calculate the overall efficiency, the efficiency of RGB source are needed.	100	A. L. Pyayt [555] 2008
A stacked RGB LED tower through bonding an AlInGaP red LED an InGaN green LED, & an InGaN blue LED.	20.19 lm/W & 5.94%	1000	Y. F. Cheung [459] 2013
A RGB LED chips an AlInGaP red LED an InGaN green LED, & an InGaN blue LED.	32.78 lm/W & 9.64%	2000	Y. F. Cheung [459] 2013
Color-by-blue emissive devices using blue InGaN LED backlight, and green and red phosphor.	12.3% or more, depending on the efficiency of the used blue LED (generally over 60%); the total transmission efficiency of the color-by-blue EC display is 20.5%	5000	J. R. Oh [452] 2011

In this Chapter, we have developed a drastically different approach to achieve controllable and tunable full-color light generation through the monolithic integration of laterally-arranged RGB InGaN-based nanowire LEDs on Si substrate. Such high efficiency dislocation-free InGaN nanowire LEDs, with emission wavelengths in the range from ~ 450 nm to 700 nm, were grown in sequence using a three-step growth process by MBE. This approach enables

controlled light mixing at the chip level and yield color-tunable light emission with CCT values in the range from 1900 K to 6800 K, while maintaining excellent color rendering capability. It is envisioned that this approach will further increase LED applications including mood lighting and full-color displays. Moreover, such nanowire devices can be fabricated in the sub-micron or nanoscale and can be integrated with Si electronics for applications in displays, imaging, and biochemical sensing.

3.2 Three-step Growth of Monolithic RGB Pixels on Si

In this experiment, full-color nanowire LED arrays were grown on patterned SiO_x/Si substrates using a three-step MBE growth process, wherein emission characteristics of the LED subpixels can be tuned from blue to red by controlling the compositions and sizes of the dots [119, 122, 250, 254]. The LED structure consists of one ~ 0.4 μm GaN:Si segment, ten vertically aligned InGaN/GaN dots, one ~ 10 nm *p*-doped AlGaN electron blocking layer (EBL), and one ~ 0.2 μm GaN:Mg segment. The growth temperature for GaN:Si and GaN:Mg segments was ~770 °C. Each InGaN/GaN dot consists of one ~ 3 nm InGaN and one ~ 3 nm GaN barrier layer.

Illustrated in Figure 3-3 (a), a selectively patterned SiO_x dielectric layer (~ 100 nm), with designed microscale openings, was first created on Si substrate by standard photolithography and etching techniques. In this study, the sizes of the openings were in the range of 300×300 μm^2, 100×100 μm^2 and 50×50 μm^2. Blue nanowire LEDs were first grown on the patterned substrate, shown in Figure 3-3 (b). It is important to notice that the nanowire growth takes place on the open Si area as well as on the SiO_x mask [556]. The SiO_x mask was selectively removed by buffered oxide etch (BOE) and the nanowires grown on the SiO_x mask were removed together with the mask. As a result, after the wet etching, only blue nanowire subpixels grown directly on Si were left, illustrated in Figure 3-3 (c). A SiO_x layer was then used to cover the blue LED nanowire subpixels formed on Si. Standard photolithography and wet etching

techniques were used to create additional opening apertures for the growth of the 2nd step (green/yellow) LED subpixels at desired locations, illustrated in Figures 3-4 (d) and (e). Subsequently, the 2nd step (green/yellow) and 3rd step (orange/red) LED subpixels were grown on patterned Si substrates using a similar process, shown in Figures 3-4 (f) and (g). Finally, illustrated in Figure 3-3 (h), the SiO_x mask and nanowires on SiO_x were removed to expose the three-step nanowire LED arrays.

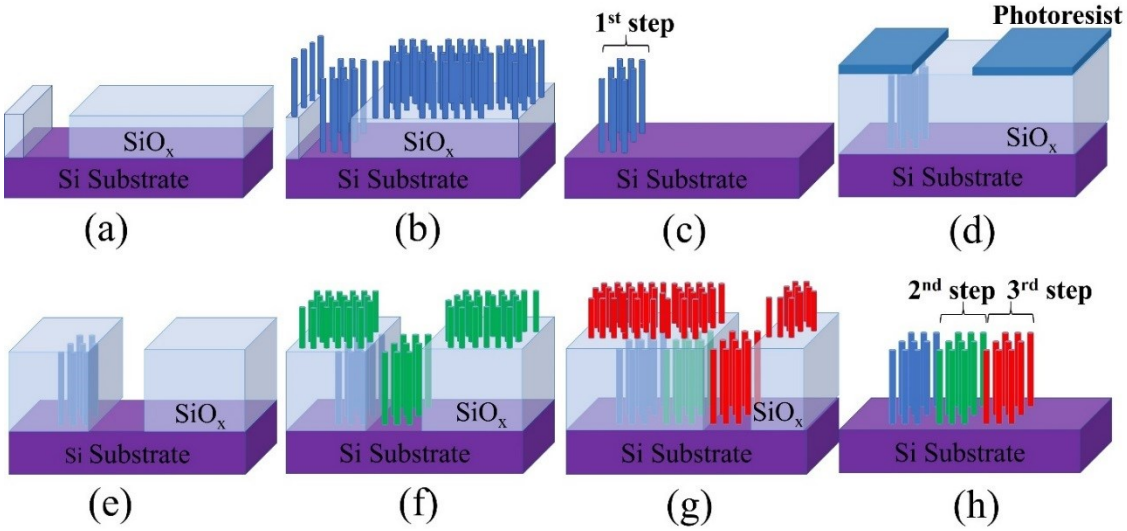

Figure 3-3: Illustrations of the three-step substrate preparation and epitaxial growth process in the present work. (a) A thin SiO_x mask was created on Si substrate. (b) Blue nanowire LED structures were grown on the patterned substrate. (c) After the selective etching, only blue nanowire subpixels grown directly on Si were left. (d) After covering the blue subpixels with SiO_x, the SiO_x/Si substrate was patterned by a thin photoresist layer. (e) New opening apertures were created for the subsequent growth of green nanowire LED structures. (f) Green nanowire LED structures were grown on the patterned substrate. (g) The blue and green subpixels were covered with SiO_x, and red nanowire LED structures were grown. (h) RGB nanowire LED arrays formed on Si after the selective etching by using BOE solution.

The growth temperatures for InGaN/GaN quantum dots were 690 °C, 650 °C, and 600 °C in the 1st, 2nd, and 3rd growth steps, in order to achieve blue, green/yellow, and orange/red emissions, respectively. It is important to notice that the RGB devices are positioned next to each other, thereby leading to seamless integration and light mixing of multi-color LEDs.

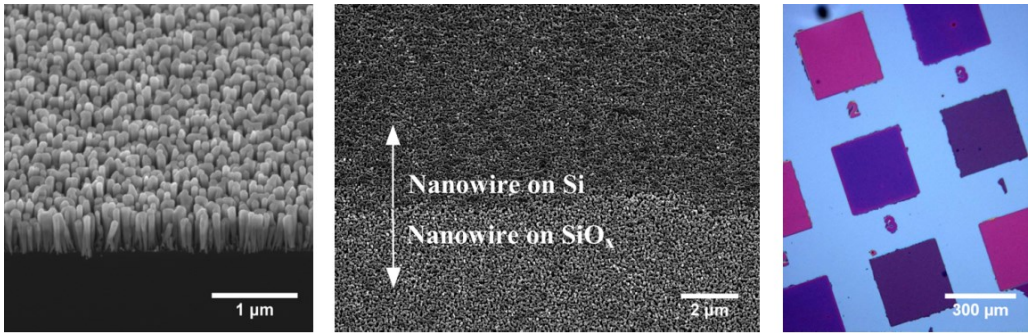

Figure 3-4: SEM images of (a) InGaN/GaN red-emitting nanowires grown on Si in the 3rd epitaxy step and (b) InGaN/GaN nanowires formed near the boundary between SiO_x mask and open Si area. (c) Optical microscope image of multi-color nanowire LED arrays grown using three-step MBE process after the removal of the SiO_x mask. The blue, green/yellow, and orange/red-emitting nanowire LEDs grown in the 1st, 2nd, and 3rd step are denoted as 1, 2, and 3, respectively.

Detailed structural studies further confirm that nanowire LED arrays grown in the three-step process exhibit high size uniformity. Their structural and optical properties were nearly identical to those grown directly on Si substrate. Shown in Figure 3-4 (a) is the SEM image of InGaN/GaN red-emitting nanowires grown in the 3rd epitaxy step. The resulting nanowire arrays exhibit high density (~ 1.5×10^{10} cm^{-2}). As mentioned above, nanowires are formed both on Si and SiO_x in the three-step growth process, which can be clearly observed in Figure 3-4 (b). Figure 3-4 (c) shows the optical image of three-step nanowire LED subpixels on Si substrate after SiO_x removal, which exhibit slightly different color contrast. The three-step arrays were sorted in this order as illustrated so that they were close enough for the formation of triple-color pixels to yield good light mixing. It is important to notice in Figure 3-4 (c) that the number below each LED square corresponds to the step number in the three-step growth.

3.3 Photoluminescence and Electroluminescence of Monolithic RGB Pixels

InGaN/GaN dot-in-a-wire LED heterostructures exhibit strong PL emission at room-temperature. Three growths (three steps) differed in the growth conditions, resulting in different InGaN compositions and different PL emissions in three steps. Shown in the Figure

3-5 (a), tunable PL emissions across the entire visible spectral range (~ 450 nm to 700 nm) can be achieved on a single Si wafer. Moreover, for each growth step, the peak position and spectral linewidth of the PL emission, e.g., the green and yellow PL spectra obtained in the 2nd step, and the orange and red spectra in the 3rd step shown in Figure 3-5 (a), can be further engineered by varying the growth conditions, thereby providing a great level of flexibility in tuning the emission color of the integrated LED arrays.

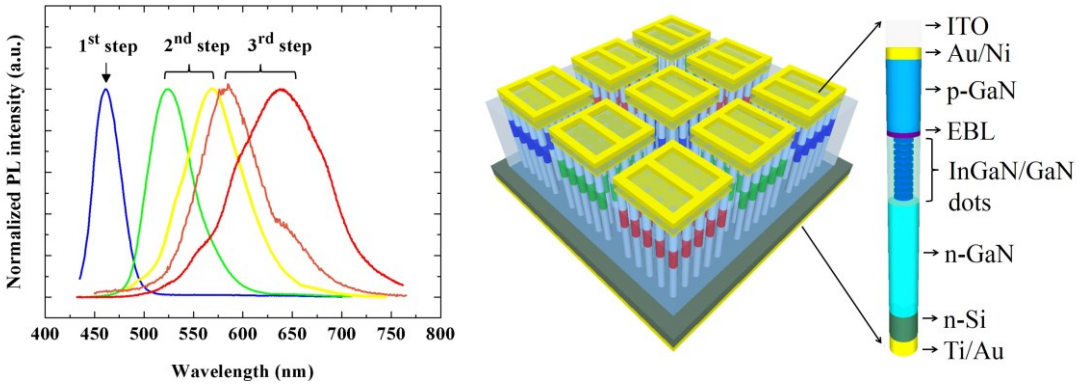

(a) (b)

Figure 3-5: (a) Normalized PL spectra of multi-color nanowire LED subpixels monolithically grown on Si substrate measured at room temperature. (b) Schematic of multi-color nanowire LED devices on the same chip. The thickness of each layer is not drawn to scale.

Subsequently, nanowire LED devices with areal sizes of 300×300 μm^2, 100×100 μm^2 and 50×50 μm^2 were fabricated. In the fabrication process, a polyimide resist layer was spin-coated onto the nanowires for planarization, followed by O_2 dry etching to expose the GaN:Mg region at the top of the nanowires. Ni (5 nm)/Au (5 nm)/indium tin oxide (100 nm) layers and Ti (20 nm)/Au (100 nm) layers were deposited on GaN:Mg and the backside of the Si substrate to form *p*- and *n*- contacts, respectively. After appropriate contact annealing, metal grid patterns were deposited on the device surface to facilitate carrier spreading. The fabricated nanowire LED arrays are schematically shown in Figure 3-5 (b). The detailed device fabrication process and device structure were described elsewhere. [119, 254]

The multi-color nanowire LEDs grown on Si substrate exhibit excellent current-voltage characteristics. Illustrated in Figure 3-6 (a) are representative I-V curves of red, yellow and

green-emitting devices, which have negligible leakage current under reverse bias. The EL spectra for devices grown at different steps are shown in Figure 3-6 (b), which span from ~ 450 nm to 700 nm. It is worthwhile mentioning that nanowire LEDs generally exhibit some degree of nonuniform emission under electrical injection [104], which is primarily due to insufficient current spreading, nonuniform surface planarization, and variations in the nanowire diameters.

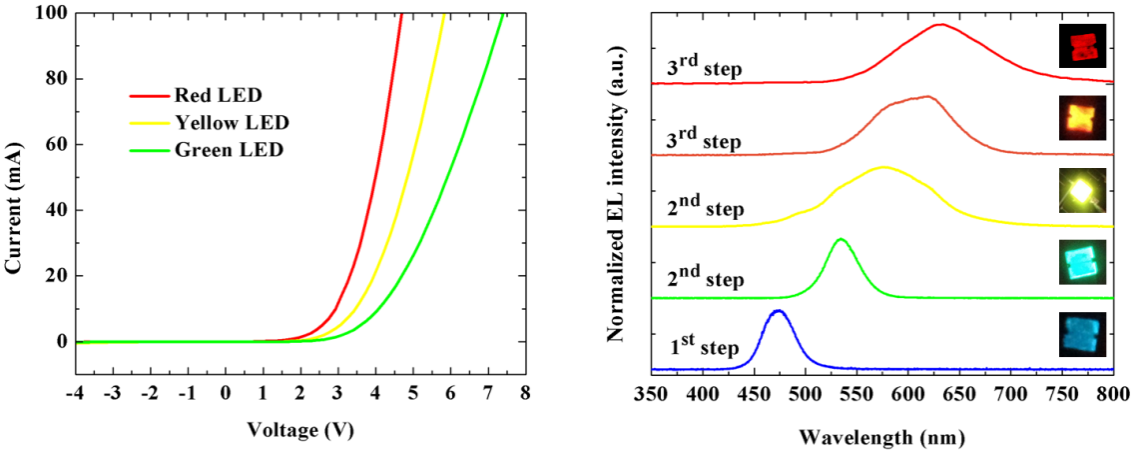

(a) (b)

Figure 3-6: (a) Current-voltage characteristics of 300×300 μm^2 LED subpixels with red, yellow and green emissions. (b) Normalized EL spectra of nanowire LED subpixels monolithically integrated on Si substrate. The corresponding optical images are shown in the inset.

3.4 High CRI and Tunable CCT Achieved through Light Mixing

Shown in Figure 3-7 (a), relatively light output powers of blue, green, yellow, orange and red-emitting devices were measured under various injection currents (1% duty cycle pulsed biasing). It is worthwhile mentioning that the peak wavelengths for LEDs grown at each step can be further tuned by varying the growth conditions, which can lead to full-color LED chips tailored for specific applications. Moreover, each single LED device can exhibit a broad spectrum, due to variations of In compositions in the dots [467], which can enable a phosphor-free orange, red, or even white light emission with a relatively high CRI.

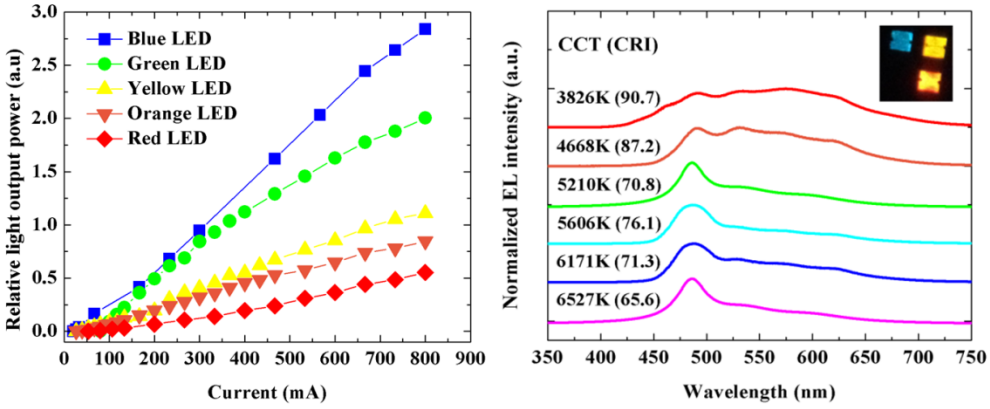

(a) (b)

Figure 3-7: (a) Relative light power of blue, green, yellow, orange and red-emitting LED subpixels under various injection currents up to 800 mA (1% duty cycle pulsed biasing) at room-temperature. (b) The output spectra of a representative triple-color LED pixel with three 300×300 μm^2 devices independently biased at various CW injection current, showing the wide range of tunability. A triple-color LED pixel is shown in the inset.

In this study, each full-color LED pixel consists of three multi-color subpixels, shown in the inset of Figure 3-7 (b), which can be separately biased and exhibit emission in the blue, green/yellow, and orange/red spectral range. Consequently, light mixing at the chip level can be readily achieved. More importantly, by varying the injection current to each LED subpixel, the spectral power density and the CCT can be controllably tuned. The output spectra of a representative triple-color LED pixel consisting of blue, green and orange/red subpixels are shown in Figure 3-7 (b). It is seen that by adding green and orange/red light components, the CCT can be varied from ~ 6500 to 3800 K. For the operation at CCT of 3826 K, the CRI can be as high as 90.7. The injection currents measured for these emission characteristics are shown in Table 3-2. Also included in the Table 3-2 are the relative external quantum efficiencies (REQEs) of blue, green and orange/red-emitting subpixels measured under these injection currents; the REQE was derived by dividing the integrated light intensity (in arbitrary units) by the corresponding injection current. It is worth noting that the REQE of blue subpixel under 85 mA CW injection current is defined as 100%. Such a wide tuning range can be achieved at various output power levels.

Table 3-2: Injection current and relative EQE measured for different LED pixels with different CCT(CRI)s.

	Blue Subpixel		Green Subpixel		Orange/red Subpixel	
CCT(CRI)	*I (mA)*	*REQE*	*I (mA)*	*REQE*	*I (mA)*	*REQE*
3826 K (90.7)	20	77.3%	35	56.1%	140	32.1%
4668 K (87.2)	20	77.3%	65	77.3%	130	32.0%
5210 K (70.8)	60	90.4%	100	84.4%	75	31.8%
5606 K (76.1)	30	77.6%	18	42.0%	45	19.7%
6171 K (71.3)	35	77.9%	35	56.1%	90	31.9%
6527 K (65.6)	85	100%	95	83.9%	78	31.8%

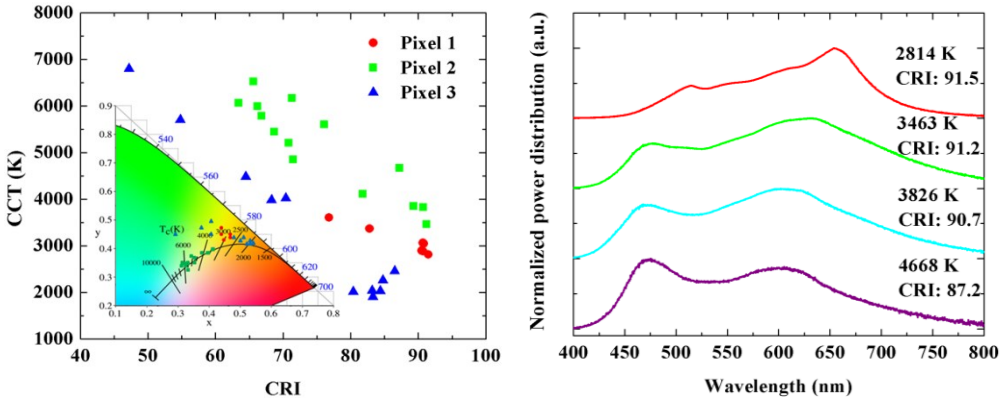

(a) (b)

Figure 3-8: (a) CCT and CRI values of the emission measured from three triple-color LED pixels. The inset shows the corresponding locations in the CIE chromaticity diagram. (b) Normalized spectral power distribution of representative triple-color LED pixels with high CRI.

Figure 3-8 (a) shows the summary of the emission characteristics of three different triple-color LED pixels, which were grown at different conditions. It is observed that the CCT values can be varied from ~1900 K to 6800 K. Very large CRI values (> 85) can be achieved for devices with warm and neutral white light emissions (CCT < 5000 K). The output characteristics of these devices are further shown in the CIE chromaticity diagram, illustrated in the inset of Figure 3-8 (a). The spectral power distributions of representative high-CRI triple-color LED pixels are shown in Figure 3-8 (b).

3.5 Summary

In summary, a drastically different approach has been developed in this work to achieve controllable and tunable emission through the monolithic integration of full-color InGaN/GaN dot-in-a-wire multi-color LEDs directly on Si substrate, after extensive efforts on the optimization for growth parameter and fabrication processes. Such laterally arranged nanowire LED pixels yield color temperatures from ~ 1900 K to 6800 K, while maintaining excellent color rendering capability. Importantly, such wide color tunability as well as high color rendering index can be repeated on many color-tunable nanowire chips. This approach overcomes the manufacturing complexity and the overall luminous efficacy and light quality tradeoff associated with conventional phosphor-based LEDs and will further enable a broad range of applications including mood lighting and full-color displays. Moreover, such nanowire devices can be fabricated in the sub-micron or nanoscale and can be integrated with Si electronics for applications in projection displays, imaging, and biochemical sensing.

One disadvantage of Si substrate for this application is the light absorption. For practical device applications, the underlying Si substrate can be selectively removed by wet chemical etching process. For enhanced light extraction and more effective thermal management, nanowire LEDs grown on SiO_2/Si substrates can be transferred to Cu substrate [272, 557], or a reflective metal layer can be grown on Si substrates [558-562]. It is also promising to develop three-step spontaneously grown InGaN/AlGaN core-shell color-tunable nanowire LED arrays on Si substrates to reduce the surface recombination and enhance the carrier injection efficiency [254].

Chapter 4: Micro-scale and Nano-scale Color-Tunable Pixels Using Full-Color InGaN Nanowires Selective-Area Grown on GaN/sapphire Substrates

4.1 Introduction

The demanding applications, especially the display applications such as three-dimensional (3D) projection display, high-resolution flat-panel displays, flexible display, and near-to-eye displays also known as virtual retinal display [563-568], requires the miniaturization of color-tunable solid-state light sources, which can be realized by using RGB nanowire LEDs monolithically integrated over a single chip.

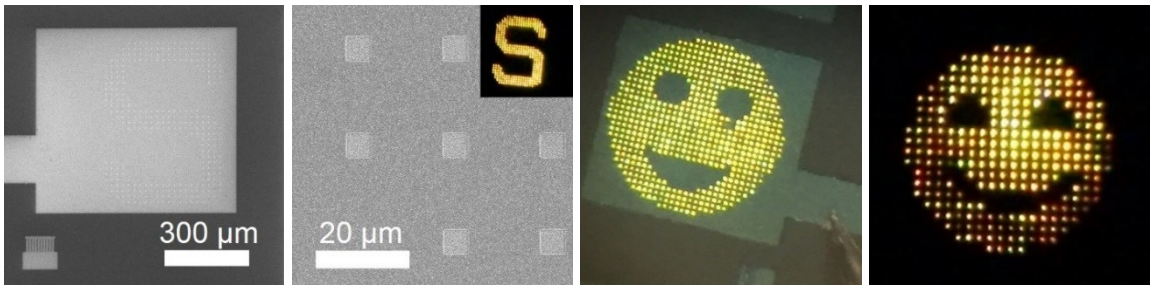

(a) (b) (c) (d)

Figure 4-1: (a) Top-view SEM image of μm-scale LED array arranged in an S shape, and the μm-scale LEDs were made by using spontaneously grown InGaN/GaN nanowires. (b) Top-view SEM image of LED array arranged in a periodicity of 20 μm to form an S shape shown in (a), and the nanowire LED is a 5×5 μm^2 square device. The inset is an optical microscopy image of an S-shape LED array exhibiting amber EL. Top-view optical microscopy images of (c) face-shape LED arrays exhibiting yellow EL and (d) face-shape LED arrays exhibiting multi-color EL.

In the Chapter 3, through the monolithic integration of blue, green/yellow, and orange/red InGaN nanowire LEDs (λ: ~ 450 nm to 700 nm), controllable and tunable light generation has been achieved directly on Si substrate using a three-step SiO_x-mask selective-area MBE growth process. However, this approach requires three growth processes to integrate nanowires with three different compositions on the same substrates. A single growth of spontaneously grown nanowires can only emit single-color light, as shown in Figure 4-1 (c). The single-color μm-

scale LED array shown in Figure 4-1 was made by arranging μm-scale LEDs into different shape, as shown in Figures 4-1 (a) and (b). Each μm-scale LED consists of a few thousand spontaneously grown InGaN/GaN nanowires. The fluctuations in nanowire length, diameter and position is another challenge for spontaneously grown nanowires, which may result in multi-color emission and broad EL over a small area. As shown in Figure 4-1 (d), the μm-scale LED array exhibits multi-color emission from different LED devices, due to the large fluctuations in InGaN composition and non-uniform current injection. This shows that it is difficult to precisely control the emission color of μm-scale LED made using spontaneously grown nanowire heterostructures. White LEDs can be made using the spontaneously grown nanowire exhibiting extremely large fluctuations in nanowire length, diameter and position [463]. However, the fluctuations in nanowire length, diameter and position is detrimental to make color-tunable LED pixels.

In Chapter 3, the smallest RGB pixel size (~ 0.016 mm^2) has been achieved with LED areal sizes of 50×50 μm^2. It is expected that the RGB pixel size can be further reduced to a few μm and sub-μm scale by introduction of high-resolution lithography techniques such as EBL. To obtain high luminous efficiency and fine control of the emission color of RGB nanowire LEDs, selective area epitaxy technique of InGaN/GaN nanocolumns has been recently developed by using MBE [399]. Due to the beam shadowing effect of the neighboring nanocolumns, the emission color of InGaN/GaN nanocolumn changes from blue to red with increasing diameter [105]. The selective area epitaxy technique enables a precise tuning of alloy compositions over the same substrate. Such compositional variations can be ideally introduced in a single growth process.

The Ti-mask selective area epitaxy has been introduced in sections 2.1.3, 2.1.4 and 2.4.2. In this chapter, by using Ti-mask selective area epitaxy, the progress in epitaxy of full-color InGaN nanowire array on the same GaN/sapphire substrate will be discussed. Based on that,

using the same approach, the color-tunable pixels with the size of a few μm and sub-μm scale have been achieved on single GaN/sapphire substrates. In these color-tunable devices monolithically integrated on single chips, a nanowire LED made using single or a few nanowire heterostructures is considered as one monochromatic LED subpixel.

4.2 The Effects of Growth Parameters on the Size and Length of GaN Nanowires

The growth conditions largely affect the sticking coefficients, diffusion lengths and desorption rates of the metal adatoms on the substrates. Therefore, selectivity and formation of GaN nanowires depend on the growth parameters such as N_2 flow rate, Ga/N ratio and growth temperature [405, 569, 570]. Ga beam equivalent pressure (BEP) plays a major role in determining nanowire diameter and growth rate [569]. Additionally, for a given values of Ga BEP and N_2 flow rate, the growth temperature is also an important parameter to control the formation of selective-area grown GaN nanowires [569]. At a relatively low growth temperature in the window of optimum growth parameters, Ga adatoms has a short diffusion length, contributing more to lateral growth. At a relatively high growth temperature in the parameter window, the Ga adatoms has a relatively long diffusion length which makes Ga adatoms possible to reach the growth front at the top of nanowires, resulting in a larger vertical growth rate. As a conclusion, the nanowire size and the spacing (the gap between neighboring nanowires) can also be controlled by varying the growth parameters, besides varying the patterning design of Ti mask.

4.3 The Effect of Nanowire Size and Array Spacing on Photoluminescence

Using a single growth process in GEN-II^{TM} MBE, full-color InGaN/GaN nanowire arrays have been monolithically grown on the same GaN/sapphire wafer. Prior to the growth, a thin (~ 10 nm) Ti layer was utilized as the mask, and nanohole-array patterns with various diameter and array periodicity were defined by using EBL on the Ti layer. In the growth, first, Si-doped *n*-type GaN segment (~ 420 nm in height) were grown for 3 h at 915 °C. Subsequently, a six-

pair InGaN (3 nm)/GaN (3 nm) active region was grown at 670 °C; and a Mg-doped *p*-type GaN layer (~ 250 nm in height) was grown at 915°C, following the growth of active region. The growth conditions for the active region include BEP_{In} of 2.05×10^{-7} Torr, and BEP_{Ga} of 4.31×10^{-8} Torr. The N_2 flow rate used for the growth of GaN and InGaN-based active region was 0.33 sccm and 1 sccm, repectively.

The effects of nanowire diameter and spacing on the tuning of the emission wavelengths of InGaN/GaN nanowire array have been investigated. PL emission of nanowire array was measured using a micro-PL measurement system at room-temperature with a 405 nm laser as the excitation source. Shown in Figures 4-3 (a) and (b), by varying the nanowire diameters and array periodicity, multi-color emissions across nearly the entire visible spectral range can be achieved in a single molecular epitaxial growth step by using selective area epitaxy.

Similar results was reported previously [105]. It was reported that double-peak emission was observed from ~ 480 nm to ~ 550 nm, the growth mechanism of which remains unclear and requires further study [105]. In our study, single-peak emission was achieved in nearly the entire visible wavelength range, which enable more precise and wider color tunability of light mixing. Shown in Figure 4-3 (b), the PL emission of nanowire array with diameters varying from ~ 90 nm to 500 nm covers the entire visible wavelength range. It is worthwhile mentioning that double-peak emission was observed for the nanowire array with diameter of 500 nm. H. Sekiguchi et al. speculated that long-wavelength peak originated from the sixfold side faces of InGaN/GaN active region and the shorter one from angle areas of InGaN/GaN pyramids [255]. This double-peak emission might be also due to interdiffusion between InGaN and GaN layers. The PL emissions of selective-area grown InGaN/GaN nanowire array (in the wavelength range from ~ 490 nm to 610 nm) exhibits full-width-at-half-maximum (FWHM) of 35-45 nm, which are much narrower than that of spontaneously formed InGaN/GaN nanowire arrays [533], due to more uniform nanowire size and In distribution as well as better crystal quality.

The PL peak intensity of selective-area grown green-emitting ten-pair InGaN/GaN nanowire array was measured to be ~ 36.7 times higher than that of the reported ten-pair InGaN/AlGaN nanowire array spontaneously grown on Si substrate. Top-view and side-view SEM images of representative nanowire array with different diameters are shown in Figure 4-2.

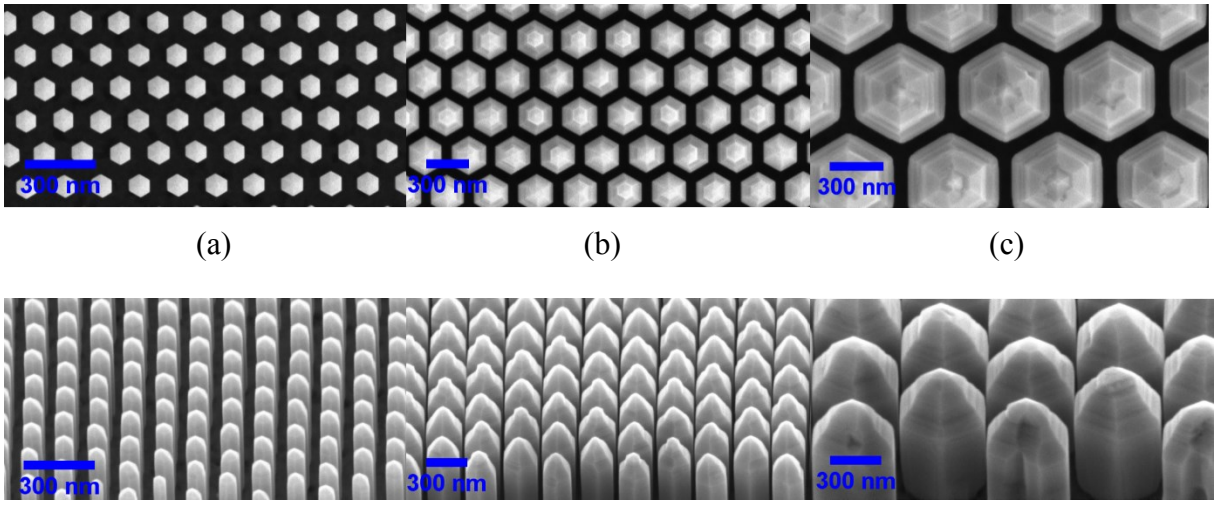

Figure 4-2: Top-view SEM images of LED arrays consisting of nanowires with (a) 90 nm, (b) 260 nm and (c) 500 nm in diameter. Side-view SEM images of LED array consisting of nanowires with (d) 90 nm, (e) 260 nm and (f) 500 nm in diameter.

In the single MBE growth, two groups of nanowire array with the spacing of 56 nm and 72 nm were grown on the same substrate. Illustrated in Figure 4-3 (c) is the variations of PL peak emission wavelength with respect to nanowire diameter for InGaN/GaN nanowire arrays grown with two different spacings. Here, the term "spacing" is used to represent the gap between outer surfaces of two adjacent nanowires, instead of center-to-center spacing used as an array lattice constant. Because the growth mechanism is closely related to the gap between the lateral surfaces of neighboring nanowire. Center-to-center spacing, which is called as periodicity in this dissertation, is important for the study on photonic properties of nanowire arrays such as photonic crystal effect. Samples in Group 1, denoted as blue dot in Figure 4-3 (c), have a spacing of 56 nm and diameters in the range of 130 to 260 nm, corresponding to the PL spectra shown in Figure 4-3 (a). Samples in Group 2, denoted as red dot in Figure 4-3 (c),

have an average spacing of 72 nm and diameters in the range of 90 to 500 nm, corresponding to the PL spectra shown in Figure 4-3 (b). Tunable-color emissions can be achieved by varying the nanowire diameter in each group of nanowire arrays, which are shown in Figures 4-3 (a) and (b).

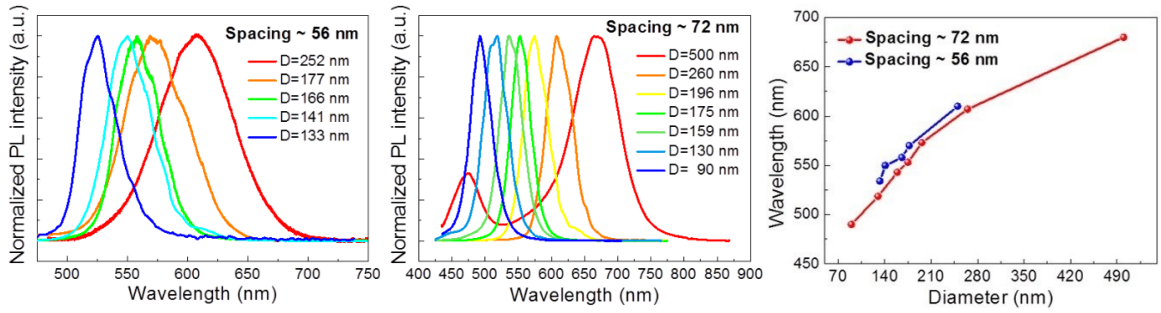

(a) (b) (c)

Figure 4-3: Normalized PL spectra of InGaN/GaN nanowire arrays (a) with nanowire diameters of 133 nm, 141 nm, 166 nm, 177 nm and 252 nm while keeping a constant spacing of 56 nm, and (b) with nanowire diameters of 90 nm, 130 nm, 159 nm, 175 nm, 196 nm, 260 nm and 500 nm while keeping a constant spacing of 72 nm. (c) Peak emission wavelength versus nanowire diameter with a spacing of 56 nm (blue) and 72 nm (red).

It was observed in the experiment conducted by H. Sekiguchi et al. that the PL peak emission wavelength showed a redshift with increasing nanowire diameter (decreasing nanowire spacing) [105, 487]. In this study, it is seen that the PL emission wavelength also shows a consistent redshift with increasing diameter, which is achieved, however, by keeping the nanowire spacing constant. In this study, the way to change nanowire diameter is different from that in the experiment conducted by H. Sekiguchi et al. [105], illustrated in Figure 4-4.

Ga and In atoms incorporation at the nanowire growth front is supplied through two pathways, including impingent atoms as well as atoms diffused along the lateral sides of nanowires. Considering the nanowire spacing is constant, on the nanowire top surface, the ratio of Ga atoms diffused from the lateral sides to the directly impingent Ga atoms is approximately proportional to L/D, where L and D are the diffusion length of Ga atoms and the nanowire

diameter, respectively. It is therefore evident that the incorporation of Ga atoms into the active region is reduced with increasing nanowire diameter, thereby leading to a reduced Ga composition and hence a redshift in the PL emission wavelength. In this analysis it is assumed that In incorporation at the growth front has a small, or negligible dependence on the nanowire diameter, which can be justified by the significantly smaller diffusion length of In atoms compared to that of Ga atoms at relatively high growth temperatures [105].

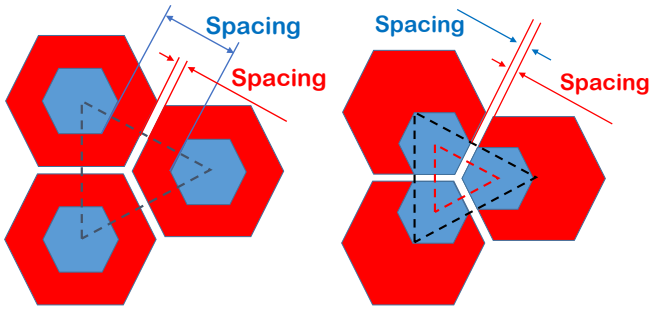

(a) (b)

Figure 4-4: (a) Variations in nanowire diameter in the experiment conducted by H. Sekiguchi et al. [105]. With a constant array periodicity, nanowire diameter increases from blue hexagon to red hexagon, but nanowire spacing decrease at the same time. (b) Variations in nanowire diameter in this study. With a constant nanowire spacing, nanowire diameter increases from blue hexagon to red hexagon, and array periodicity increase at the same time.

In addition, the PL emission wavelength for samples in Group 1 shows a small redshift (~ 5-13 nm), compared to that for samples in Group 2 with the same nanowire diameters, shown in Figure 4-2 (c). The small redshift with decreasing nanowire spacing is due to the beam shadowing effect that leads to reduced Ga incorporation in the nanowire growth front.

4.4 Micro-Scale Color-Tunable Nanowire Pixels on GaN/Sapphire

The color-tunable pixel size of InGaN/GaN nanowire LEDs can be reduced to micro scale or smaller using the Ti-mask SAG technique. These nano-scale LEDs are well suited for high-resolution display and imaging applications. We have developed 2.8×2.8 μm^2 multi-color nanowire subpixels selective-area grown on GaN/sapphire substrate. The LED structure consists of a GaN:Si segment, ten InGaN/GaN, and a GaN:Mg segment. Each InGaN/GaN

consists of 3 nm InGaN and is capped by 3 nm GaN barrier layer. The emission characteristics of nanowire LED subpixel can be controllably varied by changing the diameters of nanowires on the same substrate. Shown in Figure 4-5 (a), four subpixels with different nanowire diameters were integrated into one pixel for color-tunable light mixing.

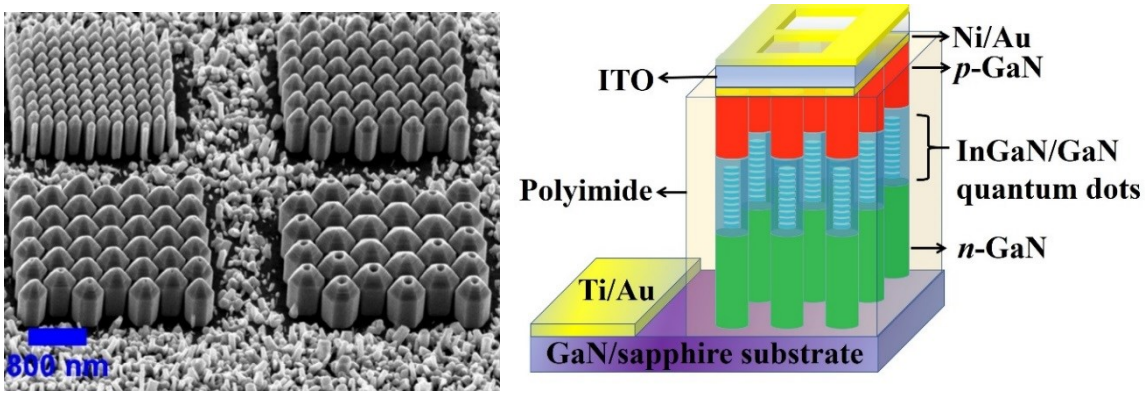

(a) (b)

Figure 4-5: (a) Bird's-eye-view SEM image of a multi-color nanowire pixel consisting of four 2.8×2.8 μm^2 InGaN/GaN nanowire LED subpixels, wherein the nanowire diameters are ~ 170 nm, 295 nm, 401 nm and 620 nm, respectively. (b) Schematic of one nanowire LED subpixel fabricated on GaN/sapphire substrate. The thickness of each layer is not drawn to scale.

In the fabrication process of selective-area grown nanowire arrays, a polyimide resist layer was spin-coated onto the nanowire array for planarization, followed by O_2 dry etching to expose the GaN:Mg region at the top of the nanowires. Ni (5 nm)/Au (5 nm)/ITO (100 nm) layers and Ti (20 nm)/Au (100 nm) layers were deposited to form *p*- and *n*-contacts, respectively. The *n*-contact was deposited at the lateral side of nanowire array. The schematic of one fabricated nanowire LED subpixel is shown in Figure 4-5 (b). It is worthwhile mentioning that the process of transferring nanowire LEDs from sapphire substrates to flexible substrates have been realized by using laser liftoff process [75, 571, 572] on the fabricated LED devices consisting of nanowire arrays selective-area grown on GaN/sapphire substrates.

Illustrated in Figure 4-6 (a), 2.8×2.8 μm^2 multi-color nanowire LED subpixels were laterally arranged on the same substrate. By separately biasing such lateral-arranged LED

subpixels, the CCT value can be varied by tailoring the spectral power distributions of the multi-color LED pixels. The LED subpixels exhibit different EL emissions covering the spectral range from ~ 450 nm to ~ 610 nm, as shown in Figure 4-6 (b). Such a color-tunable pixel size is 7×7 μm^2, which is smaller than the smallest pixel size (~ 45 μm) used in the stat-of-the-art "WQHD Super AMOLED" [6-8].

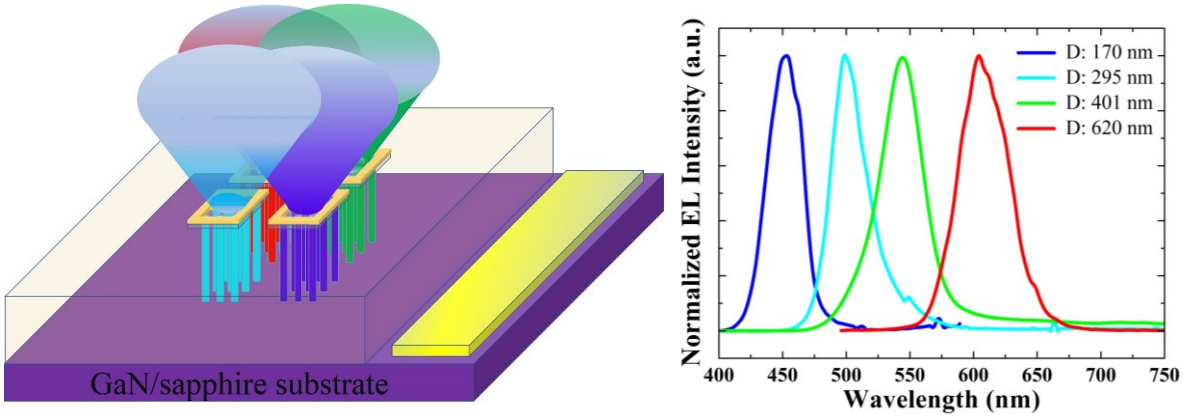

(a) (b)

Figure 4-6: (a) Schematic of a color-tunable nanowire LED pixel selective-area grown on GaN/sapphire substrate. The thickness of each layer is not drawn to scale. (b) EL spectra of four InGaN/GaN LED subpixels on the GaN/sapphire substrate. Four nanowire arrays with nanowire diameter (D) of 170 nm, 295 nm, 401 nm and 620 nm are four subpixels with different color emissions.

4.5 Nano-Scale Color-Tunable Pixels Using Single Nanowires on GaN/sapphire

The color-tunable pixel size can be further reduced to nano scale by using full-color single nanowires as subpixels. We have developed, for the first time, the world's smallest color-tunable pixel size, high performance full-color InGaN/GaN single nanowire LED arrays optimized for ultra-fine projection displays by only one step epitaxial growth process using SAE technique. Compared to conventional GaN-based planar LEDs and organic LEDs, these single nanowire LEDs exhibited much better performance, including high light extraction efficiency, precisely tunable color emission, low cost, higher integration density, and much less power consumption. Moreover, this is the first demonstration on monolithic integration of full-

color single nanowire LEDs on the same substrate. The method used to make μm-scale color-tunable nanowire arrays, takes advantage of shadowing effect of neighboring nanowires to alter the InGaN composition [104], as presented in section 4.3. To date, however, little is known about the mechanism on how to controllably vary the alloy compositions at the single nanowire level without changing the global growth parameters. The monolithic integration of multi-color, single nanowire LEDs on the same chip has thus remained elusive. In our experiments, it was observed that the position, size, and composition of InGaN quantum dots depend critically on the nanowire diameter. Full-color emissions have been achieved on the same substrate by varying the nanowire diameter of single nanowires. Single nanowire LED subpixels, with emission characteristics of red, green, blue and orange (RGBO), have been realized on a single chip with nanowire diameter in the range from 215 to 630 nm and single nanowire exhibit excellent electrical properties.

4.6 The Pattern Preparation and Selective Area Epitaxy of Single Nanowires

In this work, single InGaN nanowires of various sizes have been fabricated on the same substrate by selective area epitaxy using MBE. The epitaxy takes place on an GaN/sapphire substrate with a thin Ti layer (10 nm) being employed as the growth mask [399, 405]. Opening sizes in the range of 80 nm to 1.9 μm were created on the Ti mask by using EBL and RIE, leading to a precise control of the nanowire diameter.

Schematically shown in Figure 4-7 (a), each nanowire consists of ~ 0.35 μm *n*-GaN, five InGaN/GaN QDs and ~ 0.15 μm *p*-GaN capping layer. These nanowires were grown using a Veeco GENxplor^{TM} MBE system. The growth conditions include a substrate temperature of 1030 °C and a Ga beam equivalent pressure (BEP) of 3×10^{-7} torr for the *n*-GaN segment. The substrate temperature was reduced to 795 °C, 810 °C and 825 °C for the growth of InGaN/GaN QD active regions in Samples I, II, and III, respectively. The growth temperature mentioned here refers to the thermocouple reading on the backside (coated with molybdenum and titanium)

of the sapphire substrate. In and Ga BEPs in the ranges of 1.2-1.5×10^{-7} torr and 5-7×10^{-9} torr were used for the growth of the QD active regions. Lastly, the *p*-GaN capping layer used a substrate temperature of 1030 °C, with a Ga BEP of 3×10^{-7} torr and a Mg BEP of 2×10^{-9} torr.

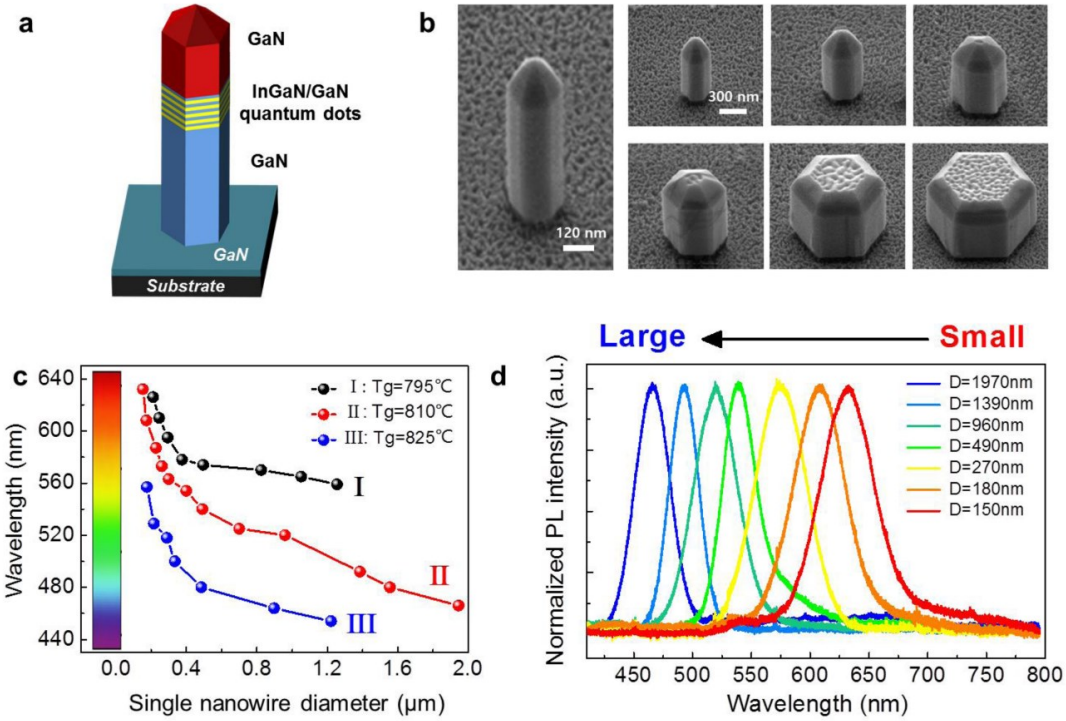

Figure 4-7: (a) Schematic of a single InGaN/GaN dot-in-nanowire structure grown on GaN/ sapphire substrate. (b) 30° tilted SEM image of single InGaN/GaN nanowires with various diameters. (c) The peak emission wavelength of single InGaN/GaN nanowires versus nanowire diameter with the quantum dot active regions grown at 795 ºC (Sample I), 810 ºC (Sample II), and 825 ºC (Sample III). (d) Normalized PL spectra of InGaN/GaN dot-in-nanowire structures in Sample II with different diameters (D) measured at room-temperature, showing a blueshift in the emission peak with increasing nanowire diameter.

Figure 4-7 (b) shows the field-emission SEM image of the single nanowire structures grown with various diameters. The nanowires exhibit near-perfect hexagonal morphology and possess Ga-polarity [573].

4.7 Diameter-Dependent PL of Single Nanowires and the Underlying Mechanism

PL emission for single InGaN/GaN nanowires was measured using a micro-PL measurement system at room-temperature with a 405 nm laser as the excitation source.

Variations of the peak emission wavelengths versus nanowire diameters are shown in Figure 4-7 (c). Nanowires in each group were grown on the same substrate with identical epitaxy conditions, except that their lateral size (also referred as diameters in the subsequent text) was varied in the range from 150 nm to ~ 2 μm. Intriguingly, it is seen that the optical emission shows a consistent blueshift with increasing nanowire diameter under identical epitaxy conditions. Taking nanowires in Sample II as an example, the emission wavelengths can be continuously varied from 640 nm to 465 nm by increasing the nanowire diameters from 150 nm to 2 μm with identical epitaxy conditions. Similar trend is also observed for nanowires in Sample I and Sample III, though the tuning range is less broad due to variations in the growth conditions. The PL emission spectra for nanowires with different diameters are further shown in Figure 4-7 (d).

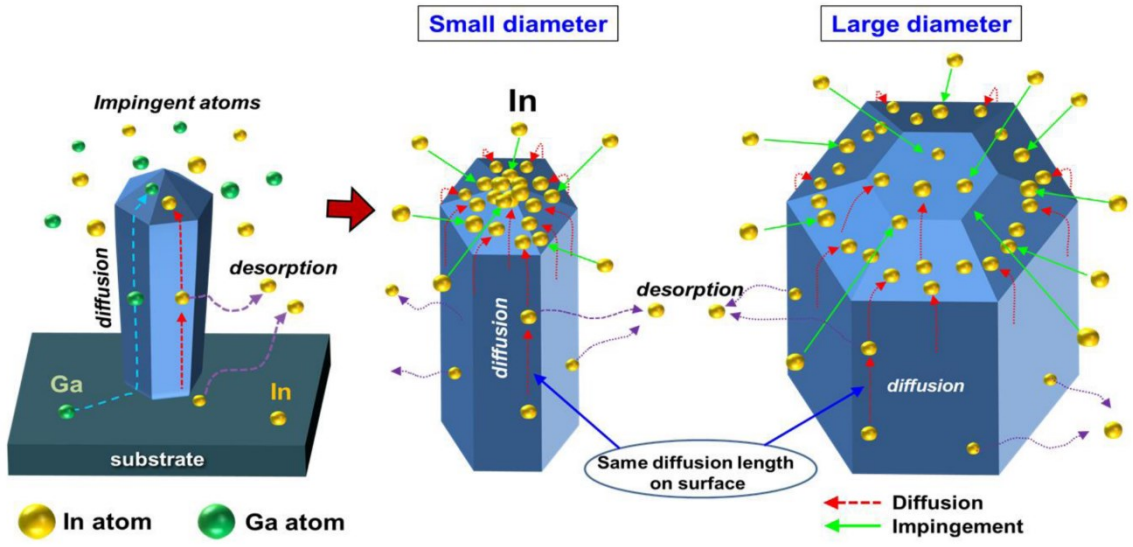

Figure 4-8: Schematic illustrations of the adatom incorporation at the nanowire growth front due to both direct impingement and lateral diffusion (left), the significant contribution of In adatom incorporation due to lateral diffusion for small diameter nanowires (center), and the reduced indium incorporation from lateral diffusion for large diameter nanowires (right).

The unique size-dependent optical emission from single nanowires has not been reported previously in catalyst-assisted or spontaneously formed InGaN nanowire arrays. The underlying mechanism is directly related to the diameter-dependent incorporation of In atoms

at the nanowire growth front. Illustrated in Figure 4-8, compared to the conventional planar epitaxy, the adatom incorporation in single nanowire epitaxy consists of directly impingent adatoms as well as adatoms migrated from the lateral surfaces.

Under relatively high growth temperatures, Ga adatoms have much larger diffusion lengths (~ 1 μm) than In adatoms (~ 100 nm), with the latter limited by thermal desorption [255]. Since the Ga diffusion length is comparable to, or larger than the nanowire diameters, it is expected that the Ga adatom incorporation shows a small, or negligible dependence on nanowire size. However, significantly reduced In incorporation is expected with increasing nanowire diameter, due the reduced In adatom incorporation from lateral diffusion. As a consequence, in a single epitaxy step, InGaN nanowires with larger diameters will have reduced In incorporation and therefore shorter emission wavelength, shown in Figures 4-7 (c) and Figure 4-7 (d). As the diameter increases, the role of direct impingent In atoms does not lead to an increased In-content (ratio in InGaN), since the In BEP is same. In contrast to that, as the diameter increases, the reduced In adatoms incorporation from lateral diffusion results in a reduced In-content, even though the role of In diffusion current is reduced. It shows that, in the single nanowire epitaxy, the variation of In-content is independent on the directly impingent In atoms, but only dependent on the variation of In atoms diffusing from lateral surface. This composition-tuning mechanism of selective-area grown single nanowires will be justified by STEM characterizations in section 4.8.

These results are distinctly different from those of InGaN/GaN nanowire array grown by using selective area epitaxy technique. As discussed in section 4.3, InGaN/GaN nanowire array showed a redshift in emission with increasing nanowire diameter but a consistent spacing, due to the shadowing effect of neighboring nanowires in arrays with high packing density. Shown in Figure 4-2 (c), a consistent redshift with decreasing nanowire spacing was observed due to the reduced Ga incorporation related to the beam shadowing effect. Such beam shadowing

effect, however, is not present for single nanowire epitaxy.

4.8 STEM Characterizations and Diameter-Dependent Formation of Quantum Dots

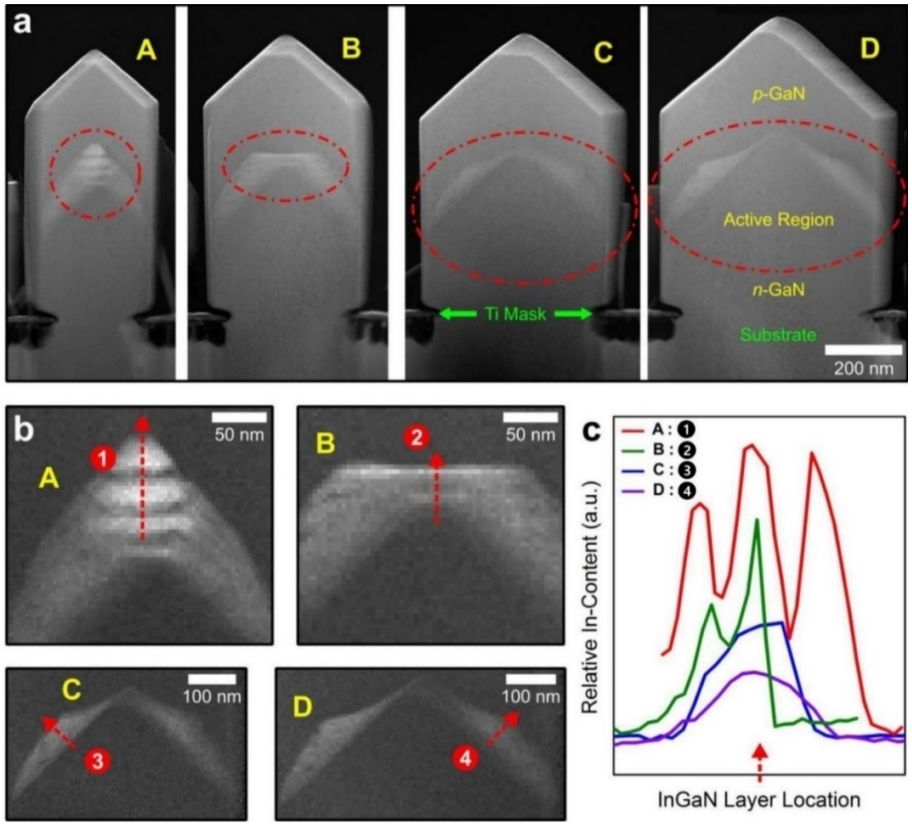

Figure 4-9: (a) A STEM-HAADF image for InGaN/GaN dot-in-nanowire structures with different diameters grown on GaN/sapphire substrate along <11-20> zone-axis. The active regions of nanowires with diameters of ~ 320 nm, ~ 420 nm, ~ 500 nm and ~ 595 nm are labelled as A, B, C, and D, respectively. (b) High-resolution STEM-EELS maps of the In-distribution of active regions A, B, C, and D normalized to the sample thickness. Line profiles were integrated along areas as marked by the dashed red line in each active region. (c) Elemental profiles of relative In-content derived from EELS analysis along line 1 in active region A, line 2 in active region B, line 3 in active region C, and line 4 in active region D, showing higher In-content in smaller diameter wires.

In order to identify the correlation between composition and structure of InGaN/GaN QDs active region associated with the nanowire sizes, extensive structural characterizations have been performed by aberration-corrected STEM using an FEI Titan Cubed 80-300 STEM operated at 200 kV. A cross-sectional sample of nanowire arrays with different diameters was prepared by focused ion beam (FIB) in a single lift-out, milling at 30 kV using a Zeiss NVision

40 dual-beam system with deposited Pt and C as protection layer, and a final polish at 5 kV. The results further reveal the nature and growth mechanism of InGaN/GaN QD nanowires with different diameters.

The high-angle annular dark-field (HAADF) atomic-number contrast images of different diameter nanowires grown on the same substrate are shown in Figure 4-9 (a). The high-resolution elemental mapping of In element using electron energy-loss spectroscopy (EELS) [574] of active regions in each nanowire, labelled with A, B, C, and D, are shown in Figure 4-9 (b). The In-distribution maps (and subsequent line profiles) have been normalized to the TEM cross-section thickness, which is approximately the same across the different diameter nanowires. In these In-distribution maps, the bright regions are rich in In element, while dark regions are In-deficient or In-free (*n*-GaN region at the bottom and *p*-GaN at the top of nanowires). InGaN QDs present clearly at the center of nanowires, shown in active regions A and B, and are vertically aligned along the *c*-axis. With increasing nanowire diameter, instead of the formation of InGaN QDs at the center of nanowires, InGaN accumulates at the semi-polar planes of nanowires, shown in active regions C and D. Shown in active regions of A, B, C, and D, the larger the nanowire diameter, the more InGaN is distributed at the semi-polar planes compared to the center of nanowire (the top of *n*-GaN). These observations clearly indicate that In incorporation at the nanowire top surface shows strong dependence on nanowire diameter. The structural analysis provides unambiguous evidence for the above hypothesis that In incorporation at the nanowire top during the growth of InGaN/GaN active region is hindered with increasing nanowire diameters due to the small diffusion length of In adatoms. Additionally, the accumulation of InGaN in larger diameter nanowires (such as active region C and D) towards the outer diameters on the semi-polar planes further suggests that In incorporation is largely dominated by In-adatom supplied from lateral diffusion.

The two-dimensional EELS maps were analyzed along line 1 in active region A, line 2 in active region B, line 3 in active region C, and line 4 in active region D. The line profiles of In-content derived from EELS analysis are summarized in Figure 4-9 (c). With increasing nanowire diameter, the In-content at the center of InGaN QDs (A) in the smallest single nanowire and InGaN QDs (B, C, and D) in the large single nanowires decreases progressively. This result is consistent with the blue-shifting of the PL peak position with increasing diameter of single nanowires, further supporting the proposed composition-tuning mechanism of selective-area grown single nanowires [575].

4.9 Epitaxy and Device Fabrications of Color-Tunable Single Nanowire Pixels

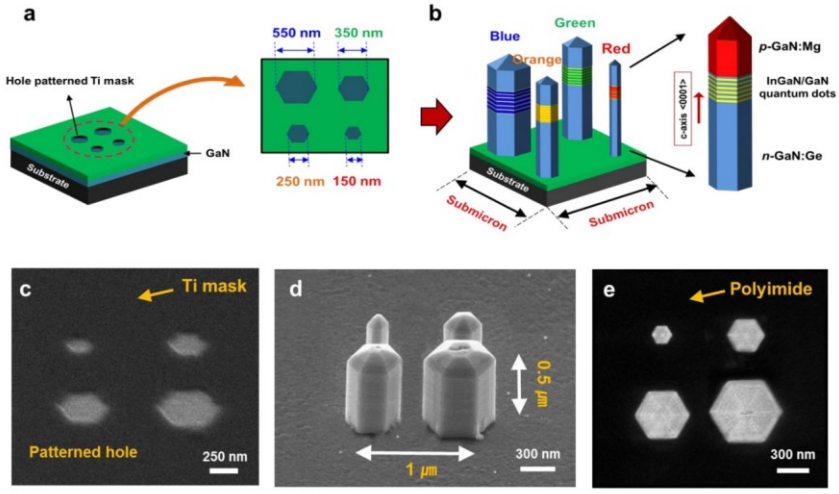

Figure 4-10: (a) and (b) Schematic illustrations for the selective area epitaxy of multi-color single nanowire LED pixel. InGaN/GaN QD single nanowire LED structures are grown on the GaN/sapphire substrate with a Ti mask. Full-color emissions (RGBO) were achieved by varying the nanowire diameters in a single epitaxy step. (c) 30° tilted SEM image of a patterned Ti mask, showing the presence of hexagonal openings with different sizes. (d) SEM image of InGaN/GaN QD single nanowires with different diameters grown by using selective area epitaxy. (e) Top-view SEM image of the exposed *p*-GaN nanowire top-surface after polyimide planarization and dry etching.

To realize full-color (RGBO) and color-tunable single nanowire LED pixels integrated on the same chip, we have grown single nanowire LED arrays consisting of single nanowires with

varying diameters. The selective area epitaxy of such full-color single nanowire LED pixels is illustrated in Figures 4-10 (a) and (b).

The InGaN/GaN QD nanowire LED heterostructures, schematically shown Figure 4-10 (b), consist of 440 nm *n*-GaN, six InGaN/GaN QDs and 150 nm *p*-GaN. These samples were grown in the Veeco GEN-II^{TM} MBE system. The growth conditions include a substrate temperature of 965 °C and a Ga beam equivalent pressure (BEP) of 3.1×10^{-7} torr for Ge and Mg-doped GaN. The substrate temperature is reduced to 715 °C for the growth of InGaN/GaN quantum dot active regions. The temperature mentioned here refers to the thermocouple reading. The In and Ga BEPs used for the growth of the QD active regions are 2.1×10^{-7} torr and 3.2×10^{-8} torr, respectively. The growth conditions for a Mg-doped GaN layer used a Ga BEP of 3.1×10^{-7} torr, a Mg BEP of 1.86×10^{-9} torr, and a substrate temperature of 965 °C. It is noticed that the growth parameters are different from those mentioned above, due to the use of a different MBE reactor and different metal layers at the backside of sapphire substrates. Under these growth conditions in the Veeco GEN-II^{TM} MBE system, emission wavelength across nearly the entire visible spectral range can be realized for nanowires with diameter varying from ~ 200 nm to ~ 600 nm. Figure 4-10 (c) shows the SEM image of patterned Ti mask with nanohole sizes of ~ 150, 250, 350 and 550 nm. The lateral growth effect was also taken into account in the pattern design. Shown in Figure 4-10 (d) is a 30° tilted SEM image of InGaN/GaN nanowire arrays grown with four different diameters of ~ 220, 320, 420 and 630 nm. The nanowires have an average height ~ 650 nm, with near-perfect hexagonal morphology and smooth lateral surface, which can contribute to the enhanced light emission from the nanowire top surface.

Single Nanowires with these design parameters and operation wavelengths also exhibit nearly maximum light extraction efficiency, according to our numerical simulation. The light extraction efficiency of single nanowires has been investigated using finite-difference time-

domain (FDTD) numerical simulation. Structures of the single nanowires for the simulation include 440 nm *n*-GaN, 150 nm *p*-GaN layer and 60 nm InGaN/GaN QDs active region. The wavelengths of various color emission, including 450, 530, 630 and 660 nm were used in the simulation. The results show that the light extraction efficiency depends on the *n*-GaN length of the nanowire, the radius of the nanowire, and the wavelength. Single nanowires with their specific geometry offer unique guiding properties which can improve the light extraction efficiency [576, 577]. Single nanowires have the ability to guide light along its axis like a waveguide [578, 579]. Some portion of the light guided through the axis of a nanowire can be extracted from the top surface. The length of *n*-GaN is very critical to have constructive light interference with the reflected light at the nanowire/substrate interface. The reflection from substrate may vary as a function of the operating wavelength and the nanowire radius [580]. The Variations of light extraction efficiency of single nanowires was calculated as a function of nanowire radius for emission wavelengths of 450, 530, 630, and 660 nm, respectively. The calculated light extraction efficiency is 65%, 55%, 68%, and 36% for a single nanowire with diameter of 220 nm and emission wavelength of 660 nm, a single nanowire with diameter of 320 nm and emission wavelength of 630 nm, a single nanowire with diameter of 420 nm and emission wavelength of 530 nm, and a single nanowire with diameter of 630 nm and emission wavelength of 450 nm, respectively. By engineering the nanowire diameter and height, single nanowire LEDs can offer high light extraction efficiency.

Schematically shown in Figure 4-11 (a), multi-color single InGaN/GaN nanowire LEDs were subsequently fabricated on a single chip. First, a polyimide resist layer was spin-coated to fully cover the nanowires, followed by oxygen plasma etching to expose the top surface of nanowires, shown in Figure 4-10 (e). Nanoscale metal electrodes, consisting of Ni (7 nm)/Au (7 nm) metal layers were then deposited on the *p*-GaN top surface of individual nanowires using e-beam lithography and metallization techniques and then annealed at ~500 °C for 1 min

in nitrogen ambient. Subsequently, a 100-nm indium tin oxide (ITO) layer was deposited to serve as a transparent electrode. The complete devices with ITO contacts were annealed at 300 °C for 1 hour in vacuum. Contact metal grids consisting of Ni(20 nm)/Au(100 nm) were then deposited on the ITO to facilitate current injection. Subsequently, a Ti(20 nm)/Au(100 nm) *n*-metal contact was deposited on the *n*-type GaN template. Shown in Figure 4-11 (b) is the optical microscopy image of the single nanowire LED pixel devices after surface passivation and contact metallization.

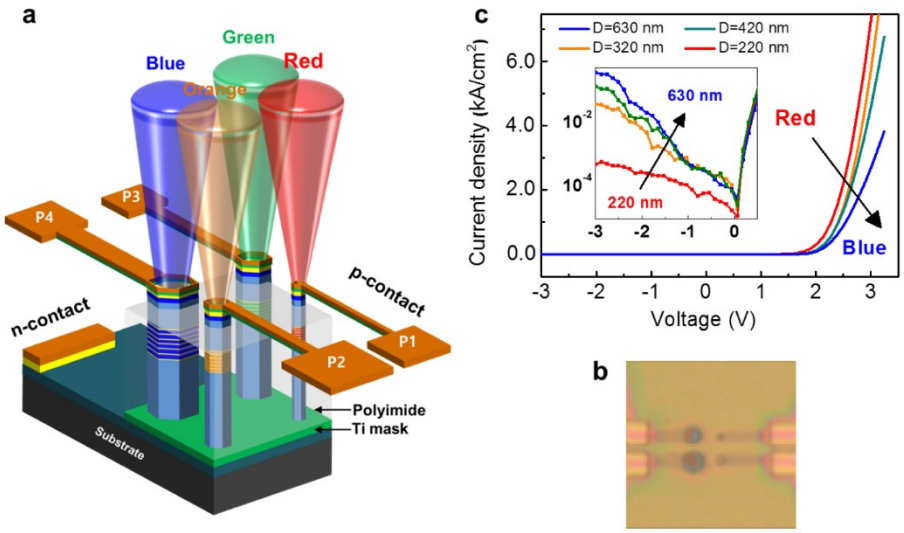

Figure 4-11: (a) Schematic illustration of monolithically integrated multi-color single nanowire LED pixels on a single chip. (b) Top-view optical microscopy image of the single nanowire LED pixel devices after surface passivation and contact metallization. (c) Current-voltage characteristics of single nanowire LEDs with different diameters. Inset: current density versus voltage in a semilog plot, showing increasing leakage current for nanowire LEDs with larger diameters.

4.10 The Performance Characteristics of Color-Tunable Single Nanowire Pixels

The performance characteristics of single InGaN/GaN QDs nanowire LEDs were measured under continuous-wave biasing conditions at room temperature. Figure 4-11 (c) shows representative current-voltage (I-V) curves of the blue (D ~ 630 nm), green (D ~ 420 nm), orange (D ~ 320 nm) and red (D ~ 220 nm) emitting devices, which exhibit excellent I-V

characteristics. The nanowire LEDs have turn-on voltages ~ 2 V, which is significantly better than previously reported ensemble nanowire LEDs and GaN-based planar devices [133, 581]. Current densities as high as 7 kA/cm^2 were measured at ~ 3 V. It is also noticed that higher current densities can be achieved in nanowire LEDs with smaller diameters. This is largely due to the enhanced dopant incorporation in smaller diameter nanowires and the resulting efficient current conduction [582, 583], as well as the more efficient heat dissipation [133]. The capacity for sustaining higher current densities with decreasing device area has also been reported previously [133, 584]. These results suggest that single nanowire optoelectronic and electronic devices can handle unusually large current densities and can deliver extremely high power density compared to conventional planar devices. It is also seen that the leakage current under reverse bias is relatively small, but increases with increasing nanowire diameter, shown in the inset of Figure 4-11 (c), which is likely due to the presence of defects in large diameter nanowires and the resulting current leakage. This observation is in reasonable agreement with previous reports [585, 586].

Such single nanowire LEDs also exhibit excellent light emission characteristics. The electroluminescence (EL) emission was collected using an optical fiber coupled to a high-resolution spectrometer and detected by a charge coupled device (CCD). Shown in Figure 4-12 (a) are the EL emission spectra of single nanowire LED subpixels with nanowire diameters of 220, 320, 420 and 630 nm, which exhibit peak emission wavelengths of 659, 625, 526 and 461 nm, respectively. The spectra were taken at an injection current of approximately 4.5 μA.

Light-current (L-I) characteristics of the red, orange, green, and blue single nanowire LED subpixels measured under nearly identical conditions are shown in Figure 4-12 (b). It is observed that the light intensity increases near-linearly with injection current for different nanowire LEDs. Stronger light intensity was measured from nanowires with larger diameters under the same injection current density, due to the larger active region area. On the other hand,

nanowire LED subpixels with smaller nanowire diameter can handle higher current density, due to the more efficient current conduction and heat dissipation. Shown in the inset of Figure 4-12 (b) are the EL spectra of the green-emitting nanowire LED subpixel. There is no significant shift in the emission peak position with increasing injection current, suggesting a very small level of quantum confined Stark effect, due to the highly efficient strain relaxation of nanowire structures.

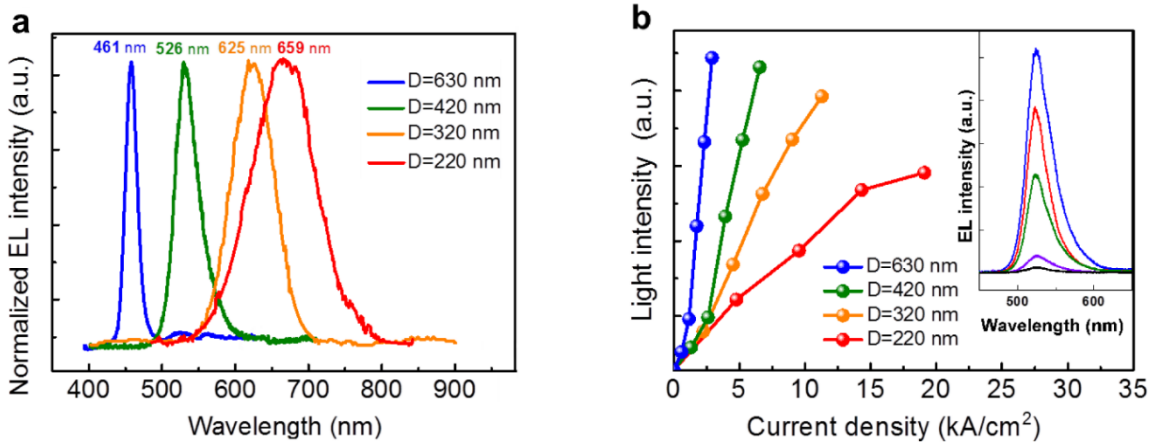

Figure 4-12: (a) Electroluminescence (EL) spectra of single nanowire LEDs with different nanowire diameters. (b) Light-current characteristics of single nanowire LED devices with different diameters. The inset shows the EL spectra measured under different injection current densities (1.3 to 6.5 kA/cm^2) for the green-emitting nanowire LED device.

With the incorporation of *p*-AlGaN electron blocking layer and core-shell schemes, the performance of single InGaN/GaN nanowire LEDs can be further improved by reducing nonradiative surface recombination and carrier leakage and overflow [254, 581, 587-589].

4.11 Summary

The Ti-mask selective area epitaxy of multi-color nanowire arrays on GaN/sapphire substrates have been studied, with the goal to achieve micro-scale and nano-scale color-tunable LED pixels. In this process, a thin (~ 10 nm) Ti layer was utilized as the mask, and nanoscale growth patterns were defined by using EBL and treated with nitridation prior to the growth of nanowires. By controlling the nanohole diameter and array periodicity, full-color emissions

have been realized from InGaN/GaN nanowire arrays on the same substrate. It was observed that, with the same spacing between grown nanowires, the peak emission wavelength of nanowire array shows a redshift with increasing nanowire diameter. A consistent redshift with decreasing nanowire spacing was observed due to the reduced Ga incorporation related to the beam shadowing effect. The results of redshift with increasing nanowire diameter has been justified repeatedly by many MBE growths. Multi-color LED subpixels of 2.8×2.8 μm^2 have been monolithically fabricated on the same sapphire wafer, enabling color-tunable light mixing. The first demonstration of full-color, single InGaN nanowires monolithically integrated on the same chip is reported. Compared to conventional planar devices, such nanowire LED pixels offer several distinct advantages, including significantly reduced dislocations and polarization fields, enhanced light extraction efficiency, controllable radiation pattern, tunable emission, and extremely efficient current conduction and heat dissipation. This work offers a new avenue for achieving multi-color photonic devices at the single nanowire level on a single chip for a broad range of applications, including ultra-fine imaging and projection display, projection displays, sensing, spectroscopy, medical diagnostics and communications.

Chapter 5: Full-Color AlInGaN Quaternary Nanowire Light Emitting Diodes with Spontaneous Core-Shell Structures on Si

5.1 Introduction

To date, InGaN-based nanowire heterostructures have been intensively studied for applications in phosphor-free solid-state lighting and full-color display. The performance of such devices, however, suffers severely from nonradiative surface recombination, which leads to extremely short carrier lifetime (~ 0.2 ns, or less) [254] and has been identified as the major cause for the low quantum efficiency and the very low output power (nW to μW) of nanowire LEDs. Such poor carrier dynamics also represent one major challenge in improving the performance of various nanowire optoelectronic devices including LEDs, lasers, solar cells, and photodetectors. In this regard, a new nanowire heterostructures have been developed, with the use of spontaneous core-shell structures that can suppress nonradiative surface recombination to achieve large area, efficient, full-color nanowire LEDs. The emission wavelengths can be tuned from ~ 430 nm to ~ 630 nm by varying the growth conditions.

In this context, taking advantages of the diffusion-controlled MBE growth of catalyst-free III-nitride nanowires, we have developed AlInGaN core-shell quaternary nanowire heterostructures, wherein an In-rich core and an Al-rich shell were spontaneously formed during the growth process. By varying the growth conditions, the emission wavelengths can be tuned across nearly the entire visible spectral range. The spontaneous formation of a relatively thick (~ 18.5 nm) AlGaN shell was demonstrated in a simple *p-i-n* axial nanowire LED heterostructure. The carrier lifetime can be enhanced from ~ 0.2 ns to 2 ns, due to the suppression of nonradiative surface recombination. The output power exceeds 30 mW for a single ~ 1×1 mm^2 non-packaged LED device under pulsed biasing conditions. The direct correlation between the output power, carrier lifetime, and shell thickness is also identified.

5.2 Growth and PL of Full-Color AlInGaN Core-Shell Nanowires

In this study, catalyst-free AlInGaN core-shell nanowire LED heterostructures were grown on Si(111) substrates by using a Veeco GEN-II™ *radio frequency plasma-assisted* MBE system under nitrogen-rich conditions [100, 120, 590]. Schematically shown in the inset of Figure 5-1(a), the AlInGaN nanowire LED heterostructure consists of ~ 200 nm GaN:Si, 70 nm AlInGaN, and 150 nm GaN:Mg segments. During the growth, the nitrogen flow rate was kept at 1 standard cubic centimeter per minute (SCCM), with a forward power of 350 W. The GaN:Si and GaN:Mg segments were grown at ~ 770 °C. For the AlInGaN active region, the substrate temperature was varied in the range of 610-700 °C. Also during the active region growth, the Ga beam equivalent pressure (BEP) was kept at 4.5×10^{-8} Torr, while the In BEP and Al BEP was varied from 1.2×10^{-7} to 2.6×10^{-7} Torr and from 1.7×10^{-9} to 1.3×10^{-8} Torr, respectively.

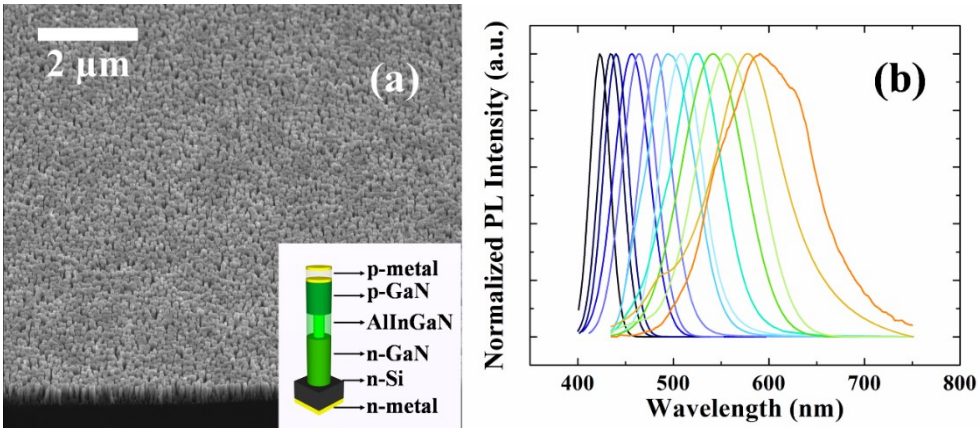

Figure 5-1: (a) Bird's-eye-view SEM image of AlInGaN core-shell nanowire arrays grown on Si substrate. (b) Normalized PL spectra of AlInGaN core-shell nanowires under different growth conditions. The schematic of such a nanowire LED is shown in the inset of (a).

Under these growth conditions, the photoluminescence (PL) emission wavelengths of AlInGaN quaternary nanowire structures can be continuously varied across nearly the entire visible spectral range, from ~ 410 nm to 630 nm, shown in Figure 5-1 (b). Moreover, through extensive studies and variations in the growth conditions, it was also found that the Al-rich shell thickness of AlInGaN quaternary nanowire heterostructures can be controllably varied

(described later), allowing for the direct correlation with the carrier dynamics and device performance.

Table 5-1: Growth conditions and characterization results for representative AlInGaN segments.

Sample	BEP_{Al} ($\times 10^{-9}$ Torr)	BEP_{In} ($\times 10^{-7}$ Torr)	T_{sample} (°C)	*Wavelength* (nm)	τ (ns)
A	3.54	1.25	625	515	0.35
B	5.70	1.38	635	515	0.96
C	10.7	2.06	670	495	1.86

Shown in Figure 5-1(a) is a bird's-eye-view SEM image of AlInGaN core-shell nanowires, which are vertically aligned on Si substrate. The nanowires exhibit a high degree of size uniformity, with the top sizes in the range of ~ 70 to 80 nm. In what follows, we describe the carrier dynamics and structural properties of three representative nanowire LED, including Samples A, B, and C, with peak emission wavelengths of 495-515 nm. The corresponding growth conditions and optical characterization results are described in Table 5-1. Growth temperatures of 625 °C, 635 °C and 670 °C were used for the active regions of Samples A, B, and C, respectively. Compared to Sample A, the Al BEP of Sample B was increased from 3.54×10^{-9} to 5.70×10^{-9} Torr. Relatively higher In and Al flux was utilized for Sample C in order to achieve enhanced shell coverage.

5.3 Carrier Dynamics of AlInGaN Core-Shell Nanowire Heterostructures

Time-resolved PL measurements were performed to study the carrier dynamics of AlInGaN core-shell nanowire heterostructures. A pulsed 375 nm diode laser with a 100 MHz repetition rate was employed as the excitation source, which was focused on the sample surface through a 50× objective lens. The signal was detected by a photon counter (TBX picosecond

detection module) with the use of a long pass filter (> 400 nm). The carrier life time τ was then derived by a standard stretched exponential model,

$$I(t) = I(0)e^{-(\frac{t}{\tau})^n} \qquad \text{Equation 5-1,}$$

where I(t) is the PL intensity as a function of time, and n is the stretching parameter [534, 591, 592]. Shown in Figure 5-2 is the representative curves measured for samples A, B, and C, with the derived carrier lifetimes ~ 0.35 ns, 0.96 ns, and 1.86 ns, respectively. The measured carrier lifetimes of AlInGaN LED heterostructures vary dramatically depending on the growth conditions.

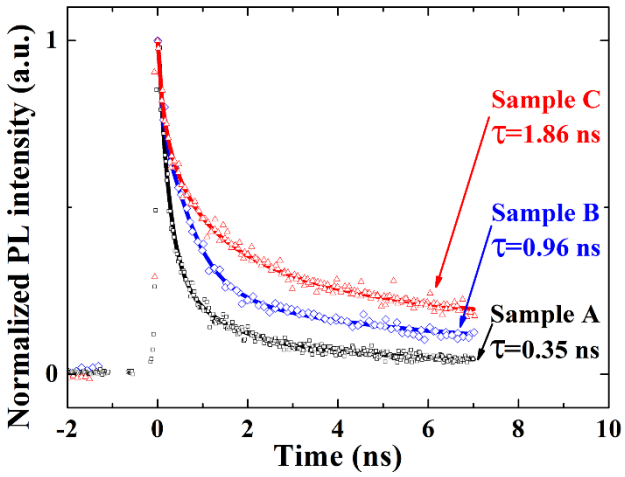

Figure 5-2: Time-resolved PL emission of three representative AlInGaN core-shell nanowire LED heterostructures, exhibiting carrier lifetime of 0.35 ns, 0.96 ns and 1.86 ns. The dot-like symbols are experimental data; and the solid curves are derived from experimental data by using the standard stretched exponential model.

For comparison, the carrier lifetime of a typical InGaN/GaN nanowire LED structure without the incorporation of any Al was measured to be in the range of 0.2 ns, dominated by nonradiative surface recombination (see Supplementary Information of the reference of [254]). The carrier lifetime of such InGaN/GaN nanowire LED structure was enhanced to ~ 0.4 ns by adding an AlGaN shell [254], consistent with the present study. It is worthwhile mentioning that the carrier lifetime remained nearly invariant when the excitation power was changed by over two orders of magnitude in the present study.

5.4 The Nature and Growth Mechanism of Spontaneous Core-Shell Structures

In order to further identify the correlation between the carrier dynamics of AlInGaN nanowire LED heterostructures and the associated growth conditions, we have performed extensive structural characterization by scanning transmission electron microscope (STEM). The high-angle annular dark-field (HAADF) atomic-number contrast image of a nanowire from Sample C (carrier lifetime ~ 1.86 ns) is shown in Figure 5-3 (a). The HAADF image shows bright contrast at the center and dark contrast at the sidewall of the AlInGaN segment, indicating the formation of a core-shell structure.

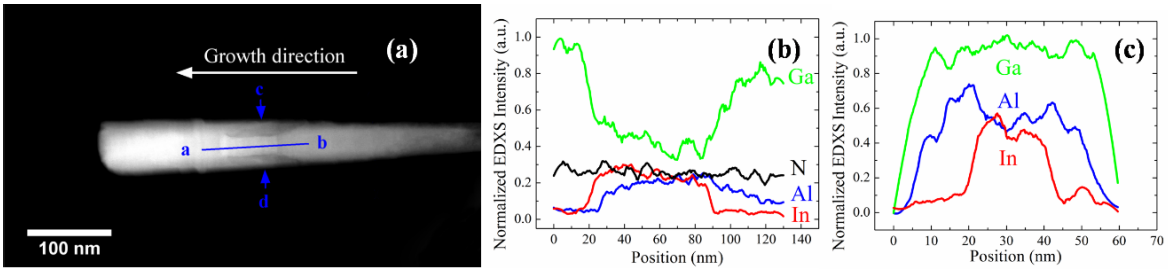

Figure 5-3: (a) An HAADF-STEM image for the AlInGaN core-shell LED nanowire (shell thickness: ~ 18.5 nm) with a peak emission of 495 nm and carrier lifetime of 1.86 ns. Elemental profiles derived from EDXS line scanning analysis (b) along a-b (axial direction) and (c) along c-d (radial direction) as indicated in (a), respectively, showing a core-shell structure.

The energy dispersive x-ray spectrometry (EDXS) analysis is shown in Figures 5-3 (b) and 5-3 (c). The elemental profiles along the axial direction (line a-b in Figure 5-3 (a)) present clearly one AlInGaN segment in the middle region and two GaN segments in the top and bottom regions of the nanowire, shown in Figures 5-3 (b). The tail of Al profile (position: 90-130 nm) is originated from the direct impingement and diffusion of Al atoms at the sidewall of the bottom GaN:Si segment during the growth of AlInGaN active region. Shown in Figure 5-3 (c) is the EDXS line-scan analysis along the lateral dimension of the nanowire active region (line c-d in Figure 5-3 (a)). The Al and Ga signals extend over a much wider range than that of In signal, providing unambiguous evidence that an AlGaN shell is formed surrounding an In-rich core region. The AlGaN shell thickness is estimated to be ~ 18.5 nm.

Similar STEM studies including HAADF and EDXS analysis were also conducted on other nanowire samples. The EDXS elemental profile along the radial direction of AlInGaN core-shell nanowires exhibiting wavelength emission of 515 nm and carrier lifetimes of 0.35 ns, 0.63 ns and 0.96 ns are shown in Figures 5-4 (a), 5-4 (b) and 5-4 (c), respectively. As observed in Figure 5-3 (c) and Figures 5-4, Ga signal remains constant over the core and shell regions, and the concentration of In is high in the core and then decreases towards the lateral surfaces. Shown in Figures 5-3 (c), 5-4 (b) and 5-4 (c), there is very little In content in the sidewall regions. By contrast, it is seen in Figure 5-4 (a) that In is present in the region close to sidewall. Different from the nanowires with carrier lifetime of 0.63 ns shown in Figure 5-4 (b), the Al signal of the nanowire of 0.96 ns shown in Figure 5-4 (c) was drastically reduced in the core region accompanied by two sharp bumps in the shell regions, and hence its Al-rich shells were thicker. The radial carrier confinement benefits from such radial elemental profiles shown in Figure 5-4 (c). This explains the increased carrier lifetime. As such, a direct correlation between the formation of an Al-rich shell structure and the carrier lifetime can be identified. For example, for Sample A shown in Figure 5-4 (a), a small Al-rich shell was formed, due to the use of very low Al flux. Accordingly, the carrier lifetime for this sample was measured to be ~ 0.35 ns, limited by nonradiative surface recombination. The AlGaN shell thicknesses were estimated to be ~ 13 nm for Sample B, shown in Figure 5-4 (b), which leads to enhanced carrier lifetime ~ 0.96 ns, due to the reduced nonradiative surface recombination. The extensive structural and optical characterizations of AlInGaN nanowire heterostructures confirmed that the carrier lifetime increased with increasing AlGaN shell thickness. It is also worthwhile mentioning some additional advantages of the AlInGaN core-shell nanowire LEDs. The incorporation of Al in the active region can effectively reduce the strain and the associated defect formation. Moreover, the use of relatively thick active regions (~ 70 nm) can

significantly reduce the carrier density under high power operation, thereby minimizing nonradiative Auger recombination and hot carrier effect under high power operation.

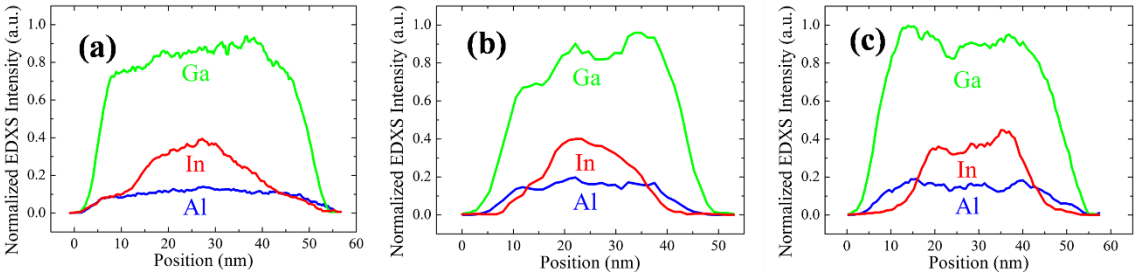

Figure 5-4: (a) Elemental profiles derived from EDXS line scanning analysis along the radial direction of 515 nm emission AlInGaN nanowires with carrier lifetime of (a) 0.35 ns (shell thickness: ~ 3 nm), (b) 0.63 ns (shell thickness: ~ 9 nm), and (c) 0.96 ns (shell thickness: ~ 13 nm), respectively.

The spontaneous formation of core-shell nanowire structures can be explained by the differences in the diffusion and desorption processes of In, Ga, and Al adatoms during the growth of the AlInGaN segment. At elevated growth temperatures, In atoms experience much stronger desorption compared to Ga and Al atoms on the nanowire lateral surfaces. The desorbed In atoms cannot be immediately compensated by impingent atoms, due to the shadowing effect of neighboring nanowires. As a consequence, an Al-rich shell is formed surrounding an In-rich core region. The spontaneous formation of core-shell structure and enhanced carrier lifetime have been measured repeatedly in many AlInGaN nanowire samples. It is also evident that properties of the core-shell structures can be controlled by varying the substrate temperature, in addition to the group III/N flux ratios, since the sticking and diffusion coefficients of atoms are very sensitive to the substrate temperature [383, 593].

5.5 The Correlation Between Output Power, Carrier Lifetime and Shell Thickness

In order to examine the impact of Al-rich shell structure on the device performance, we have fabricated and characterized large area AlInGaN nanowire LEDs with sizes in the range from ~ 0.3×0.3 mm^2 to ~ 1×1 mm^2. The device fabrication process involves the use of polyimide surface passivation and planarization, standard photolithography and contact

metallization techniques. Shown in the inset of Figure 5-1 (a), *p*- and *n*-contacts were deposited on GaN:Mg and the backside of the Si substrate, respectively. Output characteristics of ~ 1×1 mm^2 AlInGaN core-shell LEDs were measured under various injection currents under pulsed biasing conditions (1% duty cycle) to minimize junction heating effect. Shown in Figure 5-5 (a) is a representative I-V curve of AlInGaN core-shell nanowire LEDs, which exhibit excellent current-voltage characteristics. The measured electroluminescence (EL) spectra of various AlInGaN nanowire LEDs are shown in Figure 5-5 (b). Tunable emissions from ~ 430 to ~ 630 nm can be readily achieved. Variations of the output power versus injection current density for a few representative LED structures are further shown in Figure 5-5 (c). It is seen that significantly higher output power can be achieved for nanowire LEDs with longer carrier lifetime, due to the suppression of nonradiative surface recombination. Under an injection current density of 100 A/cm^2, an output power of > 30 mW was measured for Sample C, which is significantly higher than that of previously reported axial InGaN nanowire LEDs [252, 254, 593, 594].

Variations of the measured output power at an injection current density of 90 A/cm^2 versus carrier lifetime are further summarized in Figure 5-5 (d) for LEDs operating in the blue-green wavelength range (~ 480-530 nm). It is seen that the output power increases dramatically with carrier lifetime, which is also consistent with recent reports on AlGaN/InGaN dot-in-a-wire LEDs [252, 254]. Such studies provide unambiguous evidence that robust core-shell structures are essentially required in order to suppress any nonradiative surface recombination and to achieve high power operation for axial nanowire devices. The direct correlation between carrier lifetime and device performance also rules out the possibility that the enhanced carrier lifetime is caused by the quantum-confined Stark effect (QCSE) with increasing Al incorporation, since QCSE generally leads to reduced radiative recombination and output power.

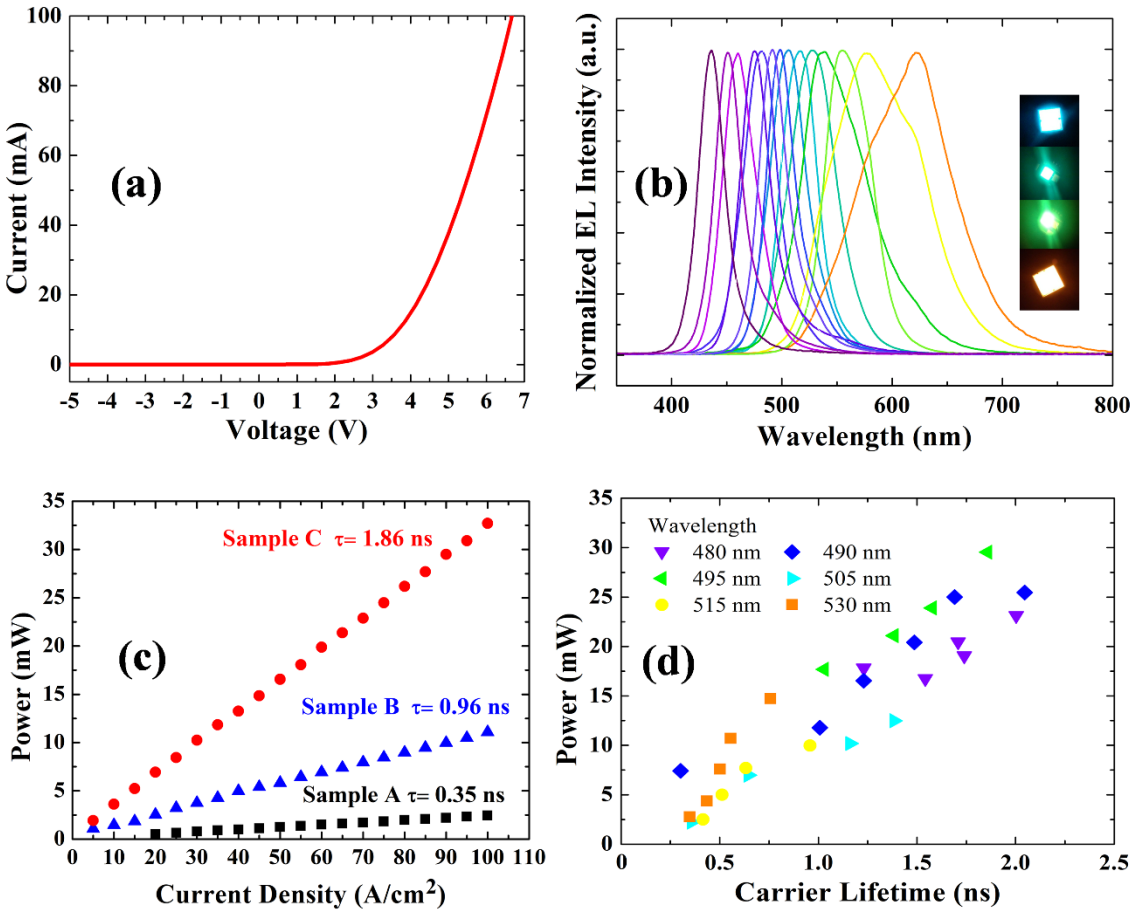

Figure 5-5: (a) Current-voltage characteristics of a representative AlInGaN nanowire LED on Si. (b) Normalized EL spectra of AlInGaN core-shell nanowires LEDs grown under different conditions. The EL images are shown in the inset of (b). (c) Light output power of AlInGaN LEDs versus injection current. The device area is ~ 1×1 mm^2. The measurements were performed under pulsed biasing conditions (1% duty cycle) at 2 °C. The measured carrier lifetime is also shown in the figure. (d) Variations of the output power of AlInGaN core-shell nanowires LEDs measured under injection current of 90 A/cm^2 versus carrier lifetime of the nanowire heterostructure.

The wavelength, carrier lifetime, shell thickness and light output power of representative AlInGaN nanowires in relatively longer wavelength range are summarized in Table 5-2. In the wavelength range from ~ 560 nm to ~ 630 nm, reduced shell thicknesses were measured, due to the usage of low Al BEP in the range of 1.77×10^{-9}-2.45×10^{-9} Torr during the AlInGaN growth. The output power was measured at injection currents of 40 A/cm^2 under pulsed biasing conditions (1% duty cycle). Compared to the output power of AlInGaN nanowire in the blue-

green wavelength range (430-530 nm), the output power decreased in the longer wavelength range, especially in the orange and red range. Such a reduction of power output is mainly due to the increased surface recombination, indicated by shorter carrier lifetimes measured in the longer wavelength range. The carrier lifetimes of AlInGaN nanowires were ~ 0.6-0.8 ns in the green range (~ 530-570 nm) and ~ 0.3-0.5 ns in the yellow, orange and red range (~ 580-630 nm), respectively.

Table 5-2: Characterization results of representative AlInGaN nanowires in the relatively longer wavelength range.

Symbol	*Wavelength* (nm)	τ (ns)	*Shell thickness*	*Output power* (40 A/cm^2)
C	560 nm	0.8	~ 11 nm	5.8 mW
D	585 nm	0.5	~ 4 nm	0.7 mW
E	630 nm	0.3	< 3 nm	0.4 mW

5.6 The Approach for Broad Emission Using AlInGaN Nanowires

Shown in Figures 5-6 (a) and 5-6 (b), broad PL and EL emissions have been achieved by varying the growth temperature during the growth of AlInGaN segments. For example, a single EL spectrum covering blue and green range (459-551 nm) was achieved by using the growth temperature gradient of 2.2 °C/min during the growth of this AlInGaN segment. In other words, in the 30 min growth duration of AlInGaN segment, the growth temperature at the beginning of AlInGaN segment was 66 °C lower than that at the end of AlInGaN segment. For the results presented above, all of the AlInGaN nanowires were grown at a constant temperature during the growth of AlInGaN segment. However, as shown in Figures 5-6, by taking advantages of growth temperature and compositional variations, spectral linewidths up to ~ 100 nm have been achieved across almost the entire visible region. More important, core-shell structures were

observed across the entire AlInGaN segments in such AlInGaN nanowires. The variations of Al, Ga and In flux ratio during the growth is expected to further increase the linewidth.

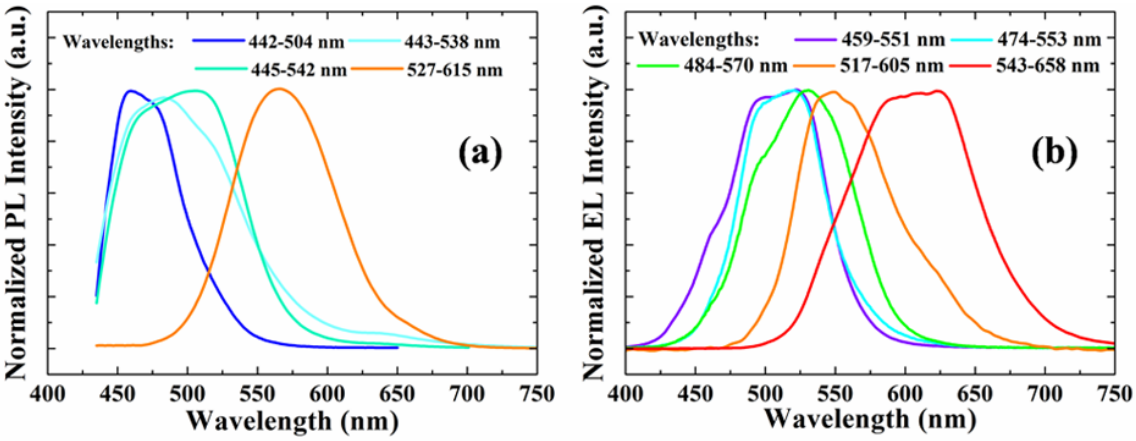

Figure 5-6: (a) Normalized PL spectra and (b) normalized EL spectra of representative AlInGaN core-shell nanowires LEDs. The linewidths of such broad spectra are presented by using wavelengths at the half maximum of peak intensity, shown in (a) and (b).

5.7 Summary

In summary, we have demonstrated full-color AlInGaN core-shell quaternary nanowire LEDs grown directly on Si. The nature and growth mechanism of AlInGaN core-shell nanowire heterostructures were further revealed through detailed STEM measurements. The spontaneous formation of an In-rich core and Al-rich shell structure establishes a radial carrier confinement which can suppress nonradiative surface recombination, leading to enhanced carrier lifetime and significantly increased output power.

Chapter 6: Selective-Area Epitaxy of GaN Nanowires on Si Substrate and Their Device Characteristics

6.1 Introduction and Preview

It is highly desirable to develop precisely-controlled GaN-based nanowires on Si substrate using selective area epitaxy for various device applications such as vertical GaN-based nanowire field effect transistors (FETs) using wrap-around gate [344] and InGaN/Si integrated double-junction solar cells. However, the current selective area epitaxy on Si substrate rely on the use of thick semiconducting buffer layers with large bandgap [404, 517-519, 522] and the electrical and thermal advantages of Si substrates cannot be used for nanowire devices. Without using thick buffer layers, the reported nanowires grown on patterned Si substrates cannot maintain the quality of selective area epitaxy [98, 402, 523].

In this chapter, uniform GaN-based nanowire arrays have been demonstrated on Si substrate using Ti-mask selective area epitaxy without the loss of the electrical and thermal advantages of Si substrate. Taking advantages of ultra-thin AlN and GaN:Ge buffer layers, the grown nanowires exhibit precisely controlled nanowire size and position on Si substrate, maintaining the quality of selective area epitaxy as well as the advantages of Si substrate including high electrical conductivity and high thermal dissipation. The relatively high electrical conductivity of ultra-thin AlN buffer layer on Si substrate has been demonstrated by the improved output characteristics of Si solar cell (with a p^+-Si/n-Si tunnel junction) deposited with an ultra-thin AlN buffer layer. The high electrical conductivity of ultra-thin AlN/GaN:Ge buffer template and the advantages of selective-area grown *n*-GaN nanowire array on Si substrates have been further justified by photoelectrochemical (PEC) hydrogen production using *n*-GaN nanowire array photoanode and the associated PEC characteristics.

Using the selective area epitaxy technique on Si substrate with ultra-thin AlN/GaN:Ge buffer template, a current density up to 4.65 MA/cm^2 has been achieved from a single *n*-*i*-*n*-n^+

GaN nanowire vertically-aligned on Si substrate, promising the scale-up of vertical GaN-based nanowire electronic devices on Si substrates. For the first time, high electrical conduction has been achieved from single GaN nanowire devices selective-area grown on Si substrate which has various advantages such as large area, low cost, high thermal conductivity and high electrical conductivity. The electrical characteristics and device failure of single GaN nanowire were investigated in previous work [595, 596]. However, those works involved transfer and horizontal suspension of single nanowires between lateral metal electrodes, which was not a trivial process and required much manipulation efforts. The electrical characteristics of suspended single *n*-GaN nanowires has been measured by direct electrical nanoprobing using tungsten nanoprobes [597]. Meanwhile, high contact resistance existing in previous work [595, 596] has resulted in relatively low maximum tolerable current density and relatively low maximum tolerable electrical field which were measured when the device failure occurred. The considerable contact resistance has hindered the precise characterizations of GaN nanowires. In addition, with high contact resistance, the electrical characteristics of single GaN nanowire devices cannot be further improved. Benefiting from the flexibility in varying the diameter of single GaN nanowires selective-area grown on the same Si substrate, the dependence of electrical characteristics (maximum tolerable voltage and current density) on nanowire diameter has been systematically investigated by using two-point electrical nanoprobing in a SEM chamber. In order to reduce the contact resistance between GaN nanowire and metal contact, n^+-GaN layer was grown as the top segment of *n*-*i*-*n*-n^+ GaN single nanowires, and the dependence of the electrical characteristics on the Si doping concentration of n^+-GaN layer has been investigated. Through the optimization of the Si doping concentration in n^+-GaN layer, high current density up to 4.65 MA/cm^2 has been achieved.

The achievements reported in this chapter promise monolithic III-nitride/Si integrated multijunction solar cells and III-nitride/Si integrated chips vertically integrating multiple GaN nanowires electronic devices which are precisely controlled in size and electrical characteristics.

6.2 Selective Area Epitaxy of GaN Nanowires Using Ultra-Thin Buffer Layers

Prior to the preparation of Ti mask and selective area epitaxy, III-nitride buffer layers were deposited on Si substrates. In order to make the resistance of the buffer layers negligible, the thickness of AlN buffer layer was reduced to few nm. After cleaning *n*-Si wafers by using acetone, isopropyl alcohol (IPA) and deionized (DI) water, the *n*-Si wafers were dipped in buffered oxide etchant (BOE) for 2 min. AlN and/or GaN:Ge buffer layers were grown on *n*-Si wafers by *radio frequency plasma-assisted* MBE (Veeco, GEN II^{TM}). By using e-beam evaporation, a thin Ti layer (10 nm) was then deposited on top of buffer layer as the mask layer. A PMMA e-beam resist layer was then spin-coated onto the Ti mask layer, and the nanohole patterns was defined into PMMA layer using e-beam lithography (MIRA3 XMH equipped with a Schottky field emission electron gun). To transfer the nanohole patterns from PMMA to Ti layer, the exposed Ti material was etched down to buffer layer using CHF_3 in a reactive ion etching (RIE) chamber. After that, the PMMA resist was removed from the surface by using a two-step process including O_2 RIE and a solvent clean using NMP based removers (Remover 1165). The patterned substrates underwent a final clean using concentrated hydrogen chloride (HCl, 37%) before being loaded into the MBE chamber for nanowire growth.

On the patterned Si substrates, GaN nanowire arrays were selectively grown in the MBE system (Veeco, GenXplor^{TM}) with *radio frequency* N_2 plasma source. Prior to the nanowire epitaxy, the nitridation of Ti mask layer was carried out in the growth chamber at 400 °C for 10 min. To achieve good epitaxy selectivity as well as acceptable growth rate, various growth parameters have been used to grow Si-doped *n*-GaN on the patterned Si substrates. The growth conditions for Si-doped *n*-GaN included a growth temperature in the range from 860 °C to

890 °C, a N_2 flow rate in the range from 0.33 sccm to 0.75 sccm, a forward plasma power in the range from 350 W to 380 W, a Ga beam equivalent pressure (BEP) of 2.35×10^{-7} Torr and Si Knudsen effusion cell temperature of 1175 °C which corresponding to a Si doping concentration estimated to be 1.43×10^{19} cm^{-3}.

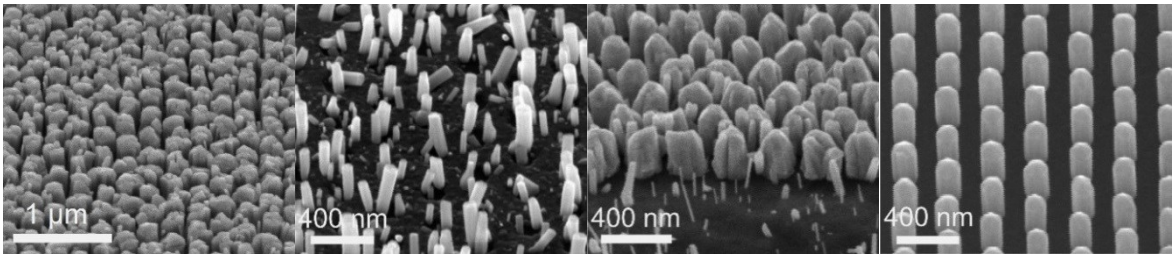

(a) (b) (c) (d)

Figure 6-1: Bird's-eye-view SEM images of GaN nanowire array selective-area grown using a similar growth condition on nanohole-array patterned Si substrates (a) without using any buffer layers, or with (b) an ultra-thin AlN buffer layer, (c) an ultra-thin GaN:Ge buffer layer and (d) ultra-thin AlN/GaN:Ge buffer template.

To search the buffer layers suitable for selective area epitaxy on Si substrates, the effects of different ultra-thin buffer layers on the morphology of GaN nanowires have been investigated. As shown in Figures 6-1 (b), (c) and (d), the morphology of selective-area grown nanowire varies significantly on different buffer layers (a single AlN layer, a single GaN:Ge layer, or AlN/GaN:Ge template). Without any buffer layers, multiple GaN nanowires grow within one nanohole and coalesce, as shown in Figure 6-1 (a). With a single AlN buffer layer, two or three nanowires grow within one nanohole but there is no coalescence, as shown in Figure 6-1 (b). It can be observed in Figure 6-1 (b) that the nanohole is filled partially and the nucleation occurs at the edge of nanohole pattern with a AlN buffer layer. With a single GaN:Ge buffer layer, multiple nanowires grow within one nanohole and merge into a large nanowire. With AlN/GaN:Ge buffer template, uniform GaN nanowires are aligned vertically on Si substrate and exhibit smooth surfaces. Patterned Si substrates with AlN/GaN:Ge buffer

layers are used for subsequent selective area epitaxy of GaN nanowires and their device applications.

Both AlN and GaN:Ge buffer layers are required for the selective area epitxy of GaN-based nanowires on Si substrates. AlN has been widely adopted as the seed layer for subsequent GaN or InGaN hetroepitaxy on Si substrate due to its good thermal and chemical stability with Si substrate, benefiting from a much smaller thermal expansion coefficient and well-suppressed interfacial reactions compared to GaN buffer layer [598-601]. There were experiments [404, 517-519] reporting that the quality and properties of grown GaN nanowire arrays are closely correlated to the crystal orientations and morphology of AlN seeding layers. Subsequently, an ultra-thin GaN:Ge layer was grown on top of the ultra-thin AlN layer. The adding of GaN:Ge layer into the buffer template is necessary for the subsequent nanowire epitaxy, due to the following reasons: I) planarization of the surface, II) protection of AlN surface in the fabrication process of Ti-mask including thermal preclean, the removal of photoresist and oxide interlayers, III) presence as a homoepitaxial buffer layer for the GaN:Si nanowire epitaxy [602].

6.3 High Electrical Conductivity of Ultra-Thin Buffer Template on Si Substrates

To make the AlN layer conductive, the method of filling the vias in AlN layer with highly conductive n-AlGaN has been used to create conductive paths through grain boundary in the AlN layer [507, 603, 604]. In the AlN/GaN:Ge buffer template, the ultra-thin AlN layer contain large amounts of grain boundaries, pits and voids. The subsequently grown GaN:Ge fill in those structural vacancies, facilitating carrier transport through the AlN/GaN:Ge buffer template. Benefiting from carrier transport through vacancies filled with GaN:Ge together with carrier tunneling mechanism through the ultra-thin AlN, the ultra-thin AlN/GaN:Ge buffer template exhibited a good electrical conductivity.

Using nanoprobes in SEM chambers, the resistances of a single Si substrate and a Si substrate deposited with ultra-thin AlN/GaN:Ge buffer template were both measured and their

resistances were almost same. This comparisive measurement indicates that the resistance of ultra-thin AlN/GaN:Ge buffer template is negligible. The top-view SEM image shown in Figure 6-2 (a) illustrates the resistance measurement conducted on Si substrate. Pt-coated tungsten nanoprobes (ST-20-0.5, GGB Industries) were used. By probing on the AlN/GaN:Ge buffer template and the double-side Cu tape attached at the backside of *n*-Si substrate, the resistance was measured. The Si substrate was deposited with Ti/Au metal layers at the backside, and Ag conductive epoxy was used to connect Ti/Au metal layers and Cu tape. A four-probe piezoelectric nanomanipulator (LF- 2000, Toronto Nano Instrumentation, TNI) which was employed for driving conductive nanoprobes for sample probing, is shown in Figure 6-2 (b).

(a) (b)

Figure 6-2: (a) Top-view SEM image illustrating resistance measurement conducted on Si substrate deposited with ultra-thin AlN/GaN:Ge buffer template. (b) Bird's-eye-view image showing a four-probe piezoelectric nanomanipulator (LF-2000, Toronto Nano Instrumentation, TNI) and a sample of single GaN nanowire devices on Si substrate.

The high electrical conductivity of ultra-thin AlN layer has been further demonstrated through the growth of ultra-thin AlN layer on Si solar cell with a p^+-Si/n-Si tunnel junction [307] and the photovoltaic characterizations of resulting Si solar cells.

The effects of different growth parameters of ultra-thin AlN layers on the output parameters of Si solar cell with a p^+-Si/*n*-Si tunnel junction has been invesitgated. The Si solar cell was prepared by thermal annealing of liquid boron dopant precursor and liquid phosphorous dopant precursor coated on the two surfaces of double-side-polished *n*-Si wafers

using the standard thermal diffusion process for the conversions to p^+-Si and n^+-Si layers, respectively. Subsequently, liquid phosphorous dopant precursor was spin-coated on the surface of p^+-Si and underwent rapid thermal annealing to form few nanometers *n*-Si layer at the top of p^+-Si layer. The as-fabricated Si solar cell is denoted as Sample I. The Si solar cell wafer with the tunnel junction were loaded into MBE system (Veeco, GEN II^{TM}) for the growth of AlN layers. The ultra-thin AlN layers were grown on the surface of p^+-Si/*n*-Si tunnel junction layer using various growth parameters, and growth parameters of two representative samples Sample II and Sample III are presented in Table 6-1. To avoid the formation of SiN_x between the Si surface and grown AlN layer, few Al monolayers were grown on p^+-Si/*n*-Si tunnel junction layer prior to excitation of N_2 plasma in the MBE chamber.

Table 6-1: Output characteristics of Si solar cells with a p^+-Si/n-Si tunnel junction and associated growth parameters for ultra-thin AlN layers.

Sample	BEP_{Al} ($\times 10^{-8}$ Torr)	T_{growth} (°C)	J_{sc} (mA/cm^2)	V_{oc} (V)	η (%)	FF (%)
I	No AlN	No AlN	26.12	0.544	7.28	51.2
II	5.46	750	28.24	0.557	9.77	62.1
III	3.18	810	31.61	0.561	11.59	65.2

Sample I, Sample II and Sample III were fabricated as the following procedures. Firstly, Ti (20 nm)/Au (100 nm) metal layers was deposited on the backside of n^+-Si layer as bottom metal-contact. Ti (20 nm)/Au (100 nm) metal grid patterns were then deposited onto AlN buffer layer grown on p^+-Si/*n*-Si tunnel junction as top metal contact by using standard photolithography and e-beam evaporation, followed by a rapid thermal annealing at ~ 550 °C in N_2 gas ambient for 1 min. In Sample II and Sample III, the top metal grid patterns fill into the grain boundaries, pits and voids in the ultra-thin AlN layer, facilitating good carrier transport properties through those vacancies filled with metal. The ultra-thin AlN layer exhibited a good electrical conduction.

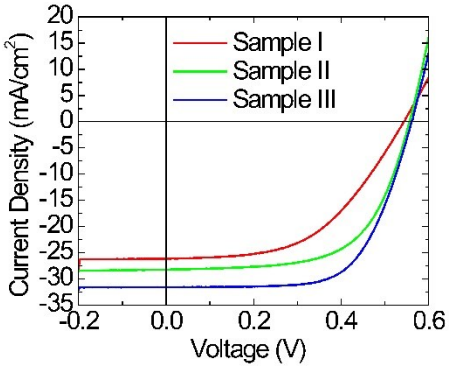

Figure 6-3: Current-voltage characteristics of Si solar cells with a Si tunnel junction. Sample I is as-fabricated Si solar cell, Sample II and Sample III are Si solar cell with an ultra-thin AlN layer grown using different parameters corresponding to Table 6-1.

Current-voltage characteristics and output parameters of Sample I, Sample II and Sample III under the illumination of 100 mW/cm^2 from an AM 1.5G solar simulator are summarized in Figure 6-3 and in Table 6-1, respectively. As shown in Table 6-1, Sample II and Sample III exhibit higher short-circuit current density (J_{sc}), conversion efficiency (η) and fill factor (FF) compared to Sample I. It is observed that the increase in open-circuit voltage (V_{oc}) of solar cells with AlN layer were negligible, which were in the range of 0.013-0.017 V. Based on those observations in Si solar cell devices with an ultra-thin AlN layer, the improved solar cell current density and efficiency are mainly due to AlN antireflection effect [605-607] instead of surface passivation effect. More importantly, this study demonstrates the good electrical conductivity of ultra-thin AlN buffer layer.

6.4 Hydrogen Production from Photoanode Using *n*-GaN Nanowires Selective-Area Grown on Si Substrates

Hydrogen production by using a photoelectrochemical (PEC) cell [608-611], which harvests solar energy and store it as chemical energy, is one of the most promising renewable and clean energy techniques. GaN-based semiconductors have attracted intense interests for PEC hydrogen production and water splitting [612-616], due to its advantages including wide and tunable absorption spectrum and high stablility in electrolytes as a photoelectrode [617-

620]. Compared to GaN-based planar structures, for PEC applications, GaN-based nanowires exhibit unique advantages including extremely low dislocation density, high aspect ratio and large surface-to-volume ratio [614, 616, 617].

With precisely-controlled length, diameter and nanowire morphology, the uniform nanowire arrays have polarity-controlled and high-quality reaction interfaces, controlled crystal orientation and uniform In distribution, improving the surface reactivity for PEC reactions [613, 614]. Compared to spontaneous grown nanowires, selective-area grown nanowire array can exhibit significant enhanced light absorption through photonic crystal effects, promising much more efficient PEC hydrogen production and water splitting. Recently, using MOVPE, GaN-InGaN core-shell microwire arrays selective-area grown on GaN/sapphire was developed as photonodes for hydrogen production [613]. This core-shell microwire array with a height of 14 μm exhibited a photocurrent density above 0.3 mA/cm^2 (at 1.35 V vs RHE) [613].

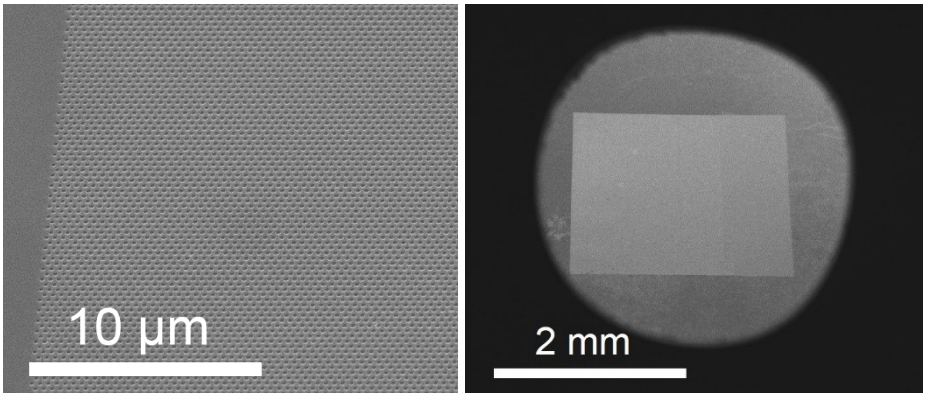

(a) (b)

Figure 6-4: Bird's-eye-view SEM images of (a) nanohole pattern on Si substrate and (b) 2.1×2.1 mm^2 *n*-GaN nanowire array selective-area grown on Si substrate.

The properties of GaN nanowire array selective-area grown on Si substrates were further investigated in PEC reactions. It will be presented in the following study that the uniform *n*-GaN nanowire array on Si is very promising for PEC hydrogen production and water splitting. On the patterned Si substrates using ultra-thin AlN/GaN template, a large area *n*-GaN nanowire

array with a height of ~ 880 nm, nanowire diameter of ~ 345 nm and nanowire spacing (gap) of ~ 55 nm were selective-area grown in the MBE system (Veeco, Gen II^{TM}). The Bird's-eye-view SEM images of 2.1×2.1 mm^2 nanohole pattern on Si substrate and grown nanowire array of 2.1×2.1 mm^2 are shown in Figures 6-4 (a) and 6-4 (b), respectively. Prior to the nanowire growth, the nitridation of Ti mask layer was carried out in the growth chamber at 400 °C for 10 min. The growth conditions for Ge-doped *n*-GaN included a growth temperature of 808 °C, a N_2 flow rate of 0.33 sccm, a forward plasma power of 350 W, a Ga BEP of 2.43×10^{-7} Torr and Ge effusion cell temperature of 1000 °C and 1050 °C.

PEC characterizations were conducted on photoanodes made from the 2.1×2.1 mm^2 selective-area grown nanowire array. The patterned Si substrates underwent multiple fabrication processes and long nitridation treatement during the nanowire growth. To rule out the effects of patterned Si substrates on the results of PEC characterizations, one substrate which underwent same fabrications processes were treated by nitridation in MBE growth chamber with the Ga shutter closed. This substrate was used as the reference for controlled experiments to study the PEC properties of nanowire.

As the first step of the device preparation for PEC characterizations [307, 621], a Cu wire was attached to backside of the Si substrate using Ag paste. After drying in air, a thin In-Ga eutectic was futher applied to the connection between the Cu wire and Si substrate. The edge and backside of sample and exposed Cu wire were capsuled with epoxy, with only nanowire regions on the front side of Si substrates exposed to solutions. The PEC characterizations were conducted in 1 M HBr solution using a three-electrode configuration (Ag/AgCl reference electrode, Pt coil and the sample as a photoanode) [307, 621]. At the photoanode, bromide ions were oxidized. Hydrogen will be generated at the Pt electrode. The electrons are transfer from photoanode to Pt electrode during the PEC reactions. Both a thermopile (818P-100-55,

Newport) and a photodiode sensor (818-ST2-UV/DB, Newport) with attenuator were used to calibrate the illumiantion intensity [307, 621].

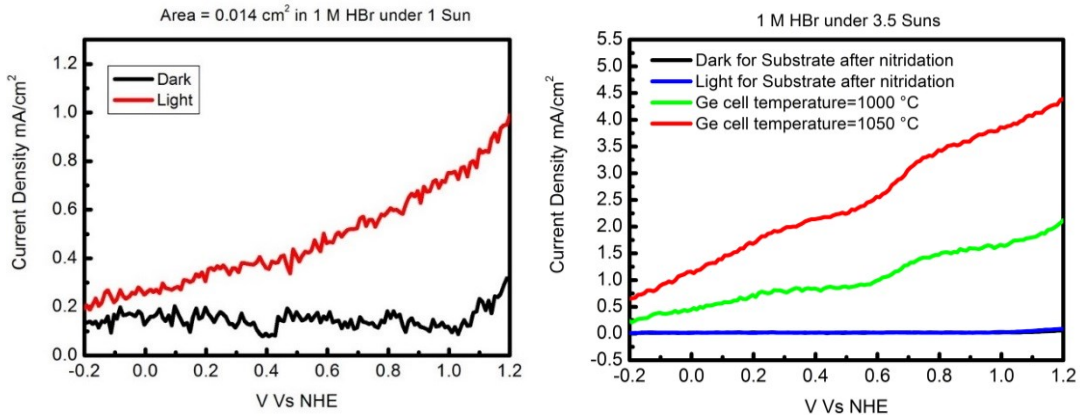

(a) (b)

Figure 6-5: The variations of current density with applied voltage versus normal hydrogen electrode (NHE) for (a) 0.014 cm^2 nanowire array (Ge doping temperature 1050 °C) exposed to 1 M HBr solution under AM 1.5G illumination of 100 mW/cm^2 and (b) substrate after nitridation (no nanowire on the sample), 0.017 cm^2 nanowire array (Ge doping temperature 1000 °C) and 0.014 cm^2 nanowire array (Ge doping temperature 1050 °C), under AM 1.5G illumination of 350 mW/cm^2.

The exposed area of a nanowire sample, which was grown by using Ge cell temperature of 1050 °C, was 0.014 cm^2. Under AM 1.5G illumination of 100 mW/cm^2, the photo-current density (J_{ph}) reached 0.98 mA/cm^2 at 1.2 V versus normal hydrogen electrode (NHE), shown in Figure 6-5 (a). The onset potential of this nanowire sample was -0.243 V. Shown in Figure 6-5 (b), its PEC characteristics was futher studied under AM 1.5G illumination of 350 mW/cm^2, and J_{ph} reached 4.39 mA/cm^2 at 1.2 V versus NHE. To study the effect of Ge doping concentration on its PEC characteristics, another nanowire sample was grown by using Ge cell temperature of 1000 °C and then characterized in 1 M HBr. Shown in Figure 6-5 (b), J_{ph} of this nanowire sample with an exposed area of 0.017 cm^2, was 2.12 mA/cm^2 at 1.2 V versus NHE, exhibiting a 51.7% reduction compared to that of the nanowire sample grown by using Ge cell temperature of 1050 °C. The increase in J_{ph} is due to the enhanced conductivity resulted from

higher Ge doping, which is consistent with what has been reported [622, 623]. It is worthwhile mentioning that J_{ph} of the substrate after nitridation (no nanowire on the sample) were 0.0869 mA/cm^2 and 0.0619 mA/cm^2 at 1.2 V versus NHE, which were measured in the dark environment and under AM 1.5G illumination of 350 mW/cm^2, respectively. These two small non-zero values might be due to the fluctuations in the measurements. Shown in Figure 6-5 (b), J_{ph} of the substrate after nitridation were negligible compared to the J_{ph} of nanowire samples, showing that the hydrogen production was only driven by the PEC reactions on the nanowire surface.

PEC results of 14 μm-long GaN-InGaN core-shell microwire arrays selective-area grown on GaN/sapphire in L. Caccamo's work [613] did not present the characteristics of current saturation. Compared to L. Caccamo's work [613], the characteristics of current saturation is much improved from the PEC results of our 880 nm-long *n*-GaN nanowire array selective-area grown on Si substrate using AlN/GaN:Ge buffer template. This improvement is likely due to less nonradiative recombination [623]. PEC results of our 880 nm-long *n*-GaN nanowire array present J_{ph} of 0.98 mA/cm^2 at 1.2 V under AM 1.5G illumination of 100 mW/cm^2, which is much higher than 0.3 mA/cm^2 (at 1.35 V vs RHE) of L. Caccamo's work [613]. This may be attributed to the difference in solutions which were used in two experiments [613]. To explain the PEC characteristics and explore the underlying PEC mechanism of *n*-GaN nanowire array selective-area grown on Si substrate, more investigations are essential.

The PEC characteristics of *n*-GaN nanowire array can be significantly improved by increase the nanowire length, and optimize the nanowire diameter and array periodicity. The PEC results of *n*-GaN nanowire array selective-area grown on Si substrate further demonstrate the high conductivity of the ultra-thin AlN/GaN:Ge buffer template. To futher improve the PEC characteristics and increase hydrogen production, thick InGaN segments can be incorporated into nanowire array for wide light absorption spectrum. A green-emitting

nanowire array consisting of a 300-nm long *n*-GaN segment and a 450 nm-thick InGaN segment has been selective-area grown on Si substrate. The bird's-eye-view SEM image is shown in Figure 6-6. The inset of Figure 6-6 is the magnified SEM image of the top of InGaN segment.

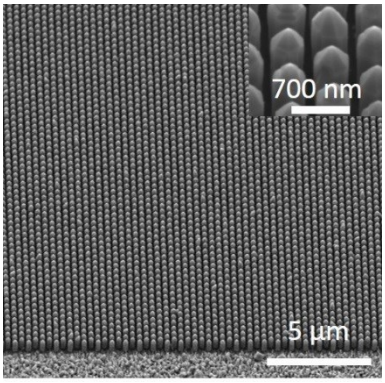

Figure 6-6: Bird's-eye-view SEM image of a InGaN-based nanowire array consisting of a 300-nm long *n*-GaN segment and a 450 nm-thick InGaN segment selective-area grown on Si substrate using ultra-thin AlN/GaN:Ge buffer template. The inset show the top of InGaN segment.

The demonstration of hydrogen production from GaN-based nanowire array selective-area grown on Si substrate using ultra-thin AlN/GaN:Ge, promise the integrations of selective-area grown III-nitride nanowire with large ara Si substrates and well-developed Si solar cell for efficient double-band InGaN/Si integrated PEC water splitting [307, 617, 624].

6.5 Selective Area Epitaxy and Structural Characterizations of *n-i-n-n*$^+$ GaN Single Nanowires on Si Substrates

On n-Si substrate, *n-i-n-n*$^+$ GaN single nanowires were epitaxially grown using the MBE system (GENxplor^{TM}, Veeco), taking advantage of Ti-mask selective area epitaxy. Shown in Figure 6-7 (b), *n-i-n-n*$^+$ GaN single nanowire heterostructure consists of ~ 100 nm lightly Si-doped *n*-GaN, ~ 500 nm non-doped GaN, ~ 100 nm lightly Si-doped *n*-GaN and ~ 100 nm heavily Si-doped n^+-GaN segments. The Ti/Au metal layers were deposited onto n^+-GaN segment in the later fabrication process (discussed in in section 6.6). The n^+-GaN segment was

heavily Si-doped to reduce the contact resistance between nanowire and Ti/Au metal layers to precisely reveal the electrical properties of non-doped GaN.

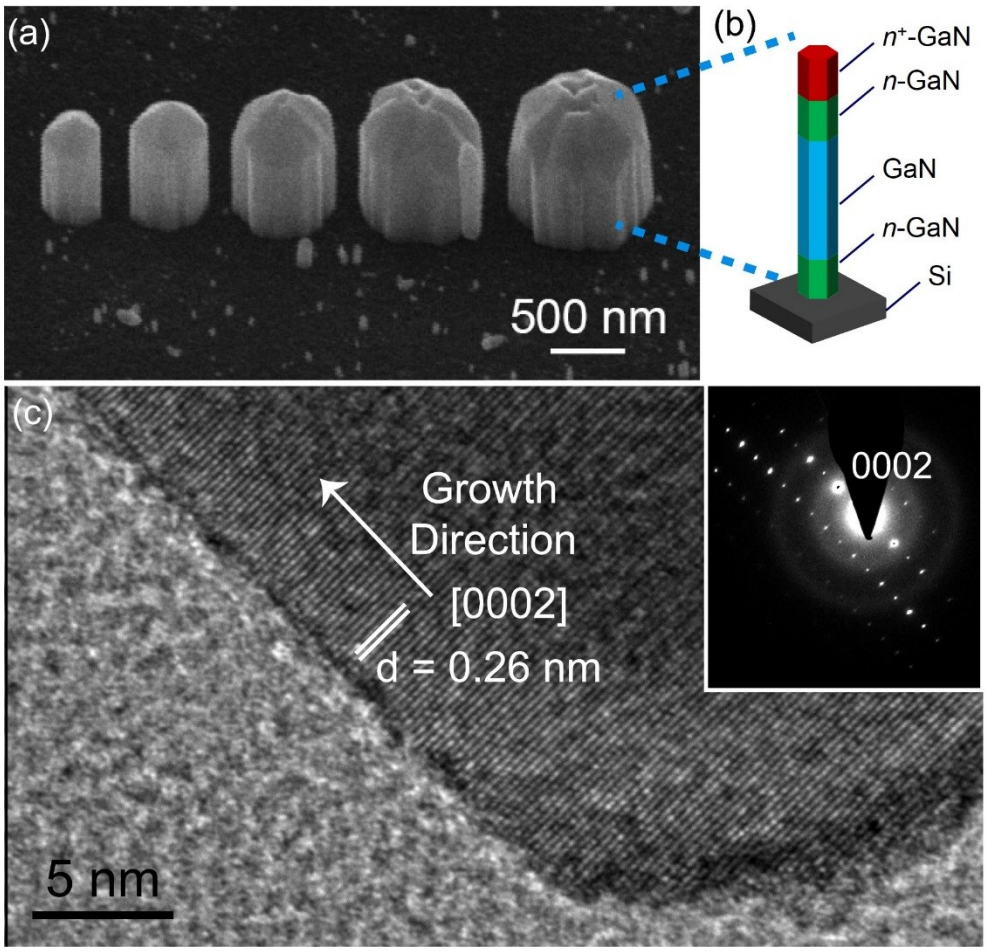

Figure 6-7: (a) Bird's-eye-view SEM image of single GaN nanowires with various diameter in the range from 400 nm to 800 nm. (b) Schematic of single *n*-*i*-*n*-n^+ GaN nanowire grown on Si substrate. (c) High-resolution TEM image of single *n*-*i*-*n*-n^+ GaN nanowire at the root region and image of electron diffraction (SAED) pattern (inset).

The growth condition of top and bottom *n*-GaN segments included a substrate temperature of 885 °C, a Ga beam equivalent pressure of 2.35×10^{-7} Torr and Si doping cell temperature of 1150 °C. For the growth of non-doped GaN segment, the substrate temperature and Ga beam equivalent pressure was 885 °C and 2.35×10^{-7} Torr, respectively. To study the effect of Si doping concentration on the electrical characteristics of *n*-*i*-*n*-n^+ GaN single nanowires, four nanowire samples were grown with different Si doping concentrations in n^+-GaN segment. The Si cell temperatures used during the epitaxial growth of n^+-GaN segment were 1150 °C,

1200 °C, 1300 °C, and 1350 °C, corresponding to Si doping concentrations estimated to be 7.65×10^{18} cm^{-3}, 2.19×10^{19} cm^{-3}, 2.12×10^{20} cm^{-3} and 6.84×10^{20} cm^{-3}, respectively.

The difficulty in growing large-diameter GaN-based nanowires and controlling the spacing between nanowires, limits the usage of spontaneous growth for direct nanoprobing which requires relatively large nanowire diameter for contacting as well as relatively large spacing for nanoprobing manipulations [355, 366, 376, 380-382]. Besides those, it is also not viable to tailor InGaN nanowire diameter and nanowire spacing over the same substrate through the approach of spontaneous growth [355, 366, 376, 380-382].

Figure 6-7 (a) shows a typical bird's-eye-view field-emission SEM of *n-i-n-n*$^+$ GaN nanowires (diameter in the range from 400 nm to 800 nm) vertically aligned on the same Si substrate. As shown in Figure 6-7 (a), the diameter of GaN single nanowires can be varied on the same Si substrate in a single epitaxial growth by using Ti-mask SAE technique. Such unique feature of Ti-mask SAE technique provides the convenience in the electrical characterization without changing the samples, enabling the systematic studies on electrical characteristics of nanowires with various size and geometry through *in-situ* nanoprobing of GaN single nanowires on the same substrates. This also paves the way to integrate dense GaN-based electronic devices with precisely-controlled geometry and electrical characteristics on the same Si substrate.

High-resolution transmission electron microscope (TEM) images were taken using a S/TEM system (Tecnai F20, FEI) equipped with a 4k×4k CCD camera (Oneview, Gatan) from the root regions (Figure 6-7 (c)) of a *n-i-n-n*$^+$ GaN single nanowire, indicating that such a nanowire exhibits high crystal quality. The interplanar spacing is measured to be 0.26 nm, confirming that the growth direction is along the [0002] direction (*c*-axis), which is consistent with the SAED pattern shown in the inset.

6.6 Device Fabrication of Single GaN Nanowires on Si and SEM-Based Nanoprobing

To characterize electrical properties of single GaN nanowires [625], two-point electrical nanoprobing technique has been employed in SEM environment [145]. In contrast to other destructive process [626] to create electrical contacts with nanostructures such as ion-beam-induced deposition (IBID) [627] and e-beam induced deposition (EBID) [628], *in-situ* nanoprobing avoids the beam-induced alterations to materials and the resulting beam-induced modifications on electrical characteristics, providing more accurate characterization [145, 625].

In the SEM chamber (Quanta 450 FEG, FEI), a four-probe piezoelectric nanomanipulator (TNI LF-2000) was mounted and communicated with computer and source meter (SMU 2400, Keithley) through electronic controller. A unique advantage of this nanomanipulator over other commercial nanomanipulators is the integration of position feedback (resolution: 0.1 nm) in each fine positioning stage, allowing closed-loop-controlled, high-precision nanopositioning and nanoprobing of single nanowires in the experiments. Shown in the inset of Figure 6-8 (a) is the nanoprobing of a GaN single nanowires with a Pt-coated tungsten nanoprobe (ST-20-0.5, GGB Industries). The detailed information of SEM-based nanoprobing electrical characterization system was described elsewhere [629].

Two metal contacts were deposited respectively on top surface of GaN nanowires and backside of Si substrate, as shown in Figure 6-8 (b). The device fabrication process involved the use of polyimide for surface passivation and planarization, standard photolithography and contact metallization. A Ti(20 nm)/Au(100 nm) was first deposited on the backside of Si substrate as a contact. A polyimide resist layer was spin-coated to cover the selective-area grown single nanowires, followed by reactive-ion etching using O_2 plasma to expose the top surface of n^+-GaN segments of single nanowires. Ti (10 nm)/Au (10 nm) metal layers was then deposited onto n^+-GaN top surface, followed by a rapid thermal annealling (RTA) at 550 °C for 1 minute in N_2 environment. Benefitting from this fabrication, destructive direct-write

lithography methods such as EBID or IBID are avoided in the *in-situ* nanoprobing. The insulating polyimide was used to electrically separate the top metal contact and bottom segments (non-doped GaN, *n*-GaN and Si substrate) to avoid the possibility of electrical leakage and short circuit, as shown in Figure 6-8 (b).

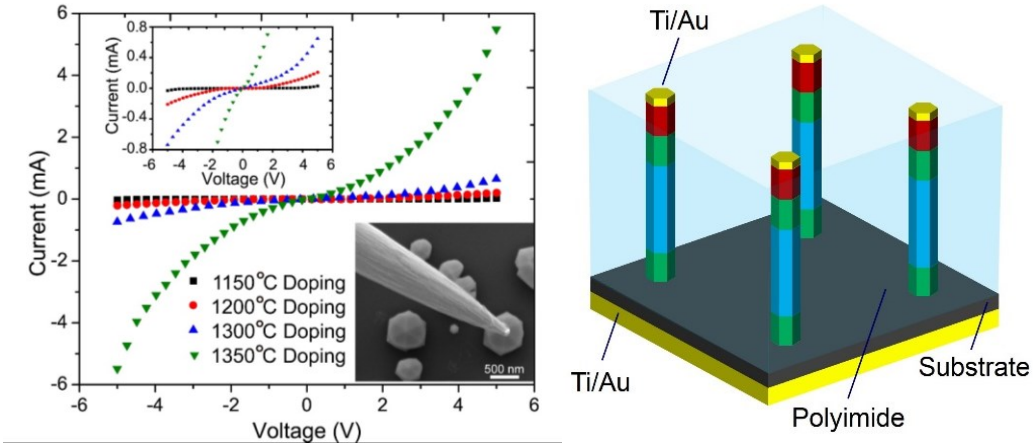

(a) (b)

Figure 6-8: (a) Representative I-V characteristics of single GaN nanowire with different Si doping concentration in n^+-GaN, the diameter of measured GaN single nanowires is ~ 500 nm. The top-left inset shows the magnified I-V curves, the bottom-right inset shows the top-view SEM image of nanoprobing a GaN single nanowire with a Pt-coated tungsten nanoprobe. (b) Schematic of selective-area grown GaN single nanowire devices fabricated on Si substrate.

6.7 Electrical Characterizations of *n-i-n-n*$^+$ GaN Single Nanowires on Si Substrates

In the two-point nanoprobing experiments, one nanoprobe contacted the metal at the top surface of single GaN nanowires, as illustrated in the inset of Figure 6-8 (a), and the other one contacted the Cu tape connecting the metal contact at the back side of Si substrate, as illustrated in Figure 6-2 (a)). The source meter (SMU 2400, Keithley) was used for I-V characterizations, the sweep voltage was increased in steps of 0.25 V and the ramp rate is 1 V/0.01 s. The e-beam was switched off to avoid electrical noise during the measurements. Representative I-V characteristics of single GaN nanowire with different Si doping concentration in n^+-GaN segment are shown in Figure 6-8 (a).

The variations of Si doping concentration in the n^+-GaN segment results in very different I-V characteristics, essentially indicating the importance of reducing the contact resistance [630]. From the slope of nearly linear I-V characteristics in the low-bias region, the resistance is estimated to be 2 MΩ, 0.5 MΩ, 16 KΩ and 3.3 KΩ for the *n*-*i*-*n*-n^+ GaN single nanowires grown by respectively using Si cell temperature of 1150 °C, 1200 °C, 1300 °C and 1350 °C in the growth of n^+-GaN segment. Conductivity (σ) of these nanowires (diameter: ~ 500 nm) vary in the range of 0.023-14.255 $(\Omega \cdot cm)^{-1}$ and increases with the increasing Si doping concentration in n^+-GaN segment. To derive the electrical properties of non-doped GaN, the conductivities of *n*-GaN and n^+-GaN segment segments are calculated via the equation $\sigma = en\mu$ [631], where e is the elemental charge, n is the carrier density and μ is the carrier mobility. The resistances of *n*-GaN and n^+-GaN segments are further calculated via the equation $R = l/(\sigma \cdot A)$, where l is the length of each segment, and A is the cross-section area of single nanowires. Neglecting the contact resistance of n^+-GaN segment grown using Si cell temperature of 1350 °C [630], the calculated conductivity of non-doped GaN is 9.49 $(\Omega \cdot cm)^{-1}$. Substituting the calculated conductivity of non-doped GaN segment and the reference value of electron mobility (650 $cm^2 \cdot V^{-1} \cdot s^{-1}$) provided in literature [632] into equation $\sigma = en\mu$, the electron density is estimated to be 9.12×10^{16} cm^{-3}. The low contact resistance was achieved by taking advantages of the flexibility of tuning Si doping concentration in MBE epitaxial growth of *n*-GaN nanowires.

6.8 Electrical Characteristics and Thermal Breakage of GaN Single Nanowires

After typical I-V characterizations using relative low bias, the single GaN nanowire devices was then tested to failure by applying forward bias which was increased in a step of 0.25 V with a ramp rate 1 V/0.01 s. When the applied bias reached a critical value, the single GaN nanowires broke as shown in sequential SEM images (Figure 6-9 (a)) during tests. For comparison, then the broken parts of nanowires were picked up using the nanoprobe tip as

shown in rightmost picture of Figure 6-9 (a). It can be observed that the cross sections of nanowires was damaged, leading to the disconnection with the Si substrate. Multiple measurements were repeated to electrically test the other GaN nanowires to failure, and same results were measured and observed. The rightmost SEM image of Figure 6-9 (a) presents the cross sections of broken single nanowires in 1st and 2nd attempts of mesurements.

The forward-biased I-V characteristics of single GaN nanowires with different diameters (400 nm - 900 nm) grown with different Si doping concentration in n^+-GaN segment are shown in Figures 6-9 (b)-(e), respectively. It can be observed that the current passing through single nanowire increased with the increasing bias until a critical point was reached when the broken nanowires was observed. Beyond this critical point, the current showed a dramatic decrease. The values of current and voltage at the critical point are denoted as the maximum current and maximum voltage of single nanowires in the subsequent context. The dependence of maximum voltage on nanowire diameter and doping level is summarized in Figure 6-10 (a), the graphs show that for same Si doping concentration in n^+-GaN segment, the maximum voltage is relatively constant with a small deviation in the measurements of nanowires with different diameters. The maximum voltage is 8.51 ± 0.28 V, 8.23 ± 0.52 V, 6.84 ± 0.78 V and 5.38 ± 0.25 V for the Si doping temperature of 1150 °C, 1200 °C, 1300 °C, and 1350 °C used for the growth of n^+-GaN segments, respectively. The maximum electric field was calculated to be 10.76-17.02 MV/m for those single nanowires depending on the Si doping temperature. The value of maximum electric field is much higher than the recent reported value (~ 4.36 MV/m) for GaN single nanowires which was arranged horizontally for the electrical characterizations [595].

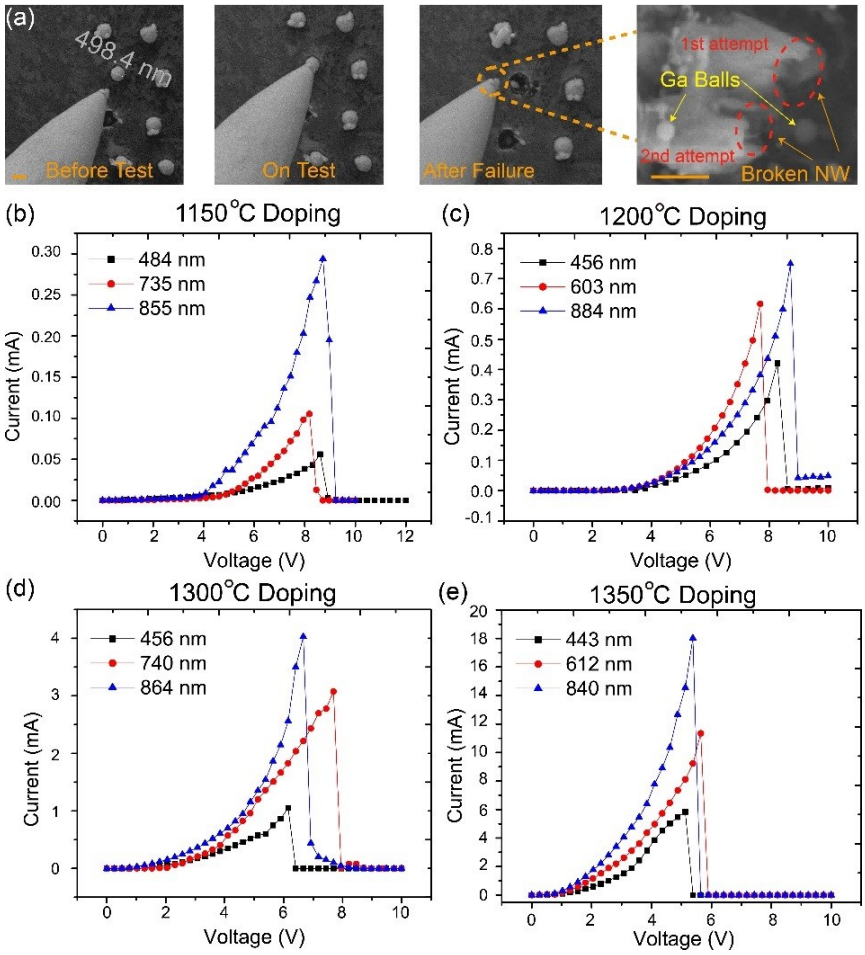

Figure 6-9: (a) Sequential SEM images of single GaN nanowire nanoprobing before/on/after I-V characterization (left scale bar: 500 nm). The 4th SEM image is magnified image of evaporated Ga balls and cross sections of 1st and 2nd broken nanowires after 1st and 2nd attempts to measure two different nanowires. (b)-(e): I-V characteristics of single GaN nanowires with different Si doping temperatures of (b) 1150 °C, (c) 1200 °C, (d) 1300 °C, (e) 1350 °C used for the growth of n^+-GaN layer.

It can be observed in Figure 6-9 and Figure 6-10 (a) that for the single nanowires with same diameter the maximum voltage decreases slightly with increasing Si doping concentration in n^+-GaN segment. It was reported in the previous study [595] that the breakage of GaN single nanowire was due to the generated Joule heating when it was applied with a DC bias. It was observed that the middle point of single nanowires reached the melting or decomposition temperature T_{max} firstly [595], leading to a localized breakage of GaN nanowires. In the present experiments, Ga balls [596] were also observed and the Ga balls remained on surfaces

of single nanowires (Figure 6-9 (a)) after the breakage. The formation of Ga balls could be a result of breaking Ga-N bonding, further supporting that the localized thermal decomposition of GaN is the key mechanism causing the breakage of GaN single nanowires and the resulting device failure.

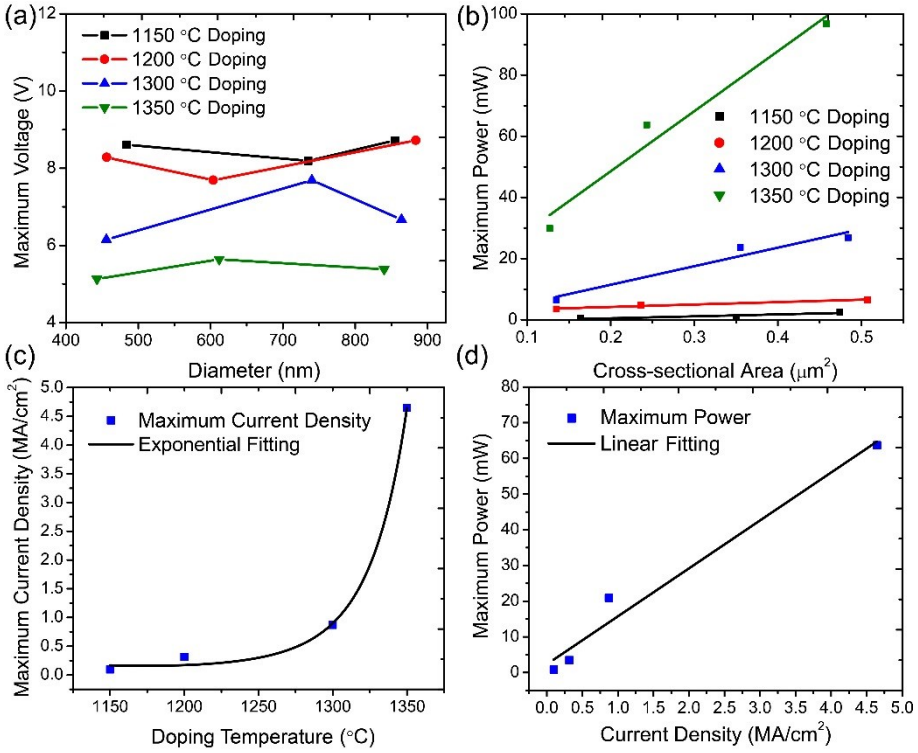

Figure 6-10: (a) Doping-dependent device-failure voltage versus nanowire diameter, (b) doping-dependent maximum power versus nanowire cross-sectional area (calculated as regular hexagonal), (c) device-failure current density versus doping temperature, (d) Maximum power versus current density (the four data points correspond to the highest current density within four doping temperature from 1150 °C to 1350 °C).

Assuming thermal conductivity is constant over the single nanowire, the maximum temperature T_{max} can be expressed by Equation 6-1 [595, 633] as below:

$$T_{max} = T_0 exp(\alpha\sigma U_{max}^2/8) \qquad \text{Equation 6-1,}$$

where the boundary temperature of the single nanowire is expressed as T_0, α is a constant related to thermal conductivity of GaN single nanowire, σ is the electrical conductivity of GaN single nanowire and U_{max} is the maximum voltage. According to Equation 6-1, the maximum

temperature T_{max} is independent of nanowire diameter and only depends on the applied DC voltage U_{max} [595]. This explains the result that maximum voltage U_{max} was relative constant versus nanowire diameter for each doping concentration, as shown in Figure 6-10 (a). In addition, as a larger electrical conductivity σ was measured from the nanowires with higher Si doping concentration in n^+-GaN segment, leading to a slight decrease of maximum voltage U_{max} for nanowire breakage (T_{max} is assumed to be fixed for certain nanowire diameter), consistent to what is observed in Figure 6-10 (a).

For different Si doping concentration in n^+-GaN segment, the dependence of maximum power (taken as the product of maximum voltage and maximum current) on cross-sectional area of single nanowire is summarized in Figure 6-10 (b). It can be observed that the maximum power is proportional to cross-sectional area of single nanowire. For a fixed cross-sectional area, the maximum power increases with the increase in the Si doping concentration in n^+-GaN segment. This observation can be explained by using Equation 6-2, which is translated from Equation 6-1 by replacing U_{max} with $U_{max} = I_{max} \cdot R$ and $R = l/\sigma A$. The Equation 6-2 is

$$T_{max} = T_0 exp(\frac{\alpha l^2}{\sigma A^2} I_{max}^2/8) \qquad \text{Equation 6-2,}$$

where l and A is the length and cross-section area of single nanowires, and I_{max} is the maximum current of single nanowires. From Equation 6-2, it can be concluded that both increased cross-sectional area A and increased Si doping concentration in n^+-GaN segment (higher electrical conductivity σ) lead to the increase of maximum current I_{max}. Meanwhile, with the same Si doping concentration in n^+-GaN segment, the maximum current I_{max} is proportional to the nanowire cross-sectional area A. Due to nearly constant maximum voltages value U_{max} versus nanowire diameter (Figure 6-10 (a)) for the same Si doping concentration, the maximum power, which is the product of I_{max} and U_{max}, is therefore proportional to cross-section area, which is consistent to what is shown in Figure 6-10 (b). Besides, based on Equation 6-2, with a constant nanowire cross-sectional area A, an increased doping

concentration (higher electrical conductivity σ) leads to an increase in maximum current I_{max}, corresponding to higher maximum power, which is also consistent to the measurements shown in Figure 6-10 (b).

Shown in Figure 6-10 (b), with Si doping temperature of 1350 °C used for the growth of n^+-GaN segment, the maximum power in a GaN single nanowire was measured to be 96.84 mW, which is comparable to results reported in [596]. In Figure 6-10 (c), it can be observed that the maximum current density increases significantly with the increased Si doping temperature used for the growth of n^+-GaN segment, because contact resistance of n^+-GaN segment decrease with the increasing Si doping concentration [630] which is in exponential relationship with Si doping temperature used for the growth of n^+-GaN segment [630, 634]. By tuning the Si doping concentration of n^+-GaN segment, the maximum current density was enhanced significantly and the maximum current density of 4.65 MA/cm^2 (11.3 mA measured from GaN single nanowire with diameter of ~ 612 nm) was achieved using Si doping temperature of 1350 °C for the growth of n^+-GaN segment. The maximum current density achieved is higher than the reported value of ~ 0.06 MA/cm^2 (244 μA measured from GaN single nanowire with diameter of ~ 800 nm) [596].

As shown in Figure 6-10 (d), the maximum power increases linearly with maximum current density. The achieved high maximum power and maximum current density show the merits of *n*-*i*-*n*-n^+ GaN single nanowires selective-area grown on Si substrates and the quality of Si doping tuning to reduce the contact resistance. The observed experimental results could be adopted as a guidance to further enhance the electrical characteristics of single nanowires.

6.9 Summary

With AlN/GaN:Ge buffer layer, selective area epitaxy of uniform GaN nanowire arrays has been achieved on Si substrates with Ti mask. The nanowire arrays are aligned vertically on Si substrate and exhibit well-controlled size and position, after extensive efforts on the

exploration of suitable buffer template and optimization for growth parameter and pattern fabrication processes. The properties of *n*-GaN nanowire array selective-area grown on Si substrates were further investigated in photoelectrochemical reactions for hydrogen production. The PEC characteristics of current saturation is much improved in our results, compared to the recent PEC study using InGaN-GaN microwire array selective-area grown on GaN/sapphire substrates. Our PEC results present a relatively high J_{ph} of 2.12 mA/cm^2 and 4.39 mA/cm^2 (at 1.2 V versus NHE) under the AM 1.5G illumination of 350 mW/cm^2. The PEC results further demonstrate the high conductivity of the ultra-thin AlN/GaN:Ge buffer template. The high electrical conductivity of ultra-thin AlN layer has been demonstrated through the growth of ultra-thin AlN layer on Si solar cell with a Si tunnel junction and photovoltaic characterizations of the resulting Si solar cells. Moreover, two-point electrical nanoprobing was performed on *n*-*i*-*n*-*n*$^+$ GaN single nanowires selective-area grown on Si substrate for a systematic investigation of electrical characteristics including maximum voltage, current density and power. The electrical characteristics of *n*-*i*-*n*-*n*$^+$ GaN single nanowires depend on nanowire diameter and contact resistance which are closely related to Si doping concentration of *n*$^+$-GaN segment. By tuning the Si doping temperature used for the growth of *n*$^+$-GaN segment, electrical characteristics of GaN single nanowires has been improved dramatically, and a high maximum current density of 4.65 MA/cm^2 and a high maximum electric field of 17.02 MV/m have been achieved. The experimental approach and results are relevant for the development of vertical GaN-based nanowire electronic devices on Si substrates and III-nitride/Si integrated multijunction solar cells.

Chapter 7: Selective-Area Grown AlInGaN Nanowires on Si: Suppressing the Nonradiative Surface Recombination for Solar Cells

7.1 Introduction

To make low cost and efficient optoelectronic devices and electronics, it is highly desired to monolithically grow and fabricate high efficiency III-V materials and III-V devices on low cost and large area Si substrate [248, 249, 283, 498-502]. While other substrates such as GaN/sapphire has a few considerable disadvantages, Si substrates exhibit comprehensive advantages, including high electrical conductivity, high crystal quality, good thermal properties and low cost [503]. Particularly important for high efficiency photovoltaics and artificial photosynthesis, the direct epitaxy of InGaN on Si substrate promise the direct integration of the commercialized Si solar cell with III-nitride devices exhibiting tunable absorption spectrum [508]. The energy bandgap or absorption spectrum of InGaN alloy can be continuously varied from 0.7 to 3.4 eV. Si with a bandgap of ~ 1.1 eV is ideally suited for the bottom junction of a double-junction solar cell. An energy bandgap in the range of 1.6 to 1.9 eV is required for the top-cell in a Si-based tandem solar cell [624], but there are few materials that can offer large open circuit voltage (V_{oc}) in this energy bandgap range.

Benefitting from the efficient strain relaxation, GaN-based nanowire can be grown with thicker absorption segments and higher In content in active segments, which are essential for high-efficiency solar cell [298] but have been greatly limited by the critical thickness related to mismatchs in multiple quantum well (MQW) epilayers and other planar heterostructures [635]. Alternative to the mechanical stacking [636, 637] and direct wafer bonding to mechanically integrate III-nitride devices and Si solar cell [638, 639], the direct epitaxy and monolithic integration of III-nitride nanowires on Si substrate is a viable method to making III-nitride/Si multiple-band or multiple-junction devices exhibiting full-solar-spectrum absorption

and hence high theoretical efficiency in the range of 31-38% under AM1.5G illumination of one Sun [640].

In the conventional spontaneous nanowire growth, the spontaneous formation leads to fluctuations in nanowire diameter, nanowire length and position, which causes a spatial variation in the In composition [253, 463] and diameter-dependent variation in the dopants incorporation [641, 642]. Such spatial variations in adatoms incorporations and variations in nanowire dimensions degrade the optical and electrical properties of optoelectronic devices including spectral intensity, spectral linewidth, current-voltage output characteristic and device efficiency.

Moreover, the light absorption and the photons converted to a photocurrent are proportional to the surface coverage of the active region [298]. In this regard, thick InGaN active regions is essential for solar cells, especially for nanowire solar cell which covers much smaller surface area vertical to incident sunlight. The spontaneous growth of multi-junction nanowire solar cells and nanowire solar cell with thick active regions encounter the difficulty of controlling the nanowire morphology, resulting in coalescence of nanowires.

In this chapter, (Al)InGaN-based nanowire arrays will be grown on Si substrates using the technique of selective area epitaxy on Si substrate which has been developed and discussed in Chapter 6. The selective area epitaxy of nanowires on Si can lead to superior structural, optical and electrical properties that are well suited for the development of large area nanowire optoelectronic devices, especially solar cells. Moreover, the flexibility of controlling nanowire dimension and position also enable the possibility of photonic crystal effects leads to the enhancement of light absorption and the reduction in light reflection for nanowire solar cells [475-484].

The commonly reported axial III-V nanowires suffer from large nonradiative surface recombination associated with the presence of surface states, leading to the behavior of low

carrier lifetime [252, 643] and large leakage current [24, 306, 644] in optoelectronics device. Due to large surface-to-volume ratio, the significant nonradiative surface recombination is one of the primary bottleneck to improve the efficiency of III-nitride nanowire devices, including poor carrier injection efficiency in InGaN/GaN nanowire LEDs [132] as well as relatively low fill factor (FF) [306, 645] and relatively low V_{oc} [645, 646] in nanowire solar cells. Great efforts have been made and various approaches have been applied to suppress nanowire surface recombination [126, 252, 254, 306]. With multiple AlGaN layers incorporated in the nanowire active region, the carrier injection efficiency and output power of nanowire LED devices can be dramatically improved [126, 252, 254]. However, the approach using multiple AlGaN layers is not suitable for photovoltaics applications, due to the creation of large barriers for the carrier collections. Other passivation techniques lead to a complexity in the device design, synthesis, and fabrication process [306]. Based on the development of self-organized AlInGaN nanowires LEDs which has been discussed in Chapter 5, in this chapter, it is demonstrated that the Al incorporation maintains its effectiveness on surface passivation in selective-area epitaxy of much thicker active segments (~ 0.29 μm) for photovoltaics applications.

To meet the needs of high efficiency nanowire optoelectronics device integrated with large area Si substrate and overcome the associated difficulties, close-packed AlInGaN quaternary nanowire arrays with precisely-controlled nanowire dimensions and positions, have been selective-area grown on Si substrate and monolithically fabricated with Si substrate into a vertical type *p-i-n* optoelectronics device with a substrate exhibiting good thermal and electrical conductivity. The Ti-mask selective area epitaxy of green-emitting AlInGaN nanowire arrays exhibiting uniform size and height distribution was conducted by using MBE. With the spontaneously-formed core-shell structure in the AlInGaN active segment, the green-emitting nanowires vertically aligned on Si substrate were precisely arranged to exhibit high pack efficiency, making efficient optoelectronic device filling the “green gap” [174, 175, 647].

The output characteristics of AlInGaN nanowire devices were measured under the AM 1.5G illuminations of one-sun and 30-sun light intensity. Without cooling and under 30-sun illumination, the nanowire devices exhibited stable and repeatable output characteristics, benefitting from the good heat dissipation of Si substrate.

This work presents the first demonstration of efficient AlInGaN nanowire optoelectronic devices selective-area grown on Si substrates, particularly for photovoltaics applications under high power and relatively high temperature operation. This green-emitting AlInGaN nanowire solar cells monolithically integrating the solar energy harvesting (from light to electricity) and light emission (from electricity to light) through a single chip [648-651]. Such a light-emitting solar cells can promise various novel functions of existing applications, such as mobile phone displays which can get recharged under sunlight, and street lights or building facade which absorb solar energy during the daytime and emit light at night [652, 653].

7.2 Selective Area Epitaxy of AlInGaN Nanowire Array on Si Substrate

A typical schematic for selective area epitaxy of GaN:Si/AlInGaN/GaN:Mg nanowire heterostructures on patterned Si wafers is shown in Figure 7-1 **(**a). As shown in the schematic of Si substrate, nanohole-array Ti mask was fabricated on a template consisting of ultra-thin AlN and GaN:Ge buffer layers. Such a ultra-thin AlN buffer layer is used as the seed layer for the ultra-thin GaN:Ge buffer layer grown above. It has been found that, the morphology and polarity of selective-area grown GaN nanowires mainly depend on the polarity of the underlying AlN buffer layer which can be controlled by varying V/III flux ratios during the AlN growth [404, 519, 602]. However, in our AlN/GaN:Ge buffer template, the effects of ultra-thin AlN buffer layer on the nucleation and polarity of GaN buffer layer and GaN nanowires still require further investigations. In order to make the resistance of the AlN/GaN buffer template negligible on the current flow through the AlInGaN nanowire device, in this study,

the used AlN and GaN:Ge buffer layers are ultra-thin. The high electrical conductivity of ultra-thin buffer temperate have been justified in Chapter 6.

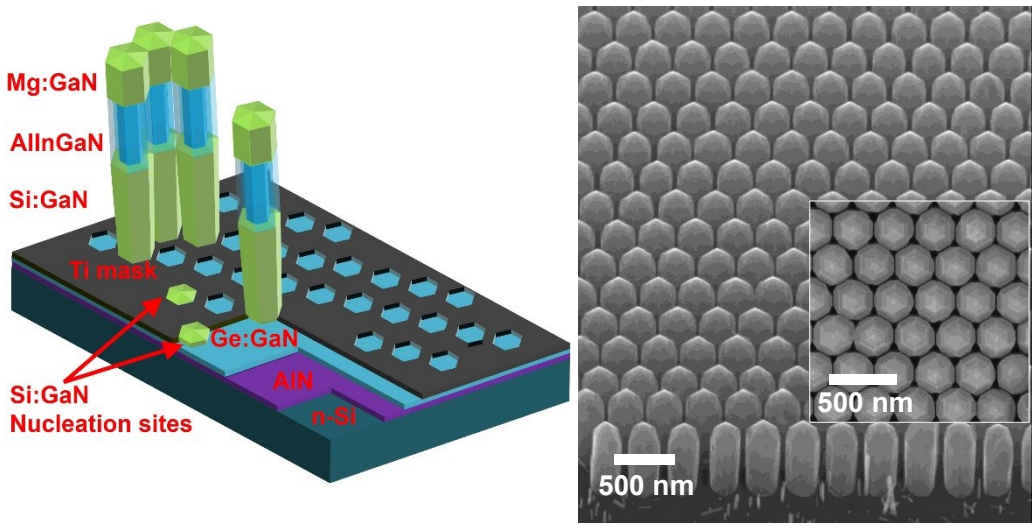

(a) (b)

Figure 7-1: (a) Schematic illustration of the selective area epitaxy of GaN:Si/AlInGaN/GaN:Mg nanowire heterostructures on *n*-Si/AlN/GaN:Ge substrate using nanohole-array Ti mask. During the selective area epitaxy, Ga atoms epitaxially accumulate in hexagonal nanohole openings and form nucleation sites. Subsequently, nucleation sites grow into full nanowire heterostructures. (b) Bird's-eye-view SEM image of close-packed AlInGaN nanowire array. The inset is the top-view SEM image. Nanaowire array was arranged in a triangular lattice with a lattice periodicity of 320 nm.

Nanohole-array patterns were defined by electron-beam lithography (EBL) on Ti layer to create the Ti mask for selective area epitaxy of III-nitride nanowire array. In this study, the pattern of Ti mask is was an array of hexagonal openings with a side length of 102 nm (a diameter of 204 nm) and such a nanohole array was arranged in triangular lattice with a periodicity of 320 nm. Taking advantages of the flexibility of controlling the diameter and periodicity of hexagonal openings, the packing efficiency of nanowire can be increased up to unity to improve light absorption of nanowire array and hence improve device efficiency. Schematically shown in Figure 7-1 (a), Ga atoms fill the hexagonal nanoholes to form Ga nucleation sites and then grows into full nanowire heterostrucutre. Each AlInGaN nanowire

heterostructure consists of ~ 0.49 μm Si doped *n*-GaN segment, ~ 0.29 μm AlInGaN active segment and ~ 0.15 μm Mg doped *p*-GaN segment. Under careful optimization of growth parameters and growth duration, high nanowire array packing efficiency was achieved, avoiding the coalescence between neighboring nanowires.

Table 7-1: Growth conditions of AlInGaN segments.

Sample	BEP_{Al} ($\times10^{-9}$ Torr)	BEP_{In} ($\times10^{-8}$ Torr)	BEP_{Ga} ($\times10^{-8}$ Torr)	T_{growth} (°C)	$\lambda_{PL\ peak}$ (nm)
A	-	7.65	1.78	700	527.9
B	1.46	7.65	1.78	700	525.5
C	3.36	8.46	1.78	710	522.3
D	4.26	9.52	1.78	715	515.9

On the patterned substrates, GaN:Si/AlInGaN/GaN:Mg nanowire heterostructures were selectively grown in a MBE system (Veeco, GenXplor^{TM}), with extensive efforts on the optimization for growth parameter and nanohole pattern designs. Prior to the nanowire epitaxy, the nitridation of Ti mask layer was carried out in the growth chamber at 400 °C for 10 min. The growth conditions for Si-doped *n*-GaN segments included a growth temperature of 885 °C, a N_2 flow rate of 0.35 sccm, a forward plasma power of 350 W, a Ga beam equivalent pressure (BEP) of 2.35×10^{-7} Torr and Si Knudsen effusion cell temperature of 1175 °C which corresponding to a Si doping concentration estimated to be 1.43×10^{19} cm^{-3}. Different Growth conditions of the AlInGaN segments are given in Table 7-1. For the growth of AlInGaN segments, the N_2 flow rate was 1.5 sccm. The Mg-doped *p*-GaN segment includes one lightly Mg-doped GaN bottom layer grown using Mg BEP of 2.04×10^{-9} Torr and one heavily Mg-doped GaN top layer grown with Mg BEP of 2.91×10^{-9} Torr. The other growth parameters for the Mg-doped *p*-GaN layer included Ga BEP of 2.35×10^{-7} Torr, substrate temperature of 870 °C and N_2 flow rate of 0.55 sccm.

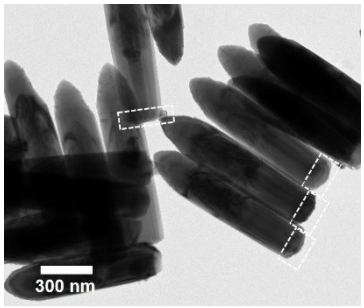

Figure 7-2: Transmission electron microscopy image of selective-area grown AlInGaN nanowire heterostructres depsersed onto copper TEM grid. The marked bottom of nanowires presents GaN:Si nucleation sites with smaller diameters.

At the elevated growth temperature much higher than the case of spontaneously-formed nanowires, which was 30-50 °C higher in both of our MBE systems (GENxplor^{TM} and GEN II^{TM}) for the selective area epitaxy of GaN:Si segments, the Ga sticking coefficient in the patterned openings with the exposed GaN:Ge surface is higher than the Ga sticking coefficient on the mask material. Taking advantages of such a difference in Ga sticking coefficient on different surfaces, with the optimized Ga flux, the epitaxy of GaN:Si segments only take place on predetermined preferential sites on the patterned substrate. The *n*-GaN nucleation site, which is confined and shaped by the hexagonal opening of Ti mask, can be clearly observed at the bottom of selective-area grown nanowires, shown in Figure 7-2. The bottom-most region of nanowire exhibits smaller diameter due to the restriction of nanohole opening, as shown in Figure 7-2. Once the *n*-GaN grows beyond the Ti mask, nanowire diameter increases dramatically. Compared to bottom *n*-GaN segment and top *p*-GaN segment, the AlInGaN active segment exhibits relatively larger diameter due to larger lateral growth rate resulted from the lowered growth temperature of AlInGaN active segment and Al incorporation.

Compared to that of Al and Ga atoms, the desorption of In atoms is much stronger [105]. To enhance the incorporation of In atoms in the AlInGaN segments, the growth temperature was reduced to 700-715 °C and N_2 plasma flow rate was increased from 0.35 to 1.5 sccm. However, the incorporation of Ga is also enhanced at lower growth temperature and higher

flow rate, compared to that at the higher growth temperatures used for *n*-GaN and *p*-GaN segments. In this regard, relatively lower Ga BEP was used for the epitaxy of AlInGaN segment. The adopted III/V ratio for AlInGaN segment was much lower than that for GaN:Si segment. Reduced growth temperature and reduced III/V ratio resulted in a low degree of growth selectivity between patterned region and mask material during the growth stage of AlInGaN segment. To achieve uniform, closed packed and high crystal quality AlInGaN nanowire arrays and hence superior device performance, it is essential to achieve uniform GaN:Si nanowire arrays with a perfect selectivity surrounding GaN:Si nanowires, which requires well-optimized growth parameters (III/V ratio, growth temperature and Ga flux) and well-controlled pattern parameters in Ti masks (nanohole size and array periodicity). In the case that undesired spontaneously formed GaN:Si nanowires nucleate and grow on mask material due to improper growth parameters used for GaN:Si, the subsequent segments including AlInGaN and GaN:Mg will also epitaxially grow on those undesired GaN nanowires. During the growth stages of AlInGaN and GaN:Mg, those undesired nanowires may grow and combine with neighboring selective-are grown nanowires, leading to undesired coalescence and hence undesired dislocation, nonuniform growth rate and nonuniform nanowire size in the selective-area grown nanowire arrays.

Figure 7-1 (b) shows the field-emission SEM image of the close-packed AlInGaN nanowire array grown on the patterned Si substrate with AlN/GaN:Ge buffer template. The morphology and size of vertically aligned AlInGaN nanowire are precisely determined by the opening in the Ti mask. The nanowire diameter and lattice periodicity of nanowire array can be varied by changing the nanohole size and lattice periodicity in the Ti mask. The uniform nanowire array exhibits Ga-polarity based on the observation of semipolar top facets and hexagonal pyramid morphology at the top. This suggests that the selective area epitaxy of well-

ordered Ga-polar AlInGaN nanowire array can be achieved on Si substrates using a ultra-thin AlN/GaN:Ge buffer template.

7.3 Characterizations of AlInGaN Nanowires Selective-Area Grown on Si Substrates

7.3.1 PL and Structural Characterization Methods

In this section, photoluminescence (PL) and structural properties of four representative green-emitting nanowire samples are presented firstly. Those four samples differed in (Al)InGaN segments grown using various MBE growth parameters, as shown in Table 7-1. During the epitaxy of those four nanowire samples, growth parameters for GaN:Si and GaN:Mg segments were same.

PL measurements were performed by using a 405 nm laser as the excitation source. A visible neutral density filter was used to adjust the power of incident laser beam in the range of 0.03-65.43 mW, which excited the (Al)InGaN nanowires. A high-resolution spectrometer was used to collect and resolve the emitted light from nanowire arrays, and a liquid N_2 cooled charge coupled device (CCD) was used for the light detection in the visible range. Low-temperature PL measurements were carried out at the temperature of 78.0 K by using a liquid N_2 closed-loop cryostat.

The structural characterizations of selective-area grown AlInGaN nanowire heterostructures were performed with transmission electron microscopy (TEM) and scanning transmission electron microscopy (STEM) by using a S/TEM system (Tecnai F20, FEI) equipped with a 4k×4k CCD camera (Oneview, Gatan). Selective-area grown AlInGaN nanowire heterostructures were dispersed onto copper grid for the S/TEM sample preparation, as shown in Figure 7-2. The high-angle annular dark-field (HAADF) atomic-number contrast images of nanowire heterostrucutres shows bright contrast at the center and dark contrast at the sidewall of the AlInGaN segment. Based on the HAADF image of nanowire heterostructures, the energy dispersive x-ray spectrometry (EDXS) analysis were further conducted to reveal the

Al, In and Ga elemental profiles of the overall nanowire by line scan along the axial direction (growth direction), and the Al, In and Ga compositional variation of AlInGaN segment by line scan along the radial direction together with EDX elemental mapping.

7.3.2 PL and STEM Characterizations of AlInGaN Nanowire Array

As shown in Figure 7-3, the PL emissions of AlInGaN nanowire samples were firstly measured at room temperature. Summarized in Table 7-1, the peak emission wavelength ($\lambda_{PL\ peak}$) of nanowires A, B, C, and D varies in the range of 515.8-527.9 nm, corresponding to the photon energy of 2.349-2.404 eV. With the increasing Al BEP and increasing growth temperature (T_{growth}), the Al content of active segment increases, leading to the blueshift of peak wavelength.

The PL emission spectral linewidths indicated by full-width-half-maximum (FWHM) vary in the range of 32.4-42.9 nm, corresponding to the energy of 146-200 meV, which are smaller than reported spectral linewidths of spontaneously grown green-emitting InGaN/GaN QDs nanowire array and InGaN QWs epilayers [513, 654, 655]. Spontaneously grown green-emitting InGaN/GaN QDs nanowire array generally exhibit spectral FWHM linewidths in the range of ~ 58-87 nm [254, 463, 472, 473]. Broad emissions of spontaneously grown InGaN/GaN QDs nanowire array are resulted from InGaN alloying, large inhomogeneous distribution of In content in each nanowire, and compositional variations due to fluctuations in nanowire diameter and position in the spontaneous formation [463]. With precisely controlled nanowire size and position, green-emitting InGaN/GaN QW nanowire arrays (thickness of active segment: ~ 50 nm) selective-area grown on GaN/sapphire generally exhibit narrower spectral linewidths, such as linewidth of 27 nm (135meV) [497] with the peak wavelength of 506 nm and linewidths of 31.5-37.5 nm with the peak wavelength of 529.1-543.3 nm [656]. In this study of nanowire arrays selective-area grown on Si substrate, the incorporation of Al in active segment and increased thickness of active segment (~ 5 times thicker) do not increase

the linewidth (32.4-42.9 nm with $\lambda_{PL\ peak}$ in the range of 515.8-527.9 nm) in a considerable difference, compared to the generally reported values for green nanowire arrays grown on GaN/sapphire [656],.

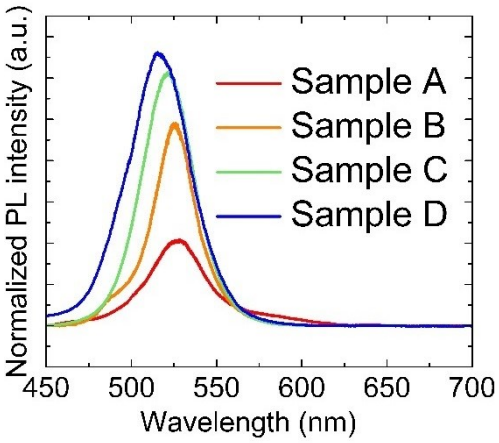

Figure 7-3: (a) PL spectra of (Al)InGaN nanowires A, B, C and D grown using different growth conditions summarized in Table 7-1, showing a blueshift in the emission peak with the increasing Al beam equivalent pressure (BEP) and increasing growth temperature (T_{growth}).

To reveal the nature and growth mechanism of selective-area grown AlInGaN nanowire heterostructures, structural characterizations were further performed using scanning transmission electron microscopy (STEM) and element energy dispersive spectroscopy (EDS) analysis. The high-angle annular dark-field (HAADF) atomic-number contrast image of a AlInGaN nanowire heterostructure is shown in Figure 7-4 (a), in which the distribution of light elements (Al element) show dark constract and heavy elements (In element) show bright constrast. In Figure 7-4 (a), it is presented clearly from bottom to top that *n*-GaN segment, AlInGaN active segment and *p*-GaN segment exhibit tapered and facted hexagonal structure with Ga polarity. The HAADF image of AlInGaN segments presents bright contrast at the center and dark contrast at the sidewall, indicating the formation of a core-shell structure.

In order to identify the Al, Ga and In element distributions, EDS elemental mapping scans was performed corresponding to AlInGaN segment in the HAADF image. As shown in Figure 7-4 (b), the Al and In elemental distributions of AlInGaN segment exhibit tapered structure,

which is consistent to what are observed from HAADF images and SEM images. The In element exhibits high-density distribution at the center and low-density distribution at the sidewall of AlInGaN segment, and In element is well confined in the center region of the AlInGaN segment. In addition, the Al and Ga element extend over a wider range than In element over the radial direction of AlInGaN segment, indicating the formation of AlGaN shell is formed surrounding an In-rich core region.

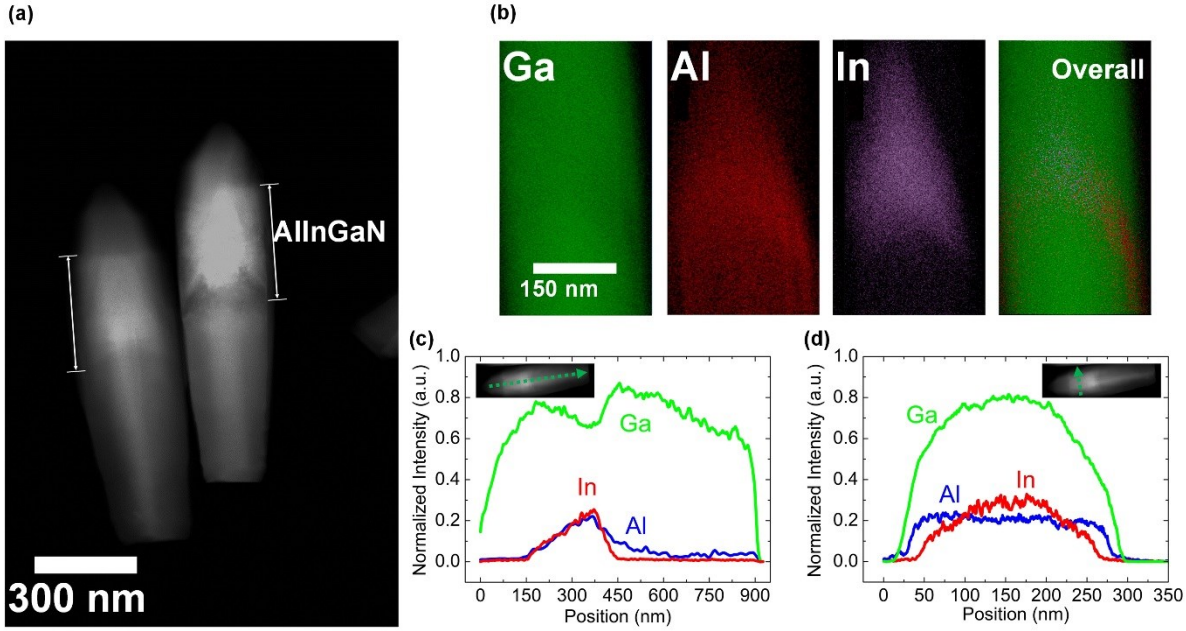

Figure 7-4: (a) An HAADF-STEM image of a GaN:Si/AlInGaN/GaN:Mg nanowire heterostructure epitaxially grown on Si substrate. The labelled regions are AlInGaN active segments showing the In-rich AlInGaN core and AlGaN shell by atomic-number contrast. (b) EDS elemental mapping images of the variations in Ga, Al, In and overall elemental distribution within AlInGaN active segment showing the presence of In-rich AlInGaN core and AlGaN shell. Quantitative variation of Ga, Al and In elemental profiles derived from EDS line scans (c) along longitudinal direction as marked by dashed line in the inset image and (d) along radial direction as marked by dashed line in the inset image, respectively, presenting an AlInGaN core-shell structure.

To further reveal the compositional variation precisely, EDS line scans were conducted along the nanowire longitudinal and radial directions. As shown in Figure 7-4 (c), the elemental profiles along the longitudinal direction (the inset image of Figure 7-4 (c)) present clearly one

AlInGaN segment in the middle region and two GaN segments in the top and bottom regions of the nanowire. The variations of In, Ga and Al signals in the active segments are resulted from the tapered nanowire heterostruture. As shown in Figure 7-4 (d), EDS line scan along the radial direction (the inset image of Figure 7-4 (d)) reveal the composition variations laterally. Shown in Figure 7-4 (d), the In content exhibits a maximum at the nanowire center and drop remarkably towards the sidewalls. In contrast, the Al and Ga signal extend over the whole line scan range. The results of EDS line scan along radial direction are consistent with conclusions based on the observations and analyses on HAADF images and EDS mapping scans, providing unambiguous evidences for the In-rich core and AlGaN shell nanoscale heterostructure formed in AlInGaN nanowires selective-area grown on Si substrate. The underlying formation mechanism of such an In-rich core and In-deficient shell structure is directly related to strong In desorption and low In incorporation at the lateral surfaces. At relatively high growth temperatures, In atoms experience much stronger thermal desorption compared to Ga and Al atoms [105]. At the top surfaces of the growth front, the direct impingent In adatoms and diffusive In adatoms can immediately compensate the desorbed In atom. In constrast, the supply of In adatoms to the lateral surfaces is limited due to the the shadowing effect of neighboring nanowires [105, 657]. In addition, In incorporation on m-plane is very low compared to that on polar and semi-polar planes under identical growth conditions [658]. The spontaneous formation of the large bandgap AlGaN shell surrounding the In-rich core is also attributed from the smaller Al adatom diffusion length compared to Ga and In adatoms [252]. Due to its small diffusion length, Al adatoms incorporate at the sidewall of bottom GaN:Si segment, which is justified by the Al signal extending over bottom GaN:Si segment (position from 450 to 940 nm in Figure 7-4 (c)). Accompanied with such Al incorporation at the sidewall of bottom GaN:Si segment, at the growth front of AlInGaN active segment, the Al adatoms facilitate the lateral growth of AlGaN shell up to the thickness of 18-37 nm as well as the

longitudinal growth. Importantly, such a large bandgap AlGaN shell provides a radial surface passivation for In-rich core to suppress nonradiative surface recombination of nanowire active segment [581].

To further reveal the effect of Al incorporation on thick active segment of SAE nanowire array, extensive power-dependent PL measurements have been conducted on Nanowires A (InGaN) at room temperature (RT) and Nanowires C (AlInGaN) at both room temperature and 78.0 K. Variations of PL peak wavelength, FWHM of PL peak, and integrated PL peak versus excitation power are summarized in Figures 7-5 (a), (b) and (c), respectively.

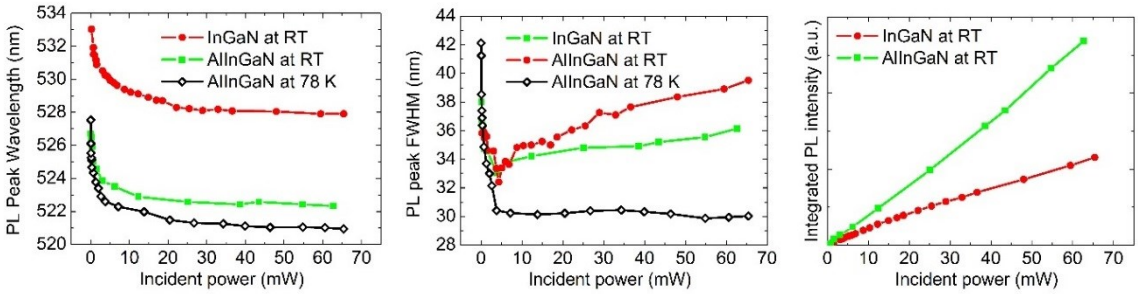

(a) (b) (c)

Figure 7-5: Variations of (a) PL peak wavelength, (b) FWHM of PL peak, and (c) integrated PL peak intensity versus excitation power, summarized from PL spectra of Nanowires A (InGaN) measured at room temperature (RT) and Nanowires C (AlInGaN) measured at both room temperature and 78.0 K. The excitation power was varied in the range of 0.24-65.42 mW for the measurement of InGaN nanowire at RT, in the range of 0.10-62.7 mW for the measurement of AlInGaN nanowire at RT, and in the range of 0.03-65.4 mW for the measurement of AlInGaN nanowire at 78.0 K.

As observed in Figures 7-5 (a) and (b), the blueshift of peak wavelengths and the narrowing of emission peaks from the measurements at both room temperature (RT) and 78.0 K are remarkable in the low-power range (less than ~ 4.34 mW), resulted mainly from state filling of localized states formed by potential fluctuation and the screening of quantum-confined Stark effect (QCSE). The presence of QCSE leads to redshift in the emission energy, however, photoexcited carrier screens the electric field and results in reduction of the QCSE

[659-662]. The screening of QCSE is enhanced with increasing excitation power, leading to blueshifts in emission energy and narrowing of emission peaks. As shown in Figures 7-5 (a) and (b), in the low-power range, the emission peak of AlInGaN nanowires measured at 78.0 K show a larger blueshift and a more significant narrowing than that measured at room temperature, indicating there are considerable thermal broadening effect and thermal redshift effect on nanowires measured without cooling at room temperature. As shown in Figure 7-5 (a), with excitation power varied in the range from 0.24 to 65.42 mW, the PL peak wavelength of InGaN nanowires exhibits a blueshift from 533.03 nm to 527.91 nm, corresponding to an increase in the peak photon energy of 22.58 meV. In the above excitation power range, the PL peak wavelength of AlInGaN nanowires exhibits a smaller blueshift from 526.48 to 522.33 nm at room temperature, corresponding to an increase in the peak photon energy of 15.27 meV which is smaller than that of InGaN nanowires. The smaller blueshift observed from AlInGaN nanowires could be attributed to reduced QCSE in AlInGaN active segment benefited from less internal stress field due to Al incorporation into InGaN. In the high-power range of Figure 7-5 (a), there are weak peak blueshifts attributed mainly from state filling effect, considering that QCSE is suppressed in high power range. In the high-power range, InGaN and AlInGaN nanowires excited at room temperature exhibit remarkable linewideth broadening, while there is no significant varations in the PL linewidths of AlInGaN nanowires cooled at 78.0 K. The linewideth broadening of AlInGaN nanowires in the high-power range is moderate compared to that of InGaN nanowires. This indicates that there are less thermal broadening effects on AlInGaN nanowires array, benefiting from suppressed non-radiative recombinations occuring at the surface of nanowire active segments. As shown in Figure 7-5 (c), with the PL intensity integrated over the 2FWHM width range of emission peaks, the integrated PL intensity of AlInGaN nanowires is nearly 2.4 times as high as that of InGaN nanowires arrays grown without Al incorporation, attributed to the reduced surface recombination and two-dimensional

radial effective carrier confinement offered by the core-shell structure. The excellent quality of these AlInGaN nanowire arrays is evidenced by the PL characteristics and the following demonstration of improved nanowire solar cells with stable and improved output characteristics compared to the previously reported.

7.4 Device Fabrication of AlInGaN Nanowires on Si Substrates

Shown in the schematic of the selective-area grown nanowire device in Figure 7-6 (a), GaN:Si/AlInGaN/GaN:Mg nanowire arrays selective-area grown can be fabricated to form a vertically conductive device integrating *n*-type Si substrate which exhibits high electrical and thermal conductivity.

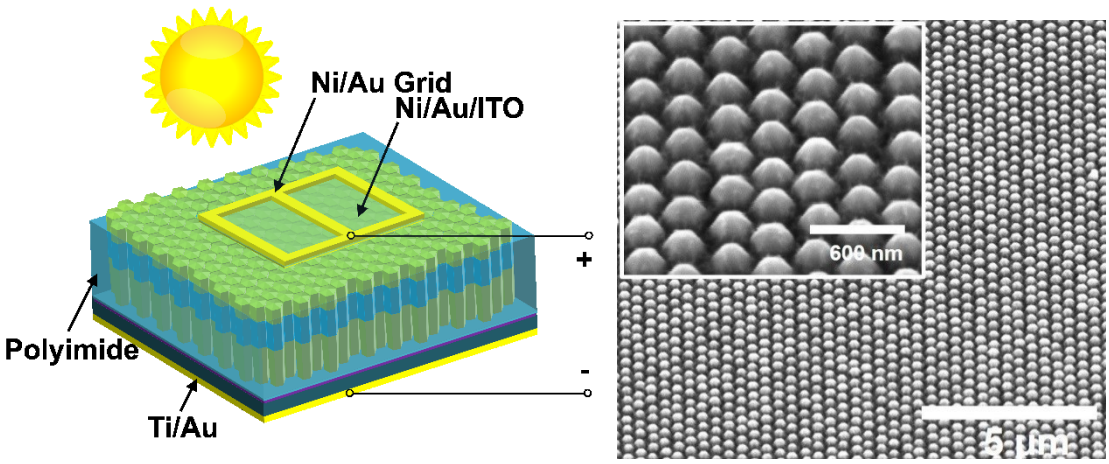

(a) (b)

Figure 7-6: (a) Schematic illustration of GaN:Si/AlInGaN/GaN:Mg nanowire solar cell device on Si substrates. The top *p*-contact consisting of thin Ni/Au layers and a ITO layer exhibits high visible transmissivity. Ni/Au metal grid and Ti/Au metal layer were deposited on the top *p*-contact and backside of *n*-type Si substrate to supply electricity to an external circuit. (b) Bird's-eye-view SEM image of exposed GaN:Mg regions of nanowire array with polyimide resist filled between nanowires. The inset is magnified image of exposed GaN:Mg regions.

The fabrication process of 10×10 μm^2, 30×30 μm^2 and 90×90 μm^2 SAE nanowire devices on Si substrates included the following steps. After the removal of SiO_x layer at the backside of Si substrates by dipping samples in BOE, Ti (20 nm)/Au (100 nm) metal layers were deposited by e-beam evaporator at the backside of Si substrates to serve as *n*-metal contacts.

A polyimide resist layer was spin-coated onto samples to fully cover the nanowire arrays for planarization, followed by O_2 plasma RIE to expose the GaN:Mg surfaces at the top of the nanowires. The exposed GaN:Mg regions were shown in Figure 7-6 (b).

Thereafter, a SiO_x dielectric layer was deposited onto exposed GaN:Mg nanowire arrays, followed by standard photolithography and etching techniques to create 10×10 μm^2, 30×30 μm^2 and 90×90 μm^2 openings. After the samples were dipped in concentrated HCl (37%) for 1 min to remove any surface oxides at the exposed GaN:Mg surfaces, thin Ni (6 nm)/Au (6 nm) metal layers were then deposited by e-beam evaporator to serve as *p*-metal contacts. Following that, a 100 nm indium tin oxide (ITO) layer was deposited by radio frequency sputtering for efficient carrier transport. Figure 7-7 (a) shows the nanowire device surface after the *p*-contact (Ni/Au/ITO) layers lift-off. The *p*-contact layers were further processed with two-step annealing including a rapid thermal annealing at ~ 550 °C in N_2 gas ambient for 1 min and an annealing at 300 ℃ for 1 hour in vacuum. To facilitate hole collection or current spreading, Ti (20 nm)/Au (100 nm) metal grid patterns were then deposited on the transparent ITO by standard photolithography, metal deposition and lift-off.

7.5 Photovoltaic Characteristics of AlInGaN Nanowire Light-Emitting Solar cells

7.5.1 Photovoltaic and EL Characterization Methods

The electroluminescence characterizations of SAE nanowire devices were performed using a source meter (Keithley, SMU 2400). The *p*-metal pad at the top surface of a sample and *n*-metal at the backside of Si substrate were probed for current injection to SAE nanowire devices.

The current-voltage characteristics of SAE nanowire solar cells were measured in the dark environment and under the illumination of 100 mW/cm^2 from an AM 1.5G solar simulator (Newport, Oriel, LCS-100). The current-voltage characterizations under concentrated light were further carried out under the illumination of 3 W/cm^2 from a Xenon arc lamp (Excelitas

Technologies, Cermax, R400-1) with an AM 1.5G filter. The filter tailors the spectral distribution of the Xenon arc lamp to match that of AM 1.5G. To study the dependences of short-circuit current density (J_{sc}), open-circuit voltage (V_{oc}), fill factor (FF) and efficiency (η) on sample temperature, current-voltage characteristics of SAE AlInGaN nanowire solar cells were further measured on a cold plate (TE technology Inc., CP-031) integrated with a thermoelectric temperature controller (TE technology Inc., TC-48-20) under the illumination of 3 W/cm^2 from a Xenon arc lamp.

7.5.2 Photovoltaic Characteristics of Light-Emitting Nanowire Solar Cells

Important to achieve high efficiency is a precise control of size and morphology of AlInGaN nanowires to achieve nearly dislocation-free nanowire array exhibiting a high degree of size uniformity as well as a high packing efficiency. Due to the insufficient absorption of solar radiation low packing efficiency or low surface coverage of nanowires practically limit the energy-conversion efficiency of nanowire photovoltaics and other nanowire optoelectronics applications. Schematically shown in Figure 7-6 (a), the top-illuminated SAE nanowire solar cell absorbs the photons through thick AlInGaN segments, produce holes and electron carriers, and supply photocurrent to an external circuit through top and bottom ohmic contacts. The device fabrication, enlargement and scale-up of such vertically conductive nanowire devices are relatively simple, compared to devices using horizontal conductions.

As shown in Figure 7-7 (b), the current-voltage output characteristic of Nanowire A (InGaN) exhibit a relatively low V_{oc} of 0.344 V and the current density increases remarkably in the reverse biasing region, indicating a considerable leakage current in the device of Nanowire A. The performance of Nanowire A (InGaN) is severely limited by carrier leakage and the significant nonradiative carrier recombination associated with the presence of surface states on the surface of nanowire active segments. V_{oc}, FF and η of nanowire devices increase remarkably with the increase in the Al incorporation in active segments, attributed to afore-

observed core-shell nanoscale heterostructures which can provide effective two-dimensional (2D) carrier confinement in the active segment and effectively suppress nonradiative carrier recombination and carrier leakage on the nanowire surface. The measured V_{oc}, FF and η of AlInGaN nanowire solar cells are much larger than the commonly reported values for InGaN nanowire solar cells [645, 646], and the measured J_{sc} is in the range of the commonly reported values [303, 645, 646].

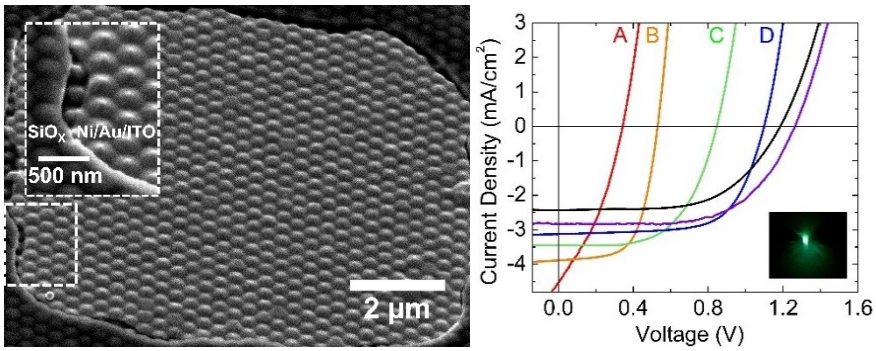

(a) (b)

Figure 7-7: (a) Bird's-eye-view SEM image of SAE AlInGaN nanowire array at the top of which *p*-contact (Ni/Au/ITO layers) are selectively deposited in the opening of SiO_x dielectric mask. The inset of (b) is magnified SEM image near the boundary between SiO_x mask and *p*-contact area. (c) Current-voltage output characteristics of SAE nanowires solar cells on Si substrates using Nanowire A, B, C, D and other two AlInGaN nanowire samples with higher Al composition. The measured samples differ in the growth parameters of (Al)InGaN active segments. The EL image of one 10×10 μm^2 green-emitted SAE AlInGaN nanowire device is shown in the inset of (b).

The EL image of one 10×10 μm^2 green-emitted SAE AlInGaN nanowire device is shown in the inset of Figure 7-7 (b). It may be noted that there is a small variation in the PL wavelengths of the devices AlInGaN segments of Nanowire A, B, C and D, which may not lead to any major difference on the V_{oc} and device efficiency. Compared to the remarkable increase in V_{oc} from 0.344 V of Nanowire A (InGaN) solar cell to 1.103 V of Nanowire D (AlInGaN) solar cell, the increase in FF from 0.385 of Nanowire A (InGaN) solar cell to 0.659 of Nanowire D (AlInGaN) solar cell and the increase in η from 0.585 % of Nanowire A

(InGaN) solar cell to 2.27% of Nanowire D (AlInGaN) solar cell achieved through optimum Al incorporation in active segments, the variation of 2.349-2.404 eV in PL peak photon energy is negligible. However, with the increase in the Al incorporation in active segments, the short-circuit current density (J_{sc}) reduced from 4.415 mA/cm^2 of Nanowire A (InGaN) solar cell to 3.123 mA/cm^2 of Nanowire D (AlInGaN) solar cell.

The usage of concentrated sunlight usually increases the production of solar energy logarithmically per unit area due to increased photovoltage efficiency with light intensity, utilizing the solar radiance better and reducing the required solar-cell area, the amount of used semiconductor material, and cost [663]. To explore the potential and performance of SAE AlInGaN nanowire devices on Si substrate for operating under highly concentrated solar radiance, the output characteristics of Nanowire D solar cell were further measured under the illumination of 30-Sun light intensity.

As shown in Figure 7-8, in the dark environment, the AlInGaN nanowire solar cell exhibit good diode characteristics, with a rectifying ratio of ~ 313 measured at −1.0 and 1.0 V. J_{sc}, V_{oc}, FF and η of Nanowire D solar cell were measured to be 83.43 mA/cm^2, 1.409 V, 0.628 and 2.46% under 30-Sun illumination. As the light intensity is increased from 100 mW/cm^2 to 3 W/cm^2, the J_{sc} increases dramatically and V_{oc} depends logarithmically on J_{sc}, driving the rise of efficiency η under concentrated solar light illuminations. However, the J_{sc} does not exhibit exactly linear dependence on intensity, which might be due to the cooling of nanowire solar cell to 1.4 °C. Notably, 30-sun illumination yielded a high J_{sc} of 83.43 mA/cm^2 and a high V_{oc} of 1.409 V for a selective-area grown AlInGaN nanowire device on Si substrate, promising for high-power photovoltaics and other nano-optoelectronics applications. Figure 7-8 shows that output characteristic of output power versus V_{oc} strongly depends on the temperature of cold plate, due to the heating effect of concentrated light generated by Xenon arc lamp as well as heat generation from the light not absorbed and not ultilized by nanowire arrays.

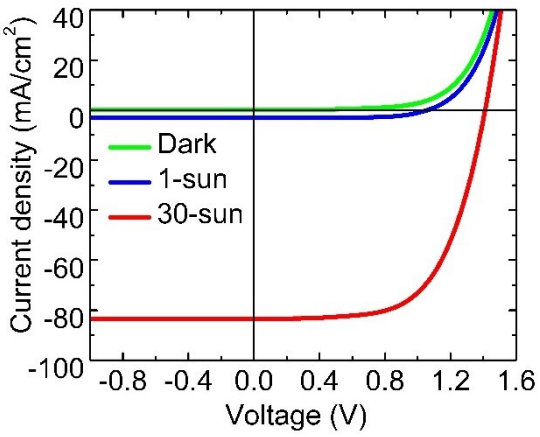

Figure 7-8: Current-voltage output characteristics of nanowire D solar cell measured in dark environment, under the illumination from an AM 1.5G solar simulator and under 30-Sun illumination from a Xenon arc lamp integrated with an AM 1.5G filter. For the measurement with 30-Sun illumination, the nanowire device was placed on a cold plate cooled to 1.4 ℃.

As summarized in Figure 7-9 (a), with the increased temperature of cold plate from 1.4 °C to 27.0 °C, V_{oc} of SAE AlInGaN nanowire solar cell decreases from 1.409 V to 1.307 V and J_{sc} increases from 83.43 mA/cm^2 to 89.43 mA/cm^2. As shown in Figure 7-9 (b), without the usage of cold plate for cooling, the AlInGaN nanowire solar cell exhibits stable and repeatable V_{oc} under the 30-Sun illumination. This observation provide unambiguous evidence for the robustness and stability of such vertical-type device of SAE AlInGaN nanowire integrated with Si substrate.

However, the further increased Al incorporation lead to reductions in J_{sc} and η measured from two other AlInGaN nanowires sample, due to the increased bandgap of AlInGaN active segment and possible generations of defect and dislocations associated with inhomogeneous strain and alloying.

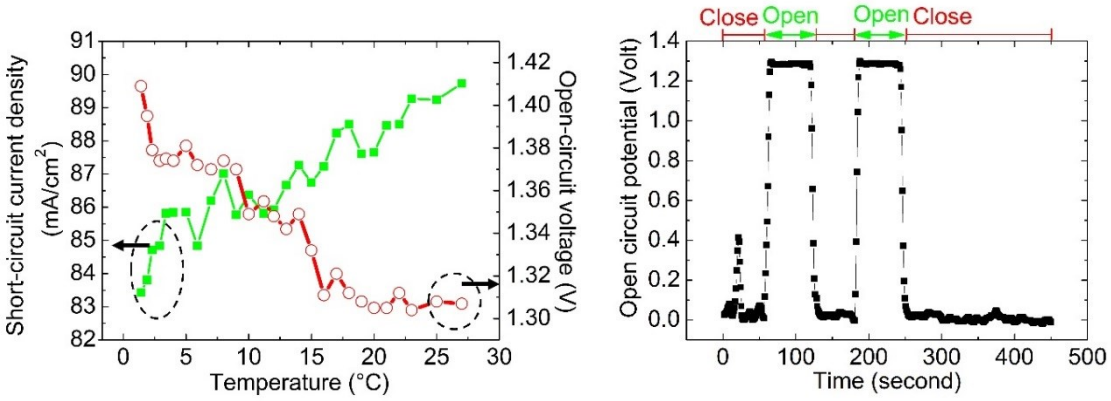

(a) (b)

Figure 7-9: (a) Variations of short-circuit current density (J_{sc}) and open-circuit voltage (V_{oc}) versus substrate temperature, summarized from current-voltage characteristics of nanowire D solar cell measured at different cold plate temperature under 30-Sun illumination. (b) Variations of open-circuit voltage (V_{oc}) versus time, indicating the stability of nanowire solar cell device. Without the cooling of cold plate, V_{oc} was measured from nanowire D solar cell in dark enviroment or under 30-Sun illumination from a Xenon arc lamp integrated with an AM 1.5G filter.

Table 7-2 summarizes the growth conditions of Nanowires E and F with higher Al compositions than those of Nanowires A, B, C and D. Compared to the small blueshift in peak wavelength of Nanowires A, B, C and D from 527.9 to 515.8 nm (photon energy of 2.349-2.404 eV), the greatly increased Al incorporation in Nanowires E and F lead to remarkable blueshift in PL emission from green emissions of Nanowires A, B, C and D to blue emission (465 nm) of Nanowire E and deep-blue emission (432 nm) of Nanowire F.

Table 7-2: Growth conditions of AlInGaN segments with higher Al composition.

Sample	BEP_{Al} ($\times 10^{-9}$ Torr)	BEP_{In} ($\times 10^{-8}$ Torr)	BEP_{Ga} ($\times 10^{-8}$ Torr)	T_{growth} [°C]
E	6.78	11.23	2.23	725
F	7.54	11.23	2.23	725

As shown in Figure 7-7 (b), the current-voltage output characteristic of Nanowires E and F exhibit relatively low current desnsity (J_{sc}) than Nanowires A, B, C and D, exhibiting relative

lower fill factor (FF) in the range of 0.594-0.615 and lower power-conversion efficiency (η) in the range of 1.71-2.19%. Open-circuit voltage of Nanowire F is 1.184 V, relatively lower than that of Nanowires E (1.264 V), possibly due to the presence of dislocation and defect associated with the dramatically increased Al incorporation.

7.6 Summary

The work discussed in this chapter presents two technical progress including I) the development of green-emitting AlInGaN nanowire array selective-area grown on patterned Si substrates with AlN/GaN:Ge buffer template, and II) the development of a relatively simple approache to suppress the nonradiative surface recombination of selective-area grown nanowires with a thick (Al)InGaN-based active segment for photovoltaics applications. This green-emitting AlInGaN nanowire solar cells monolithically integrating the solar energy harvesting and light emission through a single chip [648-651].

With precisely controlled dimensions and position, uniform and close-packed AlInGaN nanowire array can make efficient optoelectronic devices filling the "green gap" for the applications for optically-pumped green emitter, LEDs, photovoltaics and photodetections on low-cost, large-area Si substrate [174, 175, 647].

During the selective area epitaxy of AlInGaN segments, In-rich core and an Al-rich shell were spontaneously formed due to the stronger In desorption compared to Ga and Al atoms on the nanowire lateral surfaces and the smaller Al adatom diffusion length compared to Ga and In adatoms [252, 664, 665]. The spontaneously formed core-shell structure can effectively suppress the nonradiative surface recombination, leading to improved photovoltaic characteristics. The use of a relatively thick active segment (~ 0.29 μm), AlInGaN core-shell structure and Si substrate in this work significantly increase the device stability and performance under high-power and relatively high-temperature operation, by highly absorbing of concentrated light intensity, minimizing nonradiative recombination, and enhancing the heat

dissipation, respectively. The power conversion efficiency of fabricated nanowire solar cell can be further improved by increasing the In composition to improve light absorption, optimizing Mg incorporation in the *p*-GaN segment (Mg:GaN) to achieve bettter carrier collection and improving light absorption through photonic crystal effect of nanowire array.

Chapter 8: Summary and Future Work

8.1 Summary of Research Work in this Dissertation

Driven by the needs for smaller size, reduced power consumption, enhanced efficiency and more advanced functions, extensive demanding applications require the development of high efficiency micro-scale or nano-scale photonic and electronic devices. Micro-scale and nano-scale materials and devices can be used for the integration into a limited space, the integration of dense devices into photonic and electronic systems, or the shrinkage of overall systems. For example, ultrahigh-resolution display technologies require the development of micro-scale color-tunable pixels monolithically integrated on a single chip [666].

The challenges in using organic materials and devices for these applications include limited lifetime [667], relatively expensive manufacturing process, relatively low efficiency and brightness, and poor stability [171, 172, 668]. Moreover, it has remained difficult to achieve micro-scale and nano-scale devices using organic materials [669, 670]. GaN-based planar heterostrucutres are bright, stable and efficient, but it has remained difficult to achieve efficient devices in the deep green, yellow and red spectral range by using GaN-based planar heterostrucutres [55, 56, 91, 671-674]. Smaller μm-scale InGaN-based epilayer LEDs exhibit better current spreading, higher maximum endured current density, more stable performance at high temperature, and wider droop-free regions in terms of current density, compared to larger devices [133, 530, 536-539]. It is very promising to use GaN-based materials for manufacturing μm-scale color-tunable LED devices, in contrast to OLED technology which currently exhibit lower efficiencies at smaller device size. However, the fabrication of μm-scale InGaN-based epilayer emitters involves the use of dry etching process which introduce significant sidewall damage.

Dislocation-free GaN-based nanowires have emerged as a promising candidate for applications in photonic and electronic devices. GaN-based nanowire heterostructures grown

on lattice-mismatched substrate can be nearly free of defects [96-101]. To date, with the use of InGaN nanowire structures, high efficiency emissions across the entire visible spectral range have been demonstrated [104, 105, 177]. This dissertation focuses on the development of GaN-based nanowire heterostructures by using *radio frequency plasma-assisted* molecular beam epitaxy (MBE) as well as their various device applications for displays, illuminations, photovoltaics and transistors.

To realize controllable and tunable full-color light generations from μm-scale LED devices, blue, green/yellow, and orange/red InGaN nanowire LEDs have been monolithically integrated on Si substrates. Such multi-color nanowire LED arrays are fabricated using a three-step selective-area MBE growth process on Si substrates using SiO_x mask. By varying the injection current to each monochromatic LED subpixel, the spectral power distribution of mixed light can be controllably tuned. The lateral-arranged monochromatic subpixels enable controlled light mixing at the chip level and yield color-tunable light emission with CCT values in the range from 1900 K to 6800 K, while maintaining excellent color rendering capability. Very large CRI values (> 85) can be achieved for devices with warm and neutral white light emissions (CCT < 5000 K), show the capability and accuracy of this approach for color tunability. The overall color-tunable InGaN pixel size of ~ 0.016 mm^2 was achieved by using this approach. However, this approach requires three growth processes which is relatively complicated.

In previous three-step selective-area growth using SiO_x mask, each single-color μm-scale LED were made using spontaneously grown InGaN/GaN nanowires which exhibit considerable fluctuations in nanowire length, diameter and position. Such fluctuations in morphology and geometry result in considerable variations in InGaN composition and non-uniform current injection in each device. Selective area epitaxy enables one to precisely control the size, position and morphology of nanowires, and hence achieve precisely controlled and

tunable emission wavelength. By incorporating InGaN QDs in nanowire arrays, diameter-dependent emissions tuned from blue to red was achieved from the GaN-based single nanowires with different diameter on the same substrate and its mechanism was investigated. InGaN/GaN nanowire array show a redshift in emission with increasing nanowire diameter but a consistent spacing, due to the shadowing effect of neighboring nanowires in arrays with high packing density. Through selective area epitaxy of RGB GaN-based nanowire array on GaN/sapphire substrates with Ti-mask, a full-color pixel size of 7×7 μm^2 has been achieved.

The diameter-dependent emission of selective-area grown InGaN/GaN QDs single nanowires and its underlying mechanism is distinctly different from that of selective-area grown InGaN/GaN nanowire array. Due to more dominant contribution for In incorporation from the lateral diffusion of In atoms, the incorporation of In atoms at the nanowire top during the growth of InGaN/GaN active region is hindered with increasing nanowire diameters, resulting in the blue-shifting of the PL peak position with increasing diameter of single nanowires. Based on this achievement of full-color single nanowires selective-area grown on the same substrate, for the first time, the world's smallest pixel size, high performance full-color InGaN/GaN single nanowire LED pixel has been developed by using only one step epitaxial growth process. Compared to conventional planar devices, such nanowire LED pixels offer several distinct advantages, including significantly reduced dislocations and polarization fields, enhanced light extraction efficiency, controllable radiation pattern, tunable emission, and efficient current conduction and heat dissipation. Such nanowire LEDs also exhibit superior electrical performance, with a turn-on voltage of ~ 2 V and negligible leakage current under reverse bias. The monolithic integration of full-color LEDs on a single chip, coupled with the capacity to tune light emission characteristics at the single nanowire level, provides an unprecedented approach to realize ultra-small and efficient projection display, smart lighting, and on-chip spectrometer.

Recent studies have shown that the surface charge properties play a dominant role on the performance of nanowire devices such as nanowire LEDs and nanowire solar cells, due to the large surface-to-volume ratio. The commonly reported axial nanowire LEDs generally exhibit very low output power, due to large surface recombination and the resulting poor carrier injection efficiency. The output characteristics of axial nanowire solar cells are also limited by surface recombination.

Spontaneously grown AlInGaN quaternary core-shell nanowire heterostructures have been demonstrated on Si substrate, wherein an In-rich core and an Al-rich shell were spontaneously formed during the epitaxial growth process. Such core-shell structures can largely suppress nonradiative surface recombination, leading to a significant enhancement of carrier lifetime from ~ 0.2 ns to ~ 2 ns and output power. By varying the growth conditions, the emission wavelengths can be tuned from ~ 430 nm to ~ 630 nm.

It is highly desirable to develop precisely-controlled GaN-based nanowires on Si substrate using selective area epitaxy for various device applications such as vertical GaN-based nanowire field effect transistors (FETs) using wrap-around gate and InGaN/Si integrated double-junction solar cells. However, the current selective area epitaxy on Si substrate rely on the use of thick semiconducting buffer layers with large bandgap and the electrical and thermal advantages of Si substrates cannot be used for nanowire devices. To search the buffer layers suitable for selective area epitaxy on Si substrates, the effects of different ultra-thin buffer layers on the morphology of GaN nanowires have been investigated. With AlN/GaN:Ge buffer layer, uniform GaN nanowire array can be aligned vertically on Si substrate and exhibit smooth surfaces. Moreover, the high electrical conductivity of ultra-thin buffer layers has been justified by the resistance measurement of Si substrates deposited with ultra-thin AlN/GaN:Ge buffer template, output characterizations of Si solar cell with a ultra-thin AlN layer. Also, photoelectrochemical characteristics of current saturation has been improved and relatively

high photo-current density has been achieved using large area *n*-GaN nanowire array selective area grown on Si substrates. Electrical transport properties of vertically-aligned *n*-*i*-*n*-n^+ GaN single nanowires on Si substrate have been systematically studied by using *in-situ* nanoprobing inside a SEM chamber. By tuning the Si doping concentration in n^+-GaN segment, a high maximum current density of 4.65 MA/cm^2 and a high maximum electric field of 170.2 KV/cm have been achieved.

With precisely controlled dimensions and position, uniform and close-packed AlInGaN nanowire array was selective-area grown on Si substrates. Extensive structural characterizations provide unambiguous evidences for the spontanous formation of In-rich core and AlGaN shell nanoscale heterostructure in AlInGaN active segment. The spontaneously formed core-shell structure can effectively suppress the nonradiative surface recombination, leading to improved photovoltaic characteristics. It is demonstrated that the Al incorporation maintains its effectiveness on surface passivation in selective-area epitaxy of much thicker active segments (~ 0.29 μm) for photovoltaics applications. The use of a relatively thick active segment (~ 0.29 μm), AlInGaN core-shell structure and Si substrate significantly increase the device stability and performance under high-power and relatively high-temperature operation, by highly absorbing of concentrated light intensity, minimizing nonradiative recombination, and enhancing the heat dissipation, respectively. This green-emitting AlInGaN nanowire solar cells monolithically integrating the solar energy harvesting (from light to electricity) and light emission (from electricity to light) through a single chip.

8.2 Suggested Future Work

In Chapter 6 and Chapter 7, taking advantages of ultra-thin AlN/GaN:Ge buffer template, uniform and high quality GaN-based nanowire arrays and their devices have been developed on Si substrate using selective area epitaxy. However, the effects of ultra-thin AlN buffer layer on the nucleation and polarity of subsequently grown GaN buffer layer and GaN-based

nanowire still need further investigations. It is also promising to improve the characteristics of nanowire devices by controlling the polarity of nanowires selective-area grown on Si substrates. As elaborated from Chapter 3 to Chapter 7, various techniques and knowledge have been developed in the growth, device fabrications and characterizations of GaN-based nanowire heterostructures and their device applications for displays, illuminations, photovoltaics and transistors. Based on those techniques and knowledge, the following works are proposed to develop monolithic In(Ga)N/Si double-junction and multi-junction solar cells and color-tunable surface-emitting lasers.

8.2.1 Efficient Yellow, Red and Near-Infrared GaN-based Nanowire Devices Grown on Si Substates Using Polarity-Controlled Ultra-Thin AlN/GaN Buffer Template

The top morphology of nanowire, such as apex-like or being completely flat or tripod, cannot be controlled by varying the patterning design of Ti mask for selective area epitaxy. However, the top morphology of GaN nanowire is very critical for the formation of InGaN quantum dots (Figure 4-9) as well as engineering the photonic crystal effect of InGaN nanowire array. The various top morphology is results of different nanowire polarity, as shown in Figures 8-1 (a) and (b). The polarity affects many properties of GaN-based materials, including growth kinetics, incorporation of dopants and built-in polarization fields [675, 676]. Moreover, InGaN/GaN quantum nanostructures forming on r-plane facets can lead to the advantages of reduced QCSE which acts as the key factor for resolving the “efficiency gap” of GaN-based materials in the yellow, red and near-infrared spectral range. So, it is important to precisely control the top morphology of GaN-based nanowire heterostructures which is related to their polarity.

It has been recently found that, the morphology and polarity of selective-area grown GaN nanowires mainly depend on the polarity of the underlying AlN buffer layer which can be controlled by varying V/III flux ratios the AlN growth [404, 519, 602]. The different polarity

of GaN nanowire can be achieved by controlling N-polar or Ga-polar nucleation layer [404, 519, 602] which is the GaN buffer layer grown on AlN buffer layer in this study. It was reported that the polarity of GaN buffer layer is determined by the underlying AlN buffer layer which adopts N-polar by Al-rich growth conditions and Al-polar by N-rich conditions [602]. Namely, the AlN buffer layer adopting either Ga-polar or N-polar nucleation layer can be used to grow Ga-polar or N-polar GaN-based nanowire heterostructures, as shown in Figures 8-1 (a) and (b).

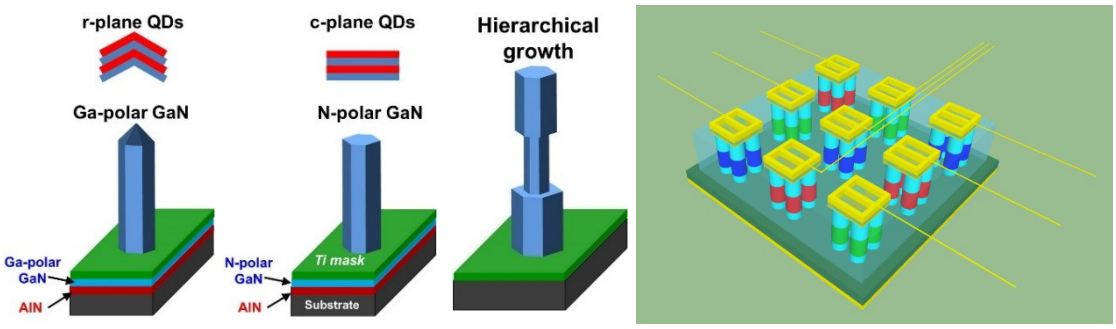

Figure 8-1: Schematics of (a) Ga-polar and (b) N-polar GaN-based nanowire heterostructures selective-area grown by controlling the polarity of underlying AlN/GaN buffer template. (c) Hierarchical structure of GaN-based nanowire heterostructure formed by using a pulsed growth mode. (d) Shematic of efficient micro-scale color-tunable array of RGB nanowire LEDs on a single Si substrate using ultra-thin polarity-controlled AlN/GaN:Ge buffer template.

Additionally, if the polarity and morphology of the GaN nanowires can be precisely controlled, it can improve a quantum confinement effect of the quantum dots, as well as light extraction efficiency by hierarchically varying the nanowire diameter, as shown in Figure 8-1 (c). The hierarchical structure can be formed through a pulsed growth mode, in which either the Ga supply or N supply alternately switching on and off [677, 678]. For example, with the constant N supply during the growth, relatively longer opening of Ga source shutter can result in the formation of nanowire segments with larger diameter [677, 678].

However, the effects of ultra-thin AlN/GaN buffer template on the nucleation and polarity of GaN buffer layer and GaN-based nanowire need further investigations. The polarity-

controlled ultra-thin AlN/GaN template, which exhibit high electrical conductivity, can enable the precise control of the morphology, size and position of GaN-based nanowires on Si substrates, promising efficient GaN-based nanowire devices in the yellow, red and near-infrared spectral range. Various growth parameters of AlN/GaN template and pattern designs can be investigated, and the growth conditions and fabrications for controlling the polarity of GaN-based nanowire heterostructure will be optimized. In addition, based on the development of efficient full-color GaN-based nanowires selective-area grown on Si substrates, it is further proposed to develop micro-scale color-tunable RGB pixels selective-area integrated on Si substrate, as shown in Figure 8-1 (d).

8.2.2 III-Nitride/Si Intregrated Double-Junction and Triple-Junction Solar Cells

To date, the energy conversion efficiency of solar cells can reach over 30% for two-junction cells and well over 40% for three-junction cells under concentrated sunlight illumination [21, 230]. InN nanowire solar cells [306] and (Al)InGaN nanowire solar cells has been demonstrated on Si substrate, respectively. It is highly desired to monolithically integrate high-efficiency III-V solar cells directly on low cost, large area Si solar cell to relalize full-spectrum multijunction III-nitride/Si integrated solar cells. The proposed future work is the demonstration of Si-based triple junction solar cells consisting of thin Si solar cells, nearly defect-free InN microwire sub-cell (~ 0.65) and InGaN microwire sub-cell (~ 1.8 eV). As illustrated in Figure 8-2, InGaN top-cell and InN bottom-cell will be integrated with the Si middle cell through novel ultralow resistivity *p*-Si/*n*-$In_{0.45}Ga_{0.55}N$ ohmic junction [679] and InGaN microwire tunnel junctions [269], respectively. The use of nearly defect-free InN and InGaN microwire arrays can exhibit reduced surface recombination, compared to nanowire structures. Such Si-based triple junction solar cells, if successfully demonstrated, can potentially exhibit an energy conversion efficiency >30% under one-Sun illumination and higher efficiency values under concentrated sunlight [680].

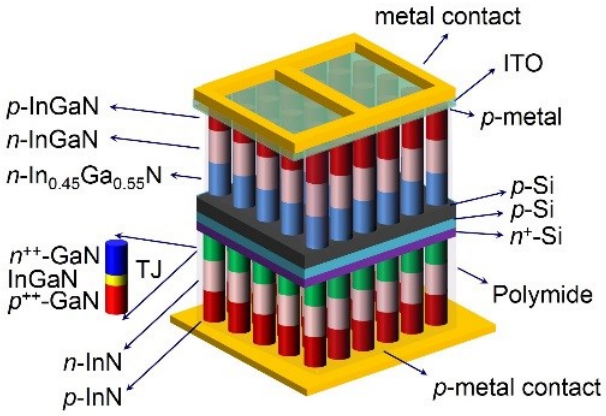

Figure 8-2: Schematic of triple-junction In(Ga)N/Si integrated solar cells. InGaN (~ 1.8 eV) top sub-cell is grown on the Si solar cell. InN solar sub-cell is grown on the opposite side of Si solar cell, and these two sub-cells are connected to the middle Si sub-cell by using the band alignment between *n*-$In_{0.45}Ga_{0.55}N$ and *p*-Si and InGaN microwire tunnel junctions, respectively.

The conduction band edge of $In_{0.45}Ga_{0.55}N$ is aligned with the valence band edge of Si. As a consequence, a low resistance ohmic junction has been demonstrated at the *n*-$In_{0.45}Ga_{0.55}N$/*p*-Si interface [679]. The electron concentration in $In_{0.45}Ga_{0.55}N$ and hole concentration in Si for this ohmic junction is ~ 1×10^{19} and 3×10^{15} cm^{-3}, respectively [679].

In this work, two critical challenges should be addressed for achieving low cost, high efficiency In(Ga)N/Si integrated multi-junction solar cells, including 1) demonstration of high quality silicon solar cell processing that is compatible with relatively low temperature growth of InGaN and InN, and 2) monolithic integration of In(Ga)N and Si solar cells through the low resistivity microwire tunnel junction which has been recently demonstrated in InGaN-based nanowires [269] and/or the low resistance ohmic junction *n*-$In_{0.45}Ga_{0.55}N$/*p*-Si interface [679]. Before the development of the triple-junction III-nitride/Si integrated solar cells, InGaN/Si integrated double-junction solar cell using *p*-Si/*n*-$In_{0.45}Ga_{0.55}N$ ohmic junction and InN/Si integrated double-junction solar cell using InGaN microwire tunnel junctions will be demonstrated firstly.

8.2.3 Micro-Scale Color-Tunable Surface-Emitting Lasers

Two-dimensional light confinement in periodic InGaN/GaN nanowire arrays and optically-pumped stimulated emissions have been demonstrated [681]. Based on the progress on micro-scale and nano-scale RGB pixels achieved by using selective area epitaxy on GaN/sapphire substrates which has been presented in Chapter 4, it is also very interesting to develop monolithically integrated color-tunable surface-emitting nanowire lasers to achieve good directionality and high output power, enabling the development of compact high-performance color-tunable miniaturized laser source for high-resolution display and visible light communications.

Some of the earliest demonstrations of GaN-based vertical-cavity surface-emitting laser (VCSELs) were achieved under optical pumping [682-688], with threshold power in the range of MW/cm^2. Recently, researchers at UCSB have demonstrated the first *m*-plane GaN VCSELs operating at 412 nm at room temperature [689]. To date, however, there have been no demonstrations of electrically injected GaN-based VCSELs operating at wavelengths beyond 465 nm. There are several critical challenges for achieving high performance GaN-based VCSELs. First, due to the relatively large lattice mismatch (~ 3%), the AlGaN DBRs generally exhibit large densities of dislocations and cracks, which leads to reduced reflectivity, enhanced nonradiative recombination, and significantly increased lasing threshold. Secondly, the realization of high efficiency electrically injected VCSELs is further limited by the poor electrical conductivity of *n*- and *p*-type $Al_xGa_{1-x}N$ layers with high-Al content.

Alternatively, surface-emitting lasers can be achieved by exploiting the two-dimensional (2D) band-edge resonant effect of a photonic crystal [488, 690-692]. At the band-edge, the group velocity of light becomes zero, and a stable 2D cavity mode is formed in the photonic crystal structure. The photonic crystal itself serves as a diffraction grating, and the output beam is emitted from the surface. Previously, an output power >1.5 W has been achieved in an

InGaAs photonic crystal surface-emitting laser operating at 941.5 nm under continuous wave operation at room-temperature [692]. However, there have been very few studies on InGaN photonic crystal surface-emitting lasers [288, 487, 693]. To date, the only reported electrically injected InGaN photonic crystal surface-emitting lasers operated in the blue-violet spectral range (λ ~ 406 nm), with large threshold current density (~ 67 kA/cm^2), due to the large densities of defects in etched planar structures [693].

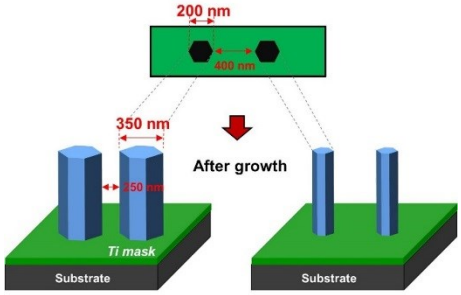

Figure 8-3 Illustrations of a pattern design of two neighboring nanoholes for the growth of nanowire array on single substrate, and two neighboring nanowires selective-area grown on the patterned substrate using different MBE growth conditions.

To achieve homogeneously distributed emission and and efficient surface-emitting InGaN-based nanowire photonic crystal laser with full-color emissions, it is very important to obtain InGaN nanowire array with uniform size, position and morphology. The nanowire sizes and nanowire positions of nanowire array, which are critical for efficient laser operation using photonic crystal effect and the mechanism of diameter-dependent tunable emission, can be controlled by using different mask designs and optimizing growth conditions, as shown in Figure 8-3.

To achieve monolithically integrated color-tunable surface-emitting nanowire lasers, the stability and yield of electrically injected InGaN nanowire photonic crystal surface-emitting lasers is also critical. Factors that may contribute to the lasing instability include variations of nanowire properties, such as size and position. In this regard, we have recently achieved uniform InGaN/GaN nanowire array with precisely controlled size and position, and the

variations were in the range of 5-10 nm. Our preliminary studies have shown that extremely uniform lasing can be achieved in a relatively large nanowire photonic crystal array (200×200 μm^2).

List of Publications

Refereed Journal Articles

1. **Renjie Wang** et al., "Selective-area grown AlInGaN quaternary nanowires on Si substrate: suppressing the nonradiative surface recombination for solar cells", 2018 (under preparation).
2. **Renjie Wang,** Yong-Ho Ra, YuanpengWu, Songrui Zhao, Hieu P. T. Nguyen, Ishiang Shih, Zetian Mi, "Tunable, full-color nanowire light emitting diode arrays monolithically integrated on Si and sapphire", Proc. SPIE 9748, Gallium Nitride Materials and Devices XI, 97481S (2016).
3. **Renjie Wang,** Xuedong Liu, Ishiang Shih, Zetian Mi, High efficiency, "Full-color AlInGaN quaternary nanowire light emitting diodes with spontaneous core-shell structures on Si", Applied Physics Letter, Vol. 106, (2015) 261104.
4. **Renjie Wang,** Hieu P. T. Nguyen, Ashfiqua T. Connie, J. Lee, Ishiang Shih, Zetian Mi, "Color-Tunable, Phosphor-Free InGaN Nanowire Light-Emitting Diode Arrays Monolithically Integrated on Silicon", Optics Express, Vol. 22, (2014) A1768.
5. Juntian Qu*, **Renjie Wang*,** Ishiang Shih, Zetian Mi, and Xinyu Liu, (* contributed equally), "Investigating the Electrical Breakage of Single GaN Nanowires", 2018 (under preparation).
6. Yong-Ho Ra*, **Renjie Wang*,** Steffi Y. Woo, Mehrdad Djavid, Sharif Md. Sadaf, Jaesoong Lee, Gianluigi A. Botton, and Zetian Mi, (* contributed equally), "Full-color single nanowire pixels for projection displays", Nano Letters Vol. 16, (2016) 4608.
7. Mohsen Asad, **Renjie Wang,** Yong-Ho Ra, Zetian Mi and William S. Wong, "Coupling of optical function and geometric structure through mechanical manipulation of InGaN nanowire light-emitting diodes", 2018 (submitted).

8. Zetian Mi, Yong-Ho Ra, **Renjie Wang,** Roksana Rashid, "Multi-color nanowire LEDs on a single chip", 2017 IEEE Photonics Conference (IPC), (2017). DOI: 10.1109/IPCon.2017.8116005.
9. Zetian Mi, Yong-Ho Ra, Roksana Rashid, **Renjie Wang,** Ishiang Shih, "InGaN nanowire integrated nanophotonics", Photonics Society Summer Topical Meeting Series, (2017). DOI: 10.1109/PHOSST.2017.8012688.

Conference/Meeting Oral Presentations

1. **Renjie Wang,** Xuedong Liu, Xianhe Liu, Ishiang Shih and Zetian Mi, "Full-color AlInGaN core-shell nanowire light emitting diodes on Si", 11th International Conference on Nitride Semiconductors, Beijing, China, Sep 3rd, 2015.
2. **Renjie Wang,** Yong-Ho Ra, Songrui Zhao, Hieu P. Nguyen, Ishiang Shih, Zetian Mi, "Tunable full-color nanowire light-emitting diode arrays monolithically-integrated on Si and sapphire", SPIE Photonics West 2016, Gallium Nitride Materials and Devices XI, San Francisco, California, Feb 18th, 2016.
3. **Renjie Wang,** Yong-Ho Ra, Zetian Mi, "High Efficiency, Color-Tunable InGaN/GaN Nanowire Light Emitting Diode Arrays", Nanotechnology General Session featuring Nanoscale Luminescent Materials 4, ECS, San Diego, California, 229th ECS Meeting, June 1st, 2016.
4. Faqrul Alam Chowdhury, **Renjie Wang,** Ishiang Shih, Hong Guo, Zetian Mi, "Synergistic effect of In and Sb in dilute-antimonide InGaSbN nanowire heterostructures for deep-visible light emitting devices", 12th International Conference on Nitride Semiconductors, Strasbourg, France, July 24th, 2017.
5. Mohsen Asad, **Renjie Wang,** Yong-Ho Ra, William S. Wong, Zetian Mi, "Electrical and optical properties of exible nanowire blue lightemitting diodes under mechanical bending",

SPIE Photonics West 2017, Gallium Nitride Materials and Devices XII, San Francisco, California, Jan 31th, 2017

6. H. P. T. Nguyen, **Renjie Wang,** Ashfiqua T. Connie, Ishiang Shih, Zetian Mi, "Color tunable phosphor-free InGaN/GaN/AlGaN core-shell nanowire light-emitting diodes on Silicon", 2014 IEEE Summer Topical Meeting Series, Montreal, Quebec, Canada July 14th-16th, 2014.

Poster Presentations

1. **Renjie Wang,** Yong-Ho Ra, Songrui Zhao, Xianhe Liu, H. P. T. Nguyen, Ishiang Shih and Zetian Mi, "Tunable, Full-color nanowire light emitting diode arrays on Si and sapphire", 11th International Conference on Nitride Semiconductors, Beijing, China, Sep 2nd, 2015.
2. Mohsen Asad, **Renjie Wang,** Yong-Ho Ra, Zetian Mi, William S. Wong, "Light extraction efficiency enhancement of InGaN nanowire light-emitting diodes on flexible substrates", 11th International Symposium on Semiconductor Light Emitting Devices, Banff, California, October 8th-12th, 2017.

Appendix I Reports of OLEDs with Different Lateral Size.

Organic LEDs & Emission Color	Overall Luminous Efficacy (lm/W) & External Quantum Efficiency (%)	Lateral Size or Pixel Pitch (μm)	First Author Year
RGB OLEDs, White color through light mixing	6.42 lm/W & 1.78%	44	R. M. Soneira [694] 2016
RGB OLEDs, White color through light mixing	13.07 lm/W & 5.15%	100	S. Krotkus [544] 2016
RGB OLEDs, White color through light mixing	10.65 lm/W & 4.8%	160	S. Krotkus [544] 2016
RGB OLEDs, White color through light mixing LEDs	3.5 lm/W & 0.97%	346	M. C. Gather [432] 2007
RGB OLEDs, White color through light mixing	52.0 lm/W & 11.56%	1071	M. S. Weaver [545] 2014
RGB OLEDs, White color through light mixing	90.0 lm/W & 34.0%	2588	S. Reineke [162] 2009
OLEDs, Blue 475 nm, Stripe	0.96 lm/W & 1.25%	7.35	A. Steude [53] 2016
OLEDs, Blue 485 nm	35.0 lm/W & 8.42%	16	M. S. Weaver [545] 2014
OLEDs, Blue 471 nm	35.9 lm/W & 25.9%	2000	T. Miwa [436] 2017
OLEDs, Green 504 nm	8.0 lm/W & 2.89%	5	H. Hwang [163] 2008
OLEDs, Green 512 nm	16.8 lm/W & 4.90%	35	G. J. McGraw [167] 2013
OLEDs, Green 555 nm	31.9 lm/W & 4.67%	50	J. Son [166] 2017
OLEDs, Green 528 nm	70.7 lm/W & 12.0 %	78	M. E. Bahlke [168] 2012
OLEDs, Green 570 nm, Stripe	89.0 lm/W & 13.69%	1071	M. S. Weaver [545] 2014
OLEDs, Green 553 nm	96.1 lm/W & 14.1%	2000	S. Park [695] 2017
OLEDs, Green 553 nm	102.2 lm/W & 15.0%	4000	S. Park [695] 2017
OLEDs, Red 610 nm	58.4 lm/W & 17.0%	20	S. Krotkus [47] 2014
OLEDs, Red 630 nm, Stripe	32.0 lm/W & 17.68%	1071	M. S. Weaver [545] 2014
OLEDs, Red 670 nm	3.93 lm/W & 18.0%	2000	Y. Nagai [543] 2017

Appendix II Summary of EQEs and Overall Luminous Efficacy (or Luminous Efficacy of a Source) of InGaN Epilayer LED versus Lateral Device Size.

InGaN epilayer LEDs & Emission Color	Overall Luminous Efficacy (lm/W) & External Quantum Efficiency (%)	Lateral Device Size (μm)	Frist Author Year
InGaN LEDs, Violet 400 nm	0.033 lm/W & 1.71%	20	Z.Gong [133] 2010
InGaN LEDs, Violet 410 nm	3.44 lm/W & 68.0%	250	M. J. Cich [696] 2012
InGaN LEDs, Violet 400 nm	0.67 lm/W & 35.0%	300	J. Edmond [697] 2004
InGaN LEDs, Blue 440 nm	1.81 lm/W & 7.0%	5	F. Olivier [535] 2017
InGaN LEDs, Blue 446 nm	2.90 lm/W & 10.0%	6	P. Tian [529] 2012
InGaN LEDs with a AlGaN EBL, Blue ~ 447 nm	~ 12.79 lm/W & ~ 42%	10	D. Hwang [536] 2017
InGaN LEDs with a AlGaN EBL, Blue ~ 447 nm	~ 12.70 lm/W & ~ 41.7%	20	D. Hwang [536] 2017
InGaN LEDs with a AlGaN EBL, Blue ~ 447 nm	~ 12.24 lm/W & 40.2%	40	D. Hwang [536] 2017
InGaN LEDs with a AlGaN EBL, Blue ~ 447 nm	~14.80 lm/W & 48.6%	60	D. Hwang [536] 2017
InGaN LEDs with a AlGaN EBL, Blue ~ 447 nm	~ 14.32 lm/W & ~ 47%	80	D. Hwang [536] 2017
InGaN LEDs with a AlGaN EBL, Blue ~ 447 nm	~ 14.62 lm/W & ~ 48%	100	D. Hwang [536] 2017
InGaN LEDs, Cyan 488 nm	90.0 lm/W & 5.1%	10	F. Olivier [530] 2017
InGaN LEDs, Cyan 488 nm	90.0 lm/W & 5.0%	15	F. Olivier [530] 2017
InGaN LEDs, Cyan 488 nm	90.0 lm/W & 6.0%	20	F. Olivier [530] 2017
InGaN LEDs, Cyan 488 nm	6.42 lm/W & 10.0%	500	F. Olivier [530] 2017
InGaN LEDs, Green 515 nm	24.51 lm/W & 5.9%	6.5	F. Templier [457] 2016

Appendix II (Continued) Summary of EQEs and Overall Luminous Efficacy of InGaN Epilayer LED versus Lateral Device Size.

InGaN epilayer LEDs & Emission Color	Overall Luminous Efficacy (lm/W) & External Quantum Efficiency (%)	Lateral Device Size (μm)	Frist Author Year
InGaN LEDs, Green 515 nm	66.45 lm/W & 16.0%	10	L. Dupré [449] 2017
InGaN LEDs, Green 517 nm	6.43 lm/W & 1.4% The efficiency was measured from the overall high-resolution microdisplays.	12	J. Day [431] 2011
InGaN LEDs, Green 525 nm	103.72 lm/W & 19.1%	300	S. Yamamoto [698] 2010
InGaN LEDs, Green 530 nm	147.19 lm/W & 25.0%	300	J. Edmond [697] 2004
InGaN LEDs, Green 526.6 nm	158.68 lm/W & 30.2%	320	A. I. Alhassan [699] 2016
InGaN LEDs, Green 532 nm	154.14 lm/W & 25.4%	600	T. Shioda [700] 2012
InGaN LEDs, Green 535 nm	193.74 lm/W & 31.0%	1000	I. Titkov [701] 2017
InGaN LEDs with a InAlGaN/GaN EBL, Green 550 nm	254.83 lm/W & ~ 37.5%	300	An-Jye Tzou [702] 2016
InGaN LEDs, Yellow-Green 560 nm	19.58 lm/W & 2.9%	350	Y. Jiang [513] 2015
InGaN LEDs, Yellow-Green 558 nm	93.34 lm/W & 13.7%	350	C. Wetzel [703] 2009
InGaN LEDs, Yellow-Green 559 nm	167.86 lm/W & 24.7%	460	S. Saito [704] 2013
InGaN LEDs, Yellow-Green 563 nm	90.29 lm/W & 13.4%	600	H. Sato [700] 2008
InGaN LEDs, Yellow-Green 560 nm	32.62 lm/W & 4.8%	600	T. Shioda [705] 2012
InGaN LEDs, Yellow-Green 558 nm	110.71 lm/W & 16.3%	750	C. Wetzel [703] 2009
InGaN LEDs, Yellow-Green 565 nm	9.19 lm/W & 1.4%	1000	K. Lee [706] 2017
InGaN LEDs, Yellow-Amber 570 nm	5.33 lm/W & 0.8%	350	W. Zhao [707] 2006
InGaN LEDs, Yellow-Amber 576 nm	83.17 lm/W & 13.3%	460	S. Saito [704] 2013
InGaN LEDs, Yellow-Amber 575 nm	9.63 lm/W & 1.5%	600	T. Shioda [700] 2012
InGaN LEDs, Yellow-Amber 590 nm	8.27 lm/W & 1.6%	1000	K. Lee [706] 2017

Appendix III Summary of EQEs and Overall Luminous Efficacy of III-Phosphide Red LED versus Lateral Device Size.

III-phosphide LEDs & Emission Color	Overall Luminous Efficacy (lm/W) & External Quantum Efficiency (%)	Lateral Device Size (μm)	Frist Author Year
InGaAlP micro-LED array of 320×240 diodes, Red	NA & ~ 0.175%	80 (100×100 μm^2 size and 20 μm isolation grooves)	C. Tian [547] 2015
InGaAlP micro-LED array of 8×8 diodes, Red	NA & ~ 2.3%	100	S. Fang [548] 2017
InGaAlP LEDs bonded to an "transparent" GaP wafer, Red 635.6 nm	35.1 lm/W & 23.7%	210	G. E. Höfler [549] 1996
InGaAlP LEDs with buried microreflectors, Red 650 nm	45.0 lm/W & 50.0%	300	R. Windisch [550] 2007
InGaAlP LEDs with buried microreflectors, Red 635 nm	70.0 lm/W & 42.5%	300	R. Windisch [550] 2007
InGaAlP LEDs with buried microreflectors, Red 620 nm	105.0 lm/W & 38.0%	300	R. Windisch [550] 2007
InGaAlP LEDs with buried microreflectors, Red 598 nm	103.0 lm/W & 23.0%	300	R. Windisch [550] 2007
InGaAlP LEDs with with a stripe-patterned omni-directional reflector, Red 630 nm	~ 32.05 lm/W & ~ 17.71%	350	Y. J. Lee [708] 2005
InGaAlP truncated-inverted-pyramid LEDs, Red 598 nm	~ 100 lm/W & ~ 17.0%	500 (~ 0.25 mm^2)	M. R. Krames [553] 1999
InGaAlP truncated-inverted-pyramid LEDs, Red 610 nm	~ 100 lm/W & 29.1%	500 (~ 0.25 mm^2)	M. R. Krames [553] 1999
InGaAlP truncated-inverted-pyramid LEDs, Red 630 nm	~ 90.5 lm/W & ~ 50%	500 (~ 0.25 mm^2)	M. R. Krames [553] 1999

Appendix III (Continued) Summary of EQEs and Overall Luminous Efficacy of III-Phosphide Red LED versus Lateral Device Size.

III-phosphide LEDs & Emission Color	Overall Luminous Efficacy (lm/W) & External Quantum Efficiency (%)	Lateral Device Size (μm)	Frist Author Year
InGaAlP truncated-inverted-pyramid LEDs, Red 650 nm	40.19 lm/W & 55%	500 (~ 0.25 mm^2)	M. R. Krames [553] 1999
InGaAlP 40-QWs LEDs on TO-18 mounts without encapsulation, Red 605 nm	189.6 lm/W & ~ 49.0%	700	K. Streubel [709] 2002
InGaAlP 40-QWs LEDs on TO-18 mounts without encapsulation, Red 625 nm	135.7 lm/W & ~ 62.0%	700	K. Streubel [709] 2002
InGaAlP 40-QWs LEDs on TO-18 mounts without encapsulation, Red 632 nm	105.3 lm/W & ~ 64.0%	700	K. Streubel [709] 2002
InGaAlP 40-QWs LEDs on TO-18 mounts without encapsulation, Red 643 nm	72.7 lm/W & 68.0%	700	K. Streubel [709] 2002
InGaAlP LEDs, Red 612-630 nm	80.0 lm/W & 30.7%	750	OSRAM Opto Semiconductors R&D lab [710] 2015
InGaAlP LEDs, Red 609 nm	201.0 lm/W & 61.0%	1000	OSRAM Opto Semiconductors R&D lab [552] 2011
InGaAlP LEDs, Red 630.75 nm	67.1 lm/W & 37.1%	1020	W.-C. Cheng [551] 2018
InGaAlP LEDs bonded to "transparent" GaP substrates Red 632 nm	57.9 lm/W & 32.0%	8500	N. F. Gardner [711, 712] 1999

References

[1] S. Marcacci. (2014). *LED Lighting Efficiency Jumps Roughly 50% Since 2012*. Available: https://cleantechnica.com/2014/11/05/led-lighting-efficiency-jumps-roughly-50-since-2012/

[2] J. Hye Oh, S. Ji Yang, and Y. Rag Do, "Healthy, natural, efficient and tunable lighting: four-package white LEDs for optimizing the circadian effect, color quality and vision performance," *Light: Science &Amp; Applications,* vol. 3, p. e141, 2014.

[3] A. Neumann, J. J. Wierer, W. Davis, Y. Ohno, S. R. J. Brueck, and J. Y. Tsao, "Four-color laser white illuminant demonstrating high color-rendering quality," *Optics Express,* vol. 19, pp. A982-A990, 2011.

[4] M. R. Krames, O. B. Shchekin, R. Mueller-Mach, G. O. Mueller, L. Zhou, G. Harbers, and M. G. Craford, "Status and Future of High-Power Light-Emitting Diodes for Solid-State Lighting," *Journal of Display Technology,* vol. 3, pp. 160-175, 2007.

[5] E. Jang, S. Jun, H. Jang, J. Lim, B. Kim, and Y. Kim, "White-Light-Emitting Diodes with Quantum Dot Color Converters for Display Backlights," *Advanced Materials,* vol. 22, pp. 3076-3080, 2010.

[6] R. M. Soneira. (2017). *Galaxy S8 OLED Display Technology Shoot-Out*. Available: http://www.displaymate.com/Galaxy_S8_ShootOut_01.htm#Display_Power

[7] R. M. Soneira. (2016). *Galaxy S7 OLED Display Technology Shoot-Out*. Available: http://www.displaymate.com/Galaxy_S7_ShootOut_1.htm

[8] R. M. Soneira. (2015). *Galaxy S6 OLED Display Technology Shoot-Out*. Available: http://www.displaymate.com/Galaxy_S6_ShootOut_1.htm

[9] J. Hruska. (2014). *OLED finally triumphant: The Galaxy S5 has the best smartphone display on the market*. Available: https://www.extremetech.com/electronics/179464-oled-finally-triumphant-the-galaxy-s5-has-the-best-smartphone-display-on-the-market

[10] R. M. Soneira. (2012). *Samsung Galaxy OLED Display Technology Shoot-Out*. Available: http://www.displaymate.com/OLED_Galaxy_S123_ShootOut_1.htm

[11] A. Frumusanu. (2015). *Analysing AMOLED Power Efficiency Improvements*. Available: https://www.anandtech.com/show/9394/analysing-amoled-power-efficiency

[12] Wikipedia. (2018). *Retina Display*. Available: https://en.wikipedia.org/wiki/Retina_Display

[13] Wikipedia. (2018). *AMOLED*. Available: https://en.wikipedia.org/wiki/AMOLED

[14] S. Rajagopal, R. D. Roberts, and S. K. Lim, "IEEE 802.15.7 visible light communication: modulation schemes and dimming support," *IEEE Communications Magazine,* vol. 50, pp. 72-82, 2012.

[15] H. Chun, S. Rajbhandari, D. Tsonev, G. Faulkner, H. Haas, and D. O. Brien, "Visible light communication using laser diode based remote phosphor technique," in *2015 IEEE International Conference on Communication Workshop (ICCW)*, 2015, pp. 1392-1397.

[16] Y. Perwej, "The Next Generation of Wireless Communication Using Li-Fi (Light Fidelity) Technology," *Journal of Computer Networks,* vol. 4, pp. 20-29, 2017.

[17] V. Sharma, S. Rajput, and P. K. Sharma, "Light fidelity (Li-Fi): An effective solution for data transmission," *AIP Conference Proceedings,* vol. 1715, p. 020061, 2016.

[18] S. I. Park, D. S. Brenner, G. Shin, C. D. Morgan, B. A. Copits, H. U. Chung, M. Y. Pullen, K. N. Noh, S. Davidson, S. J. Oh, J. Yoon, K.-I. Jang, V. K. Samineni, M. Norman, J. G. Grajales-Reyes, S. K. Vogt, S. S. Sundaram, K. M. Wilson, J. S. Ha, R. Xu, T. Pan, T.-i. Kim, Y. Huang, M. C. Montana, J. P. Golden, M. R. Bruchas, R. W. Gereau Iv, and J. A. Rogers, "Soft, stretchable, fully implantable miniaturized

optoelectronic systems for wireless optogenetics," *Nature Biotechnology,* vol. 33, p. 1280, 2015.

[19] T.-i. Kim, J. G. McCall, Y. H. Jung, X. Huang, E. R. Siuda, Y. Li, J. Song, Y. M. Song, H. A. Pao, R.-H. Kim, C. Lu, S. D. Lee, I.-S. Song, G. Shin, R. Al-Hasani, S. Kim, M. P. Tan, Y. Huang, F. G. Omenetto, J. A. Rogers, and M. R. Bruchas, "Injectable, Cellular-Scale Optoelectronics with Applications for Wireless Optogenetics," *Science,* vol. 340, pp. 211-216, 2013.

[20] N. Jain and K. Hudait Mantu, "III–V Multijunction Solar Cell Integration with Silicon: Present Status, Challenges and Future Outlook," in *Energy Harvesting and Systems* vol. 1, ed, 2014, p. 121.

[21] F. Dimroth, T. Roesener, S. Essig, C. Weuffen, A. Wekkeli, E. Oliva, G. Siefer, K. Volz, T. Hannappel, and A. W. Bett, "Comparison of direct growth and wafer bonding for the fabrication of GaInP/GaAs dual-junction solar cells on silicon," *IEEE Journal of Photovoltaics,* vol. 4, pp. 620-625, 2014.

[22] S. Essig, J. Benick, M. Schachtner, A. Wekkeli, M. Hermle, and F. Dimroth, "Wafer-bonded GaInP/GaAs//Si solar cells with 30% efficiency under concentrated sunlight," *IEEE Journal of Photovoltaics,* vol. 5, pp. 977-981, 2015.

[23] J. Yang, Z. Peng, D. Cheong, and R. Kleiman, "Fabrication of high-efficiency III-V on silicon multijunction solar cells by direct metal interconnect," *IEEE Journal of Photovoltaics,* vol. 4, pp. 1149-1155, 2014.

[24] Y. B. Tang, Z. H. Chen, H. S. Song, C. S. Lee, H. T. Cong, H. M. Cheng, W. J. Zhang, I. Bello, and S. T. Lee, "Vertically Aligned p-Type Single-Crystalline GaN Nanorod Arrays on n-Type Si for Heterojunction Photovoltaic Cells," *Nano Letters,* vol. 8, pp. 4191-4195, 2008.

[25] E. F. Schubert and J. K. Kim, "Solid-State Light Sources Getting Smart," *Science,* vol. 308, pp. 1274-1278, 2005.

[26] D. E. Blask, R. T. Dauchy, L. A. Sauer, J. A. Krause, and G. C. Brainard, "Growth and Fatty Acid Metabolism of Human Breast Cancer (MCF-7) Xenografts in Nude Rats: Impact of Constant Light-Induced Nocturnal Melatonin Suppression," *Breast Cancer Research and Treatment,* vol. 79, pp. 313-320, 2003.

[27] E. Miyazaki, S. Itami, and T. Araki, "Using a light-emitting diode as a high-speed, wavelength selective photodetector," *Review of Scientific Instruments,* vol. 69, pp. 3751-3754, 1998.

[28] L. Sang, M. Liao, Y. Koide, and M. Sumiya, "High-performance metal-semiconductor-metal InGaN photodetectors using CaF2 as the insulator," *Applied Physics Letters,* vol. 98, p. 103502, 2011.

[29] H. Yang, Z. Ma, Y. Jiang, H. Wu, P. Zuo, B. Zhao, H. Jia, and H. Chen, "The enhanced photo absorption and carrier transportation of InGaN/GaN Quantum Wells for photodiode detector applications," *Scientific Reports,* vol. 7, p. 43357, 2017.

[30] A. D. L. Bugallo, L. Rigutti, G. Jacopin, F. H. Julien, C. Durand, X. J. Chen, D. Salomon, J. Eymery, and M. Tchernycheva, "Single-wire photodetectors based on InGaN/GaN radial quantum wells in GaN wires grown by catalyst-free metal-organic vapor phase epitaxy," *Applied Physics Letters,* vol. 98, p. 233107, 2011.

[31] E. A. Berkman, N. A. El-Masry, A. Emara, and S. M. Bedair, "Nearly lattice-matched n, i, and p layers for InGaN p-i-n photodiodes in the 365–500nm spectral range," *Applied Physics Letters,* vol. 92, p. 101118, 2008.

[32] S. Shyh-Chiang, D. D. Russell, L. Zachery, L. Yi-Che, K. Tsung-Ting, Z. Yun, K. Hee-Jin, and R. Jae-Hyun, "Working toward high-power GaN/InGaN heterojunction bipolar transistors," *Semiconductor Science and Technology,* vol. 28, p. 074025, 2013.

[33] T. Itoh, A. Kobayashi, K. Ueno, J. Ohta, and H. Fujioka, "Fabrication of InGaN thin-film transistors using pulsed sputtering deposition," *Scientific Reports,* vol. 6, p. 29500, 2016.
[34] K. P. Lee, F. Ren, S. J. Pearton, A. M. Dabiran, and P. P. Chow, "Simulations of InGaN-base heterojunction bipolar transistors," *Solid-State Electronics,* vol. 47, pp. 1009-1014, 2003.
[35] A. Hiroshi, K. Masahiro, H. Kazumasa, and A. Isamu, "P-Type Conduction in Mg-Doped GaN Treated with Low-Energy Electron Beam Irradiation (LEEBI)," *Japanese Journal of Applied Physics,* vol. 28, p. L2112, 1989.
[36] A. Isamu, A. Hiroshi, K. Masahiro, and H. Kazumasa, "Photoluminescence of Mg-doped p-type GaN and electroluminescence of GaN p-n junction LED," *Journal of Luminescence,* vol. 48-49, pp. 666-670, 1991.
[37] K. S. Novoselov, A. K. Geim, S. V. Morozov, D. Jiang, Y. Zhang, S. V. Dubonos, I. V. Grigorieva, and A. A. Firsov, "Electric Field Effect in Atomically Thin Carbon Films," *Science,* vol. 306, pp. 666-669, 2004.
[38] TheNobelFoundation. (2014). *New light to illuminate the world*. Available: https://www.nobelprize.org/nobel_prizes/physics/laureates/2014/press.html
[39] TheNobelFoundation. (2010). *The Nobel Prize in Physics 2010*. Available: https://www.nobelprize.org/nobel_prizes/physics/laureates/2010/
[40] A. Nobel. (1895). *Text version of Alfred Nobel's Will*. Available: https://www.nobelprize.org/alfred_nobel/will/
[41] K. Müllen, U. Scherf, W. John, and Sons, "Organic light emitting devices : synthesis, properties and applications," 2006.
[42] N. T. Kalyani and S. J. Dhoble, "Organic light emitting diodes: Energy saving lighting technology-A review," *Renewable and Sustainable Energy Reviews,* vol. 16, pp. 2696-2723, 2012.
[43] N. T. Kalyani, H. Swart, and S. J. Dhoble, "Principles and applications of organic light emitting diodes (OLEDs)," 2017.
[44] B. Geffroy, P. le Roy, and C. Prat, "Organic light-emitting diode (OLED) technology: materials, devices and display technologies," *Polymer International,* vol. 55, pp. 572-582, 2006.
[45] S. R. Forrest, "The path to ubiquitous and low-cost organic electronic appliances on plastic," *Nature,* vol. 428, p. 911, 2004.
[46] K. Goushi, K. Yoshida, K. Sato, and C. Adachi, "Organic light-emitting diodes employing efficient reverse intersystem crossing for triplet-to-singlet state conversion," *Nature Photonics,* vol. 6, p. 253, 2012.
[47] S. Krotkus, F. Ventsch, D. Kasemann, A. A. Zakhidov, S. Hofmann, K. Leo, and M. C. Gather, "Photo-patterning of Highly Efficient State-of-the-Art Phosphorescent OLEDs Using Orthogonal Hydrofluoroethers," *Advanced Optical Materials,* vol. 2, pp. 1043-1048, 2014.
[48] H. H. Fong, J.-K. Lee, Y.-F. Lim, A. A. Zakhidov, W. W. H. Wong, A. B. Holmes, C. K. Ober, and G. G. Malliaras, "Orthogonal Processing and Patterning Enabled by Highly Fluorinated Light-Emitting Polymers," *Advanced Materials,* vol. 23, pp. 735-739, 2011.
[49] G. E. Jabbour, Y. Kawabe, S. E. Shaheen, J. F. Wang, M. M. Morrell, B. Kippelen, and N. Peyghambarian, "Highly efficient and bright organic electroluminescent devices with an aluminum cathode," *Applied Physics Letters,* vol. 71, pp. 1762-1764, 1997.
[50] M. Akiyoshi, K. Tatsuya, and T. Tetsuro, "High-Efficiency Color and White Organic Light-Emitting Devices Prepared on Flexible Plastic Substrates," *Japanese Journal of Applied Physics,* vol. 44, p. 608, 2005.

[51] VersionDaily. (2016). *Advantages and disadvantages of AMOLED*. Available: http://www.versiondaily.com/advantages-and-disadvantages-of-amoled-display-technology/
[52] Wikipedia. (2018). *Screen burn-in*. Available: https://en.wikipedia.org/wiki/Screen_burn-in
[53] A. Steude, E. C. Witts, G. B. Miles, and M. C. Gather, "Arrays of microscopic organic LEDs for high-resolution optogenetics," *Science Advances,* vol. 2, p. e1600061, 2016.
[54] J. Wu, W. Walukiewicz, K. M. Yu, W. Shan, J. W. Ager, E. E. Haller, H. Lu, W. J. Schaff, W. K. Metzger, and S. Kurtz, "Superior radiation resistance of In1−xGaxN alloys: Full-solar-spectrum photovoltaic material system," *Journal of Applied Physics,* vol. 94, pp. 6477-6482, 2003.
[55] M. Auf der Maur, A. Pecchia, G. Penazzi, W. Rodrigues, and A. Di Carlo, "Efficiency Drop in Green (InGaN)/(GaN) Light Emitting Diodes: The Role of Random Alloy Fluctuations," *Physical Review Letters,* vol. 116, p. 027401, 2016.
[56] K. A. Bulashevich, A. V. Kulik, and S. Y. Karpov, "Optimal ways of colour mixing for high-quality white-light LED sources," *physica status solidi (a),* vol. 212, pp. 914-919, 2015.
[57] Lasercomponents. (2016). Available: https://www.lasercomponents.com/de/?embedded=1&file=fileadmin/user_upload/home/Datasheets/divers-vis/lcq/lcq78530s5n_m_p.pdf&no_cache=1
[58] CoherentSemiconductorGroup. (2016). *670 to 690 nm Devices.* Available: www.coherent.com/downloads/670_to_690_nm_DevicesDS.pdf
[59] M. A. Majid, A. A. Al-Jabr, B. S. Ooi, H. M. Oubei, D. H. Anjum, T. K. Ng, and M. S. Alias, "First demonstration of InGaP/InAlGaP based orange laser emitting at 608 nm," *Electronics Letters,* vol. 51, pp. 1102-1104, 2015.
[60] K. J. Beernink, D. Sun, D. W. Treat, and B. P. Bour, "Differential Al–Ga interdiffusion in AlGaAs/GaAs and AlGaInP/GaInP heterostructures," *Applied Physics Letters,* vol. 66, pp. 3597-3599, 1995.
[61] Z. Yarar, "Transport and mobility properties of wurtzite InN and GaN," *physica status solidi (b),* vol. 244, pp. 3711-3718, 2007.
[62] I. Vurgaftman, J. R. Meyer, and L. R. Ram-Mohan, "Band parameters for III–V compound semiconductors and their alloys," *Journal of Applied Physics,* vol. 89, pp. 5815-5875, 2001.
[63] S. Strite and H. Morkoç, "GaN, AlN, and InN: A review," *Journal of Vacuum Science & Technology B: Microelectronics and Nanometer Structures Processing, Measurement, and Phenomena,* vol. 10, pp. 1237-1266, 1992.
[64] P. Rinke, M. Scheffler, A. Qteish, M. Winkelnkemper, D. Bimberg, and J. Neugebauer, "Band gap and band parameters of InN and GaN from quasiparticle energy calculations based on exact-exchange density-functional theory," *Applied Physics Letters,* vol. 89, p. 161919, 2006.
[65] J. D. Albrecht, R. P. Wang, P. P. Ruden, M. Farahmand, and K. F. Brennan, "Electron transport characteristics of GaN for high temperature device modeling," *Journal of Applied Physics,* vol. 83, pp. 4777-4781, 1998.
[66] H. Morko, *Nitride Semiconductor Devices : Fundamentals and Applications*. Hoboken: Wiley, 2013.
[67] M. van Schilfgaarde, A. Sher, and A. B. Chen, "Theory of AlN, GaN, InN and their alloys," *Journal of Crystal Growth,* vol. 178, pp. 8-31, 1997.
[68] S. K. O'Leary, P. Siddiqua, W. A. Hadi, B. E. Foutz, M. S. Shur, and L. F. Eastman, "Electron Transport Within III-V Nitride Semiconductors," in *Springer Handbook of*

Electronic and Photonic Materials, S. Kasap and P. Capper, Eds., ed Cham: Springer International Publishing, 2017, pp. 1-1.
[69] J. Wu, "When group-III nitrides go infrared: New properties and perspectives," *Journal of Applied Physics,* vol. 106, p. 011101, 2009.
[70] F. A. Ponce and D. P. Bour, "Nitride-based semiconductors for blue and green light-emitting devices," *Nature,* vol. 386, p. 351, 1997.
[71] N. Shuji, S. Masayuki, I. Naruhito, and N. Shin-ichi, "High-Brightness InGaN Blue, Green and Yellow Light-Emitting Diodes with Quantum Well Structures," *Japanese Journal of Applied Physics,* vol. 34, p. L797, 1995.
[72] N. Shuji, S. Masayuki, I. Naruhito, N. Shin-ichi, Y. Takao, and M. Takashi, "Superbright Green InGaN Single-Quantum-Well-Structure Light-Emitting Diodes," *Japanese Journal of Applied Physics,* vol. 34, p. L1332, 1995.
[73] M. H. Crawford, "LEDs for Solid-State Lighting: Performance Challenges and Recent Advances," *IEEE Journal of Selected Topics in Quantum Electronics,* vol. 15, pp. 1028-1040, 2009.
[74] S. Nakamura, "The Roles of Structural Imperfections in InGaN-Based Blue Light-Emitting Diodes and Laser Diodes," *Science,* vol. 281, pp. 956-961, 1998.
[75] W. S. Wong, T. Sands, N. W. Cheung, M. Kneissl, D. P. Bour, P. Mei, L. T. Romano, and N. M. Johnson, "Fabrication of thin-film InGaN light-emitting diode membranes by laser lift-off," *Applied Physics Letters,* vol. 75, pp. 1360-1362, 1999.
[76] C. H. Chiu, C. C. Lin, D. M. Deng, D. W. Lin, J. C. Li, Z. Y. Li, G. W. Shu, T. C. Lu, J. L. Shen, H. C. Kuo, and K. M. Lau, "Optical and Electrical Properties of GaN-Based Light Emitting Diodes Grown on Micro- and Nano-Scale Patterned Si Substrate," *IEEE Journal of Quantum Electronics,* vol. 47, pp. 899-906, 2011.
[77] S. Nakamura, M. Senoh, S. i. Nagahama, N. Iwasa, T. Yamada, T. Matsushita, H. Kiyoku, and Y. Sugimoto, "InGaN multi-quantum-well structure laser diodes grown on MgAl2O4 substrates," *Applied Physics Letters,* vol. 68, pp. 2105-2107, 1996.
[78] S. Nakamura, "First III–V-nitride-based violet laser diodes," *Journal of Crystal Growth,* vol. 170, pp. 11-15, 1997.
[79] S. Nakamura, M. Senoh, S.-i. Nagahama, N. Iwasa, T. Yamada, T. Matsushita, H. Kiyoku, Y. Sugimoto, T. Kozaki, H. Umemoto, M. Sano, and K. Chocho, "InGaN/GaN/AlGaN-based laser diodes with modulation-doped strained-layer superlattices grown on an epitaxially laterally overgrown GaN substrate," *Applied Physics Letters,* vol. 72, pp. 211-213, 1998.
[80] D. Queren, A. Avramescu, G. Brüderl, A. Breidenassel, M. Schillgalies, S. Lutgen, and U. Strauß, "500 nm electrically driven InGaN based laser diodes," *Applied Physics Letters,* vol. 94, p. 081119, 2009.
[81] F. D. Sala, A. D. Carlo, P. Lugli, F. Bernardini, V. Fiorentini, R. Scholz, and J.-M. Jancu, "Free-carrier screening of polarization fields in wurtzite GaN/InGaN laser structures," *Applied Physics Letters,* vol. 74, pp. 2002-2004, 1999.
[82] T. Anurag, M. F. Robert, M. K. Kathryn, H. Chia-Yen, H. Po Shan, A. H. Daniel, T. H. Matthew, H. Casey, F. Kenji, A. C. Daniel, O. Hiroaki, S. S. James, P. D. Steven, and N. Shuji, "AlGaN-Cladding Free Green Semipolar GaN Based Laser Diode with a Lasing Wavelength of 506.4 nm," *Applied Physics Express,* vol. 3, p. 011002, 2010.
[83] O. Jani, I. Ferguson, C. Honsberg, and S. Kurtz, "Design and characterization of GaN/InGaN solar cells," *Applied Physics Letters,* vol. 91, p. 132117, 2007.
[84] C. J. Neufeld, N. G. Toledo, S. C. Cruz, M. Iza, S. P. DenBaars, and U. K. Mishra, "High quantum efficiency InGaN/GaN solar cells with 2.95 eV band gap," *Applied Physics Letters,* vol. 93, p. 143502, 2008.

[85] X. Zheng, R.-H. Horng, D.-S. Wuu, M.-T. Chu, W.-Y. Liao, M.-H. Wu, R.-M. Lin, and Y.-C. Lu, "High-quality InGaN/GaN heterojunctions and their photovoltaic effects," *Applied Physics Letters,* vol. 93, p. 261108, 2008.
[86] R. Dahal, B. Pantha, J. Li, J. Y. Lin, and H. X. Jiang, "InGaN/GaN multiple quantum well solar cells with long operating wavelengths," *Applied Physics Letters,* vol. 94, p. 063505, 2009.
[87] J. L. Pau, J. Anduaga, C. Rivera, Á. Navarro, I. Álava, M. Redondo, and E. Muñoz, "Optical sensors based on III-nitride photodetectors for flame sensing and combustion monitoring," *Applied Optics,* vol. 45, pp. 7498-7503, 2006.
[88] Y. C. Chen, H. Y. Shih, J. Y. Chen, W. J. Tan, and Y. F. Chen, "An optically detectable CO2 sensor utilizing polyethylenimine and starch functionalized InGaN/GaN multiple quantum wells," *Applied Physics Letters,* vol. 103, p. 022109, 2013.
[89] S. Paul, A. Helwig, G. Müller, F. Furtmayr, J. Teubert, and M. Eickhoff, "Opto-chemical sensor system for the detection of H2 and hydrocarbons based on InGaN/GaN nanowires," *Sensors and Actuators B: Chemical,* vol. 173, pp. 120-126, 2012.
[90] C. Rivera, J. L. Pau, F. B. Naranjo, and E. Muñoz, "Novel photodetectors based on InGaN/GaN multiple quantum wells," *physica status solidi (a),* vol. 201, pp. 2658-2662, 2004.
[91] D. Schiavon, M. Binder, M. Peter, B. Galler, P. Drechsel, and F. Scholz, "Wavelength-dependent determination of the recombination rate coefficients in single-quantum-well GaInN/GaN light emitting diodes," *physica status solidi (b),* vol. 250, pp. 283-290, 2013.
[92] A. Adrian, L. Teresa, M. Jens, E. Christoph, B. Georg, S. Matthias, L. Stephan, and S. Uwe, "True Green Laser Diodes at 524 nm with 50 mW Continuous Wave Output Power on c -Plane GaN," *Applied Physics Express,* vol. 3, p. 061003, 2010.
[93] K. Samonji, S. Yoshida, H. Hagino, K. Yamanaka, and S. Takigawa, "High-power operation of a wide-striped InGaN laser diode array," 2012, pp. 82771K-82771K-6.
[94] Y. Sun, K. Zhou, Q. Sun, J. Liu, M. Feng, Z. Li, Y. Zhou, L. Zhang, D. Li, S. Zhang, M. Ikeda, S. Liu, and H. Yang, "Room-temperature continuous-wave electrically injected InGaN-based laser directly grown on Si," *Nature Photonics,* vol. 10, pp. 595-599, 2016.
[95] W. Guo, M. Zhang, P. Bhattacharya, and J. Heo, "Auger Recombination in III-Nitride Nanowires and Its Effect on Nanowire Light-Emitting Diode Characteristics," *Nano Letters,* vol. 11, pp. 1434-1438, 2011.
[96] K. A. Bertness, A. Roshko, N. A. Sanford, J. M. Barker, and A. V. Davydov, "Spontaneously grown GaN and AlGaN nanowires," *Journal of Crystal Growth,* vol. 287, pp. 522-527, 2006.
[97] K. Kishino, A. Kikuchi, H. Sekiguchi, and S. Ishizawa, "InGaN/GaN nanocolumn LEDs emitting from blue to red," in *Integrated Optoelectronic Devices 2007*, 2007, p. 12.
[98] E. Calleja, J. Ristić, S. Fernández-Garrido, L. Cerutti, M. A. Sánchez-García, J. Grandal, A. Trampert, U. Jahn, G. Sánchez, A. Griol, and B. Sánchez, "Growth, morphology, and structural properties of group-III-nitride nanocolumns and nanodisks," *physica status solidi (b),* vol. 244, pp. 2816-2837, 2007.
[99] S. Fernández-Garrido, J. Grandal, E. Calleja, M. A. Sánchez-García, and D. López-Romero, "A growth diagram for plasma-assisted molecular beam epitaxy of GaN nanocolumns on Si(111)," *Journal of Applied Physics,* vol. 106, p. 126102, 2009.
[100] O. Landré, C. Bougerol, H. Renevier, and B. Daudin, "Nucleation mechanism of GaN nanowires grown on (111) Si by molecular beam epitaxy," *Nanotechnology,* vol. 20, p. 415602, 2009.

[101] W. Guo, M. Zhang, A. Banerjee, and P. Bhattacharya, "Catalyst-Free InGaN/GaN Nanowire Light Emitting Diodes Grown on (001) Silicon by Molecular Beam Epitaxy," *Nano Letters,* vol. 10, pp. 3355-3359, 2010/09/08 2010.
[102] F. Glas, "Critical dimensions for the plastic relaxation of strained axial heterostructures in free-standing nanowires," *Physical Review B,* vol. 74, p. 121302, 2006.
[103] V. G. Dubrovskii and N. V. Sibirev, "Growth thermodynamics of nanowires and its application to polytypism of zinc blende III-V nanowires," *Physical Review B,* vol. 77, p. 035414, 2008.
[104] K. Kishino, K. Nagashima, and K. Yamano, "Monolithic integration of InGaN-based nanocolumn light-emitting diodes with different emission colors," *Appl. Phys. Express,* vol. 6, p. 012101, 2013.
[105] H. Sekiguchi, K. Kishino, and A. Kikuchi, "Emission color control from blue to red with nanocolumn diameter of InGaN/GaN nanocolumn arrays grown on same substrate," *Appl. Phys. Lett.,* vol. 96, p. 231104, 2010.
[106] R. Versluis, S. Poletto, N. Khammassi, B. Tarasinski, N. Haider, D. J. Michalak, A. Bruno, K. Bertels, and L. DiCarlo, "Scalable Quantum Circuit and Control for a Superconducting Surface Code," *Physical Review Applied,* vol. 8, p. 034021, 2017.
[107] G. B. Xavier, G. V. de Faria, G. P. Temporão, and J. P. von der Weid, "Full polarization control for fiber optical quantum communication systems using polarization encoding," *Optics Express,* vol. 16, pp. 1867-1873, 2008.
[108] M. A. Ghonaimy, "An overview of Quantum Information Systems," in *2013 8th International Conference on Computer Engineering & Systems (ICCES)*, 2013, pp. xx-xxxii.
[109] B. Qi, S. Liu, Q. Shen, S. Liao, Z. Lin, W. Cai, W. Liu, C. Peng, and Q. An, "A compact PCI-based measurement and control system for satellite-ground quantum communication," in *2014 19th IEEE-NPSS Real Time Conference*, 2014, pp. 1-1.
[110] L. Chassagne, S. Topcu, Y. Alayli, P. Juncar, G. Lerondel, S. Blaize, A. Bruyant, I. Stefanon, and P. Royer, "High accuracy optoelectronic control system for near field characterization of millimeter long wave guiding structures," in *Optical Metrology*, 2005, p. 7.
[111] O. Y. Sergiyenko, "Optoelectronic system for mobile robot navigation," *Optoelectronics, Instrumentation and Data Processing,* vol. 46, pp. 414-428, 2010.
[112] M. M. Gorokhov, "Digital automatic control system for the drive of a tracking optoelectronic device," *Journal of Optical Technology,* vol. 71, pp. 43-47, 2004.
[113] G. E. Moore, "Cramming more components onto integrated circuits, Reprinted from Electronics, volume 38, number 8, April 19, 1965, pp.114 ff," *IEEE Solid-State Circuits Society Newsletter,* vol. 11, pp. 33-35, 2006.
[114] G. E. Moore, "Progress in digital integrated electronics [Technical literaiture, Copyright 1975 IEEE. Reprinted, with permission. Technical Digest. International Electron Devices Meeting, IEEE, 1975, pp. 11-13.]," *IEEE Solid-State Circuits Society Newsletter,* vol. 11, pp. 36-37, 2006.
[115] IntelCorporation, "Over 6 Decades of Continued Transistor Shrinkage, Innovation," *Intel's 22 nm Technology Moves Transistor Into the 3rd Dimension,* vol. https://www.intel.com/content/www/us/en/silicon-innovations/standards-22-nanometers-technology-backgrounder.html#, 2011.
[116] N. Myhrvold. (2006). *Moore's Law Corollary: Pixel Power*. Available: http://www.nytimes.com/2006/06/07/technology/circuits/07essay.html
[117] D. C. Brock and G. E. Moore, *Understanding Moore's Law: Four Decades of Innovation*: Chemical Heritage Foundation, 2006.

[118] V. Dolores-Calzadilla, B. Romeira, F. Pagliano, S. Birindelli, A. Higuera-Rodriguez, P. J. van Veldhoven, M. K. Smit, A. Fiore, and D. Heiss, "Waveguide-coupled nanopillar metal-cavity light-emitting diodes on silicon," *Nature Communications,* vol. 8, p. 14323, 2017.
[119] H. P. T. Nguyen, S. Zhang, K. Cui, X. Han, S. Fathololoumi, M. Couillard, G. A. Botton, and Z. Mi, "p-Type Modulation Doped InGaN/GaN Dot-in-a-Wire White-Light-Emitting Diodes Monolithically Grown on Si(111)," *Nano Letters,* vol. 11, pp. 1919-1924, 2011.
[120] Y.-L. Chang, J. L. Wang, F. Li, and Z. Mi, "High efficiency green, yellow, and amber emission from InGaN/GaN dot-in-a-wire heterostructures on Si(111)," *Applied Physics Letters,* vol. 96, p. 013106, 2010.
[121] A. Kikuchi, M. Kawai, M. Tada, and K. Kishino, "InGaN/GaN multiple quantum disk nanocolumn light-emitting diodes grown on (111) Si substrate," *Japanese Journal of Applied Physics, Part 2: Letters,* vol. 43, pp. L1524-L1526, 2004.
[122] S. Jahangir, M. Mandl, M. Strassburg, and P. Bhattacharya, "Molecular beam epitaxial growth and optical properties of red-emitting ($\lambda = 650$ nm) InGaN/GaN disks-in-nanowires on silicon," *Applied Physics Letters,* vol. 102, p. 071101, 2013.
[123] H.-M. Kim, Y.-H. Cho, H. Lee, S. I. Kim, S. R. Ryu, D. Y. Kim, T. W. Kang, and K. S. Chung, "High-Brightness Light Emitting Diodes Using Dislocation-Free Indium Gallium Nitride/Gallium Nitride Multiquantum-Well Nanorod Arrays," *Nano Letters,* vol. 4, pp. 1059-1062, 2004.
[124] P. Yang, R. Yan, and M. Fardy, "Semiconductor Nanowire: What's Next?," *Nano Letters,* vol. 10, pp. 1529-1536, 2010.
[125] H. J. Joyce, Q. Gao, H. Hoe Tan, C. Jagadish, Y. Kim, J. Zou, L. M. Smith, H. E. Jackson, J. M. Yarrison-Rice, P. Parkinson, and M. B. Johnston, "III–V semiconductor nanowires for optoelectronic device applications," *Progress in Quantum Electronics,* vol. 35, pp. 23-75, 2011.
[126] F. Qian, Y. Li, S. Gradečak, D. Wang, C. J. Barrelet, and C. M. Lieber, "Gallium Nitride-Based Nanowire Radial Heterostructures for Nanophotonics," *Nano Letters,* vol. 4, pp. 1975-1979, 2004.
[127] P. Yang, S. Brittman, and C. Liu, "Chapter 6 Nanowires for Photovoltaics and Artificial Photosynthesis," in *Semiconductor Nanowires: From Next-Generation Electronics to Sustainable Energy*, ed: The Royal Society of Chemistry, 2015, pp. 277-311.
[128] H. Y. Ryu, "Extraction Efficiency in GaN Nanorod Light-emitting Diodes Investigated by Finite-difference Time-domain Simulation," *The journal of the Korean Physical Society.,* vol. 58, pp. 878-882, 2011.
[129] S. Zhao, B. H. Le, D. P. Liu, X. D. Liu, M. G. Kibria, T. Szkopek, H. Guo, and Z. Mi, "p-Type InN Nanowires," *Nano Lett,* vol. 13, pp. 5509-13, Nov 13 2013.
[130] S. Zhao, A. T. Connie, M. H. T. Dastjerdi, X. H. Kong, Q. Wang, M. Djavid, S. Sadaf, X. D. Liu, I. Shih, H. Guo, and Z. Mi, "Aluminum nitride nanowire light emitting diodes: Breaking the fundamental bottleneck of deep ultraviolet light sources," *Scientific Reports,* vol. 5, p. 8332, 2015.
[131] M. G. Kibria, S. Zhao, F. A. Chowdhury, Q. Wang, H. P. T. Nguyen, M. L. Trudeau, H. Guo, and Z. Mi, "Tuning the surface Fermi level on p-type gallium nitride nanowires for efficient overall water splitting," *Nature Communications,* vol. 5, p. 3825, 2014.
[132] S. Zhang, A. T. Connie, D. A. Laleyan, H. P. T. Nguyen, Q. Wang, J. Song, I. Shih, and Z. Mi, "On the Carrier Injection Efficiency and Thermal Property of InGaN/GaN Axial Nanowire Light Emitting Diodes," *IEEE Journal of Quantum Electronics,* vol. 50, pp. 483-490, 2014.

[133] Z. Gong, S. Jin, Y. Chen, J. McKendry, D. Massoubre, I. M. Watson, E. Gu, and M. D. Dawson, "Size-dependent light output, spectral shift, and self-heating of 400 nm InGaN light-emitting diodes," *Journal of Applied Physics,* vol. 107, p. 013103, 2010.
[134] M. Takashi, Y. Motokazu, and N. Shuji, "Characteristics of InGaN-Based UV/Blue/Green/Amber/Red Light-Emitting Diodes," *Japanese Journal of Applied Physics,* vol. 38, p. 3976, 1999.
[135] I. Vurgaftman and J. R. Meyer, "Band parameters for nitrogen-containing semiconductors," *Journal of Applied Physics,* vol. 94, pp. 3675-3696, 2003.
[136] M. S. Shur, R. F. Davis, and H. B. Dietrich, *GaN-Based Materials and Devices : Growth, Fabrication, Characterization and Performance*. Singapore, SINGAPORE: World Scientific Publishing Co Pte Ltd, 2004.
[137] A. Lidow, J. Strydom, M. de Rooij, and D. Reusch, *GaN Transistors for Efficient Power Conversion*. New York, UNITED KINGDOM: John Wiley & Sons, Incorporated, 2014.
[138] A. G. Bhuiyan, A. Hashimoto, and A. Yamamoto, "Indium nitride (InN): A review on growth, characterization, and properties," *Journal of Applied Physics,* vol. 94, pp. 2779-2808, 2003.
[139] V. W. L. Chin, T. L. Tansley, and T. Osotchan, "Electron mobilities in gallium, indium, and aluminum nitrides," *Journal of Applied Physics,* vol. 75, pp. 7365-7372, 1994.
[140] V. M. Polyakov, F. Schwierz, F. Fuchs, J. Furthmüller, and F. Bechstedt, "Low-field and high-field electron transport in zinc blende InN," *Applied Physics Letters,* vol. 94, p. 022102, 2009.
[141] W. Xinqiang, L. Shitao, M. Nan, F. Li, C. Guang, X. Fujun, T. Ning, H. Sen, J. C. Kevin, Z. Shengqiang, and S. Bo, "High-Electron-Mobility InN Layers Grown by Boundary-Temperature-Controlled Epitaxy," *Applied Physics Express,* vol. 5, p. 015502, 2012.
[142] J. R. Meyer and F. J. Bartoli, "Ionized-impurity scattering in the strong-screening limit," *Physical Review B,* vol. 36, pp. 5989-6000, 1987.
[143] J. Wu, W. Walukiewicz, W. Shan, K. M. Yu, J. W. A. III, S. X. Li, E. E. Haller, H. Lu, and W. J. Schaff, "Temperature dependence of the fundamental band gap of InN," *Journal of Applied Physics,* vol. 94, pp. 4457-4460, 2003.
[144] Z. Mi and S. Zhao, "Extending group-III nitrides to the infrared: Recent advances in InN (Phys. Status Solidi B 5/2015)," *physica status solidi (b),* vol. 252, 2015.
[145] S. Zhao, O. Salehzadeh, S. Alagha, K. L. Kavanagh, S. P. Watkins, and Z. Mi, "Probing the electrical transport properties of intrinsic InN nanowires," *Applied Physics Letters,* vol. 102, p. 073102, 2013.
[146] S. Zhao, S. Fathololoumi, K. H. Bevan, D. P. Liu, M. G. Kibria, Q. Li, G. T. Wang, H. Guo, and Z. Mi, "Tuning the surface charge properties of epitaxial InN nanowires," *Nano Lett,* vol. 12, pp. 2877-82, Jun 13 2012.
[147] S.-H. Park and S.-L. Chuang, "Comparison of zinc-blende and wurtzite GaN semiconductors with spontaneous polarization and piezoelectric field effects," *Journal of Applied Physics,* vol. 87, pp. 353-364, 2000.
[148] S. Kang, B. K. Kang, S.-W. Kim, and D. H. Yoon, "Growth and Characteristics of Zinc-Blende and Wurtzite GaN Junctioned Branch Nanostructures," *Crystal Growth & Design,* vol. 10, pp. 2581-2584, 2010.
[149] A. F. Wright, "Elastic properties of zinc-blende and wurtzite AlN, GaN, and InN," *Journal of Applied Physics,* vol. 82, pp. 2833-2839, 1997.
[150] S. Q. Zhou, A. Vantomme, B. S. Zhang, H. Yang, and M. F. Wu, "Comparison of the properties of GaN grown on complex Si-based structures," *Applied Physics Letters,* vol. 86, p. 081912, 2005.

[151] Q. Li and G. T. Wang, "Improvement in aligned GaN nanowire growth using submonolayer Ni catalyst films," *Applied Physics Letters,* vol. 93, p. 043119, 2008.
[152] J. M. Gillette, *Designing With Light: An Introduction to Stage Lighting, Fourth Edition*: McGraw Hill, 2003.
[153] R. M. Soneira. (2010). *Apple iPhone 3GS LCD Display Shoot-Out*. Available: http://www.displaymate.com/iPhone_3GS_ShootOut.htm
[154] Wikipedia. (2018). *iPhone 3GS*. Available: https://en.wikipedia.org/wiki/IPhone_3GS
[155] R. M. Soneira. (2010). *Apple iPhone 4 LCD Display Shoot-Out*. Available: http://www.displaymate.com/iPhone_4_ShootOut.htm
[156] R. M. Soneira. (2014). *iPhone 6 Display Technology Shoot-Out iPhone 6 and iPhone 6 Plus with the iPhone 5*. Available: http://www.displaymate.com/iPhone6_ShootOut.htm
[157] R. M. Soneira. (2016). *iPhone 7 Display Technology Shoot-Out iPhone 6 and iPhone 7*. Available: http://www.displaymate.com/iPhone7_ShootOut_1.htm
[158] R. M. Soneira. (2017). *iPhone X OLED Display Technology Shoot-Out*. Available: http://www.displaymate.com/iPhoneX_ShootOut_1a.htm
[159] T. Riemersma, "Candela, Lumen, Lux: the equations," *CompuPhase (statutory name: Informatie-Technologisch Bureau CompuPhase)* 2012.
[160] t. f. e. Wikipedia, "Screen burn-in," vol. https://en.wikipedia.org/wiki/Screen_burn-in, 2018.
[161] A. Steude, E. C. Witts, G. B. Miles, and M. C. Gather, "Arrays of microscopic organic LEDs for high-resolution optogenetics," *Science Advances,* vol. 2, 2016.
[162] S. Reineke, F. Lindner, G. Schwartz, N. Seidler, K. Walzer, B. Lüssem, and K. Leo, "White organic light-emitting diodes with fluorescent tube efficiency," *Nature,* vol. 459, p. 234, 2009.
[163] H. S. Hwang, A. A. Zakhidov, J.-K. Lee, X. Andrâe, J. A. DeFranco, H. H. Fong, A. B. Holmes, G. G. Malliaras, and C. K. Ober, "Dry photolithographic patterning process for organic electronic devices using supercritical carbon dioxide as a solvent," *Journal of Materials Chemistry,* vol. 18, pp. 3087-3090, 2008.
[164] H. Uoyama, K. Goushi, K. Shizu, H. Nomura, and C. Adachi, "Highly efficient organic light-emitting diodes from delayed fluorescence," *Nature,* vol. 492, p. 234, 2012.
[165] C. Adachi, M. A. Baldo, M. E. Thompson, and S. R. Forrest, "Nearly 100% internal phosphorescence efficiency in an organic light-emitting device," *Journal of Applied Physics,* vol. 90, pp. 5048-5051, 2001.
[166] J. Son, H.-T. Oh, O. J. Kwon, J.-M. Lim, H. Jung, B. J. Jung, D.-H. Hwang, C. Lee, J.-K. Lee, J. G. Yoon, and S. Y. Yoon, "Highly soluble fluorous alkyl ether-tagged imaging materials for the photo-patterning of organic light-emitting devices," *Journal of Materials Chemistry C,* vol. 5, pp. 926-930, 2017.
[167] G. J. McGraw and S. R. Forrest, "Vapor-Phase Microprinting of Multicolor Phosphorescent Organic Light Emitting Device Arrays," *Advanced Materials,* vol. 25, pp. 1583-1588, 2013.
[168] M. E. Bahlke, H. A. Mendoza, D. T. Ashall, A. S. Yin, and M. A. Baldo, "Dry Lithography of Large-Area, Thin-Film Organic Semiconductors Using Frozen CO2 Resists," *Advanced Materials,* vol. 24, pp. 6136-6140, 2012.
[169] A. Mikami, Y. Nishita, and Y. Iida, "35-3: High Efficiency Phosphorescent Organic Light-Emitting Devices Coupled with Lateral Color-Conversion Layer," *SID Symposium Digest of Technical Papers,* vol. 37, pp. 1376-1379, 2006.
[170] S. Junger, W. Tschekalinskij, and N. Weber, "Multimedia and multiservice systems for home, office, and industrial networks," in *SPIE Proceedings*, 2004, pp. 123-133.

[171] L. S. Lepnev, A. A. Vashchenko, A. G. Vitukhnovskii, S. V. Eliseeva, O. V. Kotova, and N. P. Kuzmina, "Degradation of organic light-emitting diodes based on different-ligand complexes of terbium (III) salicylate and 2-phenoxybenzoate," *Bulletin of the Lebedev Physics Institute,* vol. 34, pp. 102-106, 2007.
[172] P. E. Burrows, V. Bulovic, S. R. Forrest, L. S. Sapochak, D. M. Mccarty, and M. E. Thompson, "Reliability and Degradation of Organic Light-Emitting Devices," *Applied Physics Letters,* vol. 65, pp. 2922-2924, 1994.
[173] Y. Shi, E. Tangdiongga, A. M. J. Koonen, A. Bluschke, P. Rietzsch, J. Montalvo, M. M. d. Laat, G. N. v. d. Hoven, and B. Huiszoon, "Plastic-optical-fiber-based in-home optical networks," *IEEE Communications Magazine,* vol. 52, pp. 186-193, 2014.
[174] W. B. Im, N. George, J. Kurzman, S. Brinkley, A. Mikhailovsky, J. Hu, B. F. Chmelka, S. P. DenBaars, and R. Seshadri, "Efficient and Color-Tunable Oxyfluoride Solid Solution Phosphors for Solid-State White Lighting," *Advanced Materials,* vol. 23, pp. 2300-2305, 2011.
[175] T. Honda, T. Kobayashi, S. Egawa, M. Sawada, K. Sugimoto, and T. Baba, "Integrated light-emitting diodes grown by MOVPE for flat panel displays," *Journal of Crystal Growth,* vol. 298, pp. 736-739, 2007.
[176] E. F. Schubert, *Light-Emitting Diodes*: Cambridge University Press, 2006.
[177] R. Wang, H. P. T. Nguyen, A. T. Connie, J. Lee, I. Shih, and Z. Mi, "Color-tunable, phosphor-free InGaN nanowire light-emitting diode arrays monolithically integrated on silicon," *Optics Express,* vol. 22, pp. A1768-A1775, 2014.
[178] S. Grzanka, P. Perlin, R. Czernecki, L. Marona, M. Boćkowski, B. Łucznik, M. Leszczyński, and T. Suski, "Effect of efficiency "droop" in violet and blue InGaN laser diodes," *Applied Physics Letters,* vol. 95, p. 071108, 2009.
[179] C. Lok, "Vision science: Seeing without seeing," *Nature,* vol. 469, pp. 284-5, 2011.
[180] M. W. Kowarz, J. G. Phalen, and C. J. Johnson, "67.2: Line-Scanned Laser Display Architectures Based on GEMS Technology: From Three-Lens Three-Chip Systems to Low-Cost Optically Efficient Trilinear Systems," *SID Symposium Digest of Technical Papers,* vol. 37, pp. 1908-1911, 2006.
[181] Laserfocusworld. (2004). *Laser light shows take on new dimensions - Advances in solid-state RGB lasers and graphics software have expanded the market for laser-based entertainment, especially in smaller venues*. Available: https://www.laserfocusworld.com/articles/print/volume-40/issue-11/features/optoelectronic-applications-entertainment/laser-light-shows-take-on-new-dimensions.html
[182] J. C. Brazas and M. W. Kowarz, "High-resolution laser-projection display system using a grating electromechanical system (GEMS)," in *Micromachining and Microfabrication*, 2004, p. 11.
[183] S. Liu, X. Dong, X. Yu, X. Chen, and C. Tian, "Hybrid wavelength- and frequency-division multiplexed fiber laser sensor array," *Optics Letters,* vol. 42, pp. 159-162, 2017.
[184] A. A. Al-Jabr, M. Abdulmajed, M. S. Bin Alias, T. Ng, and B. Ooi, "Achieving Room Temperature Orange Lasing Using InGaP/InAlGaP Diode Laser," in *Advanced Solid State Lasers*, Berlin, 2015, p. AM5A.46.
[185] G. Duggan, D. A. Barrow, T. Calvert, M. Maute, V. Hung, B. McGarvey, J. D. Lambkin, and T. Wipiejewski, "Red vertical cavity surface emitting lasers (VCSELs) for consumer applications," 2008, pp. 69080G-69080G-12.
[186] M. Belli, C. R. Fernandes, L. M. G. Neves, V. Mourão, R. Barbieri, M. A. M. Esquisatto, M. E. C. Amaral, G. M. T. Santos, and F. A. S. Mendonça, "Application of 670 nm InGaP laser and microcurrent favors the healing of second-degree burns in Wistar rats," *Laser Physics,* vol. 25, p. 025602, 2015.

[187] S. Nakamura, M. Senoh, S.-i. Nagahama, N. Iwasa, T. Yamada, T. Matsushita, H. Kiyoku, and Y. Sugimoto, "InGaN-based multi-quantum-well-structure laser diodes," *Japanese Journal of Applied Physics,* vol. 35, p. 74, 1996.
[188] H. Yoshida, M. Kuwabara, Y. Yamashita, K. Uchiyama, and H. Kan, "The current status of ultraviolet laser diodes," *Physica Status Solidi (A),* vol. 208, pp. 1586-1589, 2011.
[189] K. Katayama, N. Saga, M. Ueno, T. Ikegami, and T. Nakamura, "High-power true green laser diodes on semipolar {2021} GaN substrates," *Electronics and Communications in Japan,* vol. 98, pp. 9-14, 2015.
[190] E. Yohei, Y. Yusuke, K. Takashi, A. Katsushi, U. Masaki, A. Masahiro, S. Takamichi, T. Shinji, I. Takatoshi, K. Koji, and N. Takao, "531 nm Green Lasing of InGaN Based Laser Diodes on Semi-Polar {2021} Free-Standing GaN Substrates," *Applied Physics Express,* vol. 2, p. 082101, 2009.
[191] Y. Yusuke, A. Masahiro, E. Yohei, K. Takashi, T. Shinji, S. Takamichi, A. Katsushi, I. Takatoshi, U. Masaki, K. Koji, and N. Takao, "Continuous-Wave Operation of 520 nm Green InGaN-Based Laser Diodes on Semi-Polar {2021} GaN Substrates," *Applied Physics Express,* vol. 2, p. 092101, 2009.
[192] L. You-Da, Y. Shuichiro, H. Chia-Yen, H. Chia-Lin, W. Feng, F. Kenji, O. Hiroaki, S. S. James, P. D. Steven, and N. Shuji, "High Quality InGaN/AlGaN Multiple Quantum Wells for Semipolar InGaN Green Laser Diodes," *Applied Physics Express,* vol. 3, p. 082001, 2010.
[193] M. Takashi, M. Shingo, O. Takeshi, Y. Tomoya, K. Tokuya, N. Shin-ichi, and M. Takashi, "510–515 nm InGaN-Based Green Laser Diodes on c -Plane GaN Substrate," *Applied Physics Express,* vol. 2, p. 062201, 2009.
[194] K. Okamoto, J. Kashiwagi, T. Tanaka, and M. Kubota, "Nonpolar m-plane InGaN multiple quantum well laser diodes with a lasing wavelength of 499.8 nm," *Applied Physics Letters,* vol. 94, p. 071105, 2009.
[195] A. Masahiro, Y. Yusuke, E. Yohei, K. Takashi, S. Takamichi, T. Shinji, T. Shinpei, S. Kazuhide, S. Nobuhiro, I. Takatoshi, U. Masaki, K. Koji, and N. Takao, "Low threshold current density ingan based 520–530 nm green laser diodes on semi-polar {2021} free-standing GaN substrates," *Applied Physics Express,* vol. 3, p. 121001, 2010.
[196] W.-C. Chen, S.-Y. Kuo, W.-L. Wang, J.-S. Tian, W.-T. Lin, F.-I. Lai, and L. Chang, "Study of InN epitaxial films and nanorods grown on GaN template by RF-MOMBE," *Nanoscale Research Letters,* vol. 7, pp. 1-7, 2012.
[197] C. J. Rawn, Chaudhuri. J., *Lattice parameters of gallium nitride at high temperatures and resulting epitaxial misfits with alumina and silicon carbide substrates. Adv. X-Ray Anal. 43, 338–343.,* 2000.
[198] Y. Masaichi, O. Mitsuo, Y. Yoke Khin, Y. Masashi, M. Yusuke, and S. Takatomo, "Control of Nucleation Site and Growth Orientation of Bulk GaN Crystals," *Japanese Journal of Applied Physics,* vol. 38, p. L1121, 1999.
[199] F. Medjdoub, "Gallium Nitride (GaN): Physics, Devices, and Technology," *CRC Press,* p. 238, 2015
[200] A. Nebel and R. E. Wallenstein, "Concepts and performance of solid state RGB laser sources for large-frame laser projection displays," 2000, pp. 163-166.
[201] H. Peng, W. Hou, Y. Chen, D. Cui, Z. Xu, C. Chen, F. Fan, and Y. Zhu, "Generation of 7.6-W blue laser by frequency-tripling of a Nd:YAG laser in LBO crystals," *Optics Express,* vol. 14, pp. 6543-6549, 2006.
[202] J. J. D. McKendry, D. Massoubre, S. Zhang, B. R. Rae, R. P. Green, E. Gu, R. K. Henderson, A. E. Kelly, and M. D. Dawson, "Visible-Light Communications Using a

CMOS-Controlled Micro-Light- Emitting-Diode Array," *Journal of Lightwave Technology,* vol. 30, pp. 61-67, 2012.
[203] I. Takai, S. Ito, K. Yasutomi, K. Kagawa, M. Andoh, and S. Kawahito, "LED and CMOS Image Sensor Based Optical Wireless Communication System for Automotive Applications," *IEEE Photonics Journal,* vol. 5, pp. 6801418-6801418, 2013.
[204] I. Takai, T. Harada, M. Andoh, K. Yasutomi, K. Kagawa, and S. Kawahito, "Optical Vehicle-to-Vehicle Communication System Using LED Transmitter and Camera Receiver," *IEEE Photonics Journal,* vol. 6, pp. 1-14, 2014.
[205] Y. C. Lee, J. L. Lai, C. H. Yu, and C. S. A. Gong, "The high-efficiency LED driver for visible light communication applications," in *2016 Eighth International Conference on Ubiquitous and Future Networks (ICUFN)*, 2016, pp. 56-58.
[206] K. Liang, C.-W. Chow, and Y. Liu, "RGB visible light communication using mobile-phone camera and multi-input multi-output," *Optics Express,* vol. 24, pp. 9383-9388, 2016.
[207] Y. Goto, I. Takai, T. Yamazato, H. Okada, T. Fujii, S. Kawahito, S. Arai, T. Yendo, and K. Kamakura, "A New Automotive VLC System Using Optical Communication Image Sensor," *IEEE Photonics Journal,* vol. 8, pp. 1-17, 2016.
[208] T. Luettel, M. Himmelsbach, and H. J. Wuensche, "Autonomous Ground Vehicles-Concepts and a Path to the Future," *Proceedings of the IEEE,* vol. 100, pp. 1831-1839, 2012.
[209] Y.-C. Chi, D.-H. Hsieh, C.-Y. Lin, H.-Y. Chen, C.-Y. Huang, J.-H. He, B. Ooi, S. P. DenBaars, S. Nakamura, H.-C. Kuo, and G.-R. Lin, "Phosphorous Diffuser Diverged Blue Laser Diode for Indoor Lighting and Communication," *Scientific Reports,* vol. 5, p. 18690, 2015.
[210] Y. Wang, X. Huang, L. Tao, J. Shi, and N. Chi, "4.5-Gb/s RGB-LED based WDM visible light communication system employing CAP modulation and RLS based adaptive equalization," *Optics Express,* vol. 23, pp. 13626-13633, 2015.
[211] Y. Wang, L. Tao, X. Huang, J. Shi, and N. Chi, "8-Gb/s RGBY LED-Based WDM VLC System Employing High-Order CAP Modulation and Hybrid Post Equalizer," *IEEE Photonics Journal,* vol. 7, pp. 1-7, 2015.
[212] A. Polley and S. E. Ralph, "100 m, 40 Gb/s Plastic Optical Fiber Link," in *Optical Fiber communication/National Fiber Optic Engineers Conference, 2008. OFC/NFOEC 2008. Conference on*, 2008, pp. 1-3.
[213] S. Junger, W. Tschekalinskij, and N. Weber, "Multimedia and multiservice systems for home, office, and industrial networks," 2004, pp. 123-133.
[214] T. Ishigure, E. Nihei, S. Yamazaki, K. Kobayashi, and Y. Koike, "2.5 Gbit/s 100 m data transmission using graded-index polymer optical fibre and high-speed laser diode at 650 nm wavelength," *Electronics Letters,* vol. 31, pp. 467-469, 1995.
[215] T. Ishigure, E. Nihei, and Y. Koike, "Graded-index polymer optical fiber for high-speed data communication," *Applied Optics,* vol. 33, pp. 4261-4266, 1994.
[216] G. Giaretta, W. White, M. Wegmuller, and T. Onishi, "High-speed (11 Gbit/s) data transmission using perfluorinated graded-index polymer optical fibers for short interconnects (<100 m)," *IEEE Photonics Technology Letters,* vol. 12, pp. 347-349, 2000.
[217] H.-C. Peng, H.-H. Lu, C.-Y. Li, H.-S. Su, and C.-T. Hsu, "Integration of FTTH and GI-POF in-house networks based on injection locking and direct-detection techniques," *Optics Express,* vol. 19, pp. 6749-6755, 2011.
[218] E. T. S. Institute, *Access, Terminals, Transmission and Multiplexing (ATTM); Integrated Broadband Cable and Television Networks; IPCablecom 1.5; Part 19:*

IPCablecom Audio Server Protocol Specification - MGCP option, vol. TS 103 161-19 - V1.1.1 2011 2011.
[219] O. Ziemann, "POF handbook : optical short range transmission systems," 2008.
[220] Y. Koike, T. Ishigure, and E. Nihei, "High-bandwidth graded-index polymer optical fiber," *Journal of Lightwave Technology,* vol. 13, pp. 1475-1489, 1995.
[221] T. Ishigure, Y. Koike, and J. W. Fleming, "Optimum index profile of the perfluorinated polymer-based GI polymer optical fiber and its dispersion properties," *Journal of Lightwave Technology,* vol. 18, pp. 178-184, 2000.
[222] G. Parkinson. (2017). *Stunning new low for solar PV as even IEA hails "age of solar"*. Available: http://reneweconomy.com.au/stunning-new-low-for-solar-pv-as-even-iea-hails-age-of-solar-43509/
[223] M. Osborne. (2016). *SolarEdge sales slow on US residential market sluggishness*. Available: https://www.pv-tech.org/news/solaredge-sales-slow-on-us-residential-market-sluggishness
[224] G. Carr. (2012). *Alternative energy will no longer be alternative*. Available: https://www.economist.com/news/21566414-alternative-energy-will-no-longer-be-alternative-sunny-uplands
[225] TrendforcePVenergytrend. (2017). *Price Quotes*. Available: http://pv.energytrend.com/pricequotes.html
[226] R. M. Swanson, "A vision for crystalline silicon photovoltaics," *Progress in Photovoltaics: Research and Applications,* vol. 14, pp. 443-453, 2006.
[227] I. I. Novikov, "The efficiency of atomic power stations (a review)," *Journal of Nuclear Energy (1954),* vol. 7, pp. 125-128, 1958.
[228] T. D. Navarrete-González, J. A. Rocha-Martínez, and F. Angulo-Brown, "A Müser - Curzon - Ahlborn engine model for photothermal conversion," *Journal of Physics D: Applied Physics,* vol. 30, p. 2490, 1997.
[229] A. Belghachi, "Theoretical Calculation of the Efficiency Limit for Solar Cells," in *Solar Cells - New Approaches and Reviews*, L. A. Kosyachenko, Ed., ed Rijeka: InTech, 2015, p. Ch. 02.
[230] T. Soga, K. Baskar, T. Kato, T. Jimbo, and M. Umeno, "MOCVD growth of high efficiency current-matched AlGaAsSi tandem solar cell," *Journal of Crystal Growth,* vol. 174, pp. 579-584, 1997.
[231] N. V. Yastrebova, "High-efficiency multi-junction solar cells: Current status and future potential," *University of Ottawa,* 2008.
[232] B. Hekmatshoar, D. Shahrjerdi, M. Hopstaken, K. Fogel, and D. K. Sadana, "High-efficiency heterojunction solar cells on crystalline germanium substrates," *Applied Physics Letters,* vol. 101, p. 032102, 2012.
[233] S. Essig, M. A. Steiner, C. Allebe, J. F. Geisz, B. Paviet-Salomon, S. Ward, A. Descoeudres, V. LaSalvia, L. Barraud, N. Badel, A. Faes, J. Levrat, M. Despeisse, C. Ballif, P. Stradins, and D. L. Young, "Realization of GaInP/Si dual-junction solar cells with 29.8% 1-sun efficiency," *IEEE Journal of Photovoltaics,* vol. 6, pp. 1012-1019, 2016.
[234] G. J. Bauhuis, P. Mulder, E. J. Haverkamp, J. C. C. M. Huijben, and J. J. Schermer, "26.1% thin-film GaAs solar cell using epitaxial lift-off," *Solar Energy Materials and Solar Cells,* vol. 93, pp. 1488-1491, 2009.
[235] K. Lee, K.-T. Shiu, J. D. Zimmerman, C. K. Renshaw, and S. R. Forrest, "Multiple growths of epitaxial lift-off solar cells from a single InP substrate," *Applied Physics Letters,* vol. 97, p. 101107, 2010.
[236] R. Dahal, J. Li, K. Aryal, J. Y. Lin, and H. X. Jiang, "InGaN/GaN multiple quantum well concentrator solar cells," *Appl Phys Lett,* vol. 97, 2010.

[237] X. B. Zhang, X. L. Wang, H. L. Xiao, C. B. Yang, J. X. Ran, C. M. Wang, Q. F. Hou, and J. M. Li, "Simulation of In0.65Ga0.35N single-junction solar cell," *J Phys D Appl Phys,* vol. 40, 2007.
[238] X. B. Zhang, X. L. Wang, H. L. Xiao, C. B. Yang, J. X. Ran, C. M. Wang, Q. F. Hou, J. M. Li, and Z. G. Wang, "Theoretical design and performance of InxGa1-xN two-junction solar cells," *J Phys D Appl Phys,* vol. 41, 2008.
[239] O. Jani, *Development Of Wide-Band Gap InGaN Solar Cells For High-Efficiency Photovoltaics, PhD Dissertation, Georgia Institute of Technology August,,* 2008.
[240] O. Jani, I. Ferguson, C. Honsberg, and S. Kurtz, "Design and characterization of GaN/InGaN solar cells," *Appl Phys Lett,* vol. 91, 2007.
[241] K. Yosuke, F. Takahiro, F. Yasuharu, S. Tohru, I. Motoaki, T. Tetsuya, K. Satoshi, A. Isamu, and A. Hiroshi, "Realization of Nitride-Based Solar Cell on Freestanding GaN Substrate," *Applied Physics Express,* vol. 3, p. 111001, 2010.
[242] B. W. Liou, "Design and fabrication of InxGa1 − xN/GaN solar cells with a multiple-quantum-well structure on SiCN/Si(111) substrates," *Thin Solid Films,* vol. 520, pp. 1084-1090, 2011.
[243] B. W. Liou, "Temperature of $In_xGa_{1-x}N$/GaN solar cells with a multiple-quantum-well structure on SiCN/Si(111) substrates," *Solar Energy Materials and Solar Cells,* vol. 114, pp. 141-146, 2013.
[244] M. Lourassi and B. Soudini, "Simulation of piezoelectric and spontaneous polarization effect on the InGaN/Si tandem solar cell," *Optik - International Journal for Light and Electron Optics,* vol. 127, pp. 3091-3094, 2016.
[245] K. W. Böer, *Survey of semiconductor physics*. New York: Wiley, 2002.
[246] J. S. Im, H. Kollmer, J. Off, A. Sohmer, F. Scholz, and A. Hangleiter, "Effects of Piezoelectric Fields in GaInN/GaN and GaN/AlGaN Heterostructures and Quantum Wells," *MRS Proceedings,* vol. 482, 2011.
[247] J. S. Im, H. Kollmer, O. Gfrörer, J. Off, F. Scholz, and A. Hangleiter, "Piezoelectric Field Effect on Optical Properties of GaN/GaInN/AlGaN Quantum Wells," *MRS Proceedings,* vol. 537, 2011.
[248] R. K. Ahrenkiel, M. M. Al-Jassim, D. J. Dunlavy, K. M. Jones, S. M. Vernon, S. P. Tobin, and V. E. Haven, "Minority carrier lifetime of GaAs on silicon," in *Photovoltaic Specialists Conference, 1988., Conference Record of the Twentieth IEEE*, 1988, pp. 684-688 vol.1.
[249] M. R. Lueck, C. L. Andre, A. J. Pitera, M. L. Lee, E. A. Fitzgerald, and S. A. Ringel, "Dual junction GaInP/GaAs solar cells grown on metamorphic SiGe/Si substrates with high open circuit voltage," *IEEE Electron Device Letters,* vol. 27, pp. 142-144, 2006.
[250] H. P. T. Nguyen, S. Zhang, K. Cui, A. Korinek, G. A. Botton, and Z. Mi, "High-Efficiency InGaN/GaN Dot-in-a-Wire Red Light-Emitting Diodes," *IEEE Photonics Technology Letters,* vol. 24, pp. 321-323, 2012.
[251] N. Hieu Pham Trung, C. Kai, Z. Shaofei, F. Saeed, and M. Zetian, "Full-color InGaN/GaN dot-in-a-wire light emitting diodes on silicon," *Nanotechnology,* vol. 22, p. 445202, 2011.
[252] H. P. Nguyen, M. Djavid, S. Y. Woo, X. Liu, A. T. Connie, S. Sadaf, Q. Wang, G. A. Botton, I. Shih, and Z. Mi, "Engineering the Carrier Dynamics of InGaN Nanowire White Light-Emitting Diodes by Distributed p-AlGaN Electron Blocking Layers," *Sci. Rep.,* vol. 5, p. 7744, 2015.
[253] H. P. T. Nguyen, K. Cui, S. Zhang, M. Djavid, A. Korinek, G. A. Botton, and Z. Mi, "Controlling Electron Overflow in Phosphor-Free InGaN/GaN Nanowire White Light-Emitting Diodes," *Nano Letters,* vol. 12, pp. 1317-1323, 2012.

[254] H. P. Nguyen, S. Zhang, A. T. Connie, M. G. Kibria, Q. Wang, I. Shih, and Z. Mi, "Breaking the carrier injection bottleneck of phosphor-free nanowire white light-emitting diodes," *Nano Lett,* vol. 13, pp. 5437-42, 2013.
[255] H. Sekiguchi, K. Kishino, and A. Kikuchi, "Emission color control from blue to red with nanocolumn diameter of InGaN/GaN nanocolumn arrays grown on same substrate," *Applied Physics Letters,* vol. 96, p. 231104, 2010.
[256] K. Katsumi, N. Kazuya, and Y. Kouji, "Monolithic Integration of InGaN-Based Nanocolumn Light-Emitting Diodes with Different Emission Colors," *Applied Physics Express,* vol. 6, p. 012101, 2013.
[257] M. J. Grundmann and U. K. Mishra, "Multi-color light emitting diode using polarization-induced tunnel junctions," *physica status solidi (c),* vol. 4, pp. 2830-2833, 2007.
[258] F. Akyol, S. Krishnamoorthy, and S. Rajan, "Tunneling-based carrier regeneration in cascaded GaN light emitting diodes to overcome efficiency droop," *Applied Physics Letters,* vol. 103, p. 081107, 2013.
[259] S. J. Chang, W. H. Lin, and C. T. Yu, "GaN-Based Multiquantum Well Light-Emitting Diodes With Tunnel-Junction-Cascaded Active Regions," *IEEE Electron Device Letters,* vol. 36, pp. 366-368, 2015.
[260] J. Simon, Z. Zhang, K. Goodman, H. Xing, T. Kosel, P. Fay, and D. Jena, "Polarization-Induced Zener Tunnel Junctions in Wide-Band-Gap Heterostructures," *Physical Review Letters,* vol. 103, p. 026801, 2009.
[261] K. Zhang, H. Liang, R. Shen, D. Wang, P. Tao, Y. Liu, X. Xia, Y. Luo, and G. Du, "Negative differential resistance in low Al-composition p-GaN/Mg-doped Al0.15Ga0.85N/n+-GaN hetero-junction grown by metal-organic chemical vapor deposition on sapphire substrate," *Applied Physics Letters,* vol. 104, p. 053507, 2014.
[262] J. Piprek, "Origin of InGaN/GaN light-emitting diode efficiency improvements using tunnel-junction-cascaded active regions," *Applied Physics Letters,* vol. 104, p. 051118, 2014.
[263] S. Krishnamoorthy, F. Akyol, P. S. Park, and S. Rajan, "Low resistance GaN/InGaN/GaN tunnel junctions," *Applied Physics Letters,* vol. 102, p. 113503, 2013.
[264] S. Krishnamoorthy, F. Akyol, and S. Rajan, "InGaN/GaN tunnel junctions for hole injection in GaN light emitting diodes," *Applied Physics Letters,* vol. 105, p. 141104, 2014.
[265] A. T. Connie, S. Zhao, S. M. Sadaf, I. Shih, Z. Mi, X. Du, J. Lin, and H. Jiang, "Optical and electrical properties of Mg-doped AlN nanowires grown by molecular beam epitaxy," *Applied Physics Letters,* vol. 106, p. 213105, 2015.
[266] S. Krishnamoorthy, T. F. Kent, J. Yang, P. S. Park, R. C. Myers, and S. Rajan, "GdN Nanoisland-Based GaN Tunnel Junctions," *Nano Letters,* vol. 13, pp. 2570-2575, 2013.
[267] S. Krishnamoorthy, D. N. Nath, F. Akyol, P. S. Park, M. Esposto, and S. Rajan, "Polarization-engineered GaN/InGaN/GaN tunnel diodes," *Applied Physics Letters,* vol. 97, p. 203502, 2010.
[268] S. Krishnamoorthy, P. S. Park, and S. Rajan, "Demonstration of forward inter-band tunneling in GaN by polarization engineering," *Applied Physics Letters,* vol. 99, p. 233504, 2011.
[269] S. M. Sadaf, Y. H. Ra, H. P. T. Nguyen, M. Djavid, and Z. Mi, "Alternating-Current InGaN/GaN Tunnel Junction Nanowire White-Light Emitting Diodes," *Nano Letters,* vol. 15, pp. 6696-6701, 2015.
[270] T. Frost, S. Jahangir, E. Stark, S. Deshpande, A. Hazari, C. Zhao, B. S. Ooi, and P. Bhattacharya, "Monolithic electrically injected nanowire array edge-emitting laser on (001) silicon," *Nano Lett,* vol. 14, pp. 4535-41, Aug 13 2014.

[271] S. Zhao, H. P. T. Nguyen, M. G. Kibria, and Z. Mi, "III-Nitride nanowire optoelectronics," *Progress in Quantum Electronics,* vol. 44, pp. 14-68, 2015.
[272] H. P. T. Nguyen, Q. Wang, and Z. Mi, "Phosphor-Free InGaN/GaN Dot-in-a-Wire White Light-Emitting Diodes on Copper Substrates," *Journal of Electronic Materials,* vol. 43, pp. 868-872, 2014.
[273] J. C. Johnson, H. J. Choi, K. P. Knutsen, R. D. Schaller, P. Yang, and R. J. Saykally, "Single gallium nitride nanowire lasers," *Nat Mater,* vol. 1, pp. 106-10, Oct 2002.
[274] F. Qian, Y. Li, S. Gradecak, H. G. Park, Y. Dong, Y. Ding, Z. L. Wang, and C. M. Lieber, "Multi-quantum-well nanowire heterostructures for wavelength-controlled lasers," *Nat Mater,* vol. 7, pp. 701-6, 2008.
[275] Q. Li, J. B. Wright, W. W. Chow, T. S. Luk, I. Brener, L. F. Lester, and G. T. Wang, "Single-mode GaN nanowire lasers," *Optics Express,* vol. 20, pp. 17873-17879, 2012.
[276] M. Sakai, Y. Inose, K. Ema, T. Ohtsuki, H. Sekiguchi, A. Kikuchi, and K. Kishino, "Random laser action in GaN nanocolumns," *Applied Physics Letters,* vol. 97, p. 151109, 2010.
[277] J. B. Wright, S. Campione, S. Liu, J. A. Martinez, H. Xu, T. S. Luk, Q. Li, G. T. Wang, B. S. Swartzentruber, L. F. Lester, and I. Brener, "Distributed feedback gallium nitride nanowire lasers," *Applied Physics Letters,* vol. 104, p. 041107, 2014.
[278] H. Gao, A. Fu, S. C. Andrews, and P. Yang, "Cleaved-coupled nanowire lasers," *Proceedings of the National Academy of Sciences,* vol. 110, pp. 865-869, 2013.
[279] H. Xu, J. B. Wright, A. Hurtado, Q. Li, T.-S. Luk, J. J. Figiel, K. Cross, G. Balakrishnan, L. F. Lester, I. Brener, and G. T. Wang, "Gold substrate-induced single-mode lasing of GaN nanowires," *Applied Physics Letters,* vol. 101, p. 221114, 2012.
[280] Q. Zhang, G. Li, X. Liu, F. Qian, Y. Li, T. C. Sum, C. M. Lieber, and Q. Xiong, "A room temperature low-threshold ultraviolet plasmonic nanolaser," *Nat Commun,* vol. 5, p. 4953, 2014.
[281] Y. J. Lu, C. Y. Wang, J. Kim, H. Y. Chen, M. Y. Lu, Y. C. Chen, W. H. Chang, L. J. Chen, M. I. Stockman, C. K. Shih, and S. Gwo, "All-color plasmonic nanolasers with ultralow thresholds: autotuning mechanism for single-mode lasing," *Nano Lett,* vol. 14, pp. 4381-8, 2014.
[282] Y.-J. Lu, J. Kim, H.-Y. Chen, C. Wu, N. Dabidian, C. E. Sanders, C.-Y. Wang, M.-Y. Lu, B.-H. Li, X. Qiu, W.-H. Chang, L.-J. Chen, G. Shvets, C.-K. Shih, and S. Gwo, "Plasmonic Nanolaser Using Epitaxially Grown Silver Film," *Science,* vol. 337, pp. 450-453, 2012.
[283] T. Frost, S. Jahangir, E. Stark, S. Deshpande, A. Hazari, C. Zhao, B. S. Ooi, and P. Bhattacharya, "Monolithic Electrically Injected Nanowire Array Edge-Emitting Laser on (001) Silicon," *Nano Letters,* vol. 14, pp. 4535-4541, 2014.
[284] S. Jahangir, T. Frost, A. Hazari, L. Yan, E. Stark, T. LaMountain, J. M. Millunchick, B. S. Ooi, and P. Bhattacharya, "Small signal modulation characteristics of red-emitting ($\lambda = 610$ nm) III-nitride nanowire array lasers on (001) silicon," *Applied Physics Letters,* vol. 106, p. 071108, 2015.
[285] A. Hazari, A. Aiello, T.-K. Ng, B. S. Ooi, and P. Bhattacharya, "III-nitride disk-in-nanowire 1.2 μm monolithic diode laser on (001)silicon," *Applied Physics Letters,* vol. 107, p. 191107, 2015.
[286] A. C. Scofield, S.-H. Kim, J. N. Shapiro, A. Lin, B. Liang, A. Scherer, and D. L. Huffaker, "Bottom-up Photonic Crystal Lasers," *Nano Letters,* vol. 11, pp. 5387-5390, 2011.
[287] J. Heo, W. Guo, and P. Bhattacharya, "Monolithic single GaN nanowire laser with photonic crystal microcavity on silicon," *Applied Physics Letters,* vol. 98, p. 021110, 2011.

[288] J. B. Wright, S. Liu, G. T. Wang, Q. Li, A. Benz, D. D. Koleske, P. Lu, H. Xu, L. Lester, T. S. Luk, I. Brener, and G. Subramania, "Multi-colour nanowire photonic crystal laser pixels," *Sci Rep,* vol. 3, p. 2982, 2013.
[289] I. Shusuke, K. Katsumi, A. Ryuichi, K. Akihiko, and S. Shuichi, "Optically Pumped Green (530–560 nm) Stimulated Emissions from InGaN/GaN Multiple-Quantum-Well Triangular-Lattice Nanocolumn Arrays," *Applied Physics Express,* vol. 4, p. 055001, 2011.
[290] M. Law, L. E. Greene, J. C. Johnson, R. Saykally, and P. Yang, "Nanowire dye-sensitized solar cells," *Nat Mater,* vol. 4, pp. 455-459, 06//print 2005.
[291] K. Zhu, N. R. Neale, A. Miedaner, and A. J. Frank, "Enhanced Charge-Collection Efficiencies and Light Scattering in Dye-Sensitized Solar Cells Using Oriented TiO2 Nanotubes Arrays," *Nano Letters,* vol. 7, pp. 69-74, 2007.
[292] S. Funk, B. Hokkanen, U. Burghaus, A. Ghicov, and P. Schmuki, "Unexpected Adsorption of Oxygen on TiO2 Nanotube Arrays: Influence of Crystal Structure," *Nano Letters,* vol. 7, pp. 1091-1094, 2007.
[293] S. P. Albu, A. Ghicov, J. M. Macak, R. Hahn, and P. Schmuki, "Self-Organized, Free-Standing TiO2 Nanotube Membrane for Flow-through Photocatalytic Applications," *Nano Letters,* vol. 7, pp. 1286-1289, 2007.
[294] J. Park, S. Bauer, K. von der Mark, and P. Schmuki, "Nanosize and Vitality: TiO2 Nanotube Diameter Directs Cell Fate," *Nano Letters,* vol. 7, pp. 1686-1691, 2007.
[295] I. Lombardi, A. I. Hochbaum, P. Yang, C. Carraro, and R. Maboudian, "Synthesis of High Density, Size-Controlled Si Nanowire Arrays via Porous Anodic Alumina Mask," *Chemistry of Materials,* vol. 18, pp. 988-991, 2006.
[296] B. Tian, T. J. Kempa, and C. M. Lieber, "Single nanowire photovoltaics," *Chemical Society Reviews,* vol. 38, pp. 16-24, 2009.
[297] B. Tian, X. Zheng, T. J. Kempa, Y. Fang, N. Yu, G. Yu, J. Huang, and C. M. Lieber, "Coaxial silicon nanowires as solar cells and nanoelectronic power sources," *Nature,* vol. 449, pp. 885-9, 2007.
[298] J. Wallentin, N. Anttu, D. Asoli, M. Huffman, I. Aberg, M. H. Magnusson, G. Siefer, P. Fuss-Kailuweit, F. Dimroth, B. Witzigmann, H. Q. Xu, L. Samuelson, K. Deppert, and M. T. Borgstrom, "InP nanowire array solar cells achieving 13.8% efficiency by exceeding the ray optics limit," *Science,* vol. 339, pp. 1057-60, 2013.
[299] E. C. Garnett, M. L. Brongersma, Y. Cui, and M. D. McGehee, "Nanowire Solar Cells," *Annual Review of Materials Research,* vol. 41, pp. 269-295, 2011.
[300] T. J. Kempa, J. F. Cahoon, S. K. Kim, R. W. Day, D. C. Bell, H. G. Park, and C. M. Lieber, "Coaxial multishell nanowires with high-quality electronic interfaces and tunable optical cavities for ultrathin photovoltaics," *Proc Natl Acad Sci U S A,* vol. 109, pp. 1407-12, 2012.
[301] I. Aberg, G. Vescovi, D. Asoli, U. Naseem, J. P. Gilboy, C. Sundvall, A. Dahlgren, K. E. Svensson, N. Anttu, M. T. Bj, and L. Samuelson, "A GaAs Nanowire Array Solar Cell With 15.3% Efficiency at 1 Sun," *IEEE Journal of Photovoltaics,* vol. 6, pp. 185-190, 2016.
[302] M.-L. Zhang, F. Jin, M.-L. Zheng, J. Liu, Z.-S. Zhao, and X.-M. Duan, "High efficiency solar cell based on ZnO nanowire array prepared by different growth methods," *RSC Advances,* vol. 4, pp. 10462-10466, 2014.
[303] Y. Dong, B. Tian, T. J. Kempa, and C. M. Lieber, "Coaxial Group III−Nitride Nanowire Photovoltaics," *Nano Letters,* vol. 9, pp. 2183-2187, 2009.
[304] M. F. Cansizoglu, S. M. Hamad, D. P. Norman, F. Keles, E. Badraddin, T. Karabacak, and H.-W. Seo, "PiN InGaN nanorod solar cells with high short-circuit current," *Applied Physics Express,* vol. 8, p. 042302, 2015.

[305] J. J. Wierer, Jr., Q. Li, D. D. Koleske, S. R. Lee, and G. T. Wang, "III-nitride core-shell nanowire arrayed solar cells," *Nanotechnology,* vol. 23, p. 194007, 2012.
[306] H. P. T. Nguyen, Y. L. Chang, I. Shih, and Z. Mi, "InN p-i-n Nanowire Solar Cells on Si," *IEEE Journal of Selected Topics in Quantum Electronics,* vol. 17, pp. 1062-1069, 2011.
[307] S. Fan, I. Shih, and Z. Mi, "A monolithically integrated InGaN nanowire/si tandem photoanode approaching the ideal bandgap configuration of 1.75/1.13 eV," *Advanced Energy Materials,* p. 1600952, 2016.
[308] A. Lidow, J. Strydom, M. De Rooij, and D. Reusch, "GaN Transistors for Efficient Power Conversion," 2014.
[309] J. Roberts, H. Lafontaine, and C. McKnight-MacNeil, "Advanced SPICE models applied to high power GaN devices and integrated GaN drive circuits," in *2014 IEEE Applied Power Electronics Conference and Exposition - APEC 2014*, 2014, pp. 493-496.
[310] S. Ming, C. Chingchi, and R. Siddharth, "Prospects for the application of GaN power devices in hybrid electric vehicle drive systems," *Semiconductor Science and Technology,* vol. 28, p. 074012, 2013.
[311] E. A. Jones, F. Wang, and B. Ozpineci, "Application-based review of GaN HFETs," in *2014 IEEE Workshop on Wide Bandgap Power Devices and Applications*, 2014, pp. 24-29.
[312] G. Sabui, V. Z. Zubialevich, M. White, P. Pampili, P. J. Parbrook, M. McLaren, M. Arredondo-Arechavala, and Z. J. Shen, "GaN Nanowire Schottky Barrier Diodes," *IEEE Transactions on Electron Devices,* vol. 64, pp. 2283-2290, 2017.
[313] R. Chu, A. Corrion, M. Chen, R. Li, D. Wong, D. Zehnder, B. Hughes, and K. Boutros, "1200-V Normally Off GaN-on-Si Field-Effect Transistors With Low Dynamic on - Resistance," *IEEE Electron Device Letters,* vol. 32, pp. 632-634, 2011.
[314] K. Ota, K. Endo, Y. Okamoto, Y. Ando, H. Miyamoto, and H. Shimawaki, "A normally-off GaN FET with high threshold voltage uniformity using a novel piezo neutralization technique," in *2009 IEEE International Electron Devices Meeting (IEDM)*, 2009, pp. 1-4.
[315] N. Kaneko, O. Machida, M. Yanagihara, S. Iwakami, R. Baba, H. Goto, and A. Iwabuchi, "Normally-off AlGaN/GaN HFETs using NiO_x gate with recess," in *2009 21st International Symposium on Power Semiconductor Devices & IC's*, 2009, pp. 25-28.
[316] T. Oka and T. Nozawa, "AlGaN/GaN Recessed MIS-Gate HFET With High-Threshold-Voltage Normally-Off Operation for Power Electronics Applications," *IEEE Electron Device Letters,* vol. 29, pp. 668-670, 2008.
[317] N. Ikeda, R. Tamura, T. Kokawa, H. Kambayashi, Y. Sato, T. Nomura, and S. Kato, "Over 1.7 kV normally-off GaN hybrid MOS-HFETs with a lower on-resistance on a Si substrate," in *2011 IEEE 23rd International Symposium on Power Semiconductor Devices and ICs*, 2011, pp. 284-287.
[318] T. Hirose, M. Imai, K. Joshin, K. Watanabe, T. Ogino, Y. Miyazaki, K. Shono, T. Hosoda, and Y. Asai, "Dynamic performances of GaN-HEMT on Si in cascode configuration," in *2014 IEEE Applied Power Electronics Conference and Exposition - APEC 2014*, 2014, pp. 174-181.
[319] P. C. Howard Sin. *Normally-off and Current Collapse free GaN Transistor*. Available: https://ca.mouser.com/applications/wide-bandgap-gan-transistor/
[320] M. Meneghini, I. Rossetto, D. Bisi, A. Stocco, A. Cester, G. Meneghesso, E. Zanoni, A. Chini, A. Pantellini, and C. Lanzieri, "Role of buffer doping and pre-existing trap

states in the current collapse and degradation of AlGaN/GaN HEMTs," in *2014 IEEE International Reliability Physics Symposium*, 2014, pp. 6C.6.1-6C.6.7.
[321] A. P. Zhang, L. B. Rowland, E. B. Kaminsky, V. Tilak, J. C. Grande, J. Teetsov, A. Vertiatchikh, and L. F. Eastman, "Correlation of device performance and defects in AlGaN/GaN high-electron mobility transistors," *Journal of Electronic Materials,* vol. 32, pp. 388-394, 2003.
[322] P. B. Klein and S. C. Binari, "Photoionization spectroscopy of deep defects responsible for current collapse in nitride-based field effect transistors," *Journal of Physics: Condensed Matter,* vol. 15, p. R1641, 2003.
[323] M. T. Hasan, "Mechanism and Suppression of Current Collapse in AlGaN/GaN High Electron Mobility Transistors," Ph.D Ph.D dissertation, Electrical and Electronics Engineering, University of Fukui, Japan, 2013.
[324] Y. Puzyrev, X. Shen, and S. Pantelides, "Identification of the defect responsible for current collapse in GaN/AlGaN HEMTs," in *APS March Meeting 2013, Session B23: Focus Session: Dopants and Defects in Semiconductors II*, Baltimore, Maryland, 2013.
[325] G. A. Umana-Membreno, G. Parish, N. Fichtenbaum, S. Keller, U. K. Mishra, and B. D. Nener, "Electrically Active Defects in GaN Layers Grown With and Without Fe-doped Buffers by Metal-organic Chemical Vapor Deposition," *Journal of Electronic Materials,* vol. 37, pp. 569-572, 2008.
[326] M. J. Uren, D. G. Hayes, R. S. Balmer, D. J. Wallis, K. P. Hilton, J. O. Maclean, T. Martin, C. Roff, P. McGovern, J. Benedikt, and P. J. Tasker, "Control of Short-Channel Effects in GaN/AlGaN HFETs," in *2006 European Microwave Integrated Circuits Conference*, 2006, pp. 65-68.
[327] M. J. Uren, K. J. Nash, R. S. Balmer, T. Martin, E. Morvan, N. Caillas, S. L. Delage, D. Ducatteau, B. Grimbert, and J. C. D. Jaeger, "Punch-through in short-channel AlGaN/GaN HFETs," *IEEE Transactions on Electron Devices,* vol. 53, pp. 395-398, 2006.
[328] H. Sarvari, A. H. Ghayour, Z. Chen, and R. Ghayour, "Analyses of Short Channel Effects of Single-Gate and Double-Gate Graphene Nanoribbon Field Effect Transistors," *Journal of Materials,* vol. 2016, p. 8, 2016.
[329] Y. Zenji, T. A. Joel, and H. Tamotsu, "Insulated gate and surface passivation structures for GaN-based power transistors," *Journal of Physics D: Applied Physics,* vol. 49, p. 393001, 2016.
[330] D. Lizzit, O. Badami, R. Specogna, and D. Esseni, "Improved surface-roughness scattering and mobility models for multi-gate FETs with arbitrary cross-section and biasing scheme," *Journal of Applied Physics,* vol. 121, p. 245301, 2017.
[331] Y. V. Fedorov and S. V. Mikhaylovich, "Effect of heterostructure parameters and fabrication technology on the noise properties of AlGaN/GaN HEMT," in *2015 10th European Microwave Integrated Circuits Conference (EuMIC)*, 2015, pp. 144-147.
[332] K. S. Im, R. H. Kim, K. W. Kim, D. S. Kim, C. S. Lee, S. Cristoloveanu, and J. H. Lee, "Normally Off Single-Nanoribbon Al_2O_3/GaN MISFET," *IEEE Electron Device Letters,* vol. 34, pp. 27-29, 2013.
[333] K. S. Im, Y. W. Jo, J. H. Lee, S. Cristoloveanu, and J. H. Lee, "Heterojunction-Free GaN Nanochannel FinFETs With High Performance," *IEEE Electron Device Letters,* vol. 34, pp. 381-383, 2013.
[334] K. S. Im, C. H. Won, Y. W. Jo, J. H. Lee, M. Bawedin, S. Cristoloveanu, and J. H. Lee, "High-Performance GaN-Based Nanochannel FinFETs With/Without AlGaN/GaN Heterostructure," *IEEE Transactions on Electron Devices,* vol. 60, pp. 3012-3018, 2013.

[335] Y. Q. Wu, R. S. Wang, T. Shen, J. J. Gu, and P. D. Ye, "First experimental demonstration of 100 nm inversion-mode InGaAs FinFET through damage-free sidewall etching," in *2009 IEEE International Electron Devices Meeting (IEDM)*, 2009, pp. 1-4.
[336] J. J. Gu, O. Koybasi, Y. Q. Wu, and P. D. Ye, "III-V-on-nothing metal-oxide-semiconductor field-effect transistors enabled by top-down nanowire release process: Experiment and simulation," *Applied Physics Letters,* vol. 99, p. 112113, 2011.
[337] T. Sekigawa and Y. Hayashi, "Calculated threshold-voltage characteristics of an XMOS transistor having an additional bottom gate," *Solid-State Electronics,* vol. 27, pp. 827-828, 1984.
[338] K.-S. Im, V. Sindhuri, Y.-W. Jo, D.-H. Son, J.-H. Lee, S. Cristoloveanu, and J.-H. Lee, "Fabrication of AlGaN/GaN Ω-shaped nanowire fin-shaped FETs by a top-down approach," *Applied Physics Express,* vol. 8, p. 066501, 2015.
[339] K.-S. Im, C.-H. Won, S. Vodapally, R. Caulmilone, S. Cristoloveanu, Y.-T. Kim, and J.-H. Lee, "Fabrication of normally-off GaN nanowire gate-all-around FET with top-down approach," *Applied Physics Letters,* vol. 109, p. 143106, 2016.
[340] J. P. Colinge, M. H. Gao, A. Romano-Rodriguez, H. Maes, and C. Claeys, "Silicon-on-insulator 'gate-all-around device'," in *International Technical Digest on Electron Devices*, 1990, pp. 595-598.
[341] V. K. Khanna, "Short-Channel Effects in MOSFETs," in *Integrated Nanoelectronics: Nanoscale CMOS, Post-CMOS and Allied Nanotechnologies*, ed New Delhi: Springer India, 2016, pp. 73-93.
[342] L. Sung-Young, K. Sung-Min, Y. Eun-Jung, O. Chang Woo, C. Ilsub, P. Donggun, and K. Kinam, "Three-dimensional MBCFET as an ultimate transistor," *IEEE Electron Device Letters,* vol. 25, pp. 217-219, 2004.
[343] O. Ambacher, B. Foutz, J. Smart, J. R. Shealy, N. G. Weimann, K. Chu, M. Murphy, A. J. Sierakowski, W. J. Schaff, L. F. Eastman, R. Dimitrov, A. Mitchell, and M. Stutzmann, "Two dimensional electron gases induced by spontaneous and piezoelectric polarization in undoped and doped AlGaN/GaN heterostructures," *Journal of Applied Physics,* vol. 87, pp. 334-344, 2000.
[344] F. Yu, D. Rümmler, J. Hartmann, L. Caccamo, T. Schimpke, M. Strassburg, A. E. Gad, A. Bakin, H.-H. Wehmann, B. Witzigmann, H. S. Wasisto, and A. Waag, "Vertical architecture for enhancement mode power transistors based on GaN nanowires," *Applied Physics Letters,* vol. 108, p. 213503, 2016.
[345] M. A. Khan, Q. Chen, C. J. Sun, J. W. Yang, M. Blasingame, M. S. Shur, and H. Park, "Enhancement and depletion mode GaN/AlGaN heterostructure field effect transistors," *Applied Physics Letters,* vol. 68, pp. 514-516, 1996.
[346] C. Yong, Z. Yugang, K. J. Chen, and K. M. Lau, "High-performance enhancement-mode AlGaN/GaN HEMTs using fluoride-based plasma treatment," *IEEE Electron Device Letters,* vol. 26, pp. 435-437, 2005.
[347] R. G. Hobbs, N. Petkov, and J. D. Holmes, "Semiconductor Nanowire Fabrication by Bottom-Up and Top-Down Paradigms," *Chemistry of Materials,* vol. 24, pp. 1975-1991, 2012.
[348] J. Bai, Q. Wang, and T. Wang, "Characterization of InGaN-based nanorod light emitting diodes with different indium compositions," *Journal of Applied Physics,* vol. 111, p. 113103, 2012.
[349] Y. D. Zhuang, C. J. Lewins, S. Lis, P. A. Shields, and D. W. E. Allsopp, "Fabrication and Characterization of Light-Emitting Diodes Comprising Highly Ordered Arrays of Emissive InGaN/GaN Nanorods," *IEEE Photonics Technology Letters,* vol. 25, pp. 1047-1049, 2013.

[350] S. Keller, C. Schaake, N. A. Fichtenbaum, C. J. Neufeld, Y. Wu, K. McGroddy, A. David, S. P. DenBaars, C. Weisbuch, J. S. Speck, and U. K. Mishra, "Optical and structural properties of GaN nanopillar and nanostripe arrays with embedded InGaN/GaN multi-quantum wells," *Journal of Applied Physics,* vol. 100, p. 054314, 2006.

[351] J. Zhu, L. Wang, S. Zhang, H. Wang, D. Zhao, J. Zhu, Z. Liu, D. Jiang, and H. Yang, "The fabrication of GaN-based nanopillar light-emitting diodes," *Journal of Applied Physics,* vol. 108, p. 074302, 2010.

[352] Q. Li, K. R. Westlake, M. H. Crawford, S. R. Lee, D. D. Koleske, J. J. Figiel, K. C. Cross, S. Fathololoumi, Z. Mi, and G. T. Wang, "Optical performance of top-down fabricated InGaN/GaN nanorod light emitting diode arrays," *Optics Express,* vol. 19, pp. 25528-25534, 2011.

[353] V. Ramesh, A. Kikuchi, K. Kishino, M. Funato, and Y. Kawakami, "Strain relaxation effect by nanotexturing InGaN/GaN multiple quantum well," *Journal of Applied Physics,* vol. 107, p. 114303, 2010.

[354] J. C. Harmand, G. Patriarche, N. Péré-Laperne, M.-N. Mérat-Combes, L. Travers, and F. Glas, "Analysis of vapor-liquid-solid mechanism in Au-assisted GaAs nanowire growth," *Applied Physics Letters,* vol. 87, p. 203101, 2005.

[355] J. Ristić, E. Calleja, S. Fernández-Garrido, L. Cerutti, A. Trampert, U. Jahn, and K. H. Ploog, "On the mechanisms of spontaneous growth of III-nitride nanocolumns by plasma-assisted molecular beam epitaxy," *Journal of Crystal Growth,* vol. 310, pp. 4035-4045, 2008.

[356] A. P. Vajpeyi, A. O. Ajagunna, G. Tsiakatouras, A. Adikimenakis, E. Iliopoulos, K. Tsagaraki, M. Androulidaki, and A. Georgakilas, "Spontaneous growth of III-nitride nanowires on Si by molecular beam epitaxy," *Microelectronic Engineering,* vol. 86, pp. 812-815, 2009.

[357] S. Hiroto, K. Katsumi, and K. Akihiko, "Ti-mask Selective-Area Growth of GaN by RF-Plasma-Assisted Molecular-Beam Epitaxy for Fabricating Regularly Arranged InGaN/GaN Nanocolumns," *Applied Physics Express,* vol. 1, p. 124002, 2008.

[358] X. Duan and C. M. Lieber, "Laser-Assisted Catalytic Growth of Single Crystal GaN Nanowires," *Journal of the American Chemical Society,* vol. 122, pp. 188-189, 2000.

[359] S. Chattopadhyay, A. Ganguly, K.-H. Chen, and L.-C. Chen, "One-Dimensional Group III-Nitrides: Growth, Properties, and Applications in Nanosensing and Nano-Optoelectronics," *Critical Reviews in Solid State and Materials Sciences,* vol. 34, pp. 224-279, 2009.

[360] V. Gottschalch, G. Wagner, J. Bauer, H. Paetzelt, and M. Shirnow, "VLS growth of GaN nanowires on various substrates," *Journal of Crystal Growth,* vol. 310, pp. 5123-5128, 2008.

[361] P. YANG, Y. WU, and R. FAN, "INORGANIC SEMICONDUCTOR NANOWIRES," *International Journal of Nanoscience,* vol. 01, pp. 1-39, 2002.

[362] E. Stern, G. Cheng, E. Cimpoiasu, R. Klie, S. Guthrie, J. Klemic, I. Kretzschmar, E. Steinlauf, D. Turner-Evans, E. Broomfield, J. Hyland, R. Koudelka, T. Boone, M. Young, A. Sanders, R. Munden, T. Lee, D. Routenberg, and M. A. Reed, "Electrical characterization of single GaN nanowires," *Nanotechnology,* vol. 16, p. 2941, 2005.

[363] L. Geelhaar, C. Chèze, W. M. Weber, R. Averbeck, H. Riechert, T. Kehagias, P. Komninou, G. P. Dimitrakopulos, and T. Karakostas, "Axial and radial growth of Ni-induced GaN nanowires," *Applied Physics Letters,* vol. 91, p. 093113, 2007.

[364] C. Chèze, L. Geelhaar, A. Trampert, O. Brandt, and H. Riechert, "Collector Phase Transitions during Vapor−Solid−Solid Nucleation of GaN Nanowires," *Nano Letters,* vol. 10, pp. 3426-3431, 2010.

[365] R. S. Wagner and W. C. Ellis, "VAPOR-LIQUID-SOLID MECHANISM OF SINGLE CRYSTAL GROWTH," *Applied Physics Letters,* vol. 4, pp. 89-90, 1964.
[366] S. Fernández-Garrido, V. M. Kaganer, K. K. Sabelfeld, T. Gotschke, J. Grandal, E. Calleja, L. Geelhaar, and O. Brandt, "Self-Regulated Radius of Spontaneously Formed GaN Nanowires in Molecular Beam Epitaxy," *Nano Letters,* vol. 13, pp. 3274-3280, 2013.
[367] C. Chèze, L. Geelhaar, O. Brandt, W. M. Weber, H. Riechert, S. Münch, R. Rothemund, S. Reitzenstein, A. Forchel, T. Kehagias, P. Komninou, G. P. Dimitrakopulos, and T. Karakostas, "Direct comparison of catalyst-free and catalyst-induced GaN nanowires," *Nano Research,* vol. 3, pp. 528-536, 2010.
[368] R. Calarco, R. J. Meijers, R. K. Debnath, T. Stoica, E. Sutter, and H. Lüth, "Nucleation and Growth of GaN Nanowires on Si(111) Performed by Molecular Beam Epitaxy," *Nano Letters,* vol. 7, pp. 2248-2251, 2007.
[369] M.-H. Kim, I.-S. Kim, Y.-H. Park, T.-E. Park, J. H. Shin, and H.-J. Choi, "Platinum Assisted Vapor–Liquid–Solid Growth of Er–Si Nanowires and Their Optical Properties," *Nanoscale Research Letters,* vol. 5, pp. 286-290, 2010.
[370] Z. Zhang, T. Shimizu, L. Chen, S. Senz, and U. Gösele, "Bottom-Imprint Method for VSS Growth of Epitaxial Silicon Nanowire Arrays with an Aluminium Catalyst," *Advanced Materials,* vol. 21, pp. 4701-4705, 2009.
[371] L. Ren, H. Li, and L. Ma, "The Selective Growth of Silicon Nanowires and Their Optical Activation," in *Nanowires - Implementations and Applications*, A. Hashim, Ed., ed Rijeka: InTech, 2011, p. Ch. 17.
[372] Y. Masaki, K. Akihiko, M. Masashi, F. Nobuhiko, and K. Katsumi, "Growth of Self-Organized GaN Nanostructures on A l 2 O 3 (0001) by RF-Radical Source Molecular Beam Epitaxy," *Japanese Journal of Applied Physics,* vol. 36, p. L459, 1997.
[373] Y. L. Chang, F. Li, A. Fatehi, and Z. T. Mi, "Molecular beam epitaxial growth and characterization of non-tapered InN nanowires on Si(111)," *Nanotechnology,* vol. 20, pp. -, 2009.
[374] M. He and S. N. Mohammad, "Novelty and versatility of self-catalytic nanowire growth: A case study with InN nanowires," *Journal of Vacuum Science & Technology B: Microelectronics and Nanometer Structures Processing, Measurement, and Phenomena,* vol. 25, pp. 940-944, 2007.
[375] S. N. Mohammad, "Self-catalytic solution for single-crystal nanowire and nanotube growth," *The Journal of Chemical Physics,* vol. 127, p. 244702, 2007.
[376] M. A. Sanchez-Garcia, E. Calleja, E. Monroy, F. J. Sanchez, F. Calle, E. Muñoz, and R. Beresford, "The effect of the III/V ratio and substrate temperature on the morphology and properties of GaN- and AlN-layers grown by molecular beam epitaxy on Si(1 1 1)," *Journal of Crystal Growth,* vol. 183, pp. 23-30, 1998.
[377] E. Calleja, M. A. Sánchez-García, F. J. Sánchez, F. Calle, F. B. Naranjo, E. Muñoz, U. Jahn, and K. Ploog, "Luminescence properties and defects in GaN nanocolumns grown by molecular beam epitaxy," *Physical Review B,* vol. 62, pp. 16826-16834, 2000.
[378] E. A. Stach, P. J. Pauzauskie, T. Kuykendall, J. Goldberger, R. He, and P. Yang, "Watching GaN Nanowires Grow," *Nano Letters,* vol. 3, pp. 867-869, 2003.
[379] C. Yi-Lu, L. Feng, F. Arya, and M. Zetian, "Molecular beam epitaxial growth and characterization of non-tapered InN nanowires on Si(111)," *Nanotechnology,* vol. 20, p. 345203, 2009.
[380] R. K. Debnath, R. Meijers, T. Richter, T. Stoica, R. Calarco, and H. Lüth, "Mechanism of molecular beam epitaxy growth of GaN nanowires on Si(111)," *Applied Physics Letters,* vol. 90, p. 123117, 2007.

[381] V. Consonni, M. Hanke, M. Knelangen, L. Geelhaar, A. Trampert, and H. Riechert, "Nucleation mechanisms of self-induced GaN nanowires grown on an amorphous interlayer," *Physical Review B,* vol. 83, p. 035310, 2011.
[382] K. A. Bertness, A. Roshko, L. M. Mansfield, T. E. Harvey, and N. A. Sanford, "Mechanism for spontaneous growth of GaN nanowires with molecular beam epitaxy," *Journal of Crystal Growth,* vol. 310, pp. 3154-3158, 2008.
[383] L. Lymperakis and J. Neugebauer, "Large anisotropic adatom kinetics on nonpolar GaN surfaces: Consequences for surface morphologies and nanowire growth," *Physical Review B,* vol. 79, p. 241308, 2009.
[384] D. Zubia, S. Zhang, R. Bommena, X. Sun, S. R. J. Brueck, and S. D. Hersee, "Initial nanoheteroepitaxial growth of GaAs on Si(100) by OMVPE," *Journal of Electronic Materials,* vol. 30, pp. 812-816.
[385] S. C. Lee, L. R. Dawson, S. R. J. Brueck, and Y.-B. Jiang, "GaAs on Si(111)—crystal shape and strain relaxation in nanoscale patterned growth," *Applied Physics Letters,* vol. 87, p. 023101, 2005.
[386] C.-P. Chu, S. Arafin, T. Nie, K. Yao, X. Kou, L. He, C.-Y. Wang, S.-Y. Chen, L.-J. Chen, S. M. Qasim, M. S. BenSaleh, and K. L. Wang, "Nanoscale Growth of GaAs on Patterned Si(111) Substrates by Molecular Beam Epitaxy," *Crystal Growth & Design,* vol. 14, pp. 593-598, 2014.
[387] S. C. Lee, L. R. Dawson, B. Pattada, S. R. J. Brueck, Y.-B. Jiang, and H. F. Xu, "Strain-relieved, dislocation-free InxGa1−xAs⁄GaAs(001) heterostructure by nanoscale-patterned growth," *Applied Physics Letters,* vol. 85, pp. 4181-4183, 2004.
[388] S. C. Lee, L. R. Dawson, K. J. Malloy, and S. R. J. Brueck, "Multiple-wavelength emission from In_xGa_{1-x}As-GaAs quantum wells grown on a nanoscale faceted GaAs substrate by molecular beam epitaxy," *Selected Topics in Quantum Electronics, IEEE Journal of,* vol. 8, pp. 972-983, 2002.
[389] S.-C. Lee, K. J. Malloy, and S. R. J. Brueck, "Nanoscale selective growth of GaAs by molecular beam epitaxy," *Journal of Applied Physics,* vol. 90, pp. 4163-4168, 2001.
[390] S. C. Lee, K. J. Malloy, L. R. Dawson, and S. R. J. Brueck, "Selective growth and associated faceting and lateral overgrowth of GaAs on a nanoscale limited area bounded by a SiO2 mask in molecular beam epitaxy," *Journal of Applied Physics,* vol. 92, pp. 6567-6571, 2002.
[391] S. C. Lee, L. R. Dawson, S. R. J. Brueck, and Y.-B. Jiang, "Anisotropy of selective epitaxy in nanoscale-patterned growth: GaAs nanowires selectively grown on a SiO2-patterned (001) substrate by molecular-beam epitaxy," *Journal of Applied Physics,* vol. 98, p. 114312, 2005.
[392] S. C. Lee, L. R. Dawson, K. J. Malloy, and S. R. J. Brueck, "Molecular-beam epitaxial growth of one-dimensional rows of InAs quantum dots on nanoscale-patterned GaAs," *Applied Physics Letters,* vol. 79, pp. 2630-2632, 2001.
[393] S. C. Lee, A. Stintz, and S. R. J. Brueck, "Nanoscale limited area growth of InAs islands on GaAs(001) by molecular beam epitaxy," *Journal of Applied Physics,* vol. 91, pp. 3282-3288, 2002.
[394] D. L. Huffaker, C. P. Hains, N. Nuntawong, Y. C. Xin, P. S. Wong, L. Xue, S. R. J. Brueck, and L. Lester, "Temperature-dependent photoluminescence from patterned InAs quantum dots formed using metalorganic chemical vapor epitaxy," *Journal of Applied Physics,* vol. 99, p. 033503, 2006.
[395] P. S. Wong, B. L. Liang, J. Tatebayashi, L. Xue, N. Nuntawong, M. N. Kutty, S. R. J. Brueck, and D. L. Huffaker, "Fabrication and characteristics of broad-area light-emitting diode based on nanopatterned quantum dots," *Nanotechnology,* vol. 20, p. 035302, 2009.

[396] D. Zubia, S. H. Zaidi, S. R. J. Brueck, and S. D. Hersee, "Nanoheteroepitaxial growth of GaN on Si by organometallic vapor phase epitaxy," *Applied Physics Letters,* vol. 76, pp. 858-860, 2000.
[397] D. Zubia, S. H. Zaidi, S. D. Hersee, and S. R. J. Brueck, "Nanoheteroepitaxy: Nanofabrication route to improved epitaxial growth," *Journal of Vacuum Science & Technology B,* vol. 18, pp. 3514-3520, 2000.
[398] I. Shunsuke, K. Katsumi, and K. Akihiko, "Selective-Area Growth of GaN Nanocolumns on Si(111) Substrates Using Nitrided Al Nanopatterns by," *Applied Physics Express,* vol. 1, p. 015006, 2008.
[399] K. Kishino, H. Sekiguchi, and A. Kikuchi, "Improved Ti-mask selective-area growth (SAG) by rf-plasma-assisted molecular beam epitaxy demonstrating extremely uniform GaN nanocolumn arrays," *Journal of Crystal Growth,* vol. 311, pp. 2063-2068, 2009.
[400] X. Y. Sun, R. Bommena, D. Burckel, A. Frauenglass, M. N. Fairchild, S. R. J. Brueck, G. A. Garrett, M. Wraback, and S. D. Hersee, "Defect reduction mechanisms in the nanoheteroepitaxy of GaN on SiC," *Journal of Applied Physics,* vol. 95, pp. 1450-1454, 2004.
[401] K. Katsumi and I. Shunsuke, "Selective-area growth of GaN nanocolumns on Si(111) substrates for application to nanocolumn emitters with systematic analysis of dislocation filtering effect of nanocolumns," *Nanotechnology,* vol. 26, p. 225602, 2015.
[402] T. Schumann, T. Gotschke, F. Limbach, T. Stoica, and R. Calarco, "Selective-area catalyst-free MBE growth of GaN nanowires using a patterned oxide layer," *Nanotechnology,* vol. 22, p. 095603, 2011.
[403] T. Gotschke, T. Schumann, F. Limbach, T. Stoica, and R. Calarco, "Influence of the adatom diffusion on selective growth of GaN nanowire regular arrays," *Applied Physics Letters,* vol. 98, p. 103102, 2011.
[404] K. A. Bertness, A. W. Sanders, D. M. Rourke, T. E. Harvey, A. Roshko, J. B. Schlager, and N. A. Sanford, "Controlled Nucleation of GaN Nanowires Grown with Molecular Beam Epitaxy," *Advanced Functional Materials,* vol. 20, pp. 2911-2915, 2010.
[405] A. Bengoechea-Encabo, F. Barbagini, S. Fernandez-Garrido, J. Grandal, J. Ristic, M. A. Sanchez-Garcia, E. Calleja, U. Jahn, E. Luna, and A. Trampert, "Understanding the selective area growth of GaN nanocolumns by MBE using Ti nanomasks," *Journal of Crystal Growth,* vol. 325, pp. 89-92, 2011.
[406] Ž. Gačević, D. Gómez Sánchez, and E. Calleja, "Formation Mechanisms of GaN Nanowires Grown by Selective Area Growth Homoepitaxy," *Nano Letters,* vol. 15, pp. 1117-1121, 2015.
[407] R. A. Munden and M. A. Reed, "Chemical Beam Epitaxy of Gallium Nitride Nanowires," in *The Science and Function of Nanomaterials: From Synthesis to Application*. vol. 1183, ed: American Chemical Society, 2014, pp. 13-39.
[408] S. George, S. Ilan, M. Warren, and N. Venkatesh, "Catalytic hydride vapour phase epitaxy growth of GaN nanowires," *Nanotechnology,* vol. 16, p. 2342, 2005.
[409] M. Ebaid, J.-H. Kang, Y.-S. Yoo, S.-H. Lim, Y.-H. Cho, and S.-W. Ryu, "Vertically aligned InGaN nanowires with engineered axial In composition for highly efficient visible light emission," *Scientific Reports,* vol. 5, p. 17003, 2015.
[410] P. Grodzinski, S. P. DenBaars, and H. C. Lee, "From research to manufacture—The evolution of MOCVD," *JOM,* vol. 47, pp. 25-32, 1995.
[411] J. R. A. Jr., "Interaction of Ga and As2 Molecular Beams with GaAs Surfaces," *Journal of Applied Physics,* vol. 39, pp. 4032-4034, 1968.
[412] A. Y. Cho and J. R. Arthur, "Molecular beam epitaxy," *Progress in Solid State Chemistry,* vol. 10, pp. 157-191, 1975.

[413] VacuumElectronicEquipmentCo. (2013). *Veeco to ship first Genxplor R&D MBE system to the University of Oklahoma*. Available: http://ir.veeco.com/news-events/press-releases/press-release-details/2013/Veeco-to-Ship-First-GENxplor-RD-MBE-System-to-the-University-of-Oklahoma/default.aspx
[414] VacuumElectronicEquipmentCo. (2016). *Veeco Receives Landmark Order for MBE R&D System from Prominent Chinese University*. Available: http://www.veeco.com/company/news/veeco-receives-landmark-order-for-mbe-randd-system-from-prominent-chinese-university
[415] D. J. As and C. Mietze, "MBE growth and applications of cubic AlN/GaN quantum wells," *physica status solidi (a),* vol. 210, pp. 474-479, 2013.
[416] R. Ch., P. Tyagi, K. K. Maurya, M. S. Kumar, and S. S. Kushvaha, "Growth and characterizations of various GaN nanostructures on C-plane sapphire using laser MBE," *AIP Conference Proceedings,* vol. 1832, p. 080078, 2017.
[417] H. Shigehiko, S. Jong Uk, U. Mai, K. Mariko, and A. Hajime, "Growth and Characterization of GaN Nanostructures toward Electron Field Emitter Application," *Japanese Journal of Applied Physics,* vol. 52, p. 110103, 2013.
[418] Z. Yuji, O. Sang Ho, W. Feng, K. Yoshinobu, T. Shinichi, F. Kenji, S. S. James, P. D. Steven, and N. Shuji, "Green Semipolar (20-2-1) InGaN Light-Emitting Diodes with Small Wavelength Shift and Narrow Spectral Linewidth," *Applied Physics Express,* vol. 6, p. 062102, 2013.
[419] M. R. Philip, D. D. Choudhary, M. Djavid, K. Q. Le, J. Piao, and H. P. T. Nguyen, "High efficiency green/yellow and red InGaN/AlGaN nanowire light-emitting diodes grown by molecular beam epitaxy," *Journal of Science: Advanced Materials and Devices,* vol. 2, pp. 150-155, 2017.
[420] A. Yoshikawa, S. B. Che, N. Hashimoto, H. Saito, Y. Ishitani, and X. Q. Wang, "Fabrication and characterization of novel monolayer InN quantum wells in a GaN matrix," *Journal of Vacuum Science & Technology B: Microelectronics and Nanometer Structures Processing, Measurement, and Phenomena,* vol. 26, pp. 1551-1559, 2008.
[421] S. Zhao, S. Fathololoumi, K. H. Bevan, D. P. Liu, M. G. Kibria, Q. Li, G. T. Wang, H. Guo, and Z. Mi, "Tuning the Surface Charge Properties of Epitaxial InN Nanowires," *Nano Letters,* vol. 12, pp. 2877-2882, 2012.
[422] B. H. Le, S. Zhao, N. H. Tran, and Z. Mi, "Electrically injected near-infrared light emission from single InN nanowire p-i-n diode," *Applied Physics Letters,* vol. 105, p. 231124, 2014.
[423] B. O. Jung, S.-Y. Bae, S. Lee, S. Y. Kim, J. Y. Lee, Y. Honda, and H. Amano, "Emission Characteristics of InGaN/GaN Core-Shell Nanorods Embedded in a 3D Light-Emitting Diode," *Nanoscale Research Letters,* vol. 11, p. 215, 2016.
[424] S.-Y. Bae, J.-W. Min, H.-Y. Hwang, K. Lekhal, H.-J. Lee, Y.-D. Jho, D.-S. Lee, Y.-T. Lee, N. Ikarashi, Y. Honda, and H. Amano, "III-nitride core–shell nanorod array on quartz substrates," *Scientific Reports,* vol. 7, p. 45345, 2017.
[425] G. Avit, Y. André, C. Bougerol, D. Castelluci, A. Dussaigne, P. Ferret, S. Gaugiran, B. Gayral, E. Gil, Y. Lee, M. R. Ramdani, E. Roche, and A. Trassoudaine, "GaN Rods Grown on Si by SAG-HVPE toward GaN HVPE/InGaN MOVPE Core/Shell Structures," *Crystal Growth & Design,* vol. 16, pp. 2509-2513, 2016.
[426] M. Marcus, S. Gordon, M. Sebastian, V. Peter, B. Frank, K. Sergiy, D. Ratan, H. Jong-Yoon, W. Baomei, B. Paul, M. Abhishek, R. K. Matthew, V. D. Albert, and C. Jürgen, "Structural and optical nanoscale analysis of GaN core–shell microrod arrays fabricated by combined top-down and bottom-up process on Si(111)," *Japanese Journal of Applied Physics,* vol. 55, p. 05FF02, 2016.

[427] H. S. El-Ghoroury, C.-L. Chuang, and Z. Y. Alpaslan, "26.1: Invited Paper: Quantum Photonic Imager (QPI): A Novel Display Technology that Enables more than 3D Applications," *SID Symposium Digest of Technical Papers,* vol. 46, pp. 371-374, 2015.
[428] M. Sugawara, M. Suzuki, and N. Miyauchi, "Retinal imaging laser eyewear with focus-free and augmented reality," in *2017 24th International Workshop on Active-Matrix Flatpanel Displays and Devices (AM-FPD)*, 2017, pp. 5-8.
[429] H. Ohmae, Y. Tomita, M. Kasahara, J. Schram, E. Smits, J. van den Brand, F. Bossuyt, J. Vanfleteren, and J. De Baets, "9.4: Stretchable 45 × 80 RGB LED Display Using Meander Wiring Technology," *SID Symposium Digest of Technical Papers,* vol. 46, pp. 102-105, 2015.
[430] G. Haas, L. Espuno, E. Marcellin-Dibon, and C. Prat, "A 5.4 MDOT OLED microdisplay for digital night vision and image fusion," in *SPIE Defense, Security, and Sensing*, 2012, p. 9.
[431] J. Day, J. Li, D. Y. C. Lie, C. Bradford, J. Y. Lin, and H. X. Jiang, "III-Nitride full-scale high-resolution microdisplays," *Applied Physics Letters,* vol. 99, p. 031116, 2011.
[432] M. C. Gather, A. Köhnen, A. Falcou, H. Becker, and K. Meerholz, "Solution-Processed Full-Color Polymer Organic Light-Emitting Diode Displays Fabricated by Direct Photolithography," *Advanced Functional Materials,* vol. 17, pp. 191-200, 2007.
[433] K. Hayashi, H. Nakanotani, M. Inoue, K. Yoshida, O. Mikhnenko, T.-Q. Nguyen, and C. Adachi, "Suppression of roll-off characteristics of organic light-emitting diodes by narrowing current injection/transport area to 50 nm," *Applied Physics Letters,* vol. 106, p. 093301, 2015.
[434] C. Murawski, K. Leo, and M. C. Gather, "Efficiency Roll-Off in Organic Light-Emitting Diodes," *Advanced Materials,* vol. 25, pp. 6801-6827, 2013.
[435] J. W. Sun, J.-H. Lee, C.-K. Moon, K.-H. Kim, H. Shin, and J.-J. Kim, "A Fluorescent Organic Light-Emitting Diode with 30% External Quantum Efficiency," *Advanced Materials,* vol. 26, pp. 5684-5688, 2014.
[436] T. Miwa, S. Kubo, K. Shizu, T. Komino, C. Adachi, and H. Kaji, "Blue organic light-emitting diodes realizing external quantum efficiency over 25% using thermally activated delayed fluorescence emitters," *Scientific Reports,* vol. 7, p. 284, 2017.
[437] L. T. Sharpe, A. Stockman, W. Jagla, and H. Jägle, "A luminous efficiency function, V*(λ), for daylight adaptation," *Journal of Vision,* vol. 5, pp. 3-3, 2005.
[438] J. J. Vos, "Colorimetric and photometric properties of a 2° fundamental observer," *Color Research & Application,* vol. 3, pp. 125-128, 1978.
[439] R. Chaji, E. Fathi, and A. Zamani, "19-5: Invited Paper: Low-Cost Micro-LED Displays for All Applications," *SID Symposium Digest of Technical Papers,* vol. 48, pp. 264-267, 2017.
[440] S. Fery-Forgues, M. Abyan, and J. F. Lamere, "Nano- and microparticles of organic fluorescent dyes: self-organization and optical properties," *Annals of the New York Academy of Sciences,* vol. 1130, pp. 272-9, 2008.
[441] J. H. Kwon, R. Pode, H. D. Kim, and H. K. Chung, "High-Performance Organic Light-Emitting Diode Displays," in *Applications of Organic and Printed Electronics: A Technology-Enabled Revolution*, E. Cantatore, Ed., ed Boston, MA: Springer US, 2013, pp. 57-81.
[442] H. Sirringhaus, T. Kawase, R. H. Friend, T. Shimoda, M. Inbasekaran, W. Wu, and E. P. Woo, "High-Resolution Inkjet Printing of All-Polymer Transistor Circuits," *Science,* vol. 290, pp. 2123-2126, 2000.
[443] J. Chen, V. Leblanc, S. H. Kang, P. J. Benning, D. Schut, M. A. Baldo, M. A. Schmidt, and V. Bulović, "High Definition Digital Fabrication of Active Organic Devices by Molecular Jet Printing," *Advanced Functional Materials,* vol. 17, pp. 2722-2727, 2007.

[444] M. Shtein, P. Peumans, J. B. Benziger, and S. R. Forrest, "Direct, Mask- and Solvent-Free Printing of Molecular Organic Semiconductors," *Advanced Materials,* vol. 16, pp. 1615-1620, 2004.
[445] J. R. Bonar, G. J. Valentine, Z. Gong, J. Small, and S. Gorton, "High-brightness low-power consumption microLED arrays," in *SPIE OPTO*, 2016, p. 9.
[446] S. Cheng. (2016). *Overview of Micro-LED History and Current Developments*. Available: http://www.ledinside.com/outlook/2016/8/overview_of_micro_led_history_and_current_developments
[447] H. W. Choi, C. W. Jeon, and M. D. Dawson, "High-resolution 128 x 96 nitride microdisplay," *IEEE Electron Device Letters,* vol. 25, pp. 277-279, 2004.
[448] C. Tian, S.-x. Guo, J.-q. Liang, Z.-z. Liang, and F.-l. Gao, "Effects of unit size on current density and illuminance of micro-LED-array," *Optoelectronics Letters,* vol. 13, pp. 84-89, 2017.
[449] L. Dupré, M. Marra, V. Verney, B. Aventurier, F. Henry, F. Olivier, S. Tirano, A. Daami, and F. Templier, "Processing and characterization of high resolution GaN/InGaN LED arrays at 10 micron pitch for micro display applications," in *SPIE OPTO*, 2017, p. 8.
[450] P. N. Yocom, "Future requirements of display phosphors from an historical perspective," *Journal of the Society for Information Display,* vol. 4, pp. 149-152, 1996.
[451] N. Guan, X. Dai, A. Messanvi, H. Zhang, J. Yan, E. Gautier, C. Bougerol, F. H. Julien, C. Durand, J. Eymery, and M. Tchernycheva, "Flexible White Light Emitting Diodes Based on Nitride Nanowires and Nanophosphors," *ACS Photonics,* vol. 3, pp. 597-603, 2016.
[452] J. R. Oh, H. K. Park, J. H. Oh, T. Kouh, and Y. Rag Do, "Highly efficient full-color display based on blue LED backlight and electrochromic light-valve coupled with front-emitting phosphors," *Optics Express,* vol. 19, pp. 16022-16031, 2011.
[453] S.-L. Hsiao, N.-C. Hu, and H. Cornelissen, "Phosphor-converted LED modeling using near-field chromatic luminance data," *Optics Express,* vol. 21, pp. A250-A261, 2013.
[454] J. He, H. Chen, H. Chen, Y. Wang, S.-T. Wu, and Y. Dong, "25-2: Wide Color Gamut Display Based on Ultrastable Perovskite - Polymer Film and Red QDs/Phosphors," *SID Symposium Digest of Technical Papers,* vol. 48, pp. 349-352, 2017.
[455] P. H. Holloway, T. A. Trottier, J. Sebastian, S. Jones, X. M. Zhang, J. S. Bang, B. Abrams, W. J. Thomes, and T. J. Kim, "Degradation of field emission display phosphors," *Journal of Applied Physics,* vol. 88, pp. 483-488, 2000.
[456] S. X. Jin, J. Li, J. Z. Li, J. Y. Lin, and H. X. Jiang, "GaN microdisk light emitting diodes," *Applied Physics Letters,* vol. 76, pp. 631-633, 2000.
[457] F. Templier, "GaN-based emissive microdisplays: A very promising technology for compact, ultra-high brightness display systems," *Journal of the Society for Information Display,* vol. 24, pp. 669-675, 2016.
[458] L. Hongjian, L. Panpan, K. Junjie, L. Zhi, L. Zhicong, L. Jing, Y. Xiaoyan, and W. Guohong, "Phosphor-Free, Color-Tunable Monolithic InGaN Light-Emitting Diodes," *Applied Physics Express,* vol. 6, p. 102103, 2013.
[459] Y. F. Cheung and H. W. Choi, "Color-Tunable and Phosphor-Free White-Light Multilayered Light-Emitting Diodes," *IEEE Transactions on Electron Devices,* vol. 60, pp. 333-338, 2013.
[460] K. H. Li, Q. Wang, H. P. T. Nguyen, S. Zhao, and Z. Mi, "Polarization-resolved electroluminescence study of InGaN/GaN dot-in-a-wire light-emitting diodes grown by molecular beam epitaxy," *physica status solidi (a),* vol. 212, pp. 941-946, 2015.

[461] T. Kuykendall, P. Ulrich, S. Aloni, and P. Yang, "Complete composition tunability of InGaN nanowires using a combinatorial approach," *Nature Materials,* vol. 6, p. 951, 2007.
[462] Y. J. Hong, C.-H. Lee, A. Yoon, M. Kim, H.-K. Seong, H. J. Chung, C. Sone, Y. J. Park, and G.-C. Yi, "Visible-Color-Tunable Light-Emitting Diodes," *Advanced Materials,* vol. 23, pp. 3284-3288, 2011.
[463] Y.-J. L. Hon-Way Lin, Hung-Ying Chen, Hong-Mao Lee, and Shangjr Gwo "InGaN/GaN nanorod array white light-emitting diode," *Applied Physics Letters,* vol. 97, p. 073101, 2010.
[464] W. Guo, M. Zhang, A. Banerjee, and P. Bhattacharya, "Catalyst-free InGaN/GaN nanowire light emitting diodes grown on (001) silicon by molecular beam epitaxy," *Nano Lett,* vol. 10, 2010.
[465] S. Albert, A. Bengoechea-Encabo, M. A. Sánchez-García, X. Kong, A. Trampert, and E. Calleja, "Selective area growth of In(Ga)N/GaN nanocolumns by molecular beam epitaxy on GaN-buffered Si(111): from ultraviolet to infrared emission," *Nanotechnology,* vol. 24, p. 175303, 2013.
[466] Q. Li and G. T. Wang, "Strain influenced indium composition distribution in GaN/InGaN core-shell nanowires," *Applied Physics Letters,* vol. 97, p. 181107, 2010.
[467] A. T. Connie, H. P. T. Nguyen, S. M. Sadaf, I. Shih, and Z. Mi, "Engineering the color rendering index of phosphor-free InGaN/(Al)GaN nanowire white light emitting diodes grown by molecular beam epitaxy," *Journal of Vacuum Science & Technology B, Nanotechnology and Microelectronics: Materials, Processing, Measurement, and Phenomena,* vol. 32, p. 02C113, 2014.
[468] A. Yanagihara, S. Ishizawa, and K. Kishino, "Directional radiation beam from yellow-emitting InGaN-based nanocolumn LEDs with ordered bottom-up nanocolumn array," *Applied Physics Express,* vol. 7, p. 112102, 2014.
[469] M. Tchernycheva, C. Sartel, G. Cirlin, L. Travers, G. Patriarche, J. C. Harmand, D. Le Si, J. Renard, B. Gayral, L. Nevou, and F. Julien, "Growth of GaN free-standing nanowires by plasma-assisted molecular beam epitaxy: structural and optical characterization," *Nanotechnology,* vol. 18, p. 385306, 2007.
[470] V. G. Dubrovskii, V. Consonni, A. Trampert, L. Geelhaar, and H. Riechert, "Scaling thermodynamic model for the self-induced nucleation of GaN nanowires," *Physical Review B,* vol. 85, p. 165317, 2012.
[471] V. G. Dubrovskii, V. Consonni, L. Geelhaar, A. Trampert, and H. Riechert, "Scaling growth kinetics of self-induced GaN nanowires," *Applied Physics Letters,* vol. 100, p. 153101, 2012.
[472] K. D. Goodman, V. V. Protasenko, J. Verma, T. H. Kosel, H. G. Xing, and D. Jena, "Green luminescence of InGaN nanowires grown on silicon substrates by molecular beam epitaxy," *Journal of Applied Physics,* vol. 109, p. 084336, 2011.
[473] H. P. Nguyen, K. Cui, S. Zhang, S. Fathololoumi, and Z. Mi, "Full-color InGaN/GaN dot-in-a-wire light emitting diodes on silicon," *Nanotechnology,* vol. 22, p. 445202, 2011.
[474] J. Wallentin, N. Anttu, D. Asoli, M. Huffman, I. Åberg, M. H. Magnusson, G. Siefer, P. Fuss-Kailuweit, F. Dimroth, B. Witzigmann, H. Q. Xu, L. Samuelson, K. Deppert, and M. T. Borgström, "InP Nanowire Array Solar Cells Achieving 13.8% Efficiency by Exceeding the Ray Optics Limit," *Science,* vol. 339, pp. 1057-1060, 2013.
[475] J. Kupec, R. L. Stoop, and B. Witzigmann, "Light absorption and emission in nanowire array solar cells," *Optics Express,* vol. 18, pp. 27589-27605, 2010.

[476] N. Anttu and H. Q. Xu, "Coupling of Light into Nanowire Arrays and Subsequent Absorption," *Journal of Nanoscience and Nanotechnology,* vol. 10, pp. 7183-7187, // 2010.
[477] J. Kupec and B. Witzigmann, "Dispersion, Wave Propagation and Efficiency Analysis of Nanowire Solar Cells," *Optics Express,* vol. 17, pp. 10399-10410, 2009.
[478] S. L. Diedenhofen, G. Vecchi, R. E. Algra, A. Hartsuiker, O. L. Muskens, G. Immink, E. P. A. M. Bakkers, W. L. Vos, and J. G. Rivas, "Broad-band and Omnidirectional Antireflection Coatings Based on Semiconductor Nanorods," *Advanced Materials,* vol. 21, pp. 973-978, 2009.
[479] O. L. Muskens, J. G. Rivas, R. E. Algra, E. P. A. M. Bakkers, and A. Lagendijk, "Design of Light Scattering in Nanowire Materials for Photovoltaic Applications," *Nano Letters,* vol. 8, pp. 2638-2642, 2008.
[480] Z. Fan, R. Kapadia, P. W. Leu, X. Zhang, Y.-L. Chueh, K. Takei, K. Yu, A. Jamshidi, A. A. Rathore, D. J. Ruebusch, M. Wu, and A. Javey, "Ordered Arrays of Dual-Diameter Nanopillars for Maximized Optical Absorption," *Nano Letters,* vol. 10, pp. 3823-3827, 2010.
[481] C. Lin and M. L. Povinelli, "Optical absorption enhancement in silicon nanowire arrays with a large lattice constant for photovoltaic applications," *Optics Express,* vol. 17, pp. 19371-19381, 2009.
[482] J. Li, H. Yu, S. M. Wong, X. Li, G. Zhang, P. G.-Q. Lo, and D.-L. Kwong, "Design guidelines of periodic Si nanowire arrays for solar cell application," *Applied Physics Letters,* vol. 95, p. 243113, 2009.
[483] L. Wen, Z. Zhao, X. Li, Y. Shen, H. Guo, and Y. Wang, "Theoretical analysis and modeling of light trapping in high efficicency GaAs nanowire array solar cells," *Applied Physics Letters,* vol. 99, p. 143116, 2011.
[484] Y. Hu, R. R. LaPierre, M. Li, K. Chen, and J.-J. He, "Optical characteristics of GaAs nanowire solar cells," *Journal of Applied Physics,* vol. 112, p. 104311, 2012.
[485] Y. Hu, M. Li, J. J. He, and R. R. LaPierre, "Current matching and efficiency optimization in a two-junction nanowire-on-silicon solar cell," *Nanotechnology,* vol. 24, 2013.
[486] A. M. Mozharov, A. D. Bolshakov, G. E. Cirlin, D. A. Kudryashov, A. S. Gudovskikh, I. S. Mukhin, and Z. I. Alferov, "Simulation of photovoltaic efficiency of a tandem solar cell on Si with GaN nanowires as an emitter layer," *Journal of Physics: Conference Series,* vol. 690, p. 012041, 2016.
[487] T. Kouno, K. Kishino, K. Yamano, and A. Kikuchi, "Two-dimensional light confinement in periodic InGaN/GaN nanocolumn arrays and optically pumped blue stimulated emission," *Optics Express,* vol. 17, pp. 20440-20447, 2009.
[488] J. D. Joannopoulos, S. G. Johnson, J. N. Winn, and R. D. Meade, *Photonic crystals: molding the flow of light*: Princeton University Press, 2011.
[489] K. Busch, S. Lölkes, R. B. Wehrspohn, and H. Föll, "Photonic crystals," *New York: Willey,* pp. 241-247, 2004.
[490] T. F. Krauss, "Photonic crystals for integrated optics," in *AIP Conf. Proc.*, 2001, pp. 89-98.
[491] J. B. Wright, S. Liu, G. T. Wang, Q. Li, A. Benz, D. D. Koleske, P. Lu, H. Xu, L. Lester, and T. S. Luk, "Multi-colour nanowire photonic crystal laser pixels," *Scientific reports,* vol. 3, 2013.
[492] S. Albert, A. Bengoechea-Encabo, P. Lefebvre, F. Barbagini, M. A. Sanchez-Garcia, E. Calleja, U. Jahn, and A. Trampert, "Selective area growth and characterization of InGaN nano-disks implemented in GaN nanocolumns with different top morphologies," *Applied Physics Letters,* vol. 100, p. 231906, 2012.

[493] K. Katsumi, K. Jumpei, and K. Kouichi, "Near-Infrared InGaN Nanocolumn Light-Emitting Diodes Operated at 1.46 μm," *Applied Physics Express,* vol. 5, p. 031001, 2012.
[494] V. Ramesh, I. Yusuke, and K. Katsumi, "633 nm Red Emissions from InGaN Nanocolumn Light-Emitting Diode by Radio Frequency Plasma Assisted Molecular Beam Epitaxy," *Japanese Journal of Applied Physics,* vol. 52, p. 08JE18, 2013.
[495] K. Kishino and K. Yamano, "Green-Light Nanocolumn Light Emitting Diodes With Triangular-Lattice Uniform Arrays of InGaN-Based Nanocolumns," *Quantum Electronics, IEEE Journal of,* vol. 50, pp. 538-547, 2014.
[496] A. Bengoechea-Encabo, S. Albert, D. Lopez-Romero, P. Lefebvre, F. Barbagini, A. Torres-Pardo, J. M. Gonzalez-Calbet, M. A. Sanchez-Garcia, and E. Calleja, "Light-Emitting-Diodes based on ordered InGaN nanocolumns emitting in the blue, green and yellow spectral range," *Nanotechnology,* vol. 25, p. 435203, 2014.
[497] H. Sekiguchi, K. Kishino, and A. Kikuchi, "Ti-mask Selective-Area Growth of GaN by RF-Plasma-Assisted Molecular-Beam Epitaxy for Fabricating Regularly Arranged InGaN/GaN Nanocolumns," *Applied Physics Express,* vol. 1, p. 124002, 2008.
[498] D. L. Mathine, "The integration of III-V optoelectronics with silicon circuitry," *IEEE Journal of Selected Topics in Quantum Electronics,* vol. 3, pp. 952-959, 1997.
[499] H. Mark, M. Trevor, and S. Peter, "III–V semiconductor devices integrated with silicon," *Semiconductor Science and Technology,* vol. 28, p. 090301, 2013.
[500] M. G. Kibria, F. A. Chowdhury, S. Zhao, B. AlOtaibi, M. L. Trudeau, H. Guo, and Z. Mi, "Visible light-driven efficient overall water splitting using p-type metal-nitride nanowire arrays," *Nature Communications,* vol. 6, p. 6797, 2015.
[501] S. Li and A. Waag, "GaN based nanorods for solid state lighting," *Journal of Applied Physics,* vol. 111, p. 071101, 2012.
[502] L. H.-W., L. Y.-J., C. H.-Y., L. H.-M., and G. S., *Appl. Phys. Lett.,* vol. 97, p. 073101, 2010.
[503] T. M. Adams and R. A. Layton, "The substrate and adding material to it," in *Introductory MEMS: Fabrication and Applications*, ed Boston, MA: Springer US, 2010, pp. 17-63.
[504] S. F. Yu, *Analysis and design of vertical cavity surface emitting lasers*. Hoboken, N.J.: Wiley-Interscience, 2003.
[505] Princetonoptronics. (2018). *VCSEL Diode Laser Advantages*. Available: http://www.princetonoptronics.com/technology/our_technology/
[506] Myvcsel. (2018). *The resource for VCSEL technology*. Available: http://www.myvcsel.com/key-advantages-of-vcsel-technology/
[507] N. Kurose, N. Iwata, I. Kamiya, and Y. Aoyagi, "Formation of conductive spontaneous via holes in AlN buffer layer on n+Si substrate by filling the vias with n-AlGaN by metal organic chemical vapor deposition and application to vertical deep ultraviolet photo-sensor," *AIP Advances,* vol. 4, p. 123007, 2014.
[508] S. Fan, I. Shih, and Z. Mi, "A Monolithically Integrated InGaN Nanowire/Si Tandem Photoanode Approaching the Ideal Bandgap Configuration of 1.75/1.13 eV," *Advanced Energy Materials,* vol. 7, pp. 1600952-n/a, 2017.
[509] K. Kawasaki, C. Koike, Y. Aoyagi, and M. Takeuchi, "Vertical AlGaN deep ultraviolet light emitting diode emitting at 322nm fabricated by the laser lift-off technique," *Applied Physics Letters,* vol. 89, p. 261114, 2006.
[510] K. J. Lee, S. J. Kim, J. J. Kim, K. Hwang, S. T. Kim, and S. J. Park, "Enhanced performance of InGaN/GaN multiple-quantum-well light-emitting diodes grown on nanoporous GaN layers," *Opt Express,* vol. 22 Suppl 4, pp. A1164-73, 2014.

[511] A. Kinoshita, H. Hirayama, M. Ainoya, Y. Aoyagi, and A. Hirata, "Room-temperature operation at 333 nm of Al0.03Ga0.97N/Al0.25Ga0.75N quantum-well light-emitting diodes with Mg-doped superlattice layers," *Applied Physics Letters,* vol. 77, pp. 175-177, 2000.
[512] C. L. Tsai and W. C. Wu, "Effects of Asymmetric Quantum Wells on the Structural and Optical Properties of InGaN-Based Light-Emitting Diodes," *Materials (Basel),* vol. 7, pp. 3758-3771, 2014.
[513] Y. Jiang, Y. Li, Y. Li, Z. Deng, T. Lu, Z. Ma, P. Zuo, L. Dai, L. Wang, H. Jia, W. Wang, J. Zhou, W. Liu, and H. Chen, "Realization of high-luminous-efficiency InGaN light-emitting diodes in the "green gap" range," *Sci Rep,* vol. 5, p. 10883, 2015.
[514] A. L. Bavencove, P. Gilet, A. Dussaigne, L. S. Dang, B. Martin, P. Ferret, J. Eymery, C. Durand, M. Lafossas, D. Salomon, B. André, and F. Levy, "Light emitting diodes based on GaN core/shell wires grown by MOVPE on n-type Si substrate," *Electronics Letters,* vol. 47, pp. 765-767, 2011.
[515] H. Liang, Y. Saripalli, P. K. Kandaswamy, E. P. Carlson, P. Favia, O. Richard, H. Bender, M. Zhao, S. B. Thapa, and E. Vancoille, "Growth techniques to reduce V-defect density in GaN and AlGaN layers grown on 200 mm Si (111) substrate," *physica status solidi (c),* vol. 11, pp. 533-536, 2014.
[516] H. F. Liu, S. B. Dolmanan, L. Zhang, S. J. Chua, D. Z. Chi, M. Heuken, and S. Tripathy, "Influence of stress on structural properties of AlGaN/GaN high electron mobility transistor layers grown on 150 mm diameter Si (111) substrate," *Journal of Applied Physics,* vol. 113, p. 023510, 2013.
[517] C. H. Wu, P. Y. Lee, K. Y. Chen, Y. T. Tseng, Y. L. Wang, and K. Y. Cheng, "Selective area growth of high-density GaN nanowire arrays on Si(111) using thin AlN seeding layers," *Journal of Crystal Growth,* vol. 454, pp. 71-81, 2016.
[518] S. Albert, A. Bengoechea-Encabo, M. A. Sanchez-Garcia, X. Kong, A. Trampert, and E. Calleja, "Selective area growth of In(Ga)N/GaN nanocolumns by molecular beam epitaxy on GaN-buffered Si(111): from ultraviolet to infrared emission," *Nanotechnology,* vol. 24, p. 175303, 2013.
[519] M. D. Brubaker, I. Levin, A. V. Davydov, D. M. Rourke, N. A. Sanford, V. M. Bright, and K. A. Bertness, "Effect of AlN buffer layer properties on the morphology and polarity of GaN nanowires grown by molecular beam epitaxy," *Journal of Applied Physics,* vol. 110, p. 053506, 2011.
[520] Ž. Gačević, A. Bengoechea-Encabo, S. Albert, A. Torres-Pardo, J. M. González-Calbet, and E. Calleja, "Crystallographically uniform arrays of ordered (In)GaN nanocolumns," *Journal of Applied Physics,* vol. 117, p. 035301, 2015.
[521] K. Kishino, T. Hoshino, S. Ishizawa, and A. Kikuchi, "Selective-area growth of GaN nanocolumns on titanium-mask-patterned silicon (111) substrates by RF-plasma-assisted molecular-beam epitaxy," *Electronics Letters,* vol. 44, p. 819, 2008.
[522] Y. Nakada, I. Aksenov, and H. Okumura, "GaN heteroepitaxial growth on silicon nitride buffer layers formed on Si (111) surfaces by plasma-assisted molecular beam epitaxy," *Applied Physics Letters,* vol. 73, pp. 827-829, 1998.
[523] K. Kishino, T. Hoshino, S. Ishizawa, and A. Kikuchi. (2008, Selective-area growth of GaN nanocolumns on titanium-mask-patterned silicon (111) substrates by RF-plasma-assisted molecular-beam epitaxy. *Electronics Letters 44(13),* 819-821. Available: http://digital-library.theiet.org/content/journals/10.1049/el_20081323
[524] J. Piprek and S. Li, "Electron leakage effects on GaN-based light-emitting diodes," *Optical and Quantum Electronics,* vol. 42, pp. 89-95, 2010.

[525] H. P. T. Nguyen, S. Zhang, A. T. Connie, M. G. Kibria, Q. Wang, I. Shih, and Z. Mi, "Breaking the carrier injection bottleneck of phosphor-free nanowire white light-emitting diodes," *Nano Letters,* vol. 13, pp. 5437-5442, 2013.
[526] C. G. V. d. Walle and D. Segev, "Microscopic origins of surface states on nitride surfaces," *Journal of Applied Physics,* vol. 101, p. 081704, 2007.
[527] R. Calarco, T. Stoica, O. Brandt, and L. Geelhaar, "Surface-induced effects in GaN nanowires," *Journal of Materials Research,* vol. 26, pp. 2157-2168, 2011.
[528] A. Armstrong, Q. Li, Y. Lin, A. A. Talin, and G. T. Wang, "GaN nanowire surface state observed using deep level optical spectroscopy," *Applied Physics Letters,* vol. 96, p. 163106, 2010.
[529] P. Tian, J. J. D. McKendry, Z. Gong, B. Guilhabert, I. M. Watson, E. Gu, Z. Chen, G. Zhang, and M. D. Dawson, "Size-dependent efficiency and efficiency droop of blue InGaN micro-light emitting diodes," *Applied Physics Letters,* vol. 101, p. 231110, 2012.
[530] F. Olivier, S. Tirano, L. Dupré, B. Aventurier, C. Largeron, and F. Templier, "Influence of size-reduction on the performances of GaN-based micro-LEDs for display application," *Journal of Luminescence,* vol. 191, pp. 112-116, 2017.
[531] Y. Yang and X. A. Cao, "Removing plasma-induced sidewall damage in GaN-based light-emitting diodes by annealing and wet chemical treatments," *Journal of Vacuum Science & Technology B: Microelectronics and Nanometer Structures Processing, Measurement, and Phenomena,* vol. 27, pp. 2337-2341, 2009.
[532] D. O., H. M., B. J., M. H., and F. i. M. A., "Impact of surfaces on the optical properties of GaAs nanowires," *Appl. Phys. Lett.,* vol. 97, p. 201907, 2010.
[533] H. P. T. Nguyen, M. Djavid, S. Y. Woo, X. Liu, A. T. Connie, S. Sadaf, Q. Wang, G. A. Botton, I. Shih, and Z. Mi, "Engineering the carrier dynamics of InGaN nanowire white light-emitting diodes by distributed p-AlGaN electron blocking layers," *Scientific Reports,* vol. 5, p. 7744, 2015.
[534] M. Pophristic, F. H. Long, C. Tran, I. T. Ferguson, and R. F. K. Jr., "Time-resolved photoluminescence measurements of InGaN light-emitting diodes," *Applied Physics Letters,* vol. 73, pp. 3550-3552, 1998.
[535] F. Olivier, A. Daami, L. Dupré, F. Henry, B. Aventurier, and F. Templier, "25-4: Investigation and Improvement of 10μm Pixel-pitch GaN-based Micro-LED Arrays with Very High Brightness," *SID Symposium Digest of Technical Papers,* vol. 48, pp. 353-356, 2017.
[536] H. David, M. Asad, D. P. Christopher, N. Shuji, and P. D. Steven, "Sustained high external quantum efficiency in ultrasmall blue III–nitride micro-LEDs," *Applied Physics Express,* vol. 10, p. 032101, 2017.
[537] N. L. Ploch, H. Rodriguez, C. Stolmacker, M. Hoppe, M. Lapeyrade, J. Stellmach, F. Mehnke, T. Wernicke, A. Knauer, V. Kueller, M. Weyers, S. Einfeldt, and M. Kneissl, "Effective Thermal Management in Ultraviolet Light-Emitting Diodes With Micro-LED Arrays," *IEEE Transactions on Electron Devices,* vol. 60, pp. 782-786, 2013.
[538] Z. Gong, H. X. Zhang, E. Gu, C. Griffin, M. D. Dawson, V. Poher, G. Kennedy, P. M. W. French, and M. A. A. Neil, "Matrix-Addressable Micropixellated InGaN Light-Emitting Diodes With Uniform Emission and Increased Light Output," *IEEE Transactions on Electron Devices,* vol. 54, pp. 2650-2658, 2007.
[539] J. Herrnsdorf, J. J. D. McKendry, S. Zhang, E. Xie, R. Ferreira, D. Massoubre, A. M. Zuhdi, R. K. Henderson, I. Underwood, S. Watson, A. E. Kelly, E. Gu, and M. D. Dawson, "Active-Matrix GaN Micro Light-Emitting Diode Display With Unprecedented Brightness," *IEEE Transactions on Electron Devices,* vol. 62, pp. 1918-1925, 2015.

[540] Q. Q. Jiao, Z. Z. Chen, J. Ma, S. Y. Wang, Y. Li, S. Jiang, Y. L. Feng, J. Z. Li, Y. F. Chen, T. J. Yu, S. F. Wang, G. Y. Zhang, P. F. Tian, E. Y. Xie, Z. Gong, E. D. Gu, and M. D. Dawson, "Capability of GaN based micro-light emitting diodes operated at an injection level of kA/cm2," *Optics Express,* vol. 23, pp. 16565-16574, 2015.

[541] T.-i. Kim, Y. H. Jung, J. Song, D. Kim, Y. Li, H.-s. Kim, I.-S. Song, J. J. Wierer, H. A. Pao, Y. Huang, and J. A. Rogers, "High-Efficiency, Microscale GaN Light-Emitting Diodes and Their Thermal Properties on Unusual Substrates," *Small,* vol. 8, pp. 1643-1649, 2012.

[542] D. S. Meyaard, Q. Shan, J. Cho, E. F. Schubert, S.-H. Han, M.-H. Kim, C. Sone, S. J. Oh, and J. K. Kim, "Temperature dependent efficiency droop in GaInN light-emitting diodes with different current densities," *Applied Physics Letters,* vol. 100, p. 081106, 2012.

[543] Y. Nagai, H. Sasabe, J. Takahashi, N. Onuma, T. Ito, S. Ohisa, and J. Kido, "Highly efficient, deep-red organic light-emitting devices using energy transfer from exciplexes," *Journal of Materials Chemistry C,* vol. 5, pp. 527-530, 2017.

[544] S. Krotkus, D. Kasemann, S. Lenk, K. Leo, and S. Reineke, "Adjustable white-light emission from a photo-structured micro-OLED array," *Light: Science &Amp; Applications,* vol. 5, p. e16121, 2016.

[545] M. S. Weaver, X. Xu, H. Pang, R. Ma, J. J. Brown, and M.-H. Lu, "47.1: Invited Paper: Color Tunable Phosphorescent White OLED Lighting Panel," *SID Symposium Digest of Technical Papers,* vol. 45, pp. 672-674, 2014.

[546] P. Bhattacharya, A. Hazari, S. Jahangir, W. Guo, and T. Frost, "Chapter Eleven - III-Nitride Electrically Pumped Visible and Near-Infrared Nanowire Lasers on (001) Silicon," in *Semiconductors and Semimetals*. vol. 96, Z. Mi and C. Jagadish, Eds., ed: Elsevier, 2017, pp. 385-409.

[547] C. Tian, W. Wang, J. Liang, Z. Liang, Y. Qin, and J. Lv, "Theoretical and experimental analysis of AlGaInP micro-LED array with square-circle anode," *AIP Advances,* vol. 5, p. 041309, 2015.

[548] S. Fang, W. Wang, J. Liang, Z. Liang, Y. Qin, and J. Lv, "Heat dissipation analysis of bendable AlGaInP micro-LED arrays," *AIP Advances,* vol. 7, p. 015209, 2017.

[549] G. E. Höfler, D. A. Vanderwater, D. C. DeFevere, F. A. Kish, M. D. Camras, F. M. Steranka, and I. H. Tan, "Wafer bonding of 50-mm diameter GaP to AlGaInP-GaP light-emitting diode wafers," *Applied Physics Letters,* vol. 69, pp. 803-805, 1996.

[550] R. Windisch, R. Butendeich, S. Illek, S. Kugler, R. Wirth, H. Zull, and K. Streubel, "100-lm/W InGaAlP Thin-Film Light-Emitting Diodes With Buried Microreflectors," *IEEE Photonics Technology Letters,* vol. 19, pp. 774-776, 2007.

[551] L. J. Mawst, A. Bhattacharya, M. Nesnidal, J. Lopez, D. Botez, J. A. Morris, and P. Zory, "High continuous wave output power InGaAs/InGaAsP/InGaP diode lasers: Effect of substrate misorientation," *Applied Physics Letters,* vol. 67, pp. 2901-2903, 1995.

[552] OSRAM. (2011). *Laboratory Record: Red LED Breaks Through the 200 lm/W Barrier*. Available: http://www.ledinside.com/news/2011/10/osram_20111011

[553] M. R. Krames, M. Ochiai-Holcomb, G. E. Höfler, C. Carter-Coman, E. I. Chen, I.-H. Tan, P. Grillot, N. F. Gardner, H. C. Chui, J.-W. Huang, S. A. Stockman, F. A. Kish, M. G. Craford, T. S. Tan, C. P. Kocot, M. Hueschen, J. Posselt, B. Loh, G. Sasser, and D. Collins, "High-power truncated-inverted-pyramid (AlxGa1−x)0.5In0.5P/GaP light-emitting diodes exhibiting >50% external quantum efficiency," *Applied Physics Letters,* vol. 75, pp. 2365-2367, 1999.

[554] R. G. W. Brown, H. Denboer, H. S. El-Ghoroury, A. J. Lanzone, and D. A. Mcneill, "Quantum photonic imagers and mehods of fabrication thereof," ed: Google Patents, 2010.
[555] A. L. Pyayt, G. K. Starkweather, and M. J. Sinclair, "A high-efficiency display based on a telescopic pixel design," *Nature Photonics,* vol. 2, p. 492, 2008.
[556] S. Zhao, M. G. Kibria, Q. Wang, H. P. T. Nguyen, and Z. Mi, "Growth of large-scale vertically aligned GaN nanowires and their heterostructures with high uniformity on SiOx by catalyst-free molecular beam epitaxy," *Nanoscale Nanoscale,* vol. 5, p. 5283, 2013.
[557] K. M. Lau, K. M. Wong, X. Zou, and P. Chen, "Performance improvement of GaN-based light-emitting diodes grown on patterned Si substrate transferred to copper," *Optics Express,* vol. 19, pp. A956-A961, 2011/07/04 2011.
[558] A. T. M. G. Sarwar, S. D. Carnevale, F. Yang, T. F. Kent, J. J. Jamison, D. W. McComb, and R. C. Myers, "Semiconductor Nanowire Light-Emitting Diodes Grown on Metal: A Direction Toward Large-Scale Fabrication of Nanowire Devices," *Small,* vol. 11, pp. 5402-5408, 2015.
[559] C. Zhao, T. K. Ng, R. T. ElAfandy, A. Prabaswara, G. B. Consiglio, I. A. Ajia, I. S. Roqan, B. Janjua, C. Shen, J. Eid, A. Y. Alyamani, M. M. El-Desouki, and B. S. Ooi, "Droop-Free, Reliable, and High-Power InGaN/GaN Nanowire Light-Emitting Diodes for Monolithic Metal-Optoelectronics," *Nano Letters,* vol. 16, pp. 4616-4623, 2016/07/13 2016.
[560] R.-H. Horng, B.-R. Wu, C.-H. Tien, S.-L. Ou, M.-H. Yang, H.-C. Kuo, and D.-S. Wuu, "Performance of GaN-based light-emitting diodes fabricated using GaN epilayers grown on silicon substrates," *Optics Express,* vol. 22, pp. A179-A187, 2014/01/13 2014.
[561] G. Lozano, S. R. K. Rodriguez, M. A. Verschuuren, and J. Gómez Rivas, "Metallic nanostructures for efficient LED lighting," *Light: Science &Amp; Applications,* vol. 5, p. e16080, 06/03/online 2016.
[562] S.-K. Kim, H. D. Song, H.-S. Ee, H. M. Choi, H. K. Cho, Y.-H. Lee, and H.-G. Park, "Metal mirror assisting light extraction from patterned AlGaInP light-emitting diodes," *Applied Physics Letters,* vol. 94, p. 101102, 2009.
[563] X.-J. Yu, Y. L. Ho, L. Tan, H.-C. Huang, and H.-S. Kwok, "LED-Based Projection Systems," *Journal of Display Technology,* vol. 3, pp. 295-303, 2007.
[564] U. Vogel, P. Wartenberg, B. Richter, S. Brenner, M. Thomschke, K. Fehse, and J. Baumgarten, "Paper No S16.1: SVGA Bidirectional OLED Microdisplay for Near-to-Eye Projection," *SID Symposium Digest of Technical Papers,* vol. 46, pp. 66-66, 2015.
[565] A. Gago-Calderón, J. Fernández-Ramos, and A. Gago-Bohórquez, "Visual quality evaluation of large LED displays based on subjective sensory perception," *Displays,* vol. 34, pp. 359-370, 2013.
[566] E. Chen and T. Guo, "Modified Köhler illumination for LED-based projection display," *Displays,* vol. 35, pp. 84-89, 2014.
[567] M. K. Choi, J. Yang, K. Kang, D. C. Kim, C. Choi, C. Park, S. J. Kim, S. I. Chae, T. H. Kim, J. H. Kim, T. Hyeon, and D. H. Kim, "Wearable red-green-blue quantum dot light-emitting diode array using high-resolution intaglio transfer printing," *Nat Commun,* vol. 6, p. 7149, 2015.
[568] S. Kim, H. J. Kwon, S. Lee, H. Shim, Y. Chun, W. Choi, J. Kwack, D. Han, M. Song, S. Kim, S. Mohammadi, I. Kee, and S. Y. Lee, "Low-power flexible organic light-emitting diode display device," *Adv Mater,* vol. 23, pp. 3511-6, 2011.
[569] S. Fernández-Garrido, J. Grandal, E. Calleja, M. A. Sánchez-García, and D. López-Romero, "A growth diagram for plasma-assisted molecular beam epitaxy of GaN nanocolumns on Si(111)," *Journal of Applied Physics,* vol. 106, p. 126102, 2009.

[570] K. Kishino, H. Sekiguchia, and A. Kikuchi, "Improved Ti-mask selective-area growth (SAG) by rf-plasma-assisted molecular beam epitaxy demonstrating extremely uniform GaN nanocolumn arrays," *Journal of Crystal Growth,* vol. 311, pp. 2063-2068, 2009.
[571] W. S. Wong, T. Sands, and N. W. Cheung, "Damage-free separation of GaN thin films from sapphire substrates," *Applied Physics Letters,* vol. 72, pp. 599-601, 1998.
[572] W. S. Wong, A. B. Wengrow, Y. Cho, A. Salleo, N. J. Quitoriano, N. W. Cheung, and T. Sands, "Integration of GaN thin films with dissimilar substrate materials by Pd-In metal bonding and laser lift-off," *Journal of Electronic Materials,* vol. 28, pp. 1409-1413, December 01 1999.
[573] A. Urban, J. Malindretos, J. H. Klein-Wiele, P. Simon, and A. Rizzi, "Ga-polar GaN nanocolumn arrays with semipolar faceted tips," *New Journal of Physics,* vol. 15, p. 053045, 2013.
[574] S. Y. Woo, N. Gauquelin, H. P. Nguyen, Z. Mi, and G. A. Botton, "Interplay of strain and indium incorporation in InGaN/GaN dot-in-a-wire nanostructures by scanning transmission electron microscopy," *Nanotechnology,* vol. 26, p. 344002, 2015.
[575] Ž. Gačević, N. Vukmirović, N. García-Lepetit, A. Torres-Pardo, M. Müller, S. Metzner, S. Albert, A. Bengoechea-Encabo, F. Bertram, P. Veit, J. Christen, J. M. González-Calbet, and E. Calleja, "Influence of composition, strain, and electric field anisotropy on different emission colors and recombination dynamics from InGaN nanodisks in pencil-like GaN nanowires," *Physical Review B,* vol. 93, 2016.
[576] A. Larrue, C. Wilhelm, G. Vest, S. Combrie, A. de Rossi, and C. Soci, "Monolithic integration of III-V nanowire with photonic crystal microcavity for vertical light emission," *Opt Express,* vol. 20, pp. 7758-70, 2012.
[577] J. Chesin and S. Gradecak, "Comparing directed efficiency of III-nitride nanowire light-emitting diodes," *Journal of Nanophotonics,* vol. 8, p. 083095, 2014.
[578] M. L. Kuo, Y. S. Kim, M. L. Hsieh, and S. Y. Lin, "Efficient and directed Nano-LED emission by a complete elimination of transverse-electric guided modes," *Nano Lett,* vol. 11, pp. 476-81, 2011.
[579] M. E. Reimer, G. Bulgarini, N. Akopian, M. Hocevar, M. B. Bavinck, M. A. Verheijen, E. P. Bakkers, L. P. Kouwenhoven, and V. Zwiller, "Bright single-photon sources in bottom-up tailored nanowires," *Nat Commun,* vol. 3, p. 737, 2012.
[580] N. P. Kobayashi, J. Chesin, X. Zhou, S. Gradečak, A. A. Talin, and M. S. Islam, "Light extraction in individual GaN nanowires on Si for LEDs," *SPIE NanoScience+ Engineering; International Society for Optics and Photonics,* vol. 8467, p. 846703, 2012.
[581] R. Wang, X. Liu, I. Shih, and Z. Mi, "High efficiency, full-color AlInGaN quaternary nanowire light emitting diodes with spontaneous core-shell structures on Si," *Applied Physics Letters,* vol. 106, p. 261104, 2015.
[582] M. G. Kibria, S. Zhao, F. A. Chowdhury, Q. Wang, H. P. Nguyen, M. L. Trudeau, H. Guo, and Z. Mi, "Tuning the surface Fermi level on p-type gallium nitride nanowires for efficient overall water splitting," *Nat Commun,* vol. 5, p. 3825, 2014.
[583] S. Zhao, A. T. Connie, M. H. Dastjerdi, X. H. Kong, Q. Wang, M. Djavid, S. Sadaf, X. D. Liu, I. Shih, H. Guo, and Z. Mi, "Aluminum nitride nanowire light emitting diodes: Breaking the fundamental bottleneck of deep ultraviolet light sources," *Sci Rep,* vol. 5, p. 8332, 2015.
[584] Y.-J. Lu, H.-W. Lin, H.-Y. Chen, Y.-C. Yang, and S. Gwo, "Single InGaN nanodisk light emitting diodes as full-color subwavelength light sources," *Applied Physics Letters,* vol. 98, p. 233101, 2011.
[585] T. Wei, Z. Huo, Y. Zhang, H. Zheng, Y. Chen, J. Yang, Q. Hu, R. Duan, J. Wang, Y. Zeng, and J. Li, "Efficiency enhancement of homoepitaxial InGaN/GaN light-emitting

diodes on free-standing GaN substrate with double embedded SiO2 photonic crystals," *Opt Express,* vol. 22 Suppl 4, pp. A1093-100, 2014.
[586] Q. Shan, D. S. Meyaard, Q. Dai, J. Cho, E. Fred Schubert, J. Kon Son, and C. Sone, "Transport-mechanism analysis of the reverse leakage current in GaInN light-emitting diodes," *Applied Physics Letters,* vol. 99, p. 253506, 2011.
[587] H. P. Nguyen, K. Cui, S. Zhang, M. Djavid, A. Korinek, G. A. Botton, and Z. Mi, "Controlling electron overflow in phosphor-free InGaN/GaN nanowire white light-emitting diodes," *Nano Lett,* vol. 12, pp. 1317-23, 2012.
[588] H. P. Nguyen, M. Djavid, S. Y. Woo, X. Liu, A. T. Connie, S. Sadaf, Q. Wang, G. A. Botton, I. Shih, and Z. Mi, "Engineering the carrier dynamics of InGaN nanowire white light-emitting diodes by distributed p-AlGaN electron blocking layers," *Sci Rep,* vol. 5, p. 7744, 2015.
[589] S. F. Zhang, A. T. Connie, D. A. Laleyan, H. P. T. Nguyen, Q. Wang, J. Song, I. S. Shih, and Z. T. Mi, "On the Carrier Injection Efficiency and Thermal Property of InGaN/GaN Axial Nanowire Light Emitting Diodes," *Ieee Journal of Quantum Electronics,* vol. 50, p. 483, 2014.
[590] C. T. Foxon, S. V. Novikov, J. L. Hall, R. P. Campion, D. Cherns, I. Griffiths, and S. Khongphetsak, "A complementary geometric model for the growth of GaN nanocolumns prepared by plasma-assisted molecular beam epitaxy," *Journal of Crystal Growth,* vol. 311, pp. 3423-3427, 2009.
[591] J. Klafter and M. F. Shlesinger, "On the relationship among three theories of relaxation in disordered systems," *Proceedings of the National Academy of Sciences of the United States of America,* vol. 83, pp. 848-851, 1986.
[592] J. Klafter, A. Blumen, and G. Zumofen, "Fractal behavior in trapping and reaction: A random walk study," *Journal of Statistical Physics,* vol. 36, pp. 561-577, 1984.
[593] M. Gómez-Gómez, N. Garro, J. Segura-Ruiz, G. Martinez-Criado, A. Cantarero, H. T. Mengistu, A. García-Cristóbal, S. Murcia-Mascarós, C. Denker, J. Malindretos, and A. Rizzi, "Spontaneous core–shell elemental distribution in In-rich In x Ga 1−x N nanowires grown by molecular beam epitaxy," *Nanotechnology,* vol. 25, p. 075705, 2014.
[594] A.-L. Bavencove, G. Tourbot, J. Garcia, Y. Désières, P. Gilet, F. Levy, B. André, B. Gayral, B. Daudin, and L. S. Dang, "Submicrometre resolved optical characterization of green nanowire-based light emitting diodes," *Nanotechnology,* vol. 22, p. 345705, 2011.
[595] J. Zhao, H. Sun, S. Dai, Y. Wang, and J. Zhu, "Electrical Breakdown of Nanowires," *Nano Letters,* vol. 11, pp. 4647-4651, 2011.
[596] T. Westover, R. Jones, J. Y. Huang, G. Wang, E. Lai, and A. A. Talin, "Photoluminescence, Thermal Transport, and Breakdown in Joule-Heated GaN Nanowires," *Nano Letters,* vol. 9, pp. 257-263, 2009.
[597] Y. Lin, Q. Li, A. Armstrong, and G. T. Wang, "In situ scanning electron microscope electrical characterization of GaN nanowire nanodiodes using tungsten and tungsten/gallium nanoprobes," *Solid State Communications,* vol. 149, pp. 1608-1610, 2009.
[598] H. P. D. Schenk, E. Frayssinet, A. Bavard, D. Rondi, Y. Cordier, and M. Kennard, "Growth of thick, continuous GaN layers on 4-in. Si substrates by metalorganic chemical vapor deposition," *Journal of Crystal Growth,* vol. 314, pp. 85-91, 2011.
[599] D. Zhu, C. McAleese, M. Häberlen, C. Salcianu, T. Thrush, M. Kappers, A. Phillips, P. Lane, M. Kane, D. Wallis, T. Martin, M. Astles, and C. Humphreys, "InGaN/GaN LEDs grown on Si(111): dependence of device performance on threading dislocation density and emission wavelength," *physica status solidi (c),* vol. 7, pp. 2168-2170, 2010.

[600] M. Zhao, Y. Saripalli, P. K. Kandaswamy, H. Liang, A. Firrincieli, S. Decoutere, and E. Vancoille, "Growth and characterization of DH-HEMT structures with various AlGaN barriers and AlN interlayers on 200 mm Si(111) substrates," *physica status solidi (c),* vol. 11, pp. 446-449, 2014.
[601] S. Tripathy, V. K. X. Lin, S. B. Dolmanan, J. P. Y. Tan, R. S. Kajen, L. K. Bera, S. L. Teo, M. K. Kumar, S. Arulkumaran, G. I. Ng, S. Vicknesh, S. Todd, W. Z. Wang, G. Q. Lo, H. Li, D. Lee, and S. Han, "AlGaN/GaN two-dimensional-electron gas heterostructures on 200 mm diameter Si(111)," *Applied Physics Letters,* vol. 101, p. 082110, 2012.
[602] M. D. Brubaker, S. M. Duff, T. E. Harvey, P. T. Blanchard, A. Roshko, A. W. Sanders, N. A. Sanford, and K. A. Bertness, "Polarity-Controlled GaN/AlN Nucleation Layers for Selective-Area Growth of GaN Nanowire Arrays on Si(111) Substrates by Molecular Beam Epitaxy," *Crystal Growth & Design,* vol. 16, pp. 596-604, 2016.
[603] T. Kusunose, T. Sekino, and K. Niihara, "Production of a grain boundary phase as conducting pathway in insulating AlN ceramics," *Acta Materialia,* vol. 55, pp. 6170-6175, 2007.
[604] H. Ekinci, V. V. Kuryatkov, I. Gherasoiu, S. Y. Karpov, and S. A. Nikishin, "Mechanism of Carrier Transport in Hybrid GaN/AlN/Si Solar Cells," *Journal of Electronic Materials,* vol. 46, pp. 6078-6083, 2017.
[605] P. M. Kaminski, K. Bass, and G. Claudio, "High bandgap dielectrics for antireflective coating in silicon solar cells by reactive ion sputtering," *physica status solidi (c),* vol. 8, pp. 1311-1314, 2011.
[606] G. Krugel, A. Sharma, W. Wolke, J. Rentsch, and R. Preu, "Study of hydrogenated AlN as an anti-reflective coating and for the effective surface passivation of silicon," *physica status solidi (RRL) – Rapid Research Letters,* vol. 7, pp. 457-460, 2013.
[607] C. Wang, W. Cheng, P. Ma, R. Xia, and X. Ling, "High performance Al–AlN solar spectrally selective coatings with a self-assembled nanostructure AlN anti-reflective layer," *J. Mater. Chem. A,* vol. 5, pp. 2852-2860, 2017.
[608] A. Fujishima and K. Honda, "Electrochemical Photolysis of Water at a Semiconductor Electrode," *Nature,* vol. 238, p. 37, 1972.
[609] J. Su, X. Feng, J. D. Sloppy, L. Guo, and C. A. Grimes, "Vertically Aligned WO3 Nanowire Arrays Grown Directly on Transparent Conducting Oxide Coated Glass: Synthesis and Photoelectrochemical Properties," *Nano Letters,* vol. 11, pp. 203-208, 2011.
[610] M. S. Wrighton, A. B. Ellis, P. T. Wolczanski, D. L. Morse, H. B. Abrahamson, and D. S. Ginley, "Strontium titanate photoelectrodes. Efficient photoassisted electrolysis of water at zero applied potential," *Journal of the American Chemical Society,* vol. 98, pp. 2774-2779, 1976.
[611] Y. Lin, S. Zhou, S. W. Sheehan, and D. Wang, "Nanonet-based hematite heteronanostructures for efficient solar water splitting," *Journal of the American Chemical Society,* vol. 133, pp. 2398-401, 2011.
[612] J. Li, J. Y. Lin, and H. X. Jiang, "Direct hydrogen gas generation by using InGaN epilayers as working electrodes," *Applied Physics Letters,* vol. 93, p. 162107, 2008.
[613] L. Caccamo, J. Hartmann, C. Fàbrega, S. Estradé, G. Lilienkamp, J. D. Prades, M. W. G. Hoffmann, J. Ledig, A. Wagner, X. Wang, L. Lopez-Conesa, F. Peiró, J. M. Rebled, H.-H. Wehmann, W. Daum, H. Shen, and A. Waag, "Band Engineered Epitaxial 3D GaN-InGaN Core–Shell Rod Arrays as an Advanced Photoanode for Visible-Light-Driven Water Splitting," *ACS Applied Materials & Interfaces,* vol. 6, pp. 2235-2240, 2014.

[614] Y. J. Hwang, C. H. Wu, C. Hahn, H. E. Jeong, and P. Yang, "Si/InGaN Core/Shell Hierarchical Nanowire Arrays and their Photoelectrochemical Properties," *Nano Letters,* vol. 12, pp. 1678-1682, 2012.
[615] C. Mauder, Ö. Tuna, B. Gutrath, V. Balmes, H. Behmenburg, M. V. Rzheutskii, E. V. Lutsenko, G. P. Yablonskii, M. Noyong, U. Simon, M. Heuken, H. Kalisch, and A. Vescan, "Highly n-type doped InGaN films for efficient direct solar hydrogen generation," *physica status solidi (c),* vol. 9, pp. 964-967, 2012.
[616] C. Pendyala, J. B. Jasinski, J. H. Kim, V. K. Vendra, S. Lisenkov, M. Menon, and M. K. Sunkara, "Nanowires as semi-rigid substrates for growth of thick, InxGa1-xN (x > 0.4) epi-layers without phase segregation for photoelectrochemical water splitting," *Nanoscale,* vol. 4, pp. 6269-6275, 2012.
[617] S. Fan, S. Y. Woo, S. Vanka, G. A. Botton, and Z. Mi, "An In0.5Ga0.5N nanowire photoanode for harvesting deep visible light photons," *APL Materials,* vol. 4, p. 076106, 2016.
[618] J. Benton, J. Bai, and T. Wang, "Significantly enhanced performance of an InGaN/GaN nanostructure based photo-electrode for solar power hydrogen generation," *Applied Physics Letters,* vol. 103, p. 133904, 2013.
[619] B. AlOtaibi, H. P. T. Nguyen, S. Zhao, M. G. Kibria, S. Fan, and Z. Mi, "Highly Stable Photoelectrochemical Water Splitting and Hydrogen Generation Using a Double-Band InGaN/GaN Core/Shell Nanowire Photoanode," *Nano Letters,* vol. 13, pp. 4356-4361, 2013.
[620] R. Dahal, B. N. Pantha, J. Li, J. Y. Lin, and H. X. Jiang, "Realizing InGaN monolithic solar-photoelectrochemical cells for artificial photosynthesis," *Applied Physics Letters,* vol. 104, p. 143901, 2014.
[621] S. Fan, B. AlOtaibi, S. Y. Woo, Y. Wang, G. A. Botton, and Z. Mi, "High Efficiency Solar-to-Hydrogen Conversion on a Monolithically Integrated InGaN/GaN/Si Adaptive Tunnel Junction Photocathode," *Nano Letters,* vol. 15, pp. 2721-2726, 2015.
[622] B. AlOtaibi, M. Harati, S. Fan, S. Zhao, H. P. T. Nguyen, M. G. Kibria, and Z. Mi, "High efficiency photoelectrochemical water splitting and hydrogen generation using GaN nanowire photoelectrode," *Nanotechnology,* vol. 24, p. 175401, 2013.
[623] Y. Wang, B. AlOtaibi, F. A. Chowdhury, S. Fan, M. G. Kibria, L. Li, C.-J. Li, and Z. Mi, "Photoelectrochemical reduction of carbon dioxide using Ge doped GaN nanowire photoanodes," *APL Materials,* vol. 3, p. 116106, 2015.
[624] F. Meillaud, A. Shah, C. Droz, E. Vallat-Sauvain, and C. Miazza, "Efficiency limits for single-junction and tandem solar cells," *Solar Energy Materials and Solar Cells,* vol. 90, pp. 2952-2959, 2006.
[625] A. S. Walton, C. S. Allen, K. Critchley, M. Ł. Górzny, J. E. M. c. Kendry, R. M. D. Brydson, B. J. Hickey, and S. D. Evans, "Four-probe electrical transport measurements on individual metallic nanowires," *Nanotechnology,* vol. 18, p. 065204, 2007.
[626] G. Chen, E. M. Gallo, J. Burger, B. Nabet, A. Cola, P. Prete, N. Lovergine, and J. E. Spanier, "On direct-writing methods for electrically contacting GaAs and Ge nanowire devices," *Applied Physics Letters,* vol. 96, p. 223107, 2010.
[627] A. Vilà, F. Hernández-Ramirez, J. Rodríguez, O. Casals, A. Romano-Rodríguez, J. R. Morante, and M. Abid, "Fabrication of metallic contacts to nanometre-sized materials using a focused ion beam (FIB)," *Materials Science and Engineering: C,* vol. 26, pp. 1063-1066, 2006.
[628] I. Utke, P. Hoffmann, and J. Melngailis, "Gas-assisted focused electron beam and ion beam processing and fabrication," *Journal of Vacuum Science & Technology B: Microelectronics and Nanometer Structures Processing, Measurement, and Phenomena,* vol. 26, pp. 1197-1276, 2008.

[629] Q. Juntian, L. Martin, H. Michael, and L. Xinyu, "Investigating the impact of SEM chamber conditions and imaging parameters on contact resistance of in situ nanoprobing," *Nanotechnology,* vol. 28, p. 345702, 2017.
[630] F. A. Faria, J. Guo, P. Zhao, G. Li, P. K. Kandaswamy, M. Wistey, H. Xing, and D. Jena, "Ultra-low resistance ohmic contacts to GaN with high Si doping concentrations grown by molecular beam epitaxy," *Applied Physics Letters,* vol. 101, p. 032109, 2012.
[631] S. M. Sze and K. K. Ng, *Physics of semiconductor devices*. Hoboken, N.J.: Wiley-Interscience, 2007.
[632] Y. Huang, X. Duan, Y. Cui, and C. M. Lieber, "Gallium Nitride Nanowire Nanodevices," *Nano Letters,* vol. 2, pp. 101-104, 2002.
[633] J. Zhao, J.-Q. Huang, F. Wei, and J. Zhu, "Mass Transportation Mechanism in Electric-Biased Carbon Nanotubes," *Nano Letters,* vol. 10, pp. 4309-4315, 2010.
[634] S. I. Lopatin, V. L. Stolyarova, V. G. Sevast'yanov, P. Y. Nosatenko, V. V. Gorskii, D. V. Sevast'yanov, and N. T. Kuznetsov, "Determination of the saturation vapor pressure of silicon by Knudsen cell mass spectrometry," *Russian Journal of Inorganic Chemistry,* vol. 57, pp. 219-225, 2012.
[635] B. W. Liou, "Design and fabrication of InxGa1−xN/GaN solar cells with a multiple-quantum-well structure on SiCN/Si(111) substrates," *Thin Solid Films,* vol. 520, pp. 1084-1090, 2011/11/30/ 2011.
[636] J. M. Gee and G. F. Virshup, "A 31%-efficient GaAs/silicon mechanically stacked, multijunction concentrator solar cell," in *Photovoltaic Specialists Conference, 1988., Conference Record of the Twentieth IEEE*, 1988, pp. 754-758 vol.1.
[637] Y. Yazawa, K. Tamura, S. Watahiki, T. Kitatani, H. Ohtsuka, and T. Warabisako, "Three-junction solar cells comprised of a thin-film GaInP/GaAs tandem cell mechanically stacked on a Si cell," in *Photovoltaic Specialists Conference, 1997., Conference Record of the Twenty-Sixth IEEE*, 1997, pp. 899-902.
[638] K. Derendorf, S. Essig, E. Oliva, V. Klinger, T. Roesener, S. P. Philipps, J. Benick, M. Hermle, M. Schachtner, G. Siefer, J. W, x00E, ger, and F. Dimroth, "Fabrication of GaInP/GaAs//Si Solar Cells by Surface Activated Direct Wafer Bonding," *IEEE Journal of Photovoltaics,* vol. 3, pp. 1423-1428, 2013.
[639] K. Tanabe, K. Watanabe, and Y. Arakawa, "III-V/Si hybrid photonic devices by direct fusion bonding," *Scientific Reports,* vol. 2, p. 349, 2012.
[640] Y.-L. Hu, R. M. Farrell, C. J. Neufeld, M. Iza, S. C. Cruz, N. Pfaff, D. Simeonov, S. Keller, S. Nakamura, S. P. DenBaars, U. K. Mishra, and J. S. Speck, "Effect of quantum well cap layer thickness on the microstructure and performance of InGaN/GaN solar cells," *Applied Physics Letters,* vol. 100, p. 161101, 2012.
[641] M. G. Kibria, S. Zhao, F. A. Chowdhury, Q. Wang, H. P. Nguyen, M. L. Trudeau, H. Guo, and Z. Mi, *Nat. Commun.,* vol. 5, p. 3825, 2014.
[642] S. Zhao, A. T. Connie, M. H. Dastjerdi, X. H. Kong, Q. Wang, M. Djavid, S. Sadaf, X. D. Liu, I. Shih, H. Guo, and Z. Mi, *Sci. Rep.,* vol. 5, p. 8332, 2015.
[643] O. Demichel, M. Heiss, J. Bleuse, H. Mariette, and A. F. i. Morral, "Impact of surfaces on the optical properties of GaAs nanowires," *Applied Physics Letters,* vol. 97, p. 201907, 2010.
[644] J. A. Czaban, D. A. Thompson, and R. R. LaPierre, "GaAs Core−Shell Nanowires for Photovoltaic Applications," *Nano Letters,* vol. 9, pp. 148-154, 2009.
[645] F. C. Mehmet, M. H. Samir, P. N. Dever, K. Filiz, B. Emad, K. Tansel, and S. Hye-Won, "PiN InGaN nanorod solar cells with high short-circuit current," *Applied Physics Express,* vol. 8, p. 042302, 2015.

[646] J. W. Jonathan, Jr., L. Qiming, D. K. Daniel, R. L. Stephen, and T. W. George, "III-nitride core–shell nanowire arrayed solar cells," *Nanotechnology,* vol. 23, p. 194007, 2012.
[647] E. F. Schubert, *Light-emitting diodes*. Cambridge, Uk; New York: Cambridge University Press, 2003.
[648] Y. Kanemitsu, M. Okano, L. Q. Phuong, and Y. Yamada, "Review—Light Emission from Thin Film Solar Cell Materials: An Emerging Infrared and Visible Light Emitter," *ECS Journal of Solid State Science and Technology,* vol. 7, pp. R3102-R3110, 2018.
[649] K.-T. Chen, C.-F. Lin, C.-M. Lin, C.-C. Yang, and R.-H. Jiang, "InGaN-based light-emitting solar cells with a pattern-nanoporous p-type GaN:Mg layer," *Thin Solid Films,* vol. 518, pp. 7377-7380, 2010.
[650] E. Yablonovitch, O. D. Miller, and S. R. Kurtz, "The opto-electronic physics that broke the efficiency limit in solar cells," in *2012 38th IEEE Photovoltaic Specialists Conference*, 2012, pp. 001556-001559.
[651] O. D. Miller, E. Yablonovitch, and S. R. Kurtz, "Strong Internal and External Luminescence as Solar Cells Approach the Shockley–Queisser Limit," *IEEE Journal of Photovoltaics,* vol. 2, pp. 303-311, 2012.
[652] A. Krishnappa, "LEDs application in solar cells in a unique way," in *2015 National Aerospace and Electronics Conference (NAECON)*, 2015, pp. 119-122.
[653] ScienceDaily. *Scientists discover material that can be solar cell by day, light panel by night, Nanyang Technological University*. Available: www.sciencedaily.com/releases/2014/03/140324090240.htm
[654] J.-L. Liu, J.-L. Zhang, G.-X. Wang, C.-L. Mo, L.-Q. Xu, J. Ding, Z.-J. Quan, X.-L. Wang, S. Pan, C.-D. Zheng, X.-M. Wu, W.-Q. Fang, and F.-Y. Jiang, "Status of GaN-based green light-emitting diodes," *Chinese Physics B,* vol. 24, p. 067804, 2015.
[655] M. Takashi, Y. Motokazu, and N. Shuji, "Current and Temperature Dependences of Electroluminescence of InGaN-Based UV/Blue/Green Light-Emitting Diodes," *Japanese Journal of Applied Physics,* vol. 37, p. L1358, 1998.
[656] K. Kishino and K. Yamano, "Green-Light Nanocolumn Light Emitting Diodes With Triangular-Lattice Uniform Arrays of InGaN-Based Nanocolumns," *IEEE Journal of Quantum Electronics,* vol. 50, pp. 538-547, 2014.
[657] K. Kishino, H. Sekiguchi, and A. Kikuchi, *J. Cryst. Growth,* vol. 311, p. 2063, 2009.
[658] K. Y. Lai, T. Paskova, V. D. Wheeler, T. Y. Chung, J. A. Grenko, M. A. L. Johnson, K. Udwary, E. A. Preble, and K. R. Evans, "Indium incorporation in InGaN/GaN quantum wells grown on m-plane GaN substrate and c-plane sapphire," *physica status solidi (a),* vol. 209, pp. 559-564, 2012.
[659] P. Lefebvre and B. Gayral, "Optical properties of GaN/AlN quantum dots," *Comptes Rendus Physique,* vol. 9, pp. 816-829, 2008.
[660] T. Kuroda, A. Tackeuchi, and T. Sota, "Luminescence energy shift and carrier lifetime change dependence on carrier density in In0.12Ga0.88N/In0.03Ga0.97N quantum wells," *Applied Physics Letters,* vol. 76, pp. 3753-3755, 2000.
[661] A. Chernikov, S. Schäfer, M. Koch, S. Chatterjee, B. Laumer, and M. Eickhoff, "Probing carrier populations in ZnO quantum wells by screening of the internal electric fields," *Physical Review B,* vol. 87, 2013.
[662] L. F. Zagonel, L. H. G. Tizei, G. Z. Vitiello, G. Jacopin, L. Rigutti, M. Tchernycheva, F. H. Julien, R. Songmuang, T. Ostasevicius, F. de la Peña, C. Ducati, P. A. Midgley, and M. Kociak, "Nanometer-scale monitoring of quantum-confined Stark effect and emission efficiency droop in multiple GaN/AlN quantum disks in nanowires," *Physical Review B,* vol. 93, 2016.

[663] M. A. Green, "Solar cells: operating principles, technology and system applications," *Solar Energy* vol. 28, p. 447, 1982.
[664] Y.-H. Ra, R. Wang, S. Y. Woo, M. Djavid, S. M. Sadaf, J. Lee, G. A. Botton, and Z. Mi, "Full-Color Single Nanowire Pixels for Projection Displays," *Nano Letters,* vol. 16, pp. 4608-4615, 2016.
[665] J. Qu, R. Wang, I. Shih, Z. Mi, and X. Liu, *Appl. Phys. Lett.,* Submitted.
[666] M. R. Krames, O. B. Shchekin, R. Mueller-Mach, G. Mueller, L. Zhou, G. Harbers, and M. G. Craford, "Status and Future of High-Power Light-Emitting Diodes for Solid-State Lighting," *Journal of Display Technology,* vol. 3, pp. 160-175, 2007.
[667] *Solid-state lighting research and development multi-year program plan*. Available: prepared by Bardsley Consulting, SB Consulting, SSLS, Inc., LED Lighting Advisors, and Navigant Consulting, Inc., for U.S. Department of Energy 2014; pp 1– 95.
[668] H. Yuji, A. Chihaya, T. Tetsuo, and S. Shogo, "Blue-Light-Emitting Organic Electroluminescent Devices with Oxadiazole Dimer Dyes as an Emitter," *Japanese Journal of Applied Physics,* vol. 31, p. 1812, 1992.
[669] S. Fery-Forgues, M. Abyan, and J. F. Lamere, "Nano- and microparticles of organic fluorescent dyes: self-organization and optical properties," *Ann N Y Acad Sci,* vol. 1130, pp. 272-9, 2008.
[670] C. D. Dimitrakopoulos and P. R. L. Malenfant, "Organic Thin Film Transistors for Large Area Electronics," *ADMA Advanced Materials,* vol. 14, pp. 99-117, 2002.
[671] S. Nakamura, M. Senoh, N. Iwasa, and S. Nagahama, "High-Power Ingan Single-Quantum-Well-Structure Blue and Violet Light-Emitting-Diodes," *Applied Physics Letters,* vol. 67, pp. 1868-1870, 1995.
[672] S. Pimputkar, J. S. Speck, S. P. DenBaars, and S. Nakamura, "Prospects for LED lighting," *Nature Photonics,* vol. 3, pp. 179-181, 2009.
[673] B. O. Jung, S.-Y. Bae, S. Y. Kim, S. Lee, J. Y. Lee, D.-S. Lee, Y. Kato, Y. Honda, and H. Amano, "Highly ordered catalyst-free InGaN/GaN core–shell architecture arrays with expanded active area region," *Nano Energy,* vol. 11, pp. 294-303, 2015.
[674] D. Simeonov, M. Y. Tsai, H. T. Chen, C. Weisbuch, and J. Speck, "Bonding of nitride based LEDs on tin oxide templates for advanced optoelectronic devices," *Electronics Letters,* vol. 47, pp. 556-558, 2011.
[675] R. A. Bernal, R. Agrawal, B. Peng, K. A. Bertness, N. A. Sanford, A. V. Davydov, and H. D. Espinosa, "Effect of growth orientation and diameter on the elasticity of GaN nanowires. A combined in situ TEM and atomistic modeling investigation," *Nano Lett,* vol. 11, pp. 548-55, 2011.
[676] F. Bernardini, V. Fiorentini, and D. Vanderbilt, "Spontaneous polarization and piezoelectric constants of III-V nitrides," *Physical Review B,* vol. 56, pp. 10024-10027, 1997.
[677] C. G. Tu, C. Y. Su, C. H. Liao, C. Hsieh, Y. F. Yao, H. T. Chen, C. H. Lin, C. M. Weng, Y. W. Kiang, and C. C. Yang, "Regularly patterned multi-section GaN nanorod arrays grown with a pulsed growth technique," *Nanotechnology,* vol. 27, p. 025303, 2016.
[678] C.-G. Tu, C.-Y. Su, C.-H. Liao, C. Hsieh, Y.-F. Yao, H.-T. Chen, C.-H. Lin, H.-S. Chen, Y.-W. Kiang, and C. C. Yang, "Regularly-patterned nanorod light-emitting diode arrays grown with metalorganic vapor-phase epitaxy," *Superlattices and Microstructures,* vol. 83, pp. 329-341, 2015.
[679] J. W. Ager, L. A. Reichertz, Y. Cui, Y. E. Romanyuk, D. Kreier, S. R. Leone, K. M. Yu, W. J. Schaff, and W. Walukiewicz, "Electrical properties of InGaN-Si heterojunctions," *Physica Status Solidi (C),* vol. 6, pp. S413-S416, 2009.
[680] L. Hsu and W. Walukiewicz, "Modeling of InGaN/Si tandem solar cells," *Journal of Applied Physics,* vol. 104, p. 024507, 2008.

[681] S. Ishizawa, K. Kishino, R. Araki, A. Kikuchi, and S. Sugimoto, "Optically Pumped Green (530–560 nm) Stimulated Emissions from InGaN/GaN Multiple-Quantum-Well Triangular-Lattice Nanocolumn Arrays," *Applied Physics Express,* vol. 4, p. 055001, 2011.
[682] M. A. Khan, D. T. Olson, J. M. Van Hove, and J. N. Kuznia, "Vertical-cavity, room-temperature stimulated emission from photopumped GaN films deposited over sapphire substrates using low-pressure metalorganic chemical vapor deposition," *Applied Physics Letters,* vol. 58, p. 1515, 1991.
[683] J. M. Redwing, D. A. S. Loeber, N. G. Anderson, M. A. Tischler, and J. S. Flynn, "An optically pumped GaN–AlGaN vertical cavity surface emitting laser," *Applied Physics Letters,* vol. 69, p. 1, 1996.
[684] H. Zhou, M. Diagne, E. Makarona, A. V. Nurmikko, J. Han, K. E. Waldrip, and J. J. Figiel, "Near ultraviolet optically pumped vertical cavity laser," *Electronics Letters,* vol. 36, p. 1777, 2000.
[685] A. Nurmikko and J. Han, "Blue and near-ultraviolet vertical-cavity surface-emitting lasers," *MRS Bulletin* vol. 27, p. 502, 2002.
[686] C.-C. Kao, Y. C. Peng, H. H. Yao, J. Y. Tsai, Y. H. Chang, J. T. Chu, H. W. Huang, T. T. Kao, T. C. Lu, H. C. Kuo, S. C. Wang, and C. F. Lin, "Fabrication and performance of blue GaN-based vertical-cavity surface emitting laser employing AlN/GaN and Ta_2O_5/SiO_2 distributed bragg reflector," *Applied Physics Letters,* vol. 87, p. 081105, 2005.
[687] S.-H. Park, J. Kim, H. Jeon, T. Sakong, S.-N. Lee, S. Chae, Y. Park, C.-H. Jeong, G.-Y. Yeom, and Y.-H. Cho, "Room-temperature GaN vertical-cavity surface-emitting laser operation in an extended cavity scheme," *Applied Physics Letters,* vol. 83, p. 2121, 2003.
[688] T. Tawara, H. Gotoh, T. Akasaka, N. Kobayashi, and T. Saitoh, "Low-threshold lasing of InGaN vertical-cavity surface-emitting lasers with dielectric distributed Bragg reflectors," *Applied Physics Letters,* vol. 83, p. 830, 2003.
[689] C. Holder, J. S. Speck, S. P. DenBaars, S. Nakamura, and D. Feezell, "Demonstration of nonpolar GaN-based vertical-cavity surface-emitting lasers," *Applied Physics Express,* vol. 5, p. 092104, 2012.
[690] K. Busch, S. Lölkes, R. B. Wehrspohn, and H. Föll, *Photonic crystals*: New York: Willey, 2004.
[691] T. F. Krauss, "Photonic crystals for integrated optics," in *AIP Conference Proceedings*, 2001, pp. 89-98.
[692] K. Hirose, Y. Liang, Y. Kurosaka, A. Watanabe, T. Sugiyama, and S. Noda, "Watt-class high-power, high-beam-quality photonic-crystal lasers," *Nature Photonics,* vol. 8, pp. 406-411, 2014.
[693] H. Matsubara, S. Yoshimoto, H. Saito, Y. Jianglin, Y. Tanaka, and S. Noda, "GaN Photonic-Crystal Surface-Emitting Laser at Blue-Violet Wavelengths," *Science,* vol. 319, pp. 445-447, 2008.
[694] R. M. Soneira, "Galaxy S7 OLED Display Technology Shoot-Out," *Displaymate,* vol. http://www.displaymate.com/Galaxy_S7_ShootOut_1.htm, 2016.
[695] S. Park, J. T. Lim, W.-Y. Jin, H. Lee, B.-H. Kwon, N. S. Cho, J.-H. Han, J.-W. Kang, S. Yoo, and J.-I. Lee, "Efficient Large-Area Transparent OLEDs Based on a Laminated Top Electrode with an Embedded Auxiliary Mesh," *ACS Photonics,* vol. 4, pp. 1114-1122, 2017.
[696] M. J. Cich, R. I. Aldaz, A. Chakraborty, A. David, M. J. Grundmann, A. Tyagi, M. Zhang, F. M. Steranka, and M. R. Krames, "Bulk GaN based violet light-emitting

diodes with high efficiency at very high current density," *Applied Physics Letters,* vol. 101, p. 223509, 2012.
[697] J. Edmond, A. Abare, M. Bergman, J. Bharathan, K. Lee Bunker, D. Emerson, K. Haberern, J. Ibbetson, M. Leung, P. Russel, and D. Slater, "High efficiency GaN-based LEDs and lasers on SiC," *Journal of Crystal Growth,* vol. 272, pp. 242-250, 2004.
[698] Y. Shuichiro, Z. Yuji, P. Chih-Chien, B. C. Roy, F. Kenji, S. Junichi, P. D. Steven, and N. Shuji, "High-Efficiency Single-Quantum-Well Green and Yellow-Green Light-Emitting Diodes on Semipolar (2021) GaN Substrates," *Applied Physics Express,* vol. 3, p. 122102, 2010.
[699] A. I. Alhassan, R. M. Farrell, B. Saifaddin, A. Mughal, F. Wu, S. P. DenBaars, S. Nakamura, and J. S. Speck, "High luminous efficacy green light-emitting diodes with AlGaN cap layer," *Optics Express,* vol. 24, pp. 17868-17873, 2016.
[700] H. Sato, R. B. Chung, H. Hirasawa, N. Fellows, H. Masui, F. Wu, M. Saito, K. Fujito, J. S. Speck, S. P. DenBaars, and S. Nakamura, "Optical properties of yellow light-emitting diodes grown on semipolar (112¯2) bulk GaN substrates," *Applied Physics Letters,* vol. 92, p. 221110, 2008.
[701] I. Titkov, S. Karpov, A. Yadav, D. Mamedov, V. Zerova, and E. Rafailov, "Efficiency of True-Green Light Emitting Diodes: Non-Uniformity and Temperature Effects," *Materials,* vol. 10, p. 1323, 2017.
[702] A.-J. Tzou, D.-W. Lin, C.-R. Yu, Z.-Y. Li, Y.-K. Liao, B.-C. Lin, J.-K. Huang, C.-C. Lin, T. S. Kao, H.-C. Kuo, and C.-Y. Chang, "High-performance InGaN-based green light-emitting diodes with quaternary InAlGaN/GaN superlattice electron blocking layer," *Optics Express,* vol. 24, pp. 11387-11395, 2016.
[703] C. Wetzel, M. Zhu, Y. Li, W. Hou, L. Zhao, W. Zhao, S. You, C. Stark, Y. Xia, M. DiBiccari, and T. Detchprohm, "Green LED development in polar and non-polar growth orientation," in *SPIE Optical Engineering + Applications*, 2009, p. 15.
[704] S. Shinji, H. Rei, H. Jongil, and N. Shinya, "InGaN Light-Emitting Diodes on c -Face Sapphire Substrates in Green Gap Spectral Range," *Applied Physics Express,* vol. 6, p. 111004, 2013.
[705] T. Shioda, H. Yoshida, K. Tachibana, N. Sugiyama, and S. Nunoue, "Enhanced light output power of green LEDs employing AlGaN interlayer in InGaN/GaN MQW structure on sapphire (0001) substrate," *physica status solidi (a),* vol. 209, pp. 473-476, 2012.
[706] K. Lee, H. Lee, C.-R. Lee, T.-H. Chung, Y. S. Kim, J.-Y. Leem, K.-U. Jeong, and J. S. Kim, "Yellow-red light-emitting diodes using periodic Ga-flow interruption during deposition of InGaN well," *Optics Express,* vol. 25, pp. 15152-15160, 2017.
[707] W. Zhao, E. Belhaire, Q. Mistral, C. Chappert, V. Javerliac, B. Dieny, and E. Nicolle, "Macro-model of Spin-Transfer Torque based Magnetic Tunnel Junction device for hybrid Magnetic-CMOS design," in *2006 IEEE International Behavioral Modeling and Simulation Workshop*, 2006, pp. 40-43.
[708] Y. J. Lee, H. C. Tseng, H. C. Kuo, S. C. Wang, C. W. Chang, T. C. Hsu, Y. L. Yang, M. H. Hsieh, M. J. Jou, and B. J. Lee, "Improvement in light-output efficiency of AlGaInP LEDs fabricated on stripe patterned epitaxy," *IEEE Photonics Technology Letters,* vol. 17, pp. 2532-2534, 2005.
[709] K. Streubel, N. Linder, R. Wirth, and A. Jaeger, "High brightness AlGaInP light-emitting diodes," *IEEE Journal of Selected Topics in Quantum Electronics,* vol. 8, pp. 321-332, 2002.
[710] OSRAM. (2015). *Osram Expands Automotive LED Chip Portfolio*. Available: https://www.ledinside.com/products/2015/4/osram_expands_automotive_led_chip_portfolio

[711] N. F. Gardner, H. C. Chui, E. I. Chen, M. R. Krames, J.-W. Huang, F. A. Kish, S. A. Stockman, C. P. Kocot, T. S. Tan, and N. Moll, "1.4× efficiency improvement in transparent-substrate (AlxGa1−x)0.5In0.5P light-emitting diodes with thin (⩽2000 Å) active regions," *Applied Physics Letters,* vol. 74, pp. 2230-2232, 1999.

[712] F. A. Kish, F. M. Steranka, D. C. DeFevere, D. A. Vanderwater, K. G. Park, C. P. Kuo, T. D. Osentowski, M. J. Peanasky, J. G. Yu, R. M. Fletcher, D. A. Steigerwald, M. G. Craford, and V. M. Robbins, "Very high-efficiency semiconductor wafer-bonded transparent-substrate (AlxGa1−x)0.5In0.5P/GaP light-emitting diodes," *Applied Physics Letters,* vol. 64, pp. 2839-2841, 1994.